Technische Universität Kaiserslautern

Fachbereich Chemie

Chemistry of Microsolvated Metal Ions

Björn M. Reinhard

Betreuer: Prof. Dr. G. Niedner-Schatteburg

Dem Fachbereich Chemie der Technischen Universität Kaiserslautern zur Erlangung des akademischen Grades „Doktor der Naturwissenschaften“ eingereichte Dissertation.

Datum des Antrages auf Eröffnung des Promotionsverfahrens: 29.10.2003

“One of the most challenging and scientifically exciting problems in the field of chemical physics is to elucidate the influence which solvation, degree of aggregation and the proximity of solute complexes have on the reactions and properties of reactive species, to contrast differences in their behavior between the gaseous and condensed phase and to attempt to relate the large body of detailed information known about the gas-phase to understanding phenomena in the condensed phase”

A. W. Castleman, Jr.

Contents

1. Introduction

Most chemical and biochemical processes take place in solution. A thorough understanding of solvation, the process by which solvent molecules surround and interact with solute ions or molecules, is therefore mandatory, in order to be able to predict the properties and reactivity of ions and molecules in solution. In the liquid phase atoms and molecules are in perpetual motion due to thermal excitation and quantum mechanical tunneling. In hydrogen-bonded systems the hydrogen-bonded vibrations are strongly coupled to the low-frequency local motions, contributing to strong homogenous broadening. Experimentally one usually observes broad nearly featureless spectral lines due to the intrinsic broadening of the states and due to spatial and temporal averaging. For these reasons the investigation of the solvation process in the condensed phase is complicated. In addition liquid phase studies of solvent-solute interactions are perturbed by superimposed solvent-solvent interactions which prevent us from gaining detailed information about the solvent-solute interactions.[1]

The approach to study the molecular foundation of the solvation process in gaseous clusters has distinct advantages to liquid phase studies. Provided that one can control the temperature, which in systems of limited size is best defined as the kinetic energy of the heavy particles divided by the numbers of degrees of freedom, a cluster serves as an isolated system with a defined configuration which helps to reveal fundamental properties of the clusters pertaining to energy transfer, reaction dynamics and intermolecular forces. The number of books, reviews and conferences dedicated to this field of research is abundant.[2-14] Cluster properties measured as a function of cluster size are expected to shed light to the basic understanding of the transition from gas to condensed phase. Investigation of ionic clusters has further advantages over analogous neutral clusters because mass selection can be performed prior to experimentation. Finite clusters are not only easier to study experimentally than bulk phase solutions, but they also have the advantage to be amenable to ab inito calculations, which allow for a quantum chemical modelling of the experimentally observed properties and reactivity.[15-16]

For the reasons given above solvated (metal) ions are appropriate model systems for understanding solution chemistry on a molecular level and have attracted significant interest. Solvation[17-23] and hydration[24-44] of metal ions was subject to different experimental and theoretical studies. The thermochemistry of solvated metal ions was investigated by high-pressure mass spectrometry and collision induced dissociation studies.[24-26,38] The structure of solvated metal ions and the organization of the solvent molecules around the metal ion into solvation shells was investigated through spectroscopic[42-44] and computational methods[34-37, 39-41].

Recently it was revealed that ionized solvent clusters and solvated ions represent microsolutions which allow for the investigation of condensed phase reactions under well defined conditions in the gas-phase.[45-54] These microsolutions are especially relevant as model systems for polar stratospheric clouds, where chemical reactions with direct impact on the climate take place in small water droplets.[6,55] Water is by far the most important solvent on earth as most biological processes are unthinkable without it. The presence of life itself on our planet does depend on the ubiquity of water in large areas of our planet. The physico-chemical properties of water, such as its polar nature, high dielectricity constant and ability to form hydrogen bonds, along with its abundance on our planet make water the solvent of life. Due to its eminent importance most of the work reported in this thesis deals with the solvent water.

In this work different experimental and theoretical techniques have been applied to study both structure and reactivity of microsolvated and chelated metal ions. In chapters three - five the properties of aqueous microsolutions of magnesium and aluminum monocations are investigated by ab initio calculations. By quantum chemical modelling of recent experimental observations[1], conclusive interpretation of the strongly cluster size dependent reactivity of cationic magnesium and aluminum water clusters are presented. In chapter five the electronic and geometric structures of hydrated magnesium anions are investigated as function of cluster size. Different potential decay channels of these clusters are proposed and compared. The performed studies reveal a potential co-existence of metal atoms and even metal ions and hydrated electrons in water clusters of finite size. This is important from a fundamental point of view, but also has direct consequences on the perception of everyday processes such as the corrosion of bulk metal under humid conditions.

Metal ions have tremendous significance in biological systems, they are constituent part of many biological active compounds like metalloproteins, and their concentrations within the cell lysate plays a major role in different regulative mechanisms. However metal ions are also potentially toxic as they can denature biomolecules if they coordinate unspecifically to available coordination sites. High affinity chelate ligands for various metal ions prevent high concentrations of (chelate ligand) free, hydrated metal ions under physiological conditions. These chelate ligands compete with other possible ligands, first of all water, but also other biomolecules contained in the cell for coordination of the metal ion. The chosen cluster approach facilitates separate investigation of complexation and solvation effects which cannot be divided in the liquid phase. This is extremely useful for the investigation of competitive interactions of metal ions with biological chelate ligands in the presence of water in chapter six. The (hydration of the) Zn^{II}/carnosine complex is analyzed in detail using high resolution electrospray mass spectrometric techniques, complemented by ab initio calculations.

The intramolecular reductive nitrile coupling reaction in gas-phase niobium-acetonitrile complexes is investigated in chapter seven. Product and educt complex of this reaction have different structures but the same elementary composition and can therefore not be distinguished by mass spectrometry alone. However, vibrationally resolved spectroscopic studies of gas-phase cluster ions together with proper theoretical analyses are capable of providing valuable structural information. Therefore IR spectroscopic and mass spectrometric techniques were combined to investigate the size dependent reactivity of mass selected niobium-acetonitrile complexes. Due to low number densities of the gas-phase complex ions IR Multiphoton Dissociation (IR-MPD) spectroscopy had to be applied. This technique utilizes ion dissociation detection induced by optical excitation to record the IR spectra of gas-phase ions and is significantly more sensitive than traditional IR absorption techniques. The IR-MPD spectra of niobium-acetonitrile complexes provide clear evidence of an intracluster reaction in clusters with five acetonitrile molecules opposed to ecxlusive non-reactive coordination in clusters with four acetonitrile solvent molecules. The strongly size dependent reactivity of niobium-acetonitrile solvate complexes is investigated in detail by ab initio calculations.

References

1 G. Niedner-Schatteburg, V. E. Bondybey, *Chem. Rev.* 2000, **100**, 4059.

2 A. J. Stace, *J. Phys. Chem. A* 2002, **106**, 7993.

3 B. S. Fox, O. Balaj, B. Petru, M. K. Beyer, V. E. Bondybey, *Chem.-Eur. J.* 2002, **8**, 5534.

4 V. E. Bondybey, M. Beyer, U. Achatz, B. Fox, G. Niedner-Schatteburg, *Advances in Metal and Semiconductor Clusters* 2001, 295.

5 J. V. Coe, *Inter. Rev. in Phys. Chem.* 2001, **20**, 33.

6 R. S. MacTaylor, A. W. Castleman, Jr., *Journal of Atmospheric Chemistry* 2000, **36**, 1.

7 218th ACS National Meeting with Symposium on Water and Water Clusters, New Orleans, Aug. 22-36, 1996.

8 Quantum Phenomena in Clusters and Nanostructures, Eds. S. N. Khanna, A. W. Castlemann, Jr., Springer Verlag, Berlin, 2003.

9 Cluster and Nanomaterials, Eds. Y. Kawazoe, T. Kondow, K. Ohno, Springer Verlag, Berlin, 2002.

10 NATO Advanced Study Institute on Recent Theoretical and Experimental Advances in Hydrogen-Bonded Clusters, Elounda, Crete, Greece, 1997.

11 K. Liu, J. D. Cruzan, R. J. Saykally, *Science* 1996, **271**, 929.

12 A. W. Castleman, Jr., S. Wei, *Annu. Rev. Phys. Chem.* 1994, **45**, 685.

13 *Clusters of Atoms and Molecules I-II,* Ed. H. Haberland, Springer Verlag, Berlin, 1994.

14 *Cluster Ions*, Eds. C.-Y. Ng, T. Baer, I. Powis, Wiley, Chichester, 1993.

15 B. M. Reinhard, G. Niedner-Schatteburg, *Phys. Chem. Chem Phys.* 2002, **4**, 1471.

16 B. M. Reinhard, G. Niedner-Schatteburg, *J. Chem. Phys. A.* 2002, **106**, 7988.

17 M. Velegrakis, C. Lüder, *Chem. Phys. Lett.* 1994, **223**, 831.

18 C. A. Woodward, M. P. Dobson, A. J. Stace, *J. Phys. Chem*. 1996, **100**, 5605.

19 C. A. Woodward, M. P. Dobson, A. J. Stace, *J. Phys. Chem. A* 1997, **101**, 2279.

20 M. Beyer, C. Berg, G. Albert, U. Achatz, V. E. Bondybey, *Chem. Phys. Lett.* 1997, **280**, 459.

21 T. Buthelezi, D. Bellert, T. Hayes, P. J. Brucat, *Chem. Phys. Lett.* 1996, **262**, 303.

22 C. T. Scurlock, J. S. Pilgrim, M. A. Duncan, *J. Chem. Phys.* 1995, **103**, 3293.

23 M. A. Duncan, *Adv. Met. Semicond. Clusters*, Ed. M. A. Duncan, 2001, 5.

24 I. Dzidic, P. Kebarle, *J. Phys. Chem.* 1970, **74**, 14664.

25 P. Kebarle, *Ann. Rev. Phys. Chem.* 1977, **28**, 445.

26 R. G. Keesee, A. W. Castleman, Jr., *J. Phys. Chem. Ref. Data* 1986, **15**, 1011.

27 P. Jayaweera, A. T. Blades, M. G. Ikonomou, P. Kebarle, *J. Am. Chem. Soc.* 1990, **112**, 2452.

28 A. T. Blades, P. Jajaweera, M. G. Ikonoumo, P. Kebarle, *J. Chem. Phys.* 1990, **92**, 5900.

29 A. T. Blades, P. Jajaweera, M. G. Ikonoumo, P. Kebarle, *Int. J. Mass Spectrom. Ion Proc.* 1990, **101**, 325.

30 A. T. Blades, P. Jajaweera, M. G. Ikonoumo, P. Kebarle, *Int. J. Mass Spectrom. Ion Proc.* 1990, **102**, 251.

31 K. G. Spears, F. C. Fehsenfeld, M. McFarland, E. E. Ferguson, *J. Chem. Phys.* 1972, **56**, 2562.

32 K. G. Spears, F. C. Fehsenfeld, *J. Chem. Phys.* 1972, **56**, 5698.

33 S. E. Rodriguez-Cruz, R. A. Jockusch, E. R. Williams, *J. Am. Chem. Soc.* 1998, **120**, 5842.

34 C. W. Bauschlicher, Jr., S. R. Langhoff, H. Partridge, J. D. Rice, A. Komornicki, *J. Chem. Phys.* 1991, **95**, 5142.

35 C. W. Bauschlicher, Jr., H. Partridge, *J. Chem. Phys.* 1991, **95**, 9694.

37 H. Watanabe, S. Iwata, *J. Phys. Chem.* 1996, **100**, 3377.

38 N. F. Dalleska, B. L. Tjelta, P. B. Armentrout, *J. Phys. Chem.* 1994, **98**, 4191.

39 R. Vuileumer, M. Sprik, *J. Chem. Phys.* 2001, **115**, 3454.

40 C. J. Mundy, J. Hutter, M. Parinello, *J. Am. Chem. Soc.* 2000, **122**, 4837.

41 D. Marx, M. Sprik, M. Parinello, *Chem. Phys. Lett.* 1997, **273**, 360.

42 T. J. Selegue, N. Moe, J. A. Draves, J. M. Lisy, *J. Chem. Phys.* 1992, **96**, 7268.

43 J. M. Lisy, *Int. Rev. in Phys. Chem.* 1997, **16**, 267.

44 G. N. Patwari, J. M. Lisy, *J. Chem. Phys.* 2003, **118**, 8555.

45 U. Achatz, S. Joos, C. Berg, T. Schindler, M. Beyer, G. Albert, G. Niedner-Schatteburg, V. E. Bondybey, *J. Am. Chem. Soc.*, 1998, **120**, 1876.

46 U. Achatz, S. Joos, C. Berg, M. Beyer, G. Niedner-Schatteburg, V. E. Bondybey, *Chem. Phys. Lett.* 1998, **291**, 459.

47 T. Schindler, C. Berg, G. Niedner-Schatteburg, V. E. Bondybey, *Chem. Phys. Lett.* 1994, **229**, 57.

48 A. W. Castleman, Jr*., Int. J. Mass Spectrom. Ion Proc.* 1992, **118/119**, 167.

49 T. Schindler, C. Berg, G. Niedner-Schatteburg, V. E. Bondybey, *J. Chem. Phys.* 1996, **104**, 3998.

50 Q. Zhang, C. J. Carpenter, P. R. Kemper, M. T. Bowers, *J. Am. Chem. Soc.* 2003, **125**, 3341.

51 S. Roszak, J. Leszczynski, *J. Phys. Chem. A*. 2003, **107**, 949.

52 K. LeVarbu, J. Schiedt, R. Weinkauf, E. W. Schlag, J. M. Nilles, S.-J. Xu, O. C. Thomas, K. H. Bowen, *J. Chem. Phys.* 2002, **116**, 9663.

53 B. Hartke, *Angew. Chem. Inter. Edit. Engl.* 2002, **41**, 1468.

54 H. Liu, W. Guo, S. Yang, *J. Chem. Phys.* 2001, **115**, 4612.

55 G. de Petris, *Acc. Chem. Res.* 2002, **35**, 305.

2. Methods

2.1 Experimental Methods

A. Fourier Transform Ion Cyclotron Resonance Mass Spectrometry FT-ICR-MS

Ion Cyclotron Resonance Mass Spectrometry ICR-MS utilizes the cyclotron frequency ν_c (cf. Fig. 2.1) for mass determination of an ion with charge q in a magnetic field of strength B_0:

$$\nu_c = qB_0(2\pi m)^{-1} \quad (2.1)$$

The frequency can be measured with high accuracy,[1] which enables ultra high mass resolution with the ICR technique, routinely achieving an accuracy better than $\Delta m/m=10^{-6}$.[2] This resolution is sufficient to determine the elemental composition of an ion by its mass defect. For example N_2^+ and CO^+ with an absolute mass of 28.0056 amu and 27.9944 amu, respectively, give rise to well separated peaks.[2] In 1974 Comisarow and Marshall extended ICR technology by application of Fourier Transformation (FT), which made the acquisition of mass spectra over a continous mass range possible.[3] The main distinguishing feature of the FT-ICR-MS technique is that ion detection is non-destructive. Unlike beam or quadrupole ion trap instruments that rely on destructive measurement by causing collisions between ions and detectors, FT-ICR-MS uses the non-destructive method of image-current detection.[4] Essentially ions are injected into the centre of a Penning trap, which is formed by a combination of a static magnetic field and a quadrupolar electrostatic trapping field. The ions can be visualized by applying a radio-frequency (RF) electric field with the same frequency as the ion cyclotron frequency (i.e. producing resonance). The ions are accelerated on trajectories with larger radii where they form coherent packages of ions with the same mass, as shown in Fig. 2.2. The movement of the ion packages in the magnetic field induces an image current in two conductive, directly opposing, parallel electrodes which act as the detector. A very short, intense electric-field pulse produces broadband electromagnetic radiation over a frequency range that is inversely proportional to the pulse duration. Each of the m/z values is stimulated in the time domain, and the measured response can be converted to the frequency domain (the normal mass spectrum) by FT.

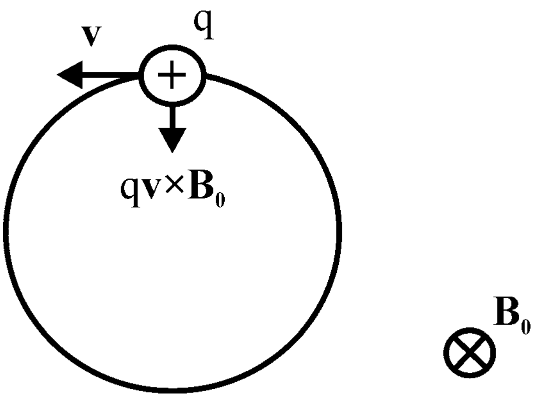

Fig. 2.1 Origin of the cyclotron motion: A particle with charge q and velocity **v** perpendicular to the magnetic field vector $\mathbf{B}_0$ follows a circular trajectory due to the Lorentz force q**v**× $\mathbf{B}_0$.[§]

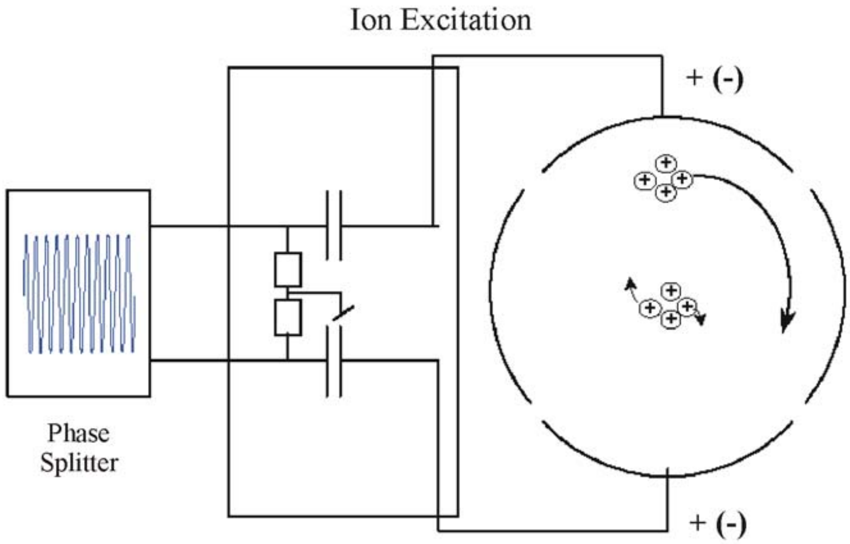

Applied dipolar RF field excites ions into coherent cyclotron motion at larger radius

Fig. 2.2 The initial thermal cyclotron motion of trapped ions with small radius is incoherent. Upon irradiadion of radio frequency on the excitation plates, an in-phase cyclotron motion with larger radius is superpositioned, forming a coherent ion package.

The coherence of the ion packages is disturbed by the coulomb repulsion of the ions and by collisions with neutral gas present in the ICR cell, causing an exponential decay of the signal intensity with time. Ultra high vacuum with pressures lower than 10^{-8} mbar can minimize collisional broadening.

FT-ICR-MS instruments have proven impressive performance capabilities. A resolving power of 100000 has been demonstrated for proteins with a mass of 100 kDa with an

---

[§] Bold character indicates a vector

accuracy of ± 3 Da.[5] The mass range is also enormous, for example a single ionized molecule of coliphage T4 DNA was trapped and the mass was determined to be 1.1 x 10^8 amu.[6] Single ions can be measured although, in general, a few hundred ions should be trapped to give a clear current. Sub-attomole sensitivity (<600.000 molecules) for MS and tandem MS (MS/MS) of intact peptides and proteins with masses up to 30 kDa has been demonstrated.[7]

B. The Kaiserslautern FT-ICR

The Kaiserslautern FT-ICR displayed schematically in Fig. 2.3 is a modified Bruker Apex III, equipped with a 7 Tesla superconducting magnet with a 15 cm room temperature bore, a cylindrical 60 mm × 60 mm infinity cell[8], and a differentially pumped ultra high vacuum system with external ion transfer optics.

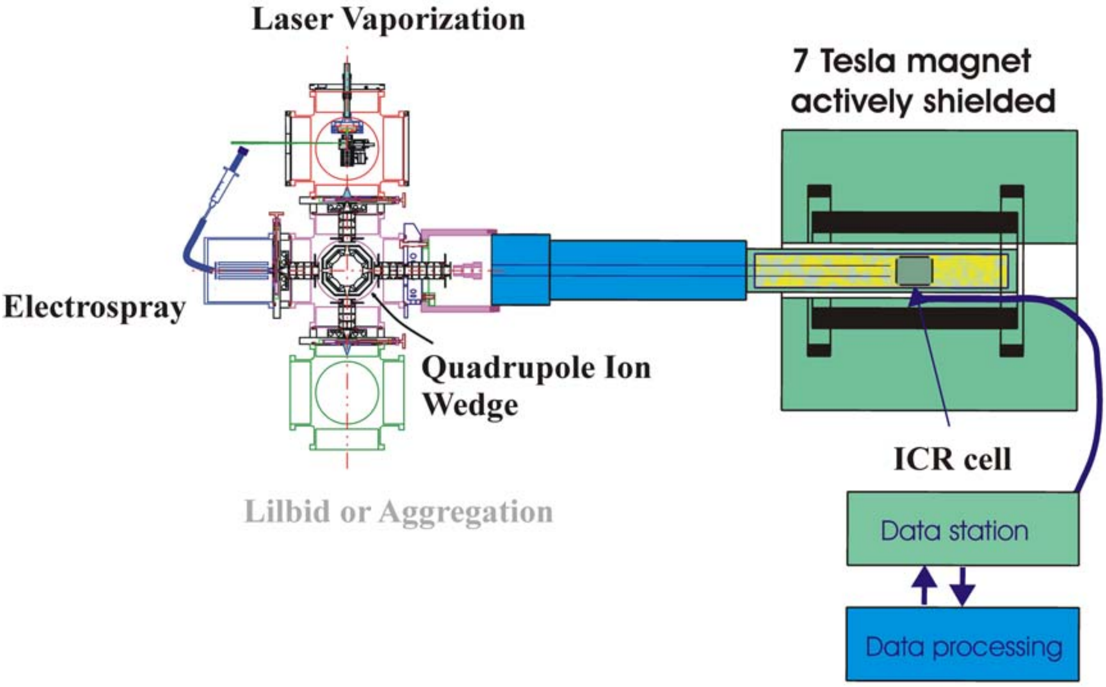

Fig. 2.3 Schematic drawing of the Kaiserslautern FT-ICR. A commercial Bruker Apex III FT-ICR was modified with a quadrupole ion wedge, for quick switching between different ion sources like the electrospray ionization soure, the laser vaporization source and in the near future also the Lilbid or aggregation source. Ions generated in one of the sources are transferred to the ICR cell inside the magnet by a system of electrostatic lenses.

The Apex III ICR was combined with a homebuild quadrupole ion wedge, which is aimed to allow rapid switching between different ion sources. Its design resembles that of Huber et al.[9] The deflection system that bends the ion beam emitted from one of the sources aligned perpendicular to the transfer optics system of the ICR (e.g. laser vaporization source) is comprised of electrostatic quadrupoles oriented perpendicular to the bending planes. Edge effects due to fringing fields at the entrance and exits of the quadrupoles are corrected with shim electrodes. After the ions have left the ion wedge they are injected into the transfer optics system. In order to guide the ion beam against the magnetic mirror effect[10] into the homogenous high field region of the magnet, it is accelerated to 3 keV kinetic energy. The beam passes through different flow constraints, separating stages of differential pumping and is finally stepwisely decelerated below the trapping potential. To increase trapping efficiency of the ions within the ICR cell, the Caravatti method, also known as "sidekick" trapping can be applied. In this method a small potential is applied perpendicular to the velocity of the ions. Thereby some fraction of the translational energy of the ions moving along the axis of the magnetic field is converted into cyclotron and magnetron motion perpendicular to it.

Ultra high vacuum in the cell region of the ICR is assured by differential pumping of the high field region of the magnet, the transfer stage, ion wedge and sources. The capillary region (~10^{-1} mbar) of the ESI source is pumped by a 20 m^3/h rotary vane pump followed by an Edwards 250 L/s turbo drag pump (~10^{-4} mbar) in the hexapole ion guide region of the ESI source. The laser vaporization source chamber (~10^{-6} mbar) is pumped by a 520 L/s turbomolecular pump backed by a 10 m^3/h rotary vane pump. The ion wedge chamber (~10^{-6} mbar) is pumped by a 520 L/s turbomolecular pump backed by a 10 m^3/h rotary vane pump. The original source chamber (~10^{-7} mbar), the intersection of the ion wedge and the ICR transfer optics, is pumped by a 520 L/s turbomolecular pump backed by a 20 m^3/h rotary vane pump. The transfer stage (~10^{-8} mbar) is pumped by a 70 L/s turbomolecular pump and the subsequent analyzer region (~10^{-10} mbar) is pumped by a 500 L/s turbomolecular pump, both backed by a 10 m^3/h rotary vane pump. The turbomolecular pumps of the transfer stage and analyzer region are shielded against the high stray field of the magnet with soft iron. Unless otherwise stated the turbomolecular pumps are from Pfeiffer, rotary vane pumps are from Edwards and Pfeiffer.

Pressure at the different pumping stages is measured by different Pirani and Penning ionization gauges by Granville-Phillips and Pfeiffer. The pressure in the ultra high vacuum region of the ICR was monitored with a Granville-Phillips Stabil-Ion Series 360 ion gauge. This gauge is placed approximately 80 cm away from the ICR cell on top of the turbomolecular pump. Upon introduction of a collision gas into the cell a constant background pressure is obtained as a stationary state between pumping, gas flowing into the cell, atoms or molecules sticking on the apparatus wall and desorbing again. The actual pressure inside the cell depends on the nature of the gas and differs from the pressure measured at the gauge. Therefore the measured pressure is to be corrected by an empirical geometry and sensitivity factor.[11]

For experiment control and data processing the Xmass software by Bruker was used. The pulse program language for Apex type instruments allows software control of the experiments. Up to 64 free programmable TTL pulses are organized as two 32-bit words (setnmr3 and setnmr4) to control or trigger the different hardware components of the instrument. The digital excitation and acquisition system (AQS) of the Bruker Apex III features two ADC analog-digital converters for transient recording. A fast ADC with 20 MHz sampling rate and 10-12 bit resolution is used for broad band detection. At max. sweep rate, i.e. lowest mass, the sampling rate is reduced to 10 MHz. The HiRes SADC+ with a 50 kHz sampling rate (max. sweep rate = 37.5 kHz) and 14-16 bit resolution is used for high resolution heterodyne detection. The actual resolution of both analog-digital converters depends on the sweeprate. The lowest detectable mass or the highest detectable frequency is limited by the sampling rate of the fast ADC to 21.5 amu. Transients up to 1 Mword (=4 Mbyte) can be recorded. The Fast Fourier Transformation (FFT) is performed by a personal computer (Intel Xeon 2.4 GHz processor, 512 Mbyte RAM). The PC is fast enough to allow for an online display of mass spectra even with a transient of 1 Mword.

Experimental data relevant for this work were recorded using the Bruker Apollo electrospray “ionization” (ESI) source depicted schematically in Fig. 2.4. The term ESI is misleading and should be avoided, as electrospray (ES) is not an ionization method in the sense that it converts neutral molecules into ions, it merely transfers ions from solution into the gas-phase. There are three major steps in the production of gas-phase ions from electrolyte ions in solution by electrospray (ES).[12-18] (1) Production of charged droplets at the ES spraying needle (capillary tip), (2) shrinkage of the charged droplets by solvent evaporation and repeated droplet disintegration, leading ultimately to small, highly charged droplets capable of producing gas-phase ions, and (3) the actual mechanism by which gas-phase ions are produced from the very small and highly charged droplets. As shown in the schematic representation of the charged-droplet formation in Fig. 2.4 a voltage of 2-3 kV is applied to a metal capillary (typically 0.2 mm o.d and 0.1 mm i.d.) located 1-3 cm away from the counter-electrode.

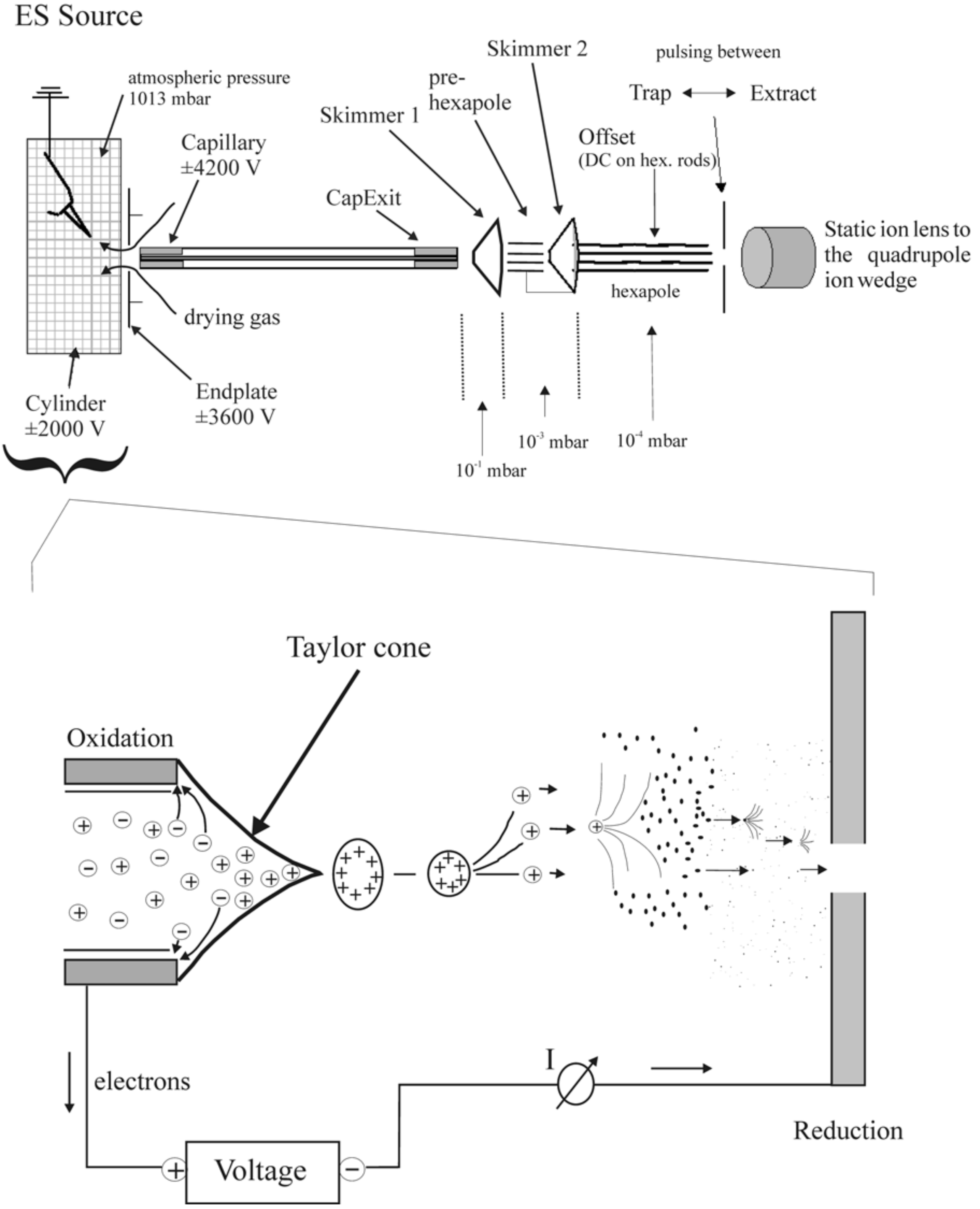

Fig. 2.4 Schematic of the used Bruker-Apollo ESI source and of major processes during the ES process according to the cone-jet mechanism. If the spraying needle has positive potential with regard to the endplate (counter-electrode) enrichment of positive charges at the surface leads to the destabilization of the meniscus and to formation of a Taylor cone and jet emitting droplets with excess of positive ions. By solvent evaporation charged droplets shrink until at a critical radius Coulomb explosion into smaller droplets occurs. Finally gas-phase ions are obtained. The gas-phase ions enter the transfer capillary through the orifice of the endplate. Ions are collected in the second hexapole, from which they are injected into the ion wedge when an extraction potential is applied.

In the used Apollo source the counter-electrode is a plate with an orifice leading to a sampling capillary, which leads to the MS. The electrospray capillary tip is thin and therefore the emitting electric field is very high ($E \approx 10^6$ V/m). The field will penetrate the solution at the capillary tip and the positive and negative electrolyte ions in the solution will move under the influence of the field resulting in a charge separation. Positive ions will drift downfield in the solution towards the meniscus of the liquid while negative ions will drift away from the surface. Eventually the Coulomb repulsion of the positive ions at the surface of the liquid overcomes the surface tension and the surface expands, allowing the positive ions and liquid to move further downfield. The so called Taylor cone forms.[19] If the applied field is sufficiently high, a fine jet emerges from the cone tip which breaks up into small droplets. Due to the excess of positive ions at the surface of the cone the droplets are positively charged. This mode of charging of the droplets, which depends on the positve and negative ions drifting in different directions, is called the electrophoretic mechanism. The charged droplets drift through the air towards the counter-electrode. Solvent evaporation at constant charge leads to droplet shrinkage and an increase of the electric field normal to the surface of the droplet. At some critical radius the mutual repulsion of the ions overcomes the surface tension (Coulomb explosion) and droplet fission occurs, followed by repeated solvent evaporation and repeated fission. Although electrospray mass spectrometry was introduced in 1984 by Yamashita and Fenn,[20-21] the exact mechanism of the ES process is not yet understood thoroughly. The cone-jet mechanism illustrated in Fig. 2.4 is only one – although the best characterized – of several possible and lively discussed ES mechanisms.[22-25]

The gas-phase ions enter a transfer capillary through an orifice in the endplate, which is counter-electrode to the spraying needle (cf. Fig. 2.4). After the ions have passed through a transfer capillary, which reduces the (neutral) gas flow from the atmospheric pressure part of the ESI source, the ions are collected in a hexapole, from which they are injected into the ion wedge of the ICR.

C. Mobile ICR Analyzer (MICRA)

MICRA is a compact FT-ICR spectrometer prototype based on a 1.25 T permanent magnet, covering a mass range of 10-1000 amu.[26] The ion trap of MICRA differs from standard FT-ICR cell geometries by its open structure. Two opposite side electrodes, perpendicular to the

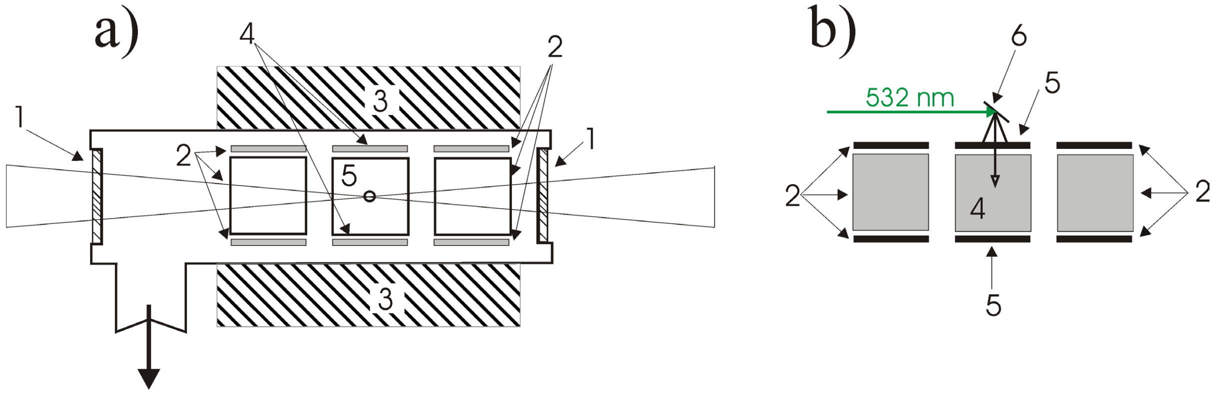

Fig. 2.5 Schematic sideview of MICRA (a) and top view of the ICR cell (b) showing the metal target mounted near the ICR cell. Details of experimental setup: (1) ZnSe optical window, (2) excitation plates, (3) permanent magnet, (4) detection plates, (5) trapping plate with hole, (6) metal target.

axis of the magnet field are replaced by four interconnected electrodes parallel to it. The open-ended ICR cell of this homebuild ICR provides a good optical access to its center, which is superior to other potential cell designs using grids as side electrodes. Because of the open structure of its ICR cell MICRA is well suited for spectroscopic investigations of ions stored within the cell. Inside the high vacuum region of MICRA a base pressure of the order of 6.7×10^{-9} mbar is maintained by a 70 L/s turbomolecular pump backed by a dry membrane pump.

In the high field region of the ICR metal cations can be generated via laser ablation from a metal rod, which is mounted in the high vacuum chamber of the ICR with a 45° degree to the ICR cell (cf. Fig. 2.5). A Nd:YAG laser beam (Continuum Surelite, λ=532 nm, 10 mJ per 5ns pulse) directed parallel to the axis of the ICR cell is focused on the niobium surface and ablates the metal ion.[27] The ablated metal ions are trapped inside the ICR cell and can be reacted with gases injected into the cell via three different pulsed valves.

D. Free Electron Laser (FEL) at the Centre Laser Infrarouge d'Orsay (CLIO)

A Free Electron Laser generates tunable, coherent, high power radiation, currently spanning wavelengths from millimeters to visible, and ultraviolett to x-ray.[28-30] It can have the optical characteristics of conventionall lasers, like e.g. high spatial coherence and near diffraction limited radiation beam. However, it differs from conventional lasers in using a relativistic electron beam as lasing medium as opposed to bound atomic or molecular states. The electron beam produced by an accelerator is sent through a wiggler, which denominates a magnet whose field varies sinusoidally with distance.

The CLIO free electron laser (FEL)

Centre Laser Infrarouge Orsay, Paris, France

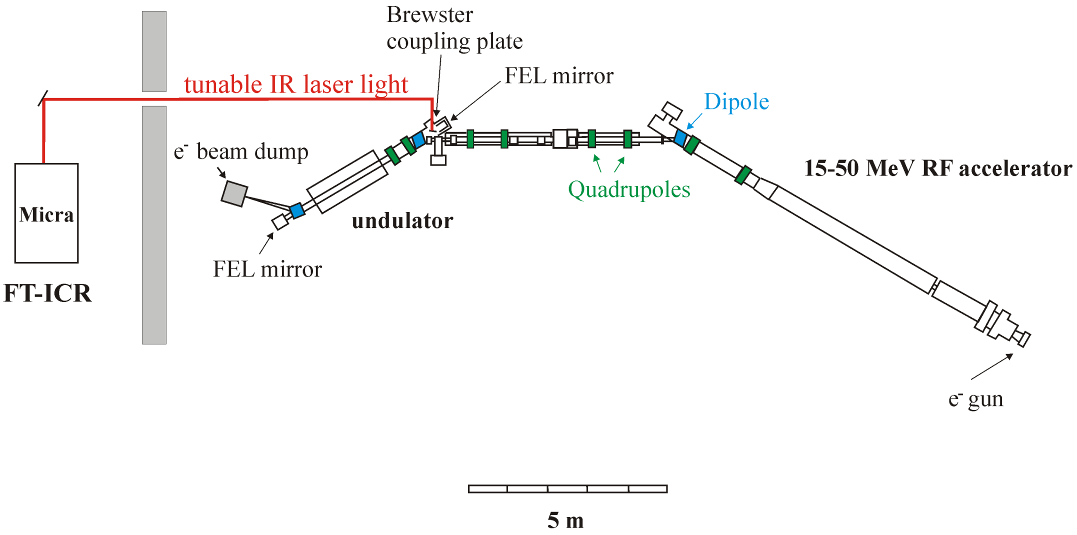

Fig. 2.6 Scheme of the CLIO FEL coupled to the MICRA FT-ICR

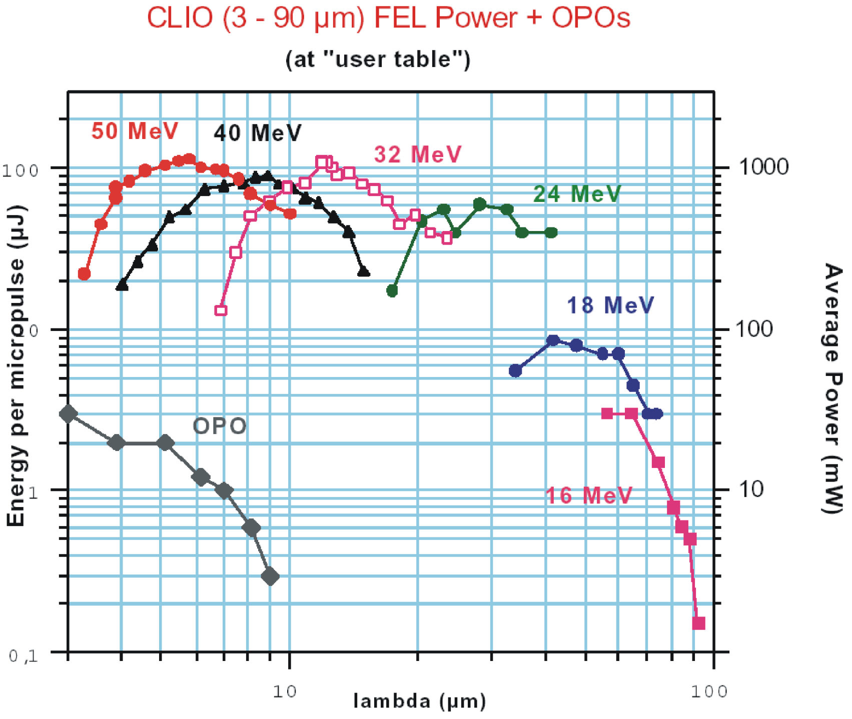

Fig. 2.7 Average power of the CLIO FEL vs. wavelength for different electron energies and typical repetition rates of 63 Mhz/25Hz for micro-/macro pulses

The electrons radiate and bunch at a resonant wavelength determined solely by the wavelength of the wiggler, the wiggler magnetic field and the electron beam energy.[31] The "CLIO" infrared Free Electron Laser at Orsay is a user facility operating in the mid-infrared.[32] Its major components are the electron accelerator, the optical resonator and the undulator, which creates a periodic transverse magnetic field. CLIO's experimental setup is depicted schematically in Fig. 2.6.

The CLIO accelerator, which is a 3 GHz RF linac,[33-34] uses a thermo-ionic gridded cathode followed by a 500 MHz buncher and a 4.5 m long accelerating section. The energies currently available range from 16 to 58 MeV, giving access to a spectral range from ~3 to ~90μm. The longest wavelength (90 μm) is limited by diffraction. The peak electron current within the undulator lies between 50 and 100 A depending on the accelerator energies and alignments. The undulator is planar and uses SmCo magnets in the Halbach configuration. It provides 38 magnetic periods of length 5 cm.[35] The measured normalized emittance ($4\pi\beta\gamma\sigma\sigma'$) is about 150 π mm mrad, which is sufficient to match the infrared spectral range. The laser power at different wavelength is shown in Fig. 2.7.[36] The laser power at a given wavelength is decreased significantly for energies below 24 MeV. This is due to an energy spread (approx. 250 keV) of the 5 MeV buncher leading to an increase of the relative energy dispersion at low energy. Moreover magnetic compression of the bunch is often used to increase the laser power, by dephasing the bunch in the main accelerating region and using the residual non-isochronism of the bend (≅ 1ps / 1%). This becomes less efficient at low energy because of the initial energy spread. The optical cavity of Clio is 4.8 m long to match the repetition rate of the linear accelerator. Silver protected mirrors are used in the cavity. The laser power is extracted by a hole in one of the mirrors and switchable mirrors allow to either monitor the beam or to send it to the user line. The beam line is flowed with dry air. Compared to vacuum pumping this offers the advantage of easy access to the equipment.

At each electron energy continous tunability is obtained over a spectral range $\Delta\lambda/\lambda \approx 2.5$ without the need to modify the accelerator settings. The FEL temporal structure consists of macropulses about 8 μs long at a repetition rate of 25 Hz, containing typically 500 micropulses a few picoseconds long each, separated by 16 ns. The typical energy content of a macropulse is 25 mJ with a peak power of 20 MW in each micropulse. CLIO emits intense laser radiation in the chemical infrared and is therefore well suited to probe molecular vibrations in gas-phase molecules/clusters by Infrared Multiphoton Dissociation Spectroscopy (IRMPD). For this purpose CLIO is coupled to the portable ICR MICRA.[26-27]

2.2 Theoretical Methods

A. Hartree-Fock Approximation

To treat the electronic states of many-atom systems, it is necessary to perform calculations for complex interacting electron systems on the basis of quantum mechanics. The simplest antisymmetric wavefunction which can be used to describe the ground state of a N-electron system is a single Slater determinant:[37]

$$|\Psi_0\rangle = |\chi_1\chi_2 \dots \chi_N\rangle \qquad (2.2)$$

According to the variation principle of quantum mechanics the best wavefunction is the one which gives the lowest energy

$$E_0=\langle\Psi_0|\mathcal{H}|\Psi_0\rangle \qquad (2.3)$$

with $\mathcal{H}$ being the full electronic Hamiltonian. By minimizing E_0 with respect to the choice of spin orbitals the Hartree-Fock equation can be derived,[38] which determines the optimal spin orbitals. The Hartree-Fock equation is an eigenvalue equation of the form

$$f(i)\chi(\mathbf{x}_i)=\varepsilon\chi(\mathbf{x}_i) \qquad (2.4)$$

where f(i) is an effective one-electron operator, called the Fock operator, which has the form

$$f(i) = -\frac{1}{2}\nabla_i^2 - \sum_{A=1}^{M}\frac{Z_A}{r_{iA}} + v^{HF}(i) \qquad (2.5)$$

$v^{HF}(i)$ is an average potential experienced by the ith electron due to the presence of the other electrons. In the Hartree-Fock approximation the complicated many electron problem is reduced to a one electron problem by introducing $v^{HF}(i)$ as the resulting field experienced by the ith electron instead of explicitly evaluating the interaction of the ith electron with each of the remaining N-1 electrons. As $v^{HF}(i)$ depends on the spin orbitals of the other electrons, the Hartree-Fock equation (2.4) is nonlinear and must be solved iteratively.

The procedure to solve (2.4) iteratively is called the self-consistent-field (SCF) method. Initially a set of spin orbitals is guessed (e.g. through an extended Hückel calculation) and the average field v^{HF} is calculated for this set of spin orbitals. Subsequently (2.5) is solved using v^{HF} yielding a new set of spin orbitals. Using these spin orbitals new fields can be generated and the procedure can be repeated until the fields do no longer change and self-consistency is reached.

As solution of the Hartree-Fock eigenvalue problem (2.4) a set of orthonormal Hartree-Fock spin orbitals $\{\chi_k\}$ with orbital energies $\{\varepsilon_k\}$ is obtained. The N spin orbitals with the lowest energies are called occupied spin orbitals. The Slater determinant formed from these spin orbitals is the Hartree-Fock ground state wavefunction and represents the best variational approximation to the ground state of the system in a single determinant form.

B. Post Hartree-Fock Techniques

A Hartree-Fock SCF wavefunction takes the interaction between electrons into account only in an average way. For a better approximation to the true wavefunction the instantenous interactions between electrons must also be considered. Due to Coulomb interactions electrons repel each other. The repulsive interactions between the electrons in an atom give rise to an area surrounding each electron in which the probability of finding a second electron is low (Coulomb hole). The motions of the electrons in an atom/molecule are not independent from one another but correlated and close approximations of the true wavefunctions often require the consideration of this electron correlation. Actually, Hartree-Fock does contain some electron correlation as the Hartree-Fock eigenfunction meets the antisymmetry requirement of the Pauli Principle. Therefore the probability of two electrons with the same spin and spatial coordinates is zero. One often refers to the Fermi hole as a region around an electron in which the probability of finding a second electron with same spin is small.

The limitations of the Hartree-Fock method can be reduced by going beyond the single determinant ansatz. There are two broad categories of such approaches: Perturbation Theory based approaches and Variational Principle based approaches.

Møller-Plesset (MP) Perturbation Theory

Perturbation theory has often been used by physicists and chemists to deal with systems of interacting particles, like nucleons in a nucleus, atoms in a solid and electrons in an atom or a molecule. In 1934 Møller and Plesset proposed a perturbation treatment of atoms and molecules, in which they referred to the Hartree-Fock eigenfunction as unperturbed wavefunction of the system.[39] The MP unperturbed Hamiltonian is taken as the sum of the one-electron Fock operators f(i) in (2.4):

$$\mathcal{H}^0 = \sum_{i=1}^{N} f(i) \qquad (2.6)$$

The ground-state Hartree-Fock wavefunction Ψ_0 is a Slater determinant, which leads – when expanded – to the sum of n! terms, where each term involves a different permutation of the electrons among the spin orbitals. Each term in this expansion of Ψ_0 is an eigenfunction of the MP $\mathcal{H}^0$. The Hermitian operator f(i) in (2.6) has a complete set of eigenfunctions which denote all the possible spin orbitals of the molecule. Only the N lowest eigenfunctions are occupied, but there are an infinite number of unoccupied (virtual) orbitals. The operator $\mathcal{H}^0$ in (2.6) is the sum of the operators f(i), and so the eigenfunctions of H^0 are all possible products of any N of the spin orbitals. As the wavefunction must be antisymmetric, the zeroth order wavefunctions $\Psi_1^{(0)}$ are all possible Slater determinants formed using any N of the infinite number of possible spin states. The eigenfunctions of the unperturbed Hamiltonian $\mathcal{H}^0$ are the zeroth-order (unperturbed) antisymmetrized wavefunctions, one is the Hartree-Fock ground state function $\Psi_0^{(0)}$ (=Ψ_0) with the energy $E_0^{(0)}$ (=E_0) and all the remaining $\Psi_\lambda^{(0)}$ correspond to excited states, if the ground state is not degenerate.

The perturbation $\mathcal{H}'$ is introduced as the difference between the true molecular electronic Hamiltonian $\mathcal{H}$ and $\mathcal{H}^0$, which is equal to the difference between the true interelectronic repulsion and the Hartree-Fock interelectronic potential:[40]

$$\mathcal{H}' = \mathcal{H} - \mathcal{H}^0 = \sum_{i}^{N}\sum_{j>i}^{N}\frac{1}{r_{ij}} - \sum_{i}^{N} v^{HF}(i) \qquad (2.7)$$

All the excited wavefunctions $\Psi_\lambda^{(0)}$ can be used in the perturbation expansion. In the frozen core approximation, excitation from core orbitals is neglected. The MP first-order energy correction $E_0^{(1)}$ is obtained through:

$$E_0^{(1)} = <\Psi_0^{(0)}|\mathcal{H}'|\Psi_0^{(0)}> \qquad (2.8)$$

Leading to the corrected energy:

$$\begin{aligned} E_0^{(0)} + E_0^{(1)} &= <\Psi_0^{(0)}|\mathcal{H}^0|\Psi_0^{(0)}> + <\Psi_0^{(0)}|\mathcal{H}'|\Psi_0^{(0)}> = <\Psi_0^{(0)}|\mathcal{H}^0+\mathcal{H}'|\Psi_0^{(0)}> \\ &= <\Psi_0^{(0)}|\mathcal{H}|\Psi_0^{(0)}> \end{aligned}$$

The expectation value $<\Psi_0^{(0)}|\mathcal{H}|\Psi_0^{(0)}>$ of the true Hamiltonian is the same as that of the Hartree-Fock operator, and $E_0^{(0)}+E_0^{(1)} = E_{HF,}$ so the first-order correction to the energy is exactly zero ($E_0^{(1)}=0$). To improve on the Hartree-Fock energy, the second order energy correction $E_0^{(2)}$ must be evaluated:

$$E_{(0)}^{(2)} = \sum_{\lambda\neq 0} |<\Psi_\lambda^{(0)}|\mathcal{H}'|\Psi_0^{(0)}>|^2 (E_0^{(0)} - E_\lambda^{(0)})^{-1} \qquad (2.9)$$

This calculation scheme is referred to as MP2, in analogy the third order and fourth order schemes are referred to as MP3 and MP4. MP calculations truncated at any order can be shown to be size consistent.[41] However, MP calculations are not variational and can produce an energy below the true energy.

Coulomb Fitting MP2 (RI-MP2)

The RI-MP2 algorithm uses the resolution of identity (RI) approximation to reduce the overall computational cost by replacing the complex four index integral with a sum of smaller set of three index and/or two index integrals that are cheaper to compute.[42] For a given closed-shell restricted Hartree-Fock (RHF) wavefunction the MP2 energy can be written as

$$E_{(0)}^{(2)} = \sum_{ijab} t_{ij}^{ab} (ia \mid jb) \qquad (2.10)$$

Where the t-amplitudes obey the following equation:

$$\sum_k (t_{ik}^{ab}\varepsilon_{kj} + \varepsilon_{ik}t_{kj}^{ab}) - \sum_c (t_{ij}^{ac}\varepsilon_{cb} + \varepsilon_{ac}t_{ij}^{cb}) = 2(ia \mid jb) - (ib \mid ja) \quad (2.11)$$

The labels a,b,c refer to virtual orbitals, while i,j,k refer to occupied MOs, (ia|jb) is the electrostatic interaction energy between the transition densities i(**r**)a(**r**) and j(**r**)b(**r**).[42] Using the RI approximation in the Coulomb metric, one obtains:

$$(ia|jb) \approx (ia|jb)_{RI} = \sum_P B_{ia}^P B_{jb}^P \qquad (2.12)$$

$$B_{ia}^P = \sum_Q (ia \mid Q) V_{QP}^{-1/2} \qquad (2.13)$$

P, Q label auxiliary basis functions.[43] Equation (2.12) is obtained upon expanding the transition densities of the type i(**r**)a(**r**) into this auxiliary basis. $V_{QP}^{-1/2}$ is an element of the inverse square root of the (positive definite) metric matrix

$$V_{QP} = (Q|P) = \int d^3\mathbf{r}_1 \int d^3\mathbf{r}_2\, Q(\mathbf{r}_1)P(\mathbf{r}_2)\, r_{12}^{-1} \qquad (2.14)$$

The main advantage of the RI-MP2 technique is considerable data reduction. The right hand side of (2.12) involves only three center integrals (ia|P) which replace the much more numerous four-center integrals (ia|jb).

Configuration Interaction

The Hartree-Fock ground state function is by definition the best single determinant based approximation to the true wavefunction. However, the true atomic or molecular wavefunction Ψ can contain (small) contributions from configuration functions other than the Hartree-Fock ground state function.

In any Configuration Interaction (CI) ansatz the exact wavefunction Ψ is expressed as linear combination of configuration functions Φ_k which are expressed as antisymmetric Slater determinants:

$$\Psi = \sum_{k=0} c_k \Phi_k \quad (2.15)$$

The configuration functions Φ_k can be any complete set of N-electron antisymmetric functions, but they are typically constructed from Hartree-Fock orbitals, with Φ_0 being the Hartree-Fock ground state function. If the correlation energy is small the Hartree-Fock energy accounts for the majority of the exact total energy and the normalized c_k are all very small except for $c_0 \approx 0$. A very large number of configuration functions is required to yield energies and wavefunctions approaching the exact many-particle wavefunction. The total number of configuration functions in a full CI calculation for a molecule with N electrons and b one-electron basis functions is:[44]

$$k_{max} = \frac{b!(b+1)!}{\left(\frac{1}{2}N\right)!\left(\frac{1}{2}N+1\right)!\left(b-\frac{1}{2}N\right)!\left(b-\frac{1}{2}N+1\right)!} \quad (2.16)$$

k_{max} increases fast with the number of basis functions and electrons. Although the CI approach is suited to solve the many-particle Hamiltonian and yields an exact solution, in practice the applicability of full CI with decent basis sets is limited to small systems due to the large number of configuration functions to be considered.

As full CI calculations are limited to small molecules, different approaches have been conceived which aim to obtain the best wavefunction and lowest CI energy with the shortest expansion length. These approaches are based on truncation of the expansion after double or quadrupole excitation from the reference configuration. These levels of truncation are referred to as CI singles-doubles (CISD) and CI singles-doubles-triples-quadrupoles (CISDTQ) methods. However, even in these methods still a large number of terms remains and the application is also limited due to computational cost. Complete Active Space Multiconfiguration SCF (CASSCF) is a combination of a SCF computation with a full CI calculation involving a subset of the orbitals.

Another major problem of CI methods is their lack of “size-extensivity”. As the size of the systems increases the fraction of electronic correlation contained in a certain reference space (e.g. all single and double excitations) decreases. Due to this lack of size-extensivity error-cancellation fails when systems of different size are compared. Therefore it is problematic to compute interactions or bonding interactions with CI based approaches.

The lack of size-extensivity and the computational cost of CI methods led to the development of different related methods, of which the most popular are the coupled clusters (CC) methods. In contrast to CI methods they are non-variational but in exchange they are size-extensive. Coupled cluster methods assume an exponential ansatz for the wavefunction:[45]

$$\Psi_{CC} = \exp\left(\hat{T}\right)\Psi_0 = \sum_{k=0}^{\infty}\frac{\hat{T}^k}{k!}\,\Psi_0 \qquad (2.17)$$

The coupled-cluster wavefunction is generated by acting with an excitation operator $\hat{T}$ to a reference wavefunction, which is normally the normalized Hartree-Fock ground state wavefunction Ψ_0. Ψ_{CC} in (2.17) is not normalized but can be normalized at the end of the calculation. The operator $\hat{T}$ generates k-fold excitation from the reference state.

$$\hat{T} = \sum_N \hat{T}_N = \hat{T}_1 + \hat{T}_2 + \hat{T}_3 + \ldots + T_N \qquad (2.18)$$

The one-particle excitation operator $\hat{T}_1$ and the two-particle excitation operator $\hat{T}_2$ are defined by

$$\hat{T}_1\Psi_0 = \sum_{a=N+1}^{\infty}\sum_{i=1}^{N} t_i^a\,\Psi_i^a \qquad (2.19)$$

$$\hat{T}_2\Psi_0 = \sum_{b=a+1}^{\infty}\sum_{a=n+1}^{\infty}\sum_{j=i+1}^{N}\sum_{i=1}^{N-1} t_{ij}^{ab}\,\Psi_{ij}^{ab} \qquad (2.20)$$

Ψ_i^a is a singly excited Slater determinant with the occupied spin orbital χ_i replaced by the virtual spin orbital χ_a, and t_i^a is a numerical coefficient whose value depends on i and a and that is determined through the constraint that (2.17) is satisfied. The operator $\hat{T}_1$ converts the Slater determinant $\Psi_0=|\chi_1 \ldots \chi_N|$ into a linear combination of all possibly excited Slater determinants. Similarly Ψ_{ij}^{ab} is a Slater derminant with the occupied spin orbitals χ_i and χ_j replaced by the virtual orbitals χ_a and χ_b and t_{ij}^{ab} is a numerical coefficient.

Through application of the $\exp(\hat{T})$ operator Ψ_{CC} is expressed as linear combination of Slater determinants that include Ψ_0 and all possible excitations of electrons from occupied to virtual orbitals. This is conceptual very similar to the CI mechanism. The aim of CC calculations is to determine the coefficients t_i^a, t_{ij}^{ab}, … for all i,j, … and a,b, …. If these coefficients (also known as amplitudes) are known, Ψ_{CC} is determined. In practice instead of including all operators $\hat{T}_1$ … $\hat{T}_N$ the operator $\hat{T}$ is approximated by including only some of these operators. The most important contribution to $\hat{T}$ is made by $\hat{T}_2$. Inclusion of only $\hat{T}_2$ leads to the approximate CC method called coupled-cluster doubles (CCD). The next step to improve on CCD is to include the operator $\hat{T}_1$ leading to CC singles and doubles (CCSD). If $\hat{T}_3$ is also included, this is called CC singles, doubles and triples (CCSDT). The cost of CCSD in terms of CPU time, memory and disk requirement scales with the number of basis functions in the sixth power. For CCSDT the costs scale in the eight power. To reduce the cost of computation hybrid procedures like CCSD(T) (scales with the number of basis functions in the seventh power) have been invented which include the effect of $\hat{T}_3$ only through perturbation.

C. Density Functional Theory (DFT)

The DFT approach is based upon a strategy of modelling electron correlation via functionals[*] of the electron density.[46] According to Hohenberg and Kohn the energy of a system is a functional of the density ρ which takes its minimum value E_0 for the ground state density ρ_0.[47-48] However, the exact form of this functional is unknown for most of all chemical systems.

The total energy of a system can be partitioned in the following form:

$$E(\rho) = E^T(\rho) + E^V(\rho) + E^J(\rho) + E^{XC}(\rho) \qquad (2.21)$$

---

[*] A functional is a function whose definition is itself a function.

E^T is the kinetic energy of the electrons, E^V includes the Coulombic repulsion energy between the atomic nuclei and attractive Coulombic interaction of the positive nuclei with the negative electron density, E^J is the Coulombic repulsion energy in between the electron density and E^{XC} is the exchange-correlation term. $E^T+E^V+E^J$ corresponds to the classical energy of the charge distribution ρ. The term E^{XC} accounts for the energy contribution arising from the antisymmetry of the quantum mechanical wavefunction and dynamic correlation in the motions of the individual electrons. While for E^T, E^V, E^J analytical expressions can be derived, the term E^{XC} cannot be expressed analytically. One difficulty in the application of DFT is to find a good approximation to E^{XC}. As shown by Hohenberg and Kohn E^{XC} is a functional of the electron density. The electron density ρ is composed of the α and β spin densities $\rho=\rho_\alpha+\rho_\beta$. In the DFT implementation of most quantum chemical software packages E^{XC} is approximated as an integral involving the spin densities and optionally also their gradients. While the first approach is referred to as local DFT, the latter is termed gradient corrected (or less precise non-local) DFT.

$$E^{XC}(\rho) = \int f(\rho_\alpha(\mathbf{r}), \rho_\beta(\mathbf{r}), \nabla\rho_\alpha(\mathbf{r}), \nabla\rho_\beta(\mathbf{r}))\, d^3\mathbf{r} \quad (2.22)$$

E^{XC} is usually subdivided into separate parts, referred to as exchange and correlation part, which correspond to same spin and mixed spin interactions, respectively.

$$E^{XC}(\rho) = E^X(\rho) + E^C(\rho) \qquad (2.23)$$

Various approximate exchange and correlational functionals have been implemented, however almost all of them base on the model system of a hypothetical uniform electron gas. This system is a good model system for simple metals with homogenous electron distributions like e.g. sodium, however, atoms or molecules are characterized by varying electron densities. Despite of this intrinsic limitation of the uniform electron gas model it is the most important model system in DFT nevertheless. This is due to the fact that it is the only system for which the form of the exchange and correlation energy functionals are known with very high accuracy. The idea to use this model to approximate E^{XC} was introduced in the original paper of Kohn and Sham. In the so-called local density approximation (LDA) the exchange energy functional E^X(LDA) has the following form:

$$E^X(\mathrm{LDA}) = -\frac{3}{2}\left(\frac{3}{4\pi}\right)^{1/3} \int \rho^{4/3}\, d^3\mathbf{r} \qquad (2.24)$$

It succeeds to reproduce the exchange energy of a uniform electron gas, however it has problems with molecular systems. To overcome this drawback Becke formulated the following gradient corrected exchange functional based on $E^X(\mathrm{LDA})$ in 1988:[49]

$$E^X(\mathrm{Becke88}) = E^X(\mathrm{LDA}) - \gamma \int \frac{\rho^{4/3} x^2}{1 + 6\gamma \sinh^{-1} x}\, d^3\mathbf{r} \qquad (2.25)$$

Here $x = \rho^{-4/3} |\nabla\rho|$ and γ is a value introduced to fit the known exchange energies of inert gas atoms, which Becke defines as 0.0042 Hartree. In analogy different local and gradient corrected correlation energy functionals have been introduced. In this work the Lee, Yang, Parr (LYP) 1988 gradient corrected correlation energy functional is mainly used.[50] The LYP functional has been implemented by fitting the gradient expansion to second-order of the approximate second-order density matrix for the He atom ($\hat{S}$ denotes the conjugate spin to S).

$$\begin{aligned} E^C(\mathrm{LYP}) = {} & 4A\rho_\alpha\rho_\beta Z\rho^{-1} + AB\varpi\sigma(\rho_\alpha\rho_\beta(47-7\sigma)/18 - 2\rho^2/3) \\ & + \sum_S AB\, \varpi\, [\rho_S\rho_{\hat{S}}\, (82^{2/3} e\rho_S{}^{8/3} - (5/2 - \delta/18)\, \sigma_{SS} - (\delta-11)\rho_S\sigma_{SS}(9\rho)^{-1}) \\ & + (2\rho^2/3 - \rho_S{}^2)\sigma_{\hat{S}\hat{S}}] \qquad (2.26) \end{aligned}$$

where $\varpi = e^{\frac{c}{\rho^{1/3}}} Z\rho^{-11/3}$

$\delta = (c+dZ)\, \rho^{-1/3}$

$B=0.04918$

$A=0.132$

$c = 0.2533$

$d = 0.349$

$e = 3/10(3/\pi^2)^{2/3}$

$Z = (1+d\rho^{-1/3})^{-1}$

Hybrid exchange approximations mix the explicitly density dependent exchange term with non-local single-determinant (Hartree-Fock) exchange:

$$E^{XC}(\text{Hybrid}) = c_{HF}\, E^{X}(\text{HF}) + c_{DFT}\, E^{XC}(\text{DFT}) \quad (2.27)$$

where c's are constants. The most widely used hybrid functional is B3LYP which does not only contain a Hartree-Fock exchange term, but also combines different exchange and correlational functionals (VWN3 = Vosko, Wilk and Nussair correlation functional):[51]

$$E^{XC}(\text{B3LYP}) = E^{X}(\text{LDA}) + c_0\,(E^{X}(\text{HF}) - E^{X}(\text{LDA})) + c_X\, \Delta E^{X}(\text{B88}) + E^{C}(\text{VWN3}) + c_C\,(E^{C}(\text{LYP}) - E^{C}(\text{VWN3})) \quad (2.28)$$

In practice each DFT calculation starts with a reasonable guess for an initial electron density $\rho(\mathbf{r})$ which is used to generate an initial energy $E(\rho)$. Subsequently in an iterative, self-consistent procedure that is analogous to a SCF calculation the ground state energy E_0 and the ground state density ρ_0 are calculated. DFT is a variational method. In most implementations of DFT the electron density is represented by a set of molecular orbital wavefunctions ψ_i, which are linear combinations of a set of K fixed functions, the basis functions ϕ_μ.

All DFT implementations in use today have one significant disadvantage: They neglect dispersion. Dispersion forces are long-attractive forces which arise from the interactions of otherwise non-interacting electron densities from different atoms or molecules. As all current approximate exchange-correlation functionals are only local or at most gradient corrected, they cannot account for interactions with another atom or molecular when no overlap of electron densities is present.

Coulomb Fitting DFT (RIDFT)

The interelectronic repulsion leads to a two electron contribution $E_2(\rho)$ to the molecular energy which can be decomposed into a Coulomb E^J and an exchange correlation term E^{XC}:

$$E_2(\rho)=E^J(\rho)+E^{XC}(\rho) \quad (2.29)$$

$$E^J=1/2 \int \rho(\mathbf{r_1})\, r_{12}^{-1}\, \rho(\mathbf{r_2})\, d\tau \qquad (2.30)$$

where $\rho(\mathbf{r})$ denotes the molecular electron density. DFT methods approximate E_{XC} by a functional of $\rho(\mathbf{r})$ and $\nabla\rho(\mathbf{r})$, which now also includes one-electron correlation terms. J can be evaluated independently and most DFT implementations take advantage of this and use special procedures to compute J. The RIDFT method[52] implemented in TURBOMOLE utilizes an approximate representation of $\rho(r)$ in terms of an auxiliary basis set, denoted α:

$$\rho(\mathbf{r})\approx \sum_{\alpha} c_\alpha\, \alpha(\mathbf{r}) = \tilde{\rho}(\mathbf{r}) \qquad (2.31)$$

D. Basis Functions and Basis Sets

Hatree-Fock and DFT based methods require basis functions to expand the molecular orbitals in the linear expansion

$$\chi_i = \sum_{\mu}^{K} C_{i\mu}\phi_\mu \qquad (2.32)$$

If the set $\{\phi_\mu\}$ was complete this would be an exact expansion. For practical reasons one is always restricted to a finite set of K basis functions. Therefore it is important to chose basis functions that facilitate an accurate expansion for the molecular orbitals $\{\chi_i\}$. Most quantum chemical packages use atom-centered gaussian-type atom functions $g(\alpha,\mathbf{r})$, the primitive gaussians.

$$g(\alpha,\mathbf{r}) = c\, x^n\, y^m\, z^l\, e^{-\alpha r^2} \qquad (2.33)$$

The quantities n,m,l are integers, which determine the spatial symmetry; x, y, z are cartesian coordinates; and α is the orbital exponent, which determines the radial extent. The constant c ensures normalization of the gaussian.

$$\int g^2\, d^3\mathbf{r} = 1 \qquad (2.34)$$

By combination of primitive gaussian functions g(α,**r**) with different α values contracted gaussian functions are constructed that approximate the radial part of the Slater-type orbitals:

$$\phi_\mu = \sum_p d_{\mu p}\, g_p \qquad (2.35)$$

$d_{\mu p}$ are fixed constants within a given basis function. A set of basis functions that describes the orbitals of an atom is called basis set. The coefficients $d_{\mu p}$ and exponents α can be defined by the user, but standard basis sets for almost all elements of the periodic table are available in the basis set libraries of most modern quantum chemical programs.

In a Mulliken population analysis[53] the electrons of a n-electron molecule are apportioned into net populations in the basis functions ϕ_μ and overlap populations for all possible pairs of basis functions. A molecular orbital χ_i gives rise to an electron density $|\chi_i{}^2| = <\chi_i|\chi_i>$, or if χ_i is expanded in ϕ_μ:

$$<\chi_i|\chi_i> = \sum_{\mu,\nu} c_{\mu i} c_{\nu i} < \phi_\mu \,|\, \phi_\nu > \qquad (2.36)$$

If $c_{\mu i}$ and $c_{\nu i}$ belong to the same atom (μ=ν), $c_{\mu i} c_{\nu i} < \phi_\mu \,|\, \phi_\nu >$ contributes exclusively to the net population of this atom, if they belong to two different atoms it is split equally between the two atoms. Applying this scheme to all molecular orbitals, the electronic charge can be distributed over all of the atoms within a molecule. The Mulliken net charge of an atom is obtained as the sum of the negative electronic charge of the atom and the positive charge of the core.

E. Efficiency of Different Ab Initio Methods

The "efficiency" of different ab initio methods is usually measured in terms of required computational resources (CPU time, memory and hard disk requirements) and the scaling of these demands with system size. In Table 2.1 the scaling with number of basis functions for different ab initio methods is summarized.

Table 2.1 Scaling with number of basis functions for different ab initio methods

Method	*DFT*	*Hartree-Fock*	*MP2*	*CCSD*	*CCSD(T)*	*CCSDT*
Scaling	N^3	N^4	N^5	N^6	N^7	N^8

RI-MP2 and RIDFT scale more favorable with size than conventional MP2 and DFT, because some steps in the corresponding algorithms are accelerated due to the RI approximations. Ahlrichs and coworkers report reduction of computation times by a factor of 2 – 5 for RI-MP2 and 4 – 10 in case of RIDFT.[43,52]

It is important to note that hybrid DFT approaches, like e.g. B3LYP, scale approximately with N^4 like Hartree-Fock. By comparison of the different scaling behaviors it becomes apparent that pure DFT has a clear advantage over Hartree-Fock based methods. Pure DFT accounts for electron correlation and has even a lower scaling with number of basis functions than Hartree-Fock. However, it must be emphasized that DFT is not a priori suited for all systems, as it does not contain dispersion. In addition Hartree-Fock based methods usually allow for a systematic improvement of the calculated properties by increasing the applied basis sets or by improvement on the method (for example going from Hartree-Fock to MP2, to CCSD …), which is not possible in DFT approaches.

2.3 References

1 D. J. Wineland, *Science* 1984, **226**, 395.

2 A. G. Marshall, P. B. Grosshahns, *Anal. Chem.* 1991, **63**, 215.

3 M. B. Comisarow, A. G. Marshall, *Chem. Phys. Lett.* 1974, **25**, 282.

4 A. G. Marshall, C. L. Hendrickson, G. S. Jackson, *Mass Spectr. Rev.* 1998, **17**, 1.

5 N. L. Kelleher, M. W. Senko, M. M. Siegel, F. W. McLafferty, *J. Am. Mass Spectr. Soc.* 1997, **8**, 380.

6 R. Chen, X. Cheng, D. W. Mitchell, S. S. Hofstadler, Q. Wu, A. L. Rockwood, M. G. Sherman, R. D. Smith, *Anal. Chem.* 1995, **67**, 1159.

7 G. A. Valaskovic, N. L. Kelleher, F. W. McLafferty, *Science* 1996, **273**, 1199.

8 P. Caravatti, M. Allemann, *Org. Mass Spectrom.* 1991, **26**, 514.

9 B. A. Huber, T. M. Miller, P.C. Cosby, H. D. Zeman, R. L. Leon, J. T. Moseley, J. R. Peterson, *Rev. Sci. Instrum.* 1977, **48**, 1306.

10 J. D. Jackson, *Klassische Elektrodynamik*, de Gruyter, Berlin, New York, 2. Auflage, 1983.

11 S. Wies, Diplomarbeit, Technische Universität Kaiserslautern, Kaiserslautern, 2003.

12 P. Kebarle, Y. Ho, *Electrospray Ionization Mass Spectrometry*, Ed. R. B. Cole, John Wiley&Sons, Inc., New York, 1997.

13 M. Clopeau, B. Prunet-Foch, *J. Aerosol Sci.* 1994, **25**, 1021.

14 D. W. Horming, C. D. Hendricks, *J. Appl. Phys.* 1979, **50**, 2614.

15 I. Hayati, A. I. Bailey, T. F. Tadros, *J. Colloid Interface Sci.* 1987, **117**, 205.

16 J. Fernandez de la Mora, I. G. Locertales, *J. Fluid Mech.* 1994, **243**, 561.

17 S. J. Gaskell, M. S. Bolgar, I. Riba, S. G. Summerfield, *Electrospray Ionization: theory and application*, Nato ASI Series, Series C, Mathematical and Physical Sciences 1997, **504**, 3.

18 S. J. Gaskell, Electrospray: principle and practice, *J. Mass. Spectrom.* 1997, **32**, 677.

19 G. I. Taylor, *Proc. R Soc. London A* 1964, **A280**, 383.

20 M. Yamashita, J. B. Fenn, *J. Phys. Chem.* 1984, 88, 4451.

21 M. Yamashita, J. B. Fenn, *J. Phys. Chem.* 1984, 88, 4671.

22 J. B. Fenn, *J. Am. Soc. Mass Spectrom.* 1993, **4**, 524.

23 J. B. Fenn, M. Mann, C.-K. Meng, S. F. Wong, C. M. Whitehouse, *Mass Spectrom. Rev.* 1990, **9**, 37.

24 P. Kebarle, L. Tang, *Anal. Chem.* 1993, **65**, 972A.

25 Electrosprays: Theory and Applications, Special Issue *J. Aerosol Sci*, 1994, 25.

26 P. Mâitre, S. Le Caër, A. Simon, W. Jones, J. Lemaire, H. Mestdagh, M. Heninger, G. Mauclaire, P. Boissel, R. Prazeres, F. Glotin, J.-M. Ortega, *Nucl. Instr. and Meth. A* 2003, in press.

27 J. Lemaire, P. Boissel, G. Mauclaire, G. Bellec, H. Mestdagh, A. Simon, S. Le Caër, J. M. Ortega, G. Glotin, P. Maitre, *Phys. Rev. Lett.* 2002, **89**, 273002.

28 W. B. Colson, E. D. Johnson, M. J. Kelley, and H. A. Schwettman, *Physics Today* January 2002, 35.

29 H. P. Freund and P. O'Shea, *Science* 2001, **292**, 1853.

30 H. P. Freund and G. R. Neil, *Proc. IEEE* 1999, **87**, 782.

31 S. V. Benson, *Optics and Photonics News* May 2003, 20.

32 J. M. Ortega, *Extension to far-infrared of the CLIO FEL facility*, presented at the International Symposium of Infrared Free Electron Laser and its application, 30.1-1.2 20002, Noda, Chiba, Japan.

33 R. Chaput, B. Kergosien, P. Joly, J. Lesrel, O. Marcouillé, *Proc. Epac 94* 1995, **1**, 728.

34 R. Chaput et al., *Nucl. Instr. and Meth.* 1993, **A331**, 267.

35 O. Marcouillé, M. Corlier, G. Humbert, F. Marteau, J.-M. Ortega, P. Peaupardin, A. Vétéran, *Nucl. Instr. and Meth* 1996, **A375**, 465.

36 R. Prazeres, F. Glotin, J.-M. Ortega, C. Rippon, R. Andouart, J. M. Berset, E. Arnaud, R. Chaput, *Nucl. Instr. and Meth.* 2000, **A445**, 204.

37 A. Szabo, N. S. Ostlund, *Modern Quantum Chemistry: introduction to advanced electronic structure theory*, Dover edition, Dover Publications, Inc., Mineola, 1996 pp. 53.

38 A. Szabo, N. S. Ostlund, *Modern Quantum Chemistry: introduction to advanced electronic structure theory*, Dover edition, Dover Publications, Inc., Mineola, 1996 pp. 115.

39 C. Møller, M. S. Plesset, *Physical Review* 1934, **48**, 302.

40 I. N. Levine, *Quantum Chemistry,* 4. edition, Prentice Hall, Englewood Cliffs, 1991, pp. 511.

41 A. Szabo, N. S. Ostlund, *Modern Quantum Chemistry: introduction to advanced electronic structure theory*, Dover edition, Dover Publications, Inc., Mineola, 1996 pp. 354.

42 F. Weigend, M. Häser, *Theor. Chem. Acc.* 1997, **97**, 331.

43 F. Weigend, M. Häser, H. Pratzelt, R. Ahlrichs, *Chem. Phys. Lett.* 1998, **294**, 143.

44 I. N. Levine, *Quantum Chemistry,* 4. edition, Prentice Hall, Englewood Cliffs, 1991, pp. 507.

45 I. N. Levine, *Quantum Chemistry,* 4. edition, Prentice Hall, Englewood Cliffs, 1991, pp. 516.

46 W. Koch, M. C. Holthausen, *A Chemist's guide to Density functional Theory*, 2. edition, Wiley-VCH, Weinheim, 2001, pp. 29.

47 P. Hohenberg, W. Kohn, *Phys. Rev.* 1964, **136**, B864.

48 W. Kohn, L. J. Sham, *Nucl. Sci. Abstr.* 1966, **20**, 31946.

49 A. D. Becke, *Phys. Rev. A* 1988, **38**, 3098.

50 C. Lee, W. Yang, R. G. Parr, *Phys. Rev. B* 1988, **37**, 785.

51 A. D. Becke, *J. Chem. Phys.* 1993, **98**, 5648.

52 K. Eichkorn, O. Treutler, H. Öhm, M. Häser, R. Ahlrichs, *Chem. Phys. Lett.* 1995, **240**, 283.

53 R. S. Mulliken, *J. Chem. Phys.* 1955, **23**, 1833.

3. Coexistence of Hydrated Electron and Metal Dication in $[Mg,nH_2O]^+$

Electronic structure calculations of hydrated magnesium monocations $[Mg,nH_2O]^+$, $1 \leq n \leq 19$, *reveal singly occupied molecular orbitals (SOMOs) that evolve from a valence state in* $Mg^+(H_2O)_n$, $n \leq 5$, *via a contact ion pair state* $Mg^{2+}(H_2O)_n^-$, $6 \leq n < 17$, *to a solvent separated ion pair state* $Mg^{2+}(H_2O)_n e^-$ *for* $n \geq 17$. *In* $[Mg,nH_2O]^+$, $n \geq 9$, *O-H bonds of adjacent* H_2O *ligands form "molecular tweezers"* $HO\text{-}H \cdots e^- \cdots H\text{-}OH$, *which induce a localization of the odd electron within the hydration sphere. The shape of the SOMOs and their position within the clusters indicate the coexistence of a hydrated electron and of a magnesium dication in* $[Mg,nH_2O]^+$, $n \geq 8$.

The vertical and adiabatic ionization energies (VIEs and AIEs) as well as the spatial volumes of the SOMO in $[Mg,nH_2O]^+$, $n \leq 19$, *were also determined by ab initio calculations. Ionization energies were evaluated from Koopmans' theorem and explicitly as differences of the total energies of* $[Mg,nH_2O]^+$ *and* $[Mg,nH_2O]^{2+}$ *as obtained by Hartree-Fock, post-Hartree-Fock and gradient corrected density functional (DFT) methods. In the case of clusters with a 6-fold coordinated magnesium cation* $[Mg(H_2O)_6,(n-6)H_2O]^+$ *Koopmans' theorem fails for n=6-8,10. In contrast this is a valid approximation for all other cluster sizes. The most stable isomers of* $[Mg,nH_2O]^+$, *n=6-9, exhibit significantly enhanced SOMO volumes. This coincides with a significant drop in ionization energies and with an increase in electron correlation. In these clusters Koopmans' theorem is a crude approximation due to the neglect of electron correlation. The cluster size dependency of orbital relaxation and change in electron correlation upon ionization allows for an analytical fit in terms of the spatial SOMO volume. Reorganization energies and SOMO volumes indicate strong structural changes in the clusters during ionization due to a significant localization of the SOMO in* $[Mg,nH_2O]^+$, $n<6$ *and* $n>8$. *The now calculated energetics of previously observed competing decay channels - reactive hydroxide formation versus* H_2O *monomer evaporation - predict the evaporation process to be favored for* $[Mg,nH_2O]^+$, $6 \geq n \geq 17$, *in very nice agreement with experiment. The switchings in the decay propensities are analysed on the basis of the computed electronic and geometrical structures of product and reactant clusters.*

3.1 Introduction

Water clusters doped with a metal cation act as model systems for fundamental interactions as involved in metal-ligand binding and metal ion hydration. The exact nature of the interactions depends on the metal ion present. In the last two decades mass spectrometers and molecular beam methods in conjunction with laser probes have served to investigate the influence of solvation on the chemical and physical properties of ions. Thereby valuable insights into the energetics and dynamics of the solvation process were obtained. With increasing computational abilities ab initio quantum chemical methods started to represent another reliable source of information. Ab initio studies are especially helpful when a conclusive interpretation of experimental data on their own is not possible. One of these cases is the hydration of open shell magnesium monocation Mg^+ in water clusters of finite size. Stability and reactivity of hydrated magnesium monocations with the formal stoichiometry $[Mg,nH_2O]^+$ have been the topic of numerous theoretical and experimental studies.[1-17] Sanekata et al.[10] investigated the reactions of Mg^+ with water clusters by time-of-flight mass spectrometry. They found $[Mg,nH_2O]^+$ and $[MgOH,nH_2O]^+$ as reaction products with characteristic size distributions: Under their experimental conditions $[Mg,nH_2O]^+$ was predominantly produced for n=1-5 and $n\geq15$, while hydroxide clusters $[MgOH,nH2O]^+$ were exclusively observed in the intermediate region n=5-15. Misaizu et al.[7-8] recorded photodissociation spectra of small size selected hydrated magnesium cations $[Mg,nH_2O]^+$, n=1-5, in the wavelength region from 720 to 250 nm. They verified the existence of two competing decay processes: the intracluster H-elimination reaction (eq. 3.1) and the evaporation of a H_2O monomer (eq. 3.2):

$$[Mg,nH_2O]^+ \text{->} [MgOH,(n-1)H_2O]^+ + H \ , \Delta E_{react} \quad (3.1)$$

$$[Mg,nH_2O]^+ \text{->} [Mg,(n-1)H_2O]^+ + H_2O \ , \Delta E_{vap} \quad (3.2)$$

The total energy changes for the decay processes (eq. 3.1) and (eq. 3.2) are subsequently denoted ΔE_{react} and ΔE_{vap} as indicated. In ion cyclotron mass spectrometry (ICR-MS) studies of $[Mg,nH_2O]^+$ Berg et al.[13-14] found the cluster size distribution to be dominated by clusters with the stoichiometry $[Mg,nH_2O]^+$ for n<4 or n>17, whereas in the range n=7-15 only the H-atom eliminated species $[MgOH,nH_2O]^+$ were observed in the mass spectra. Berg et al. also investigated the black body radiation induced decay of size selected $[Mg,nH_2O]^+$ clusters. For

$n \leq 6$ and $n \geq 17$, the clusters were found to decay exclusively by evaporation of a H_2O monomer, whereas for $7 \leq n < 17$ reactive hydroxide formation also occurred.

The first switching between non-reactive decay by evaporation and reactive hydroxide formation has been the topic of intense research in order to comprehend the effects of hydration on the intracluster H-elimination reaction (eq. 3.1). Harms et al.[9] conducted both experimental and theoretical studies. Under the thermal conditions of their flow tube experiments they observed the H-elimination reaction at room temperature for $[Mg,nH_2O]^+$, $n \geq 4$. In their theoretical studies they optimized geometries of $[Mg,nH_2O]^+$, $n \leq 6$, and $[MgOH,nH_2O]^+$, $n \leq 5$, clusters at the HF/6-31G** level of theory assuming only first shell hydration and imposing symmetry on the H_2O-Mg^+ distances and the angles in the water molecules. The energies of the optimized structures were recalculated considering electron correlation at the MP2 level of theory. Watanabe et al.[11] also took second shell coordination into account in their calculations of $[Mg,nH_2O]^+$, $n \leq 6$, and found structures with no more than three water molecules directly bound to the magnesium cation to be energetically favored. In case of $[MgOH,nH_2O]^+$, $n \leq 5$, Watanabe et al. report optimized structures in which all H_2O molecules are directly bound to the central magnesium cation. For $n>2$ the optimizations were performed at the HF/6-31G level of theory and were refined with the 6-31G* basis set. H-elimination and hydration energies were evaluated at the MP2 and MP4SDTQ level with the optimized structures. ΔH_{react} in the H-elimination reaction (eq. 3.1) was calculated to be positive for $n = 1$-5 but negative for $n=6$. Very recently Siu and Liu investigated the mechanism of the reactive hydroxide formation in $[Mg,nH_2O]^+$, $n \leq 6$.[18] Although they report 3-fold coordinated species to be slightly lower in energy for $n=6$ at the MP2/6-31G** level of theory, they find coordination numbers at the central magnesium cation which are higher than 3 to be important for the experimentally observed reaction.

The molecular core ion $MgOH^+$ in $[MgOH,nH_2O]^+$ has a strongly polarized charge distribution which polarizes the O-H bonds of all the H_2O molecules in a small cluster.[9,11] According to Harms et al. the extra gain in hydration energy due to an additional polarization of the H_2O ligands overcompensates the HO-H bond dissociation energy and the H-elimination reaction (eq. 3.1) may occur spontaneously in case of $[Mg,nH_2O]^+$, $n \geq 4$. This helps to rationalize the first product switching from non-reactive (eq. 3.1) to reactive decay (eq. 3.2) but it fails to explain the second product switching from (eq. 3.2) back to (eq. 3.1). Up to this work there was no conclusive reasoning for the second switching of the decay propensities from reactive hydroxide formation back to non reactive decay by H_2O evaporation at n≈15, and little was known about the geometric and electronic structures of larger magnesium water cluster cations. Based on the accomplished experimental data of the decay of clusters with the stoichiometry $[Mg,nH_2O]^+$, several propositions of the structural identity of $[Mg,nH_2O]^+$, n≈15, were discussed by Sanekata et al.[10]. These authors proposed the participation of a Rydberg-type ion pair state $Mg^{2+}(H_2O)_n^-$ as the origin of the second product switching. Berg et al.[14] suggested the concept of a solvated electron as an adequate model system for larger clusters sizes instead. The latter model interprets the observed second product switching in terms of an ion pair Mg^{2+}_{aq} and e^-_{aq}.

This chapter deals with the first ever ab initio calculations of $[Mg,nH_2O]^+$ and $[MgOH,nH_2O]^+$ clusters with cluster sizes n>6. In order to elucidate the cluster size dependent product switchings in the decay of $[Mg,nH_2O]^+$ clusters, several isomers of $[Mg,nH_2O]^+$ n=1-9,11,12,14,15,17-19, and $[MgOH,nH_2O]^+$, n=1-6,8,11,14,18, were investigated by density functional theory using a gradient corrected exchange-correlation functional. The changes of enthalpy ΔH_{react} and ΔH_{vap} were computed for the two competing decay channels (eq. 3.1) and (eq. 3.2) and the electronic structure of the clusters $[Mg,nH_2O]^+$, $1 \leq n \leq 19$ were analyzed. The focus of the performed studies is the oxidation state of the magnesium ion and its dependency on the degree of hydration: Does the oxidation state of the magnesium cation change from +1 to +2 with growing cluster size? In case a significant redox effect prevails, it should have strong impact on the reactivity of the clusters $[Mg,nH_2O]^+$, which might reveal a conclusive interpretation of the second product switching at n≈15.

3.2 Computational Details

All quantum chemical calculations were performed using the TURBOMOLE[19-20] program package. In order to deal with molecular clusters of considerable size a method has to be used which offers an appropriate trade-off between accuracy and computational cost. The density functional theory (DFT) approach includes correlation in a form that does not lead to the scaling problems of e.g. Post-Hartree-Fock methods. DFT is applicable to fairly large systems which are out of reach for Hartree-Fock based approaches today and in the near future.[21-22] For geometry optimizations we therefore chose the Becke88[23] exchange functional with the Lee, Yang and Parr[24] gradient corrected correlation functional (BLYP), which is known to be an efficient density functional with good overall performance and which has been applied to extremely diffuse excess electrons in $(H_2O)_n^-$ before.[25-26] Ionic hydrogen bonded clusters are certainly well treated since electrostatic interactions dominate over dispersion forces. Weigend et al.[27] as well as Smith et al.[28] proved in their MP2 treatments of $(H_2O)_n^-$, n=2,3,6 that the use of "floating points" (ghost atoms without mass and charge (m=0, z=0) and appropriate diffuse basis functions) allow for an accurate description of the highly diffuse electron. For the test case $(H_2O)_n^-$, n=2, the experimental vertical detachment energies were reproduced within a few 0.01 eV.[27,29] We adopted this method for our DFT-based approach: All clusters to be calculated were augmented by four floating points with a diffuse (3s2p) basis set as developed by Weigend et al.. Full geometry optimization including the floating centers (!) was performed for each cluster structure. For O (11s6p1d)/[5s3p1d] and H (5s1p)/[3s1p] the basis sets employed were of triple-ζ valence type plus polarization function (TZVP). For Mg (14s8p1d)/[5s4p1d] polarization functions of type 2p1d were added (TZVPP). Coulomb interactions were treated by means of an auxiliary basis set representation of the electron density. The RIDFT[30] method (RI=resolution of identity) required auxiliary basis sets as implemented. The required grids for the numerical integration of exchange and correlation contributions were chosen second but finest (m4). Different isomers were optimized for each cluster size n. Although the global minima remain unknown for cluster sizes n > 6 due to the large number of possible isomers, the obtained minima differ in energy by a few kJ mol^{-1} at the most and the energetically lowest isomer is considered characteristic for each cluster size n. Structures of the clusters $[Mg,nH_2O]^{2+}$ were obtained by BLYP geometry optimizations starting from optimized $[Mg,nH_2O]^+$ geometries.

RI-MP2[31-32] single point calculations with the standard frozen core approximation were performed for the BLYP optimized $[Mg,nH_2O]^+$ structures in the charge states +1 and +2 and for the BLYP optimized $[Mg,nH_2O]^{2+}$ clusters. The applied RI-MP2 algorithm is based on an approximate representation of products of orbital basis functions as a linear combination of atom-centered auxiliary basis functions.[31] The overall computational cost is reduced by replacing each 4 index integrals with a sum of 3 index integrals. This method is more efficient than straight MP2 at the expense of insignificant loss in accuracy.[31] The clusters $[Mg,nH_2O]^+$ contain an odd number of electrons, for all cluster sizes the expectation value of the spin operator $<S^2>$ was close to the exact value of 0.75 for a doublet (< 0.752 in all cases) indicating a clear energetic and spatial separation of the unpaired electron from the closed shell electrons and wavefunctions that are almost free from spurious spin contamination. For cluster sizes n=5-10 we also computed the single point total energies of the BLYP optimized $[Mg,nH_2O]^+$ structures in the charge states +1 and +2 and of BLYP optimized $[Mg,nH_2O]^{2+}$ clusters with the TURBOMOLE implementation of the approximate coupled cluster singles and doubles method CC2[33-34] which employs the RI approximation for two electron integrals. The RI methods RI-MP2 and RI-CC2 required auxiliar basis sets chosen as implemented.

VIEs were explicitly calculated as vertical electronic energy differences between charge states +1 and +2 at the optimized $[Mg,nH_2O]^+$ structures at different levels of theory. We refer to them as VIE_{BLYP}, VIE_{HF}, VIE_{MP2} and VIE_{CC2} (only for n=5-10), with the level of theory used in the calculation of the energies given as index. No zero-point energy corrections were applied. VIEs were also computed according to Koopmans' theorem[35] as sign-reversed SOMO energies (labelled as VIE_{KT}) in $[Mg,nH_2O]^+$ from Hartree-Fock orbitals. Adiabatic ionization energies (AIEs) were calculated as energy difference between optimized $[Mg,nH_2O]^+$ and $[Mg,nH_2O]^{2+}$ clusters and are referred to as AIE_{BLYP}, AIE_{HF}, AIE_{MP2} and AIE_{CC2} (only n=5-10).

3.3 Results and Discussion

A. Geometric and Electronic Structures of Preferential versus Non-Preferential Mg Coordination in $[Mg,nH_2O]^+$

According to textbook inorganic chemistry magnesium monocations are not existent in aqueous condensed phase. Solvation of a magnesium monocation in water clusters must eventually result in the oxidation of the magnesium monocation if the cluster size is increased. The evolution of the electronic structures of hydrated magnesium water clusters $[Mg(H_2O)_n]^+$ with cluster size is illustrated in Fig. 3.1. The preferential Mg_{aq}^+ coordination of each size n is displayed in Fig. 3.1(a). The SOMO is located at the magnesium monocation in a sp-hybrid-like orbital for n<6. At n=6 the SOMO is displaced from the magnesium monocation into the hydration sphere by the surrounding H_2O molecules and the coordination number of the central magnesium cation changes from three to six. For cluster sizes n=1-6, we conducted full geometry optimizations and determined the global minimum structures. All of them reveal at most threefold coordination of the magnesium cation. In $[Mg,nH_2O]^+$, n=4-5, the most stable structures are similar to those reported by Watanabe et al.[11] with the fourth and fifth H_2O ligand located in the second solvation shell.

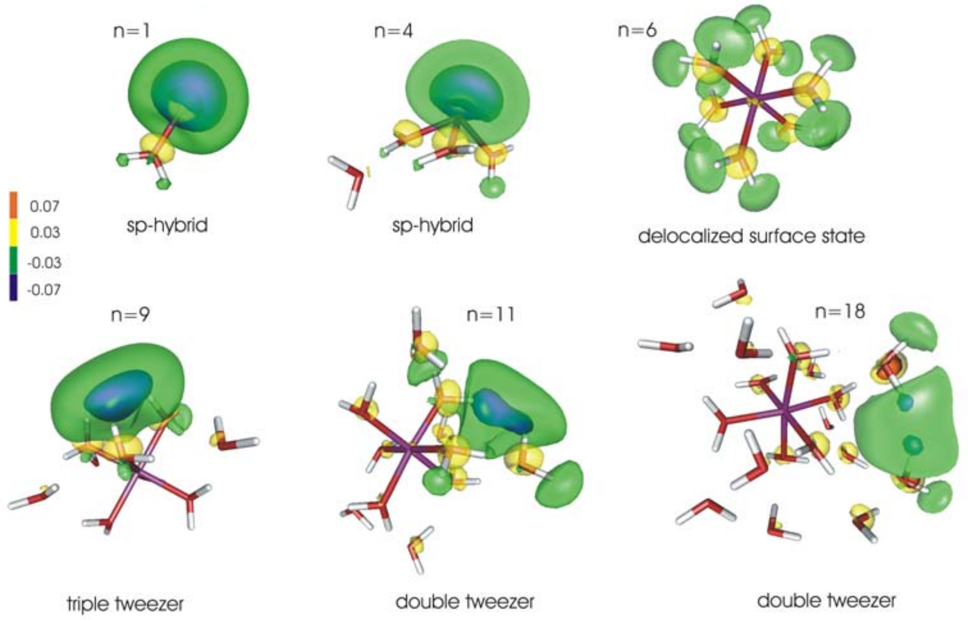
(a) preferential Mg^{+}_{aq} coordination

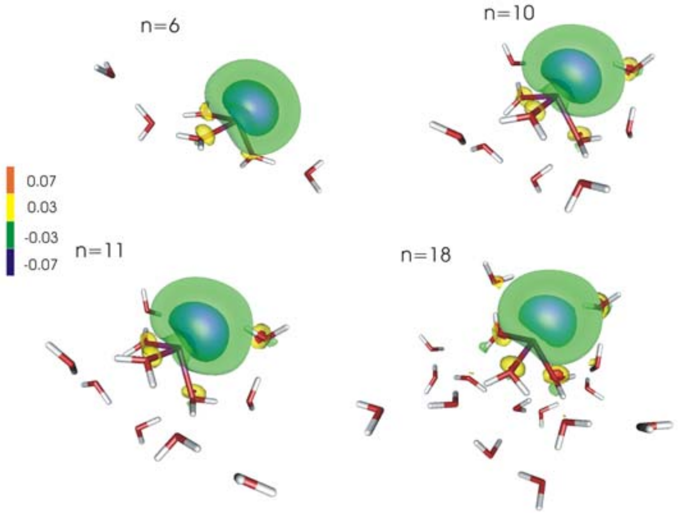
(b) less favorable Mg^{+}_{aq} coordination

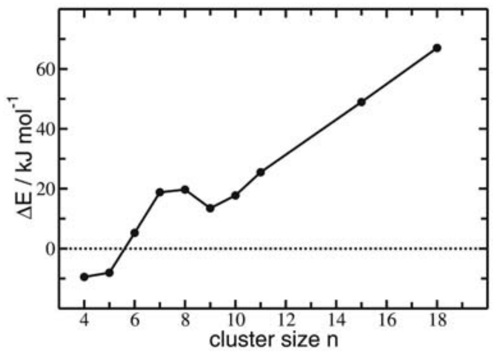
(c) energy difference ΔE(BLYP)

Fig 3.1 (a) Optimized cluster structures and isosurfaces of the singly occupied molecular orbital (SOMO) in $[Mg,nH_2O]^+$, n≤19, with preferred $Mg_{aq}{}^{+}$ coordination. The electronic structure in $[Mg,nH_2O]^+$ evolves with cluster size. In n=1-5 the SOMO which accomodates the odd electron of the cluster, has sp-hybrid-like character and is localized at the magnesium cation. In n=6-8 the SOMO is detached from the central magnesium cation and is spread over the complete cluster surface. This is accompanied by a change in the coordination number at the magnesium cation from 3 to 6 in n≥9 the SOMO is localized within the hydration sphere by molecular tweezers HO-H···e⁻···H-OH. In n=9-10 three O-H bonds of from adjacent H_2O molecules form triple tweezers whereas in n≥11 two O-H bonds form double tweezers. **(b)** Optimized cluster structures and SOMO isosurfaces for $[Mg(H_2O)_3,(n\text{-}3)H_2O]^+$, n≥6, with a threefold coordinated magnesium cation. In $[Mg(H_2O)_3,(n\text{-}3)H_2O]^+$ the SOMO remains located at the magnesium cation for all cluster sizes n. For n≥6 these structures represent high-energy isomers with respect to the sixfold coordinated species $[Mg(H_2O)_6,(n\text{-}6)H_2O]^+$ shown in (a). **(c)** Energetic difference ΔE of threefold coordination versus sixfold coordination (respectively five- and fourfold for n≤6) of the magnesium cation as a function of cluster size n in BLYP optimized $[Mg,nH_2O]^+$ cluster structures. For cluster sizes n≥6 ΔE is positive indicating that threefold coordination is energetically disfavored. As ΔE overall increases with clustersize threefold coordination becomes more and more improbable.

For $[Mg,nH_2O]^+$, n=4-5, these structures are 9.5 respectively 8.1 kJ mol^{-1} lower in energy than the optimized structures with higher coordination (fourfold or fivefold) at the magnesium cation. Our findings for $[Mg,nH_2O]^+$, n=6, deviate from the molecular orbital studies by Watanabe et al.. The isomer with a sixfold coordination of the central magnesium cation is by 4.9 kJ mol^{-1} lower in energy than the isomer with only three H_2O ligands in the first solvation shell. This might be due to the fact that the moderate 6-31G and 6-31G* basis sets applied by Watanabe et al. are not sufficiently diffuse to account for an electron transfer from the central magnesium cation to the surrounding H_2O ligands as observed in our calculations. Larger clusters $[Mg,nH_2O]^+$ with n>6 have potential hypersurfaces with numerous local minima, corresponding to different isomers. A systematic study of all of these isomers exceeds by far our computational resources. We optimized e.g. three different isomers of the cluster $[Mg(H_2O)_{12}]^+$ and found total energies to differ by less than 0.5 kJ mol^{-1}. This gives strong confidence, that the local minima are characteristic and do not differ substantially from the unknown global minimum.

The present cluster structures are determined by the interaction of attractive forces (ion-dipole and ion-induced dipole) and repulsive forces (dipole-dipole of adjacent H_2O ligands and Pauli repulsion between the odd electron and O-atom lone pairs). In $[Mg,nH_2O]^+$, n=3, this interplay of attraction and repulsion results in two quite different hemispheres around Mg^+. One hemisphere contains the three H_2O monomers, which arrange to minimize their mutual repulsion. The other hemisphere is occupied by the SOMO and is void of ligands. In $[Mg,nH_2O]^+$, n=4-5, the coordination number of the central Mg cation remains unchanged: Only three H_2O ligands are directly bound to the magnesium cation and the SOMOs are of similar shape as in n=3.

$[Mg,nH_2O]^+$, n=6, has octahedrical coordination of all six H_2O molecules in first shell so that shell closure is attained. In consequence the odd electron has detached from the magnesium cation and moved outwards, where it delocalizes equally on all six ligands. For all cluster sizes n≥9, the SOMO is characteristically "concentrated" between adjacent H-atoms at the surface of the cluster, as shown in Fig. 3.1(a) for n=9,11 and 18. We note in passing that the structure of the cluster $[Mg,nH_2O]^+$, n=6, in Fig. 3.1(a) was obtained from the optimized structure of $[Mg,nH_2O]^+$, n=9, after removal of three second shell H_2O molecules and subsequent reoptimization. We stress this aspect as in $[Mg,nH_2O]^+$, n≥9, O-H bonds of first shell H_2O molecules form an electrophilic site that localizes the SOMO (cf. Fig. 3.1(a)). The speculation that a similar state exists in $[Mg,nH_2O]^+$ turns out to be wrong. It takes at least nine water molecules to facilitate a localization of the SOMO between two or three dangling H-atoms within the hydration sphere. Schematically the localization of the odd electron between two dangling H-atoms can be described by a structure like $HO\text{-}H\cdots e^-\cdots H\text{-}OH$. The O-H bonds form a "molecular tweezer" which comprises a region of high probability density of the odd electron. In their landmark ab initio calculations of $(H_2O)_n^-$, n=6 and 12, K. S. Kim et al.[24-25,36-39] showed that a group of two or three clustered dangling H-atoms (not involved in H-bonds) may indeed act as electrophilic site which stabilizes an excess electron. Exactly this structural motive re-appears in the large hydrated magnesium clusters. In case of the hydrated electron clusters $(H_2O)_n^-$ there has also been experimental indication of clustered OH groups acting as electrophilic binding sites for an excess electron. Johnson and coworkers recorded photodetachment spectra of $(H_2O)_n^-$, $n \geq 6$, in the mid-infrared and found strong vibrational resonances.[40] These were assigned to the interaction of free O-H groups with the excess electron in a caged molecular framework.

In $[Mg,nH_2O]^+$, $n \leq 19$, two different molecular tweezer structures can be found: The double ($11 \leq n \leq 19$) and the triple tweezer (n=9-10). The double tweezer is formed by the interaction of the odd electron with two O-H bonds and the triple tweezer is formed by three O-H bonds (cf. Fig. 3.1(a)). Apparently the formation of molecular tweezers in $[Mg(H_2O)_n]^+$ is only possible when the second solvation shell is partly occupied. We propose that the minimum cluster size n=9 observed for the formation of a molecular tweezer $HO\text{-}H\cdots e^-\cdots H\text{-}OH$ is due to a stabilization of those structures by H-bonding interactions with additional H_2O molecules.

Recently Iwata et al.[41-43] investigated the electronic and geometric structures of water cluster complexes around a group 1 (alkali) metal atom $[M,nH_2O]$ $n \leq 6$, and of hydrated electron clusters $(H_2O)_n^-$, $n \leq 6$. They characterized three different types of isomers in the clusters $[M,nH_2O]$: the "surface type", the "semi internal type" and the "quasi-valence type". The present SOMOs of $[Mg,nH_2O]^+$, $n \leq 5$, are very similar to those "quasi-valence type" SOMOs: In both cases the SOMO is not yet completely detached from the metal atom and it shows characteristics of a sp-hybrid orbital (cf. Fig. 3.1(a)). The clusters $[Mg,nH_2O]^+$, $6 \leq n \leq 8$, resemble their "surface type" in which the electron is detached from the metal atom and its orbital is delocalized on the surface of the cluster. In the clusters $[Mg,nH_2O]^+$, $9 \leq n \leq 19$, the electron is largely detached from the magnesium cation and is "captured" by O-H bonds of H_2O ligands. This state is reminiscent of the "semi internal type" of Iwata et al..

Isomers with a less favorable Mg_{aq}^+ coordination for n≥6 are on display in Fig. 3.1(b). In these 3-fold coordinated species $[Mg(H_2O)_3,(n-3)H_2O]^+$ the SOMO remains located at the magnesium monocation for all cluster sizes $n \geq 6$. Resources available to us required the use of DFT methods for a systematic investigation of $[Mg,nH_2O]^+$ cluster structures with up to 19 water molecules. The BLYP optimized hydrated magnesium water clusters with a 6-fold coordinated central magnesium cation are energetically favored for all cluster sizes $n \geq 6$ and the relative energy differences between $[Mg(H_2O)_6,(n-6)H_2O]^+$ and $[Mg(H_2O)_3,(n-3)H_2O]^+$ overall increase with growing cluster size (cf. Fig. 3.1(c)). Watanabe et al. as well as Siu and Liu have reported $[Mg(H_2O)_6,(n-6)H_2O]^+$, n=6, and $[Mg(H_2O)_3,(n-3)H_2O]^+$, n=6, to be close in energy before.[11,18] Although we cannot exclude the coexistence of these two isomers in $[Mg,nH_2O]^+$ clusters at $n \approx 6$, according to our calculations $[Mg(H_2O)_6,(n-6)H_2O]^+$ is surely becoming more and more abundant the larger the clusters are. Therefore we will focus on the properties of these isomers. If not otherwise stated we refer in the following to BLYP optimized structures with a 6-fold coordinated magnesium cation in $[Mg,nH_2O]^+$, $n \geq 6$.

B. Gradual Oxidation of Mg^+ to Mg^{2+} in $[Mg,nH_2O]^+$

In $[Mg,nH_2O]^+$, $n \geq 6$, the SOMO - which accomodates the odd electron - is gradually transferred from the magnesium monocation into the hydration shell with growing cluster size (cf. Fig. 3.1(a)). In n=6-8 the SOMO is delocalized over the complete hydration sphere, but in larger clusters $n \geq 9$ it is located between free O-H bonds of adjacent H_2O molecules as shown for n=9,11, and n=18. The electronic structure in $[Mg,nH_2O]^+$ evolves from a valence state in $Mg^+(H_2O)_n$, n≤5, via a contact ion pair state $Mg^{2+}(H_2O)_n^-$, 6≤n<17, to a solvent separated ion pair state $Mg^{2+}(H_2O)_ne^-$, n>17. Hydrated magnesium clusters $[Mg,nH_2O]^+$ are isovalent to water clusters containing an alkali metal atom while the clusters differ in netto charges and oxidation states of the metal species. With growing cluster size n the magnesium monocation in $[Mg,nH_2O]^+$ is gradually oxidized to the magnesium dication and during this oxidation process the SOMO is detached from the metal cation into the hydration sphere. In clusters n≥6 the hydration enthalpy of the magnesium dication compensates for the second ionization energy. This causes the H_2O ligands to displace the SOMO from the magnesium cation into the hydration sphere and the coordination number of the magnesium cation to change from 3 (n=3-5) to 6 (n≥6).

In order to quantify the gradual oxidation process in $[Mg,nH_2O]^+$ a radial distribution function $\varrho^2(r)=4\pi r^2|\Psi(r)|^2$ of the SOMO was computed in the interval r=0-20 a.u. for all cluster sizes n=1-19. The radial distribution function $\varrho^2(r)$ is proportional to the probability of finding the odd electron in a spherical shell of thickness dr at a distance r from the Mg nucleus. The probability of the odd electron $\varrho^2(r)$ near Mg decreases with increasing cluster size n. A single H_2O ligand (n=1) suffices to shift $\varrho^2(r)$ significantly outwards and with growing cluster size the electron shifts to higher and higher r-values. The overlap between $\varrho^2(r)$ for the odd electron in $[Mg,nH_2O]^+$, n=19, and the 3s valence electron in the naked Mg^+ monocation is almost negligible. For all cluster sizes in between n=1-19 the odd electron gradually moves away from the central magnesium cation as hydration increases.

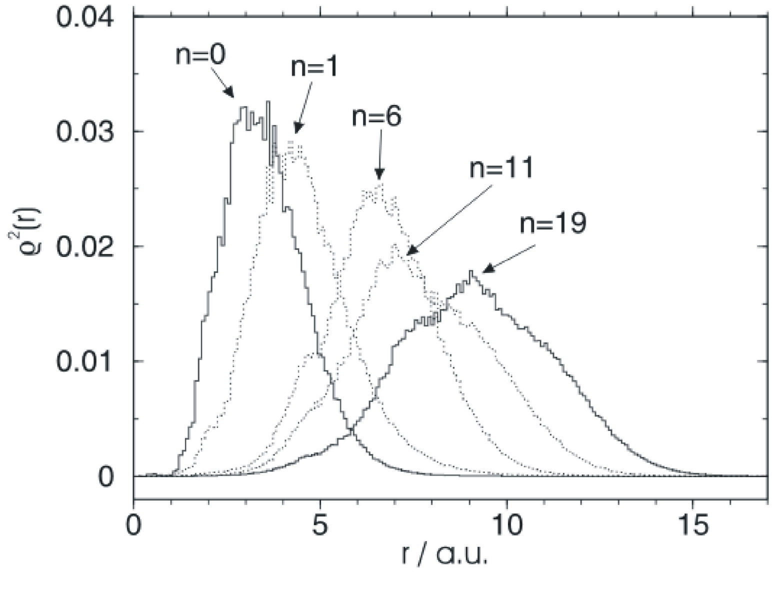

Fig. 3.2 Radial probability distribution $\varrho^2(r)$ of the odd electron in $[Mg,nH_2O]^+$, n=0,1,6,11,19. Some digital noise stems from application of finite grid size.

The expectation value $r_{av}=\int r\varrho^2(r)dr$ (r=0-20 a.u.), which provides the average radial extent of the odd electron within a cluster, smoothly increases with cluster size n as shown in Fig. 3.3. This affirms that the oxidation process is indeed a gradual process. The n dependency of r_{av} is well described by the regression function $r_{av}=2.51+1.27n^{1/2}$. This indicates a sharp increase of r_{av} with attachment of the first few H_2O ligands to the central magnesium cation and a more gentle increase of r_{av} for larger clusters.

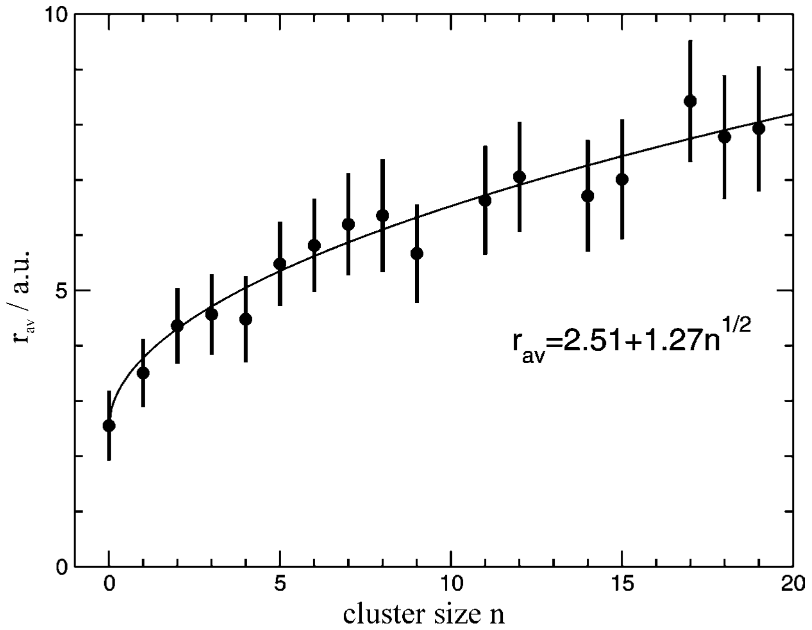

Fig. 3.3 Average radial extent r_{av} of the odd electron in $[Mg,nH_2O]^+$. The computed full width at half maximum s_n are contained as bars.

The full width at half maximum s_n of r_{av} is a measure of the odd electron's radial diffuseness within the cluster. While s_n initially increases with cluster size n, it is found to be almost independent of cluster sizes for n>8. This comes along with the appearance of molecular tweezers HO-H···e^-···H-OH. The spatial extent of the tweezer unit itself seems not to depend on the total number of H_2O molecules as only two or three H_2O ligands are directly involved. Molecular tweezers strongly contribute to the localization of the SOMO within the cluster and their almost cluster size independent spatial extent might account for an approximately constant s_n in $[Mg,nH_2O]^+$, n>8.

One quintessence of the performed investigations is that with growing cluster size n the odd electron first gradually detaches (n<6) and then further departs from the central magnesium cation (n≥6). This leads to a successive increase in the formal oxidation state of the central magnesium. Most of the investigated clusters $[Mg,nH_2O]^+$, n≤19, still show some remaining overlap of $\varrho^2(r)$ with the 3s valence state of Mg^+ (cf. Fig. 3.1), while at n=19 this overlap is negligible. In $[Mg,nH_2O]^+$, n=6-15, the odd electron is detached from the magnesium cation but is still largely located within the first hydration shell (cf. Fig. 3.1(a)). Consequently the charge distributions of Mg^{2+} and e^- remain in close contact. The electron has moved into the hydration shell and is to an increasing degree localized through cooperation of 2-3 dangling H-atoms. At least one O-H bond of the molecular tweezers found in $[Mg,nH_2O]^+$, n=9-15, belongs to a H_2O ligand located in the first hydration shell. The limited number of water molecules in these clusters is not yet sufficient to establish independent hydration spheres for both the electron e^- and for the dication Mg^{2+}. The H_2O dipoles are oriented as to hydrate both charged species. Therefore the studied cluster ions $[Mg,nH_2O]^+$, n=6-15, are best described as ion pairs $Mg^{2+}(H_2O)_n^-$ for which a mutual stabilization of the cationic and anionic species has to be assumed. The evolution of the SOMOs in Fig. 3.1(a) indicates that the limit of a solvent separated ion pair (hereafter labelled as $Mg^{2+}(H_2O)_ne^-$) is nearly reached at n=19. The odd electron is then almost completely localized in the second solvation shell and the remaining electron density in the first shell directly embracing the magnesium cation is small. The cationic and anionic charge centers are thus well separated by solvent molecules. For $[Mg,nH_2O]^+$, n=17 and 19, the molecular tweezers $HO\text{-}H\cdots e^-\cdots H\text{-}OH$ exclusively involve O-H units of second shell located H_2O molecules. This is a further indication of the preceding transition of the odd electron into the second hydration shell. It has to be assumed that these clusters are considerably stabilized by the large hydration enthalpy of the central dication Mg^{2+} which amounts to approximately 1800 kJ mol^{-1} for bulk hydration in comparison to an estimated value of 360 kJ mol^{-1} for the monocation Mg^+.[14] The large hydration enthalpy of Mg^{2+} and the electron affinity of the hydration shell - a pure water cluster $(H_2O)_{19}$ has an electron affinity of about 110 kJ mol^{-1} - overcompensate the second ionization energy of magnesium.[29]

Charge separation within solvated alkaline earth metal ions has been discussed before for $[Sr,nNH_3]^+$, n≤6. Upon photodissociation of $[Sr,nNH_3]^+$, n≤4, Shen and Farrar[44] observed that the first electronic excitation band of Sr^+ is significantly red shifted for n = 3,4. The spectra were originally interpreted as excitation from a ground state associated with a s-like metal atom orbital to an ion pair excited state $Sr^{2+}(NH_3)_{n-m}(NH_3)_m^-$ lying below the excited state of the singly charged cluster. On the basis of path integral Monte Carlo (PIMC) simulations for $[Sr,nNH_3]^+$, n≤6, Martyna and Klein[45] suggested an alternative interpretation of the experimentally observed redshift. They postulated that with increasing cluster size n the ground state of the valence electron attains Rydberg state like characteristics of s-like symmetry leading to larger cluster radii. According to this assumption of a one center charge distribution both positive and negative charges are still referenced with respect to the metal center.[45-46] Monte Carlo simulations provide photodissociation cross sections in semiquantitative agreement with the experimental values.[47] However, thermochemical analyses revealed an increasing stabilization of two-center (ion pair) states as clusters grow. In addition the assumption of a Rydberg like electronic state in $[Sr,nNH_3]^+$ is questioned by Hertel et al.[48] through studies on isovalent $[Na,nH_2O]$ clusters, which yield strong indication for the existence of a two-center localized ion pair state in $[Na,nH_2O]$, n>4. The radial probability distribution of the odd electron in $[Mg,nH_2O]^+$ (through DFT, present study) differs significantly from that of $[Sr,nNH_3]^+$ (through path integral Monte Carlo simulations[45]). A single H_2O suffices to shift the odd electron in Mg^+ outwards. In contrast a single NH_3 molecule seems to influence the odd electron in Sr^+ by a negligible margin.

Donelly and Farrar[47] discussed their experiments on $[Sr,nNH_3]^+$ in terms of ion pair states $Sr^{2+}(H_2O)_n^-$ without reaching strict conclusions. In case of the isovalent $[Mg,nH_2O]^+$ clusters our ab initio calculations offer a conclusive interpretation of the experimental findings without considering Rydberg-states for the single valence electron in Mg^+. In particular we find the model of a hydrated electron as appropriate to describe the distribution of the odd electron in $[Mg,nH_2O]^+$, n>6. Nevertheless, it remains a challenging endeavor for future studies to apply a time dependent DFT approach on the system $[Mg,nH_2O]^+$ in order to take electronically excited Mg^+ states into account.

C. Vertical Ionization Energies (VIEs) and SOMO Volumes in $[Mg,nH_2O]^+$

In this section the impact of the evolving oxidation state of the magnesium cation on the ionization energies of $[Mg,nH_2O]^+$ clusters is elucidated. In water cluster anions $(H_2O)_n^-$ the vertical detachment energies were experimentally found to decrease continously with cluster size n,[49] and the question arises, how ionization energies depend on cluster size in $[Mg,nH_2O]^+$ clusters which contain a magnesium cation whose oxidation state changes from +1 to +2 with growing cluster size n. In order to provide reliable predictions of the ionization energies of $[Mg,nH_2O]^+$, $n \leq 19$, we used different well established quantum chemical methods, applicable to systems of the investigated size, to calculate vertical and adiabatic ionization energies. We evaluated and compared ionization energies at the Hartree-Fock level of theory with two post-Hartree-Fock methods (MP2&CC2) and gradient corrected density functional theory (BLYP). We also evaluated the applicability of Koopmans' theorem[35] to clusters with a strongly cluster size dependent electronic structure like $[Mg,nH_2O]^+$. According to Koopmans' theorem the vertical ionization energy is equal to the sign-reversed orbital energy from which the electron is removed.

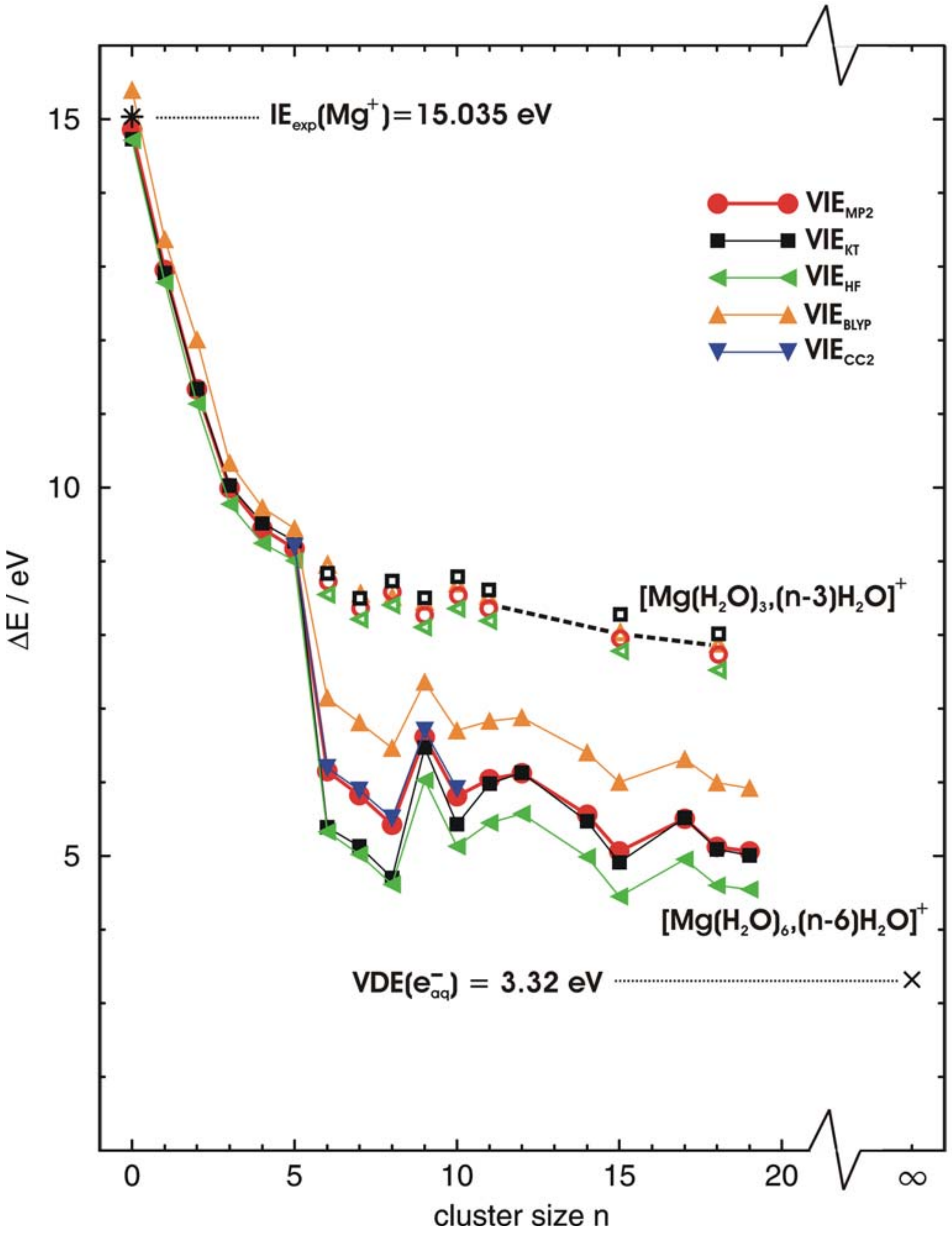

Fig. 3.4 Vertical ionization energies (VIEs) of $[Mg,nH_2O]^+$, n≤19, as calculated by various ab initio methods. For $[Mg,nH_2O]^+$ structures with preferential Mg_{aq}^+ coordination the VIEs decrease steeply with growing cluster size for n≤6. Most prominent is a drop in VIEs at n=6 which coincides with the transition of the SOMO into the hydration shell. For larger clusters the steep decrease levels out and the decline in VIEs for n≥7 is less pronounced. Except for VIE_{BLYP} the calculated VIEs of Mg^+ are in nice agreement with the ionization energy of the Mg^+ cation $IE_{exp}(Mg^+)$. For the largest investigated cluster size the VIEs are still significantly higher than the vertical detachment energy of bulk hydrated electrons $VDE(e_{aq}^-)$. This reveals that it takes clusters with more than 19 water molecules to completely screen Mg^{2+} and e^- from each other. VIEs for $[Mg(H_2O)_3,(n\text{-}3)H_2O]^+$ structures are included as open symbols. These isomers do not exhibit any distinct drop in VIEs. For n≥6 their computed VIEs are higher by 2-3.5 eV than those of $[Mg(H_2O)_6,(n\text{-}6)H_2O]^+$.

Table 3.1 Vertical ionization energies (VIEs) in eV of $[Mg,nH_2O]^+$ clusters with preferential Mg_{aq}^+ coordination

Cluster size n	VIE_{KT}	VIE_{HF}	VIE_{MP2}	VIE_{CC2}	VIE_{BLYP}
0	14.73	14.71	14.86	---	15.40
1	12.91	12.78	12.95	---	13.37
2	11.34	11.14	11.33	---	12.01
3	10.03	9.78	9.99	---	10.33
4	9.52	9.25	9.44	---	9.73
5	9.27	9.00	9.17	9.20	9.44
6	5.39	5.32	6.15	6.20	7.14
7	5.13	5.02	5.82	5.89	6.81
8	4.70	4.61	5.42	5.51	6.46
9	6.47	6.03	6.61	6.70	7.36
10	5.43	5.13	5.81	5.91	6.70
11	5.98	5.45	6.04	---	6.83
12	6.13	5.57	6.12	---	6.88
14	5.47	4.99	5.56	---	6.40
15	4.91	4.52	5.06	---	6.00
17	5.52	4.95	5.50	---	6.31
18	5.09	4.60	5.12	---	5.99
19	5.01	4.54	5.06	---	5.92

Table 3.2 Vertical ionization energies (VIEs) in eV of $[Mg(H_2O)_3,(n\text{-}3)H_2O]^+$ clusters, $n \geq 6$.

Cluster size n	VIE_{KT}	VIE_{HF}	VIE_{MP2}	VIE_{BLYP}
6	8.84	8.55	8.72	8.93
7	8.50	8.20	8.37	8.50
8	8.75	8.43	8.58	8.75
9	8.49	8.14	8.30	8.49
10	8.82	8.38	8.55	8.82
11	8.66	8.20	8.38	8.66
15	8.28	9.49	7.97	8.28
18	8.04	7.53	7.71	8.07

Although more advanced methods for evaluating ionization potentials based on the extended Koopmans' theorem (EKT)[48-51] exist, these methods have not yet found comparable acceptance in practice as they lack the clearness of Koopmans' theorem, which directly relates experimental ionization potentials with energy levels of molecular orbitals. The EKT has long been controversely discussed in literature,[52-56] until only very recently a criterion for its validity has been presented.[57] However, this turned out to be difficult to verify in practice.

Hence Koopmans' theorem remains the standard paradigm for the evaluation of vertical ionization energies from quantum chemical calculations. Its verification in $[Mg,nH_2O]^+$ clusters with an evolving electronic structure is mandatory.

The computed VIEs for $[Mg,nH_2O]^+$ (cf. Fig. 3.4 and Table 3.1) follow the same general decrease with cluster size - irrespective of the computational method applied. The singular drop in VIEs at n=6 is reproduced by all methods. This drop in VIEs coincides with the displacement of the SOMO from the magnesium cation into the hydration shell. Cluster isomers with a 3-fold coordinated magnesium cation $[Mg(H_2O)_3,(n\text{-}3)H_2O]^+$ (cf. Fig. 3.4 and Table 3.2) have VIEs (open symbols) that are significantly higher than those of the energetically favored 6-fold coordinated species. In $[Mg(H_2O)_3,(n\text{-}3)H_2O]^+$ the SOMO remains located at the magnesium cation (cf. Fig. 3.1(b)). Their VIEs amount to approx. 8.0 eV for the largest investigated cluster sizes and affirm that the magnesium monocation is not oxidized in $[Mg(H_2O)_3,(n\text{-}3)H_2O]^+$, $n \leq 18$. The large differences in VIEs of $[Mg,nH_2O]^+$ clusters with a 3-fold and 6-fold coordinated magnesium cation might facilitate a spectroscopic identification of the isomers and allow for an experimental verification of the theoretical prediction that for $n \geq 6$ magnesium dication and hydrated electron coexist within $[Mg,nH_2O]^+$.

Beyond n=6 the steep decrease of the VIEs in $[Mg,nH_2O]^+$ at small n levels out, except for n=9, where a spike in VIEs is obtained. Whereas in n=6-8 the electron is spread out over the outer cluster surface, at n=9 the SOMO is concentrated between free O-H bonds of adjacent H_2O molecules forming $HO\text{-}H\cdots e^-\cdots H\text{-}OH$ structures. These molecular tweezers are reminiscent of the $e^-\cdots H^{\delta+}$ interactions first described by Kim and coworkers[25-26,36-39] in $(H_2O)_n^-$ and later verified by Iwata and Tsurusawa[68-70] in $[M,nH_2O]$ (M=Na,Li) clusters. In $[Mg,nH_2O]^+$ the appearance of molecular tweezers at n=9 is accompanied by a significant increase in VIEs. There is a peculiarity about the minimum structures of n=9 and n=10. In these clusters three O-H bonds of adjacent H_2O molecules are involved in the formation of the molecular tweezers (triple tweezer). In contrast just two O-H bonds (double tweezer) are found to hold the electron in all other clusters of sizes n>10. The possibility that triple tweezers may exist in larger clusters n>10 as well cannot be ruled out. According to the performed calculations, they are energetically favored against double tweezers only for n=9-10, however. Furthermore the computed VIEs reveal that in solvent separated ion pairs $Mg^{2+}(H_2O)_n e^-$ the vertical ionization energies become largely independent of the cluster size n (cf. Fig. 3.4), e.g. $VIE_{MP2} \approx 5.1$ eV. In clusters of this size the solvated electron is localized in the second solvation shell. Both charged species are expected to be well screened from each other by surrounding H_2O molecules (dielectricity constant of water: $\varepsilon \approx 81$). This lets the ionization energies of the clusters ultimately converge to the vertical detachment energy in bulk water hydrated electrons. This energy was thoroughly derived from earlier experimental studies on large $(H_2O)_n^-$ clusters as $VDE(e_{aq}^-)=3.32$ eV.[29]

In the case of the isovalent but overall neutral clusters $[M,nH_2O]$, $n \leq 6$, (M=Na,Li,Cs) experimental[61-63] and theoretical studies[64-67] indicate complete screening of the solvated electron against the M^+ cation for $n \geq 4$. In $[Mg,nH_2O]^+$, $n \geq 6$ the SOMO is similarly detached from the magnesium cation and is transferred into the hydration shell. However - irrespective of the method - the VIEs of the largest $[Mg,nH_2O]^+$ clusters investigated (n=17, 18, 19) are still much larger than $VDE(e_{aq}^-)$ (cf. Fig. 3.4). It takes significantly larger cluster sizes to completely screen the solvated electron from the Mg^{2+} dication in $[Mg,nH_2O]^+$ clusters than from the alkali metal monocation M^+ in $[M,nH_2O]$.

In $[Mg,nH_2O]^+$ the computed VIEs coincide well for each cluster size $n \leq 5$. Deviations among different methods are marginal. For cluster sizes $n \geq 6$ all applied methods reveal qualitatively the same trends. However, absolute values differ more substantially and in a somewhat systematic way: $VIE_{BLYP} > VIE_{MP2} \approx VIE_{CC2} > VIE_{HF}$. Most interesting is the cluster size specific behaviour of VIE_{KT}. While it comes close to VIE_{HF} in n=6-8, it is in much better agreement with VIE_{MP2} for n>10. Koopmans' theorem serves as a starting point for any computation of vertical ionization energies. However its applicability cannot be assumed a priori. Koopmans' theorem neglects - in principle - two opposite contributions to the VIEs: The orbital relaxation upon ionization and differences in electron correlation between different charge states. Koopmans' theorem assumes that occupied orbitals in $[Mg,nH_2O]^{2+}$ are identical to those in $[Mg,nH_2O]^+$. This is of course only an approximation and consideration of orbital relaxation diminishes the VIEs. Due to the loss of an electron the correlation energies in $[Mg,nH_2O]^{2+}$ are expected to be decreased with regard to $[Mg,nH_2O]^+$, consequently VIEs are enhanced upon ionization if correlational effects are taken into account. Only as long as the two neglected energy contributions are of similar size Koopmans' theorem is a good approximation due to error cancellation. To validate the applicability of Koopmans' theorem in the case of $[Mg,nH_2O]^+$ clusters VIE_{KT} energies are to compare to VIEs from total energies of charge states +1 and +2 that are explicitly calculated at different levels of theory.

D. SOMO Volumes and Their Impact on the Contribution to VIEs from Electron Correlation and from Orbital Relaxation

SOMO volumes were evaluated by calculating SOMO extent measures (SEMs)[58] for the Hartree-Fock orbitals in [Mg,nH_2O], n≤19. The SEM is defined as the volume in Å^3 which contains half an electron in SOMO. In a fixed cubic grid with constant spacings Δx=Δy=Δz the wave function $\Psi_{SOMO}(r_{i,j,k})$ is calculated for $r_{i,j,k}$ (i=1-N, j=1-N, k=1-N). The $\Psi_{SOMO}(r_{i,j,k})$ are sorted in descending order:

$$\left|\Psi_{SOMO}(1)\right|^2 \geq \left|\Psi_{SOMO}(2)\right|^2 \geq \ldots \geq \left|\Psi_{SOMO}(p)\right|^2 \geq \ldots \geq \left|\Psi_{SOMO}(N^3)\right|^2$$

The index p is determined such that $\sum_l^p \left|\Psi_{SOMO}(l)\right|^2 \times \Delta x \Delta y \Delta z \approx 0.5$ and the SOMO extent measure (SEM) is calculated as $SEM = p \times \Delta x \Delta y \Delta z$. Iwata and Tsurusawa evaluated SEMs for various $(H_2O)_2^-$ and $(H_2O)_6^-$ isomers and found SEMs between 6300 - 5500 Å^3 in case of $(H_2O)_2^-$
and 110 - 210 Å^3 in case of $(H_2O)_6^-$.[58] Our calculated SEMs reveal that the SOMOs in [Mg,nH_2O]$^+$ are one to two orders of magnitude less diffuse than in $(H_2O)_n^-$. Weigend and Ahlrichs proved in their ab initio studies of $(H_2O)_2^-$ and $(H_2O)_6^-$ clusters that the RI-MP2 method yields accurate vertical ionization (detachment) energies even in clusters with extremely diffuse electronic states as long as the applied basis is sufficiently diffuse.[27] They showed that a basis of triple-ζ valence type plus polarization functions - TZVP for H and TZVPP for O - is well suited when it is augmented with a floating center, e.g. with a (3s2p) basis set. The basis sets in our calculations were of triple-ζ valence type plus polarization functions (O, H: TZVP; Mg: TZVPP) augmented with 4 floating centers (3s2p) as used by Weigend and Ahlrichs. Hence the applied basis sets in this work are expected to be well suited for a correct description of the SOMO in [Mg,nH_2O]$^+$ clusters. The reliability of the calculated VIE_{MP2} energies for the investigated [Mg,nH_2O]$^+$ clusters is consolidated by the close correspondence to energies from the second order approximate coupled cluster singles and doubles method CC2. Both methods explicitly include electron correlation.

In [Mg,nH_2O]$^+$ VIE_{KT} is close to VIE_{MP2} for all cluster sizes except for n=6-8 and n=10. In contrast the calculated VIE_{BLYP} and VIE_{HF} values differ systematically from VIE_{MP2} for all cluster sizes n≥9. Even for n≤5 VIE_{BLYP} values are slightly higher than those obtained through the other methods. VIE_{MP2} is in nice agreement with the experimental ionization energy of the Mg^+ monocation ($IE_{exp}(Mg^+)$=15.035 eV)[68]. VIE_{KT} and VIE_{HF} are close to $IE_{exp}(Mg^+)$ as well. VIE_{BLYP} is 0.36 eV too high. Very recently Hamel et al. showed that Kohn-Sham orbital energies calculated using the exact Kohn-Sham exchange energy potential are better approximations to experimental ionization energies than are Hartree-Fock orbital energies calculated via Koopmans' theorem.[35] However, it is well known that the available approximate functionals are not generally qualified for a truely quantitative determination of ionization energies.[21]

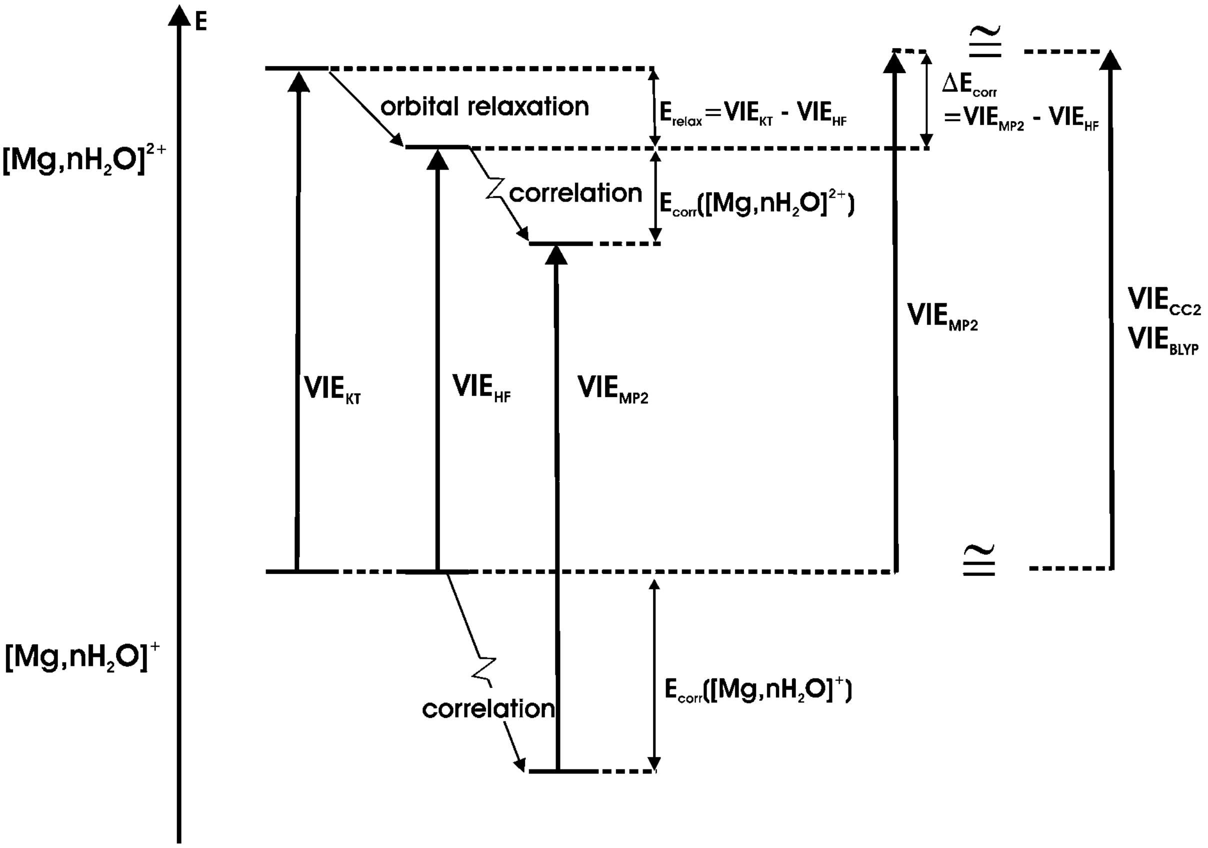

Fig. 3.5 Energy scheme for the evaluation of differences in correlation energies (ΔE_{corr}) and orbital relaxation upon ionization (E_{relax}). VIEs according to Koopmans' theorem (VIE_{KT}) neglect orbital relaxation and differences in correlation energy upon ionization in the minimum structures of $[Mg,nH_2O]^+$ and $[Mg,nH_2O]^{2+}$. Relaxation leads to a decrease in absolute energy of $[Mg,nH_2O]^{2+}$ as the orbitals are free to adjust to the higher charge in $[Mg,nH_2O]^{2+}$. VIEs are calculated explicitly as a difference of Hartree-Fock calculations (VIE_{HF}) to include this effect. Hence VIE_{HF} is decreased with regard to VIE_{KT}. Due to the loss of one electron in $[Mg,nH_2O]^{2+}$ the correlation energy $E_{corr}([Mg,nH_2O]^{2+})$ is lower than $E_{corr}([Mg,nH_2O]^+)$. VIEs obtained as difference from ab initio calculations which include correlation (e.g. VIE_{MP2}) are therefore increased with regard to VIE_{HF}. Koopmans's theorem is only a valid approximation in clusters for which E_{relax} (increase in VIE) and ΔE_{corr} (decrease in VIE) cancel.

The accuracy of the computed $\mathrm{VIE}_{\mathrm{BLYP}}$ values depend crucially on a balanced description of the exchange and correlation contributions in both charge states through the BLYP functional. We ascribe the systematic divergence between $\mathrm{VIE}_{\mathrm{BLYP}}$ and $\mathrm{VIE}_{\mathrm{MP2}}$ energies to the non-fulfillment of this prerequisite in $[\mathrm{Mg,nH_2O}]^+$, n>6.

It is noted in passing, that also the celebrated B3LYP functional did not yield significant improvements. VIEs were calculated for a limited number of cluster sizes n using the B3LYP functional and obtained $\mathrm{VIE}_{\mathrm{B3LYP}}$ energies close to the respective $\mathrm{VIE}_{\mathrm{BLYP}}$ values. Other than DFT and post-Hartree-Fock methods (MP2 and CC2) the Hartree-Fock approach does not include electron correlation and consequently underestimates VIEs. Nevertheless, the calculated $\mathrm{VIE}_{\mathrm{HF}}$ data offer valuable information. By evaluation of $\mathrm{VIE}_{\mathrm{MP2}}$ (includes orbital relaxation and electron correlation), $\mathrm{VIE}_{\mathrm{HF}}$ (only orbital relaxation) and $\mathrm{VIE}_{\mathrm{KT}}$ (neither orbital relaxation nor electron correlation) as a function of cluster size n we determined the contribution of orbital relaxation and that of electron correlation to the VIEs approximately (cf. Fig. 3.5).

ΔE_{corr} equals the difference in electron correlation energy between $[\mathrm{Mg,nH_2O}]^+$ and $[\mathrm{Mg,nH_2O}]^{2+}$ at the MP2 level of theory and is determined through:

$$\Delta E_{\mathrm{corr}}=\mathrm{VIE}_{\mathrm{MP2}} - \mathrm{VIE}_{\mathrm{HF}}. \qquad (3.3)$$

The energetic effect of orbital relaxation is quantified as:

$$E_{\mathrm{relax}} =\mathrm{VIE}_{\mathrm{HF}} - \mathrm{VIE}_{\mathrm{KT}}. \qquad (3.4)$$

ΔE_{corr} (≥0) and E_{relax} (≤0) provide opposite contributions to the VIEs. Both ΔE_{corr} and E_{relax} are expected to depend on the electronic structure of the clusters which we showed to evolve with cluster size n (cf. Fig. 3.1). We quantified SOMO volumes in $[\mathrm{Mg,nH_2O}]^+$, n≤19, through calculation of SEMs which serve as benchmark for the diffuseness of the SOMOs within the investigated clusters. Our calculations are going to indicate that ΔE_{corr} and E_{relax} are correlated with the computed SEMs. Before their interplay is analyzed. the cluster size dependency of the SOMO volumes and their effect on VIEs (cf. Fig. 3.6(a)) will be outlined.

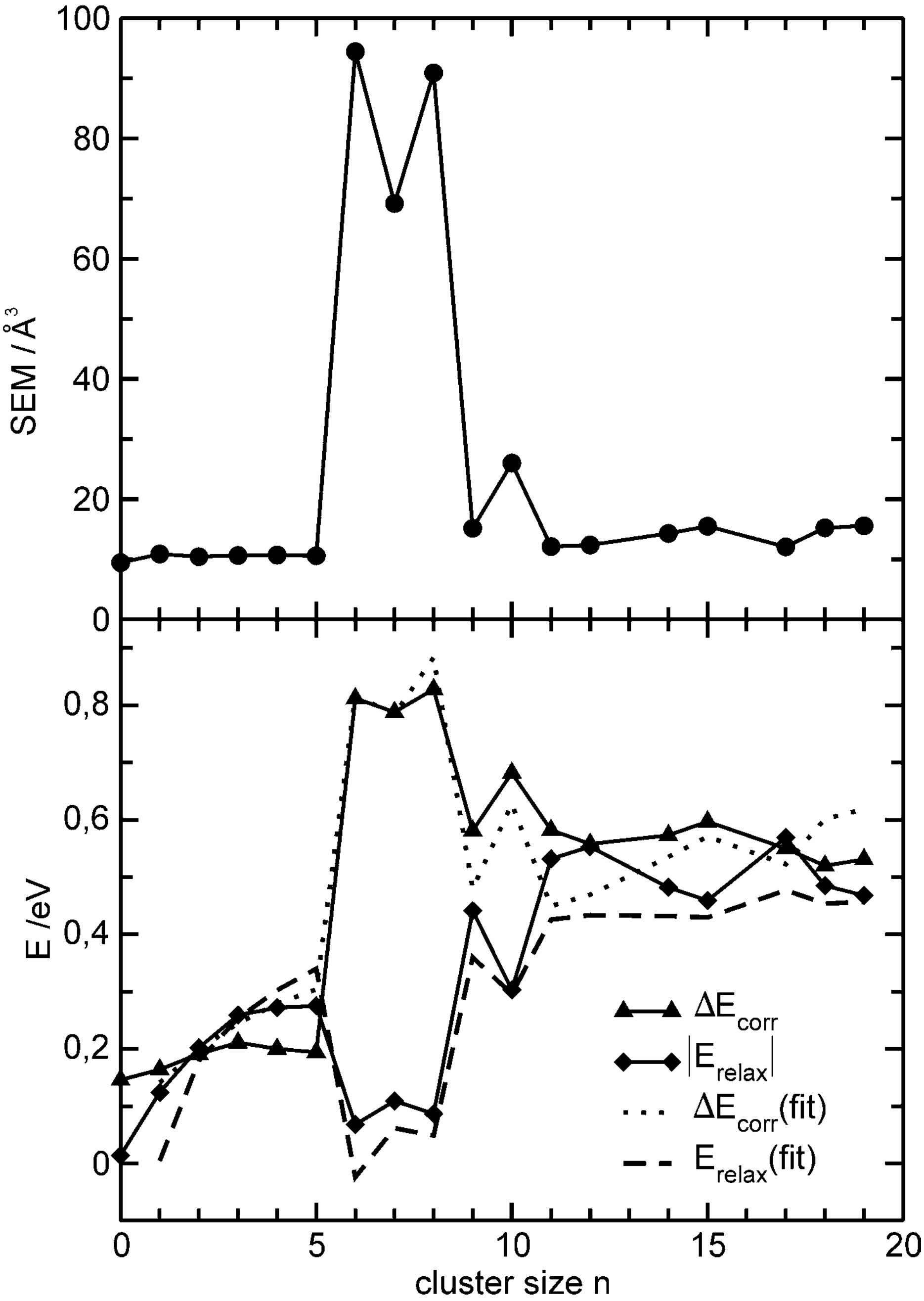

Fig. 3.6 **(a)** SOMO extent measures (SEMs) as a function of cluster size n in minimum cluster structures of $[Mg,nH_2O]^+$. In n=6-8 the odd electron is spread out across the cluster surface and the SEM become largest. For clusters which contain the SOMO either localized at the magnesium cation with sp-hybrid-like character (n≤5) or located between double tweezers in the hydration sphere (n≥9) the SEM remains essentially constant. **(b)** ΔE_{corr} and $|E_{relax}|$ are of comparable size except for clusters with large SEMs (n=6-8). In these clusters ΔE_{corr} becomes large while $|E_{relax}|$ almost vanishes. For clusters with the SOMO localized by molecular tweezers (n≥9) ΔE_{corr} and $|E_{relax}|$ are somewhat larger than for clusters with the SOMO located at the magnesium cation (n≤5). The cluster size dependent changes of ΔE_{corr} and $|E_{relax}|$ correlate closely with those of the SOMO volume. Analytical fits for ΔE_{corr} and $|E_{relax}|$ as function of the SEMs (see text) are included as dotted and dashed lines, respectively.

Attachment of up to 5 H_2O molecules to a magnesium monocation effects the SEM only to a minor degree: The difference in SEMs between $[Mg,nH_2O]^+$, n=5, and the Mg^+ cation is only 1.1 $Å^3$. For isomers with a 3-fold coordinated magnesium cation $[Mg(H_2O)_3,(n-3)H_2O]^+$ the computed SEMs do not change noticeably with cluster size (omitted in Fig. 3.6(a)). For the energetically lower 6-fold coordinated species the SEM changes drastically upon closure of the first hydration shell at n=6. The SOMO detaches from the magnesium cation and the SEM rises from 10.6 $Å^3$ for n=5 to 94.4 $Å^3$ for n=6, which is an increase by more than 800%.

With occurence of molecular tweezers HO-H···e^-···H-OH at n=9 the SEM drops as drastically to 15.2 $Å^3$ and at n=10 the SEM slightly increases again to 26.0 $Å^3$. Both cluster sizes n=9 and n=10 contain triple tweezers, but while in n=9 the molecular tweezer is formed exclusively by first shell H_2O molecules, in n=10 the triple tweezer stretches into the second solvation shell. One O-H bond of the tweezer belongs to a second solvation shell located H_2O molecule (cf. n=10 Fig. 3.1). In even larger clusters the solvated electron is completely shifted into the second hydration shell by double tweezers. For these clusters the SEMs constantly amount to ~14 $Å^3$. The mean O-H···H-O distances in triple tweezers are longer than those of double tweezers in clusters of comparable size. In n=9,10 the mean O-H···H-O distances are 2.49 Å and 3.02 Å, whereas in n=11,12 the O-H···H-O distances are 2.30 Å and 2.23 Å respectively. The differences in SEMs between these clusters are correlated with the dimensions of the tweezers. For simple geometric reasons the alignment of just two O-H bonds, as in case of the double tweezers, allowsfor shorter O-H···H-O distances. Since the SOMOs are largely localized between the O-H bonds this results in smaller SEM values.

The now computed SEMs verify that the SOMO volumes in $[Mg,nH_2O]^+$ clusters - at least for structures with preferred Mg_{aq}^+ coordination - do not increase continously with cluster size but exhibit a most prominent maximum in $[Mg,nH_2O]^+$, n=6-8. The large SEMs as well as the shape of the SOMOs (cf. Fig. 1(a)) indicate that the electronic structures in n=6-8 are best described as diffuse surface states, with the electron smeared out all over the cluster surface. In contrast small clusters n<6 have the SOMOs localized in sp-hybrid-like orbitals at the magnesium cation. In large clusters n≥9 molecular tweezers are outermost effective in the localization of the SOMOs within the hydration sphere.

In the following possible dependencies between SEMs, ΔE_{corr} and E_{relax} will be addressed. For all clusters $[Mg,nH_2O]^+$ with SEMs below 20 $Å^3$ ΔE_{corr} and $|E_{relax}|$ are of comparable quantity and differences in their absolute values are less than 0.15 eV. For these clusters

Koopmans' theorem performs as well as MP2. ΔE_{corr} (≥ 0) and E_{relax} (≤ 0) compensate each other (error cancellation). In $[Mg,nH_2O]^+$, n=6-8, ΔE_{corr} and the absolute value of the relaxation energy $|E_{relax}|$ differ substantially from each other. $|E_{relax}|$ diminishes while ΔE_{corr} becomes large (~0.8 eV). In this respect $[Mg,nH_2O]^+$, n=6-8, differ from clusters with localized SOMOs for which the contributions of orbital relaxation are approximately equal to those stemming from correlation. In $[Mg,nH_2O]^+$ clusters which contain the solvated electron localized within the hydration shell by molecular tweezers (n≥9) $|E_{relax}|$ and ΔE_{corr} fluctuate around 0.55 eV while in clusters with sp-hybrid-like SOMOs (n≤5) they range from 0.15 to 0.3 eV. The only significant deviation is found for n=10. The larger SOMO volume for this cluster size (SEM=26.1 Å^3) causes a rise in ΔE_{corr} to 0.68 eV. This rise occurs at the expense of the absolute value of the relaxation energy which drops to $|E_{relax}|$=0.30 eV and thus comes close to the $|E_{relax}|$ values obtained for smaller cluster sizes with sp-hybrid-like SOMOs. Although the SEM for n=10 is still much lower than for clusters with a diffuse surface state (n=6-8) $|E_{relax}|$ and ΔE_{corr} differ more substantially than for any other cluster size with a localized SOMO. Apparently the ratio ΔE_{corr} / $|E_{relax}|$ is very sensitive to changes in the SOMO volume. We find these two entities to be balanced only in $[Mg,nH_2O]^+$ clusters with SEMs < 20 Å^3.

The cluster size dependent changes of ΔE_{corr} correlate closely with those of the SOMO volume. Most notably those of $|E_{relax}|$ anti-correlate with the SOMO volume. Correlations are close enough to allow for approximate fits according to:

$$\left|E_{relax}(n)\right| = -\frac{1}{3n^{1/3}}\ln SEM + 0.8 \qquad (3.5)$$

$$\Delta E_{corr}(n) = \frac{n^{1/4}}{7}\ln SEM - 0.2 \qquad (3.6)$$

These fits (cf. Fig. 3.6(b)) emphasize the seemingly close relation between SOMO volume on the one hand and orbital relaxation and correlation loss upon ionization on the other. It is not clear whether the analytical form of the fits may be derived directly from quantum chemistry. As a matter of fact we seriously doubt that this may be the case. Nevertheless, we once more emphasize the obvious connection between SOMO volume and corrections to Koopmans’ theorem. A qualitative understanding of these corrections is possible. In the present case orbital relaxation upon ionization of the very diffuse SOMO electron is small due to the lack of strong overlap with any valence electrons. Large molecular orbitals are known to introduce more correlation than compact ones. While the former statement is obvious the later stems from extended experience with valence and core orbitals. It is far from obvious that this “experience” may indeed be extended to a weakly bound solvated electron. In conclusion we have found strong correlation and anti-correlation of various corrections to Koopmans’ theorem with the orbital volume of the odd electron in $[Mg,nH_2O]^+$ clusters. These findings hold irrespective of the cluster size dependent change of the orbitals character (sp-hybrid to delocalized diffuse surface state to localized triple and double tweezers). It is a future task to elaborate whether and how far our present conclusions apply to other molecular systems.

E. Adiabatic Ionization Energies (AIEs) and Cluster Reorganization

The adiabatic ionization energy (AIE) of the $[Mg,nH_2O]^+$ clusters is defined as the difference in total energy of the located (global) minimum structures for the charge states +2 and +1. Other than for the VIEs this implies geometry optimizations of the +2 states. The decrease of the AIEs with growing cluster size n (cf. Fig. 3.7 and Table 3.3) is steeper than that of the VIEs. This holds true except for n=6-8, where AIEs and VIEs are almost equal. This makes the drop of AIEs at n=6 less pronounced than that of the VIEs. The AIEs as calculated through various methods coincide well for n≤5 but differ somewhat for large cluster sizes. These differences behave in the same systematic way as in the case of the VIEs ($AIE_{BLYP}>AIE_{MP2}\approx AIE_{CC2}>AIE_{HF}$) and as discussed in section C The AIEs of clusters with a 3-fold coordinated magnesium cation $[Mg(H_2O)_3,(n-3)H_2O]^+$, n≥6, are provided in Table 3.4.

The AIEs exhibit a continous decrease and differences between 3-fold and 6-fold coordination of the magnesium cation within the clusters are less pronounced than for the VIEs. As in section D the focus of this analysis will be focussed on isomers with the preferential Mg_{aq}^+ coordination.

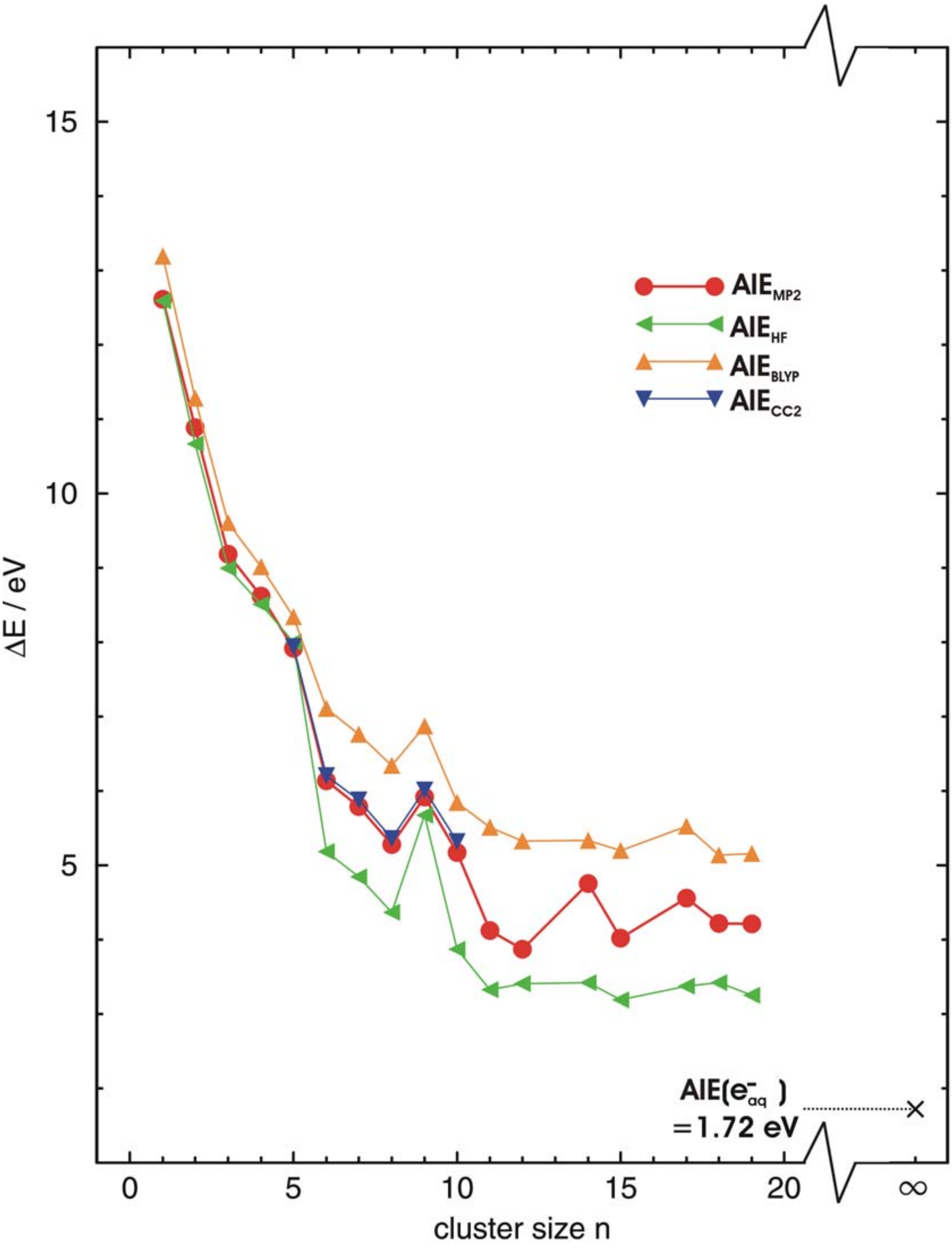

Fig. 3.7 Adiabatic ionization energies (AIEs) for $[Mg,nH_2O]^+$, $n \leq 19$, as calculated by various ab initio methods. Due to reorganization of the cluster upon ionization the AIEs are decreased with regard to the VIEs except for clusters with a diffuse electronic surface state (n=6-8). In $[Mg,nH_2O]^+$, $n \leq 19$, the AIEs are well above the adiabatic ionization energy of the solvated electron in bulk water AIE(e_{aq}^-). These AIEs imply an incomplete screening of the solvated electron and the magnesium dication against each other within clusters of the investigated size.

Table 3.3 Adiabatic ionization energies (AIEs) in eV of $[Mg,nH_2O]^+$ clusters with preferential Mg_{aq}^+ coordination

Cluster size n	*AIE$_{HF}$*	*AIE$_{MP2}$*	*AIE$_{CC2}$*	*AIE$_{BLYP}$*
1	12.59	12.61	---	13.19
2	10.67	10.88	---	11.28
3	8.99	9.19	---	9.61
4	8.51	8.62	---	9.01
5	8.00	7.92	7.94	8.34
6	5.18	6.14	6.20	7.11
7	4.84	5.79	5.88	6.76
8	4.37	5.28	5.36	6.34
9	5.67	5.92	6.02	6.87
10	3.87	5.17	5.32	5.85
11	3.33	4.12	---	5.51
12	3.41	3.87	---	5.32
14	3.42	4.75	---	5.34
15	3.19	4.02	---	5.20
17	3.37	4.56	---	5.53
18	3.42	4.22	---	5.14
19	3.26	4.21	---	5.16

Table 3.4 Adiabatic ionization energies (AIEs) in eV of $[Mg(H_2O)_3,(n\text{-}3)H_2O]^+$ clusters, $n \geq 6$.

Cluster size n	*VIE$_{HF}$*	*VIE$_{MP2}$*	*VIE$_{BLYP}$*
6	6.84	7.10	7.43
7	6.41	6.60	6.91
8	5.88	6.27	6.51
9	5.52	5.94	6.22
10	5.42	5.77	6.07
11	5.10	5.61	5.91
15	4.28	4.82	5.16
18	3.84	4.47	4.85

The reorganization energy

$$E_{reorg}=\text{VIE-AIE} \qquad (3.7)$$

is the energy released when the cluster adjusts to the new charge state in the course of the ionization process. E_{reorg} is typically assigned a positive value, so E_{reorg} is the negative of the described reorientation process. E_{reorg} (cf. Fig. 3.8) provides valuable information about the extent of the structural reorganization upon ionization in $[Mg,nH_2O]^+$, n≤19. In case of n=9-10 we also included E_{reorg} for some cluster isomers with double tweezers instead of triple tweezers. The absolute value of the reorganization energy E_{reorg} increases continously with growing cluster size n for clusters with sp-hybrid-like SOMOs (n=1-5), but drops essentially to zero for n=6-8. In $[Mg,nH_2O]^+$, n≤5, there are two different hemispheres around the magnesium cation (cf. Fig. 3.1(a)). One hemisphere contains the H_2O ligands and the other is occupied by the SOMO and is void of ligands. With removal of the odd electron occupying the SOMO the geometries change in order to minimize repulsive forces between adjacent H_2O ligands and thus the mean distance between the H_2O ligands increases. E.g. for n=2 the valence angle formed by the two H_2O ligands and the magnesium cation enlarges from 93.58° to 178.60° resulting in a linear cluster geometry. In this geometry the distance between the two H_2O ligands is certainly at maximum (3.93 Å in $[Mg,nH_2O]^{2+}$ vs. 3.09 Å in $[Mg,nH_2O]^+$).

In contrast there is no reorganization upon ionization in $[Mg,nH_2O]^+$, n=6-8, with a 6-fold coordinated magnesium cation. The solvated electron in its delocalized surface state has a negligible effect on the cluster structure. Thus the geometry change upon ionization is marginal in $[Mg,nH_2O]^+$, n=6-8. This is different from all other clusters in which the SOMO has either distinct sp-hybrid-like character and is localized at the magnesium cation (n≤5) or is localized within the hydration shell through molecular tweezers (n≥9). In all of these clusters the localized SOMO has a strong impact on the structure. Non-zero E_{reorg} values for n≠6-8 indicate substantial reorganization of these cluster structures upon ionization.

The molecular tweezers $HO\text{-}H\cdots e^-\cdots H\text{-}OH$ in $[Mg,nH_2O]^+$, n≥9, become obsolete with removal of the solvated electron. Subsequently, the hydrogen bonded network in their vicinity reorganizes upon ionization. In n>10 all of the located minimum structures contain

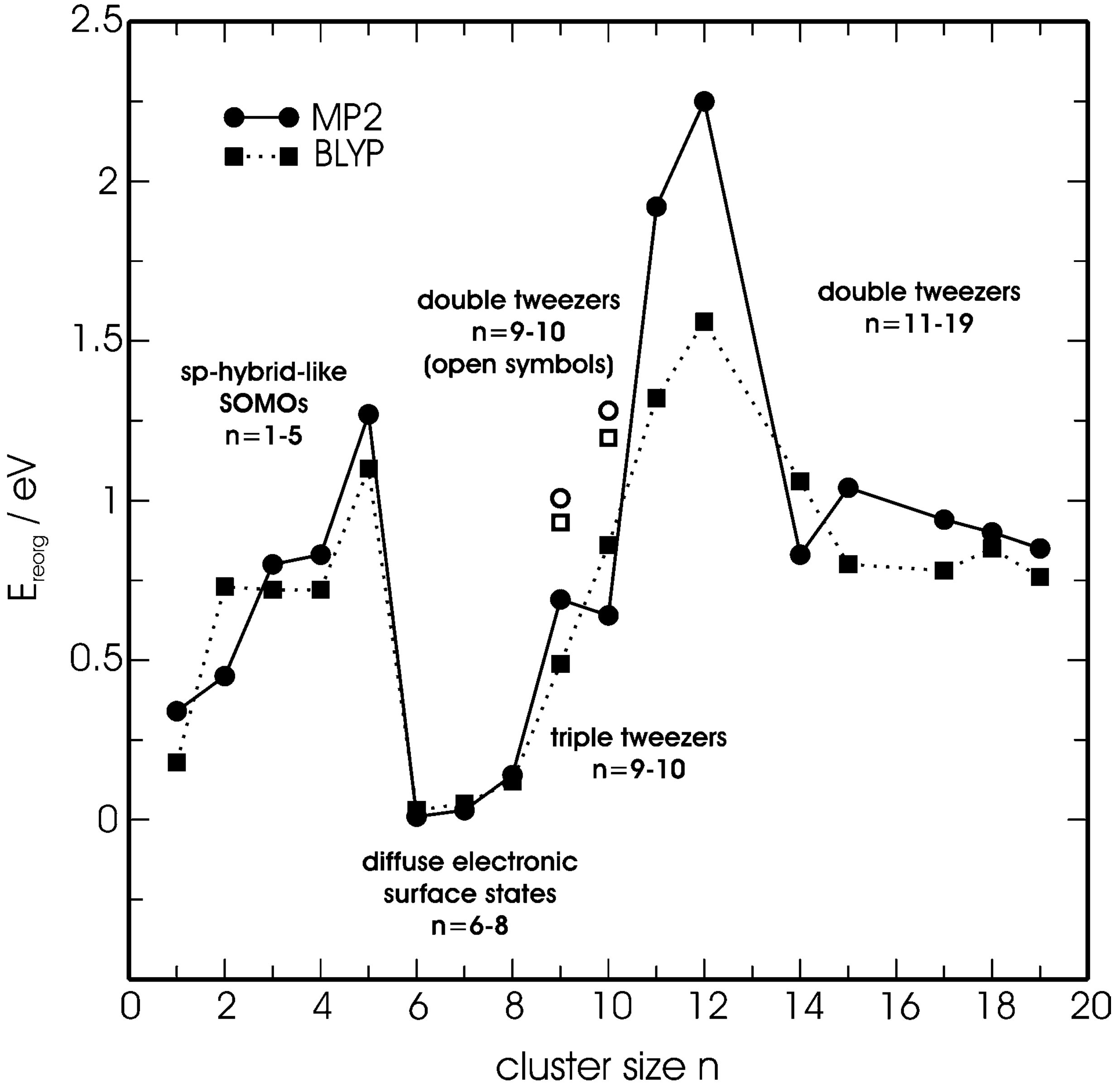

Fig. 3.8 Reorganization energies E_{reorg} in $[Mg,nH_2O]^+$, $n \leq 19$, as evaluated by MP2 and BLYP calculations. Calculations refer to cluster isomers of preferred Mg_{aq}^+ coordination. E_{reorg} for some high energy isomers (double tweezers in n=9-10) are indicated by open symbols. E_{reorg} is clearly correlated with the electronic structure of the clusters (see text).

double tweezers. We have reported before the gradual shift of the SOMOs' radial probability density distribution to higher r values as clusters grow.[74] Clusters of size n=11-12 have first shell H_2O molecules form double tweezers to hold the solvated electron within the first hydration shell (cf. n=11 Fig. 3.1(a)). Consequently the localized electron strongly influences the structure of the first hydration shell and subsequently that of the second solvation shell as well. Here the SOMO ultimately affects the whole cluster structure. In n>14 the SOMOs are located between molecular tweezers formed exclusively by second hydration shell located H_2O molecules at the periphery of the cluster (cf. n=18 Fig. 3.1(a)). In these clusters the effect of the SOMOs on the cluster structure is local, limited on adjacent H_2O molecules. Thus the reorganization energy can be substantially larger for smaller clusters with the electron localized in the first hydration shell than for large clusters with the solvated electron shifted into the second solvation shell.

The minimum structures of n=9-10 contain triple tweezers instead of double tweezers and the SOMOs are located within the first hydration shell (cf. n=10 Fig. 3.1(a)). Nevertheless the E_{reorg} energies are close to those of clusters with the solvated electron shifted in the second solvation shell (cf. n=18 Fig. 3.1(a)). Triple tweezers differ from double tweezers in the number of O-H bonds and in their arrangement. The double tweezer O-H bonds in n=11-12 are in plane. The triple tweezer O-H bonds in n=9-10 are twisted. The O-H···H-O dihedral angles amount to 23° and higher. When comparing clusters of the same size the mean O-H···H-O distance in triple tweezers (2.49 Å (n=9); 3.02 Å (n=10)) is longer than in double tweezers (2.30 Å (n=11); 2.23 Å (n=12)). The twisted alignment and the elongated O-H···H-O distance reduce repulsion, that otherwise arises upon ionization of triple tweezers. This results in a significant decrease of E_{reorg} with respect to double tweezer structures.

For the largest studied cluster sizes the AIEs at the MP2 level of theory converge towards $AIE_{MP2} \approx 4.2$ eV. Complete and independent solvation of both charged species in $[Mg,nH_2O]^+$ clusters – Mg^{2+}_{aq} and e^-_{aq} – should have the AIEs converge to the adiabatic ionization energy of the solvated electron in bulk water $AIE(e_{aq}^-)$. Coe et al. utilized cluster studies to approach the electronic structure of bulk water.[68] They determined the adiabatic electron affinity of bulk water and found $AEA_\infty=1.72$ eV. In case of $(H_2O)_n^-$ clusters the adiabatic electron affininity AEA equals the adiabatic ionization energy AIE ($AIE=AEA=VIE-E_{reorg}$). For an independent solvation of both charged species in $[Mg,nH_2O]^+$ $AIE(e_{aq}^-)=AEA_\infty=1.72$ eV is expected. Irrespective of the ab initio method, our calculations yielded AIEs that are significantly larger than $AIE(e_{aq}^-)$. This holds even for the largest $[Mg,nH_2O]^+$ clusters investigated. Apparently the charge density of the magnesium dication is partly screened in $[Mg,nH_2O]^+$, n≤19. An independent solvation of both the magnesium dication and the coexisting hydrated electron is not reached within the investigated cluster size regime n≤19. The description of these clusters as solvent separated ion pairs $Mg^{2+}(H_2O)_ne^-$, which implies that both charged species are separated by H_2O ligands but not completely screened, is once more found to be most appropriate for a vivid description of the electronic structure. In our studies the reorganization energy upon ionization of separated ion pairs $Mg^{2+}(H_2O)_ne^-$ converges to approximately E_{reorg}≈0.9 eV. Coe et al. also determined the reorganization energy of aqueous electron solvation and found $E_{reorg}(e_{aq}^-)$ =1.6 eV.[68]

Although the E_{reorg} energies of the largest investigated $[Mg,nH_2O]^+$ clusters are still somewhat lower than $E_{reorg}(e_{aq}^-)$, we expect E_{reorg} to increase as soon as the cluster size of $[Mg,nH_2O]^+$ suffices for a separate solvation of both charged species within the cluster. This is anticipated to take 100 water molecules or even more.

F. Hydrated Magnesium Hydroxide Clusters $[MgOH,nH_2O]^+$

Calculations were performed on $[MgOH,nH_2O]^+$ clusters with $n \leq 18$. Starting geometries of the clusters $[MgOH,nH_2O]^+$, $n \geq 6$, assumed sixfold coordination of Mg. For $n \leq 5$ only first shell coordination was taken into account. The optimized structures of all cluster sizes revealed OH to be located in the first hydration shell. It is directly bound to the central magnesium cation, and together they form the molecular monocation $MgOH^+$. Any optimization with OH placed in the second solvation shell of $[MgOH,nH_2O]^+$, even for the largest investigated cluster size n=18, led to the formation of a first shell OH through intracluster proton transfer. Different isomers of e.g. $[MgOH,nH_2O]^+$, n=18, differ in total energy only by small amounts (-0.6 kJ mol^{-1}). A sytematic search for the global minimum of each cluster size n was not performed, as this is off scale for n>6.

Nevertheless, the calculated local minima are characteristic, as long as the total number of hydrogen bonds is kept at maximum. The atomic net electron populations at the OH (Mulliken charges) range from -0.62 in $MgOH^+$ to -0.57 in $[MgOH,nH_2O]^+$, n=18 (cf. Table 3.5). Thus a significant overall negative partial charge is located at OH in all clusters $[MgOH,nH_2O]^+$ studied. This justifies the treatment of OH as basically a hydroxyl ion OH^- bound to the dication Mg^{2+} in $[MgOH,nH_2O]^+$, $n \leq 18$.

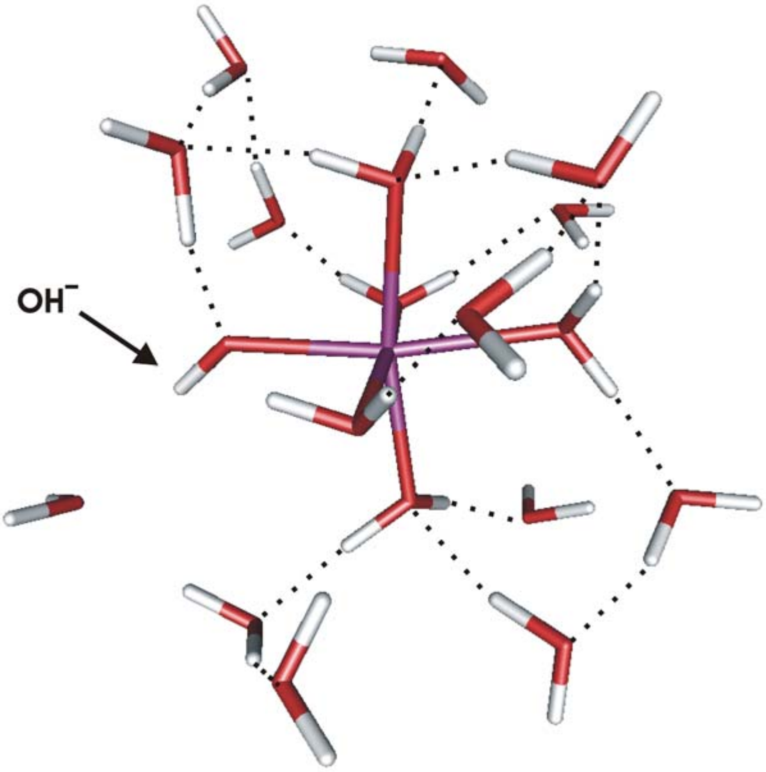

Fig. 3.9 Fully optimized geometrical structure of $[MgOH,18H_2O]^+$. H···O distances ≤1.90 Å are indicated as dotted lines.

Table 3.5 Mulliken charges in the molecular core ion $MgOH^+$ of hydrated magnesium hydroxide clusters $[MgOH,nH_2O]^+$ in atomic units.

n	$q_{Mg}(n)/a.u.$	$q_O(n)/a.u.$	$q_H(n)/a.u.$
0	1.4830	-0.9811	0.3660
1	1.4620	-0.9150	0.3413
2	1.4308	-0.9452	0.3176
3	1.3509	-0.9442	0.3115
4	1.3387	-0.9502	0.3006
5	1.2087	-0.9619	0.3078
6	1.1657	-0.9900	0.3019
8	1.1784	-0.9263	0.3048
11	1.1925	-0.9100	0.3114
14	1.2195	-0.9043	0.3114
18	1.2530	-0.9003	0.3261

In previous studies of $[MgOH,nH_2O]^+$, n=1-5, it was concluded that the effective charge at the magnesium cation decreases with increasing number of H_2O ligands.[9,11] The dominant interaction between the Mg^{2+} ion and the H_2O molecules in the clusters $[MgOH,nH_2O]^+$, n≤5, is surely electrostatic. As first shell H_2O ligands come close enough to have their O-atom lone pairs overlap with the vacant Mg^{2+} 3s and 3p orbitals, some covalent character will arise in addition. This results in the reduction of the effective charge at Mg^{2+}. Consistent with the overall decreasing effective charge of the magnesium cation in $[MgOH,nH_2O]^+$, n=0-5, the Mg-OH distance increases from 1.80 Å for $MgOH^+$ to 1.98 Å for $[MgOH,5H_2O]^+$. The addition of second shell H_2O ligands (n>5) leads to a slight inrease of the effective charge at the magnesium cation. This is due to first shell OH^- forming donor H-bonds ($HO^- \cdots HOH$) to second shell H_2O molecules. Second shell H_2O molecules have only a minor effect on the Mg-OH distance, it remains almost constant for n=6-18 (2.01 Å - 2.05 Å).

Because of the attractive ion-dipole interactions and because of some covalent bonding to the Mg^{2+} the first and second shell H_2O ligands are aligned with the O-atom pointing towards the central metal ion. H-bonds between first and second shell H_2O further stabilize this structure. The OH^- ligand provides a single H-bond donor site for an acceptor within the second hydration shell. Furthermore the negative charge located at OH^- effectively shields the positive charge of the central magnesium ion. Therefore the coordination space around OH^- becomes less favorable for the attachment of second shell H_2O ligands as compared to other prospective first shell water molecules (cf. Fig. 3.9).

G. Thermochemistry of Reactive versus Non-Reactive Evaporation and Switching of Propensities

On the basis of the published experimental data it was anticipated that the enthalpies ΔH_{vap} and ΔH_{react} for the two competing decay channels of $[Mg(H_2O)_n]^+$, evaporation of a H_2O monomer (eq. 3.1) and elimination of a H-atom (eq. 3.2), cross twice as a function of cluster size.[10,13-14] The two concommitant product switchings were experimentally observed at n=5-7 and at n≥15.[10,14] The first limit seems to depend on the experimental conditions whereas the second one is more sturdy.

The changes in enthalpies (T=0 K) of the two processes (eq. 3.1) and (eq. 3.2) were calculated as a function of cluster size n.

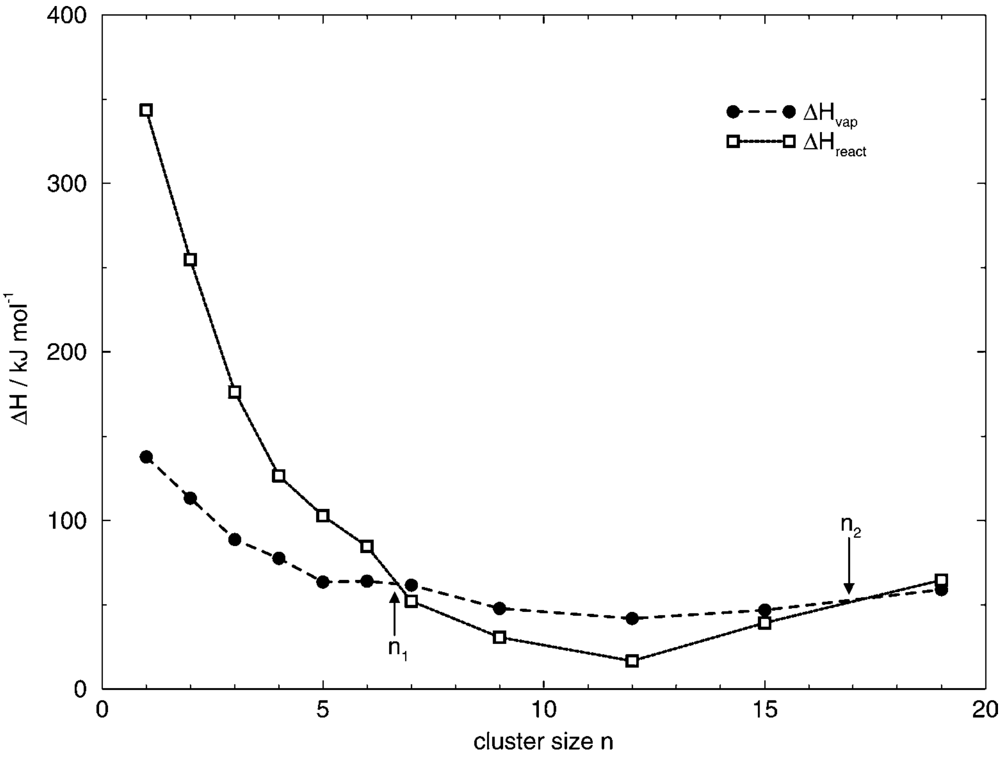

Fig. 3.10 Reaction enthalpies (0 K) of nonreactive fragmentation (filled circles) versus energies of reactive hydroxide formation (open squares) in $[Mg,nH_2O]^+$ as a function of cluster size. The first / second product switching proceeds at n_I/n_2, respectively.

These quantities were obtained as differences between the computed total energies of the products and educts in the decay pathways (eq. 3.1) and (eq. 3.2). Our results are visualized in Fig. 3.10. The computed curves indeed cross twice (at $n_I=6$ to 7 and at $n_2\approx 17$). Accordingly the most probable evaporation products are predicted to switch twice as well.

The first of these cluster size limits, n_I, was discussed at length before.[9,11] In contrast profound knowledge about possible reasons for the second cluster size limit, n_2, was lacking completely. Therefore the discussion of this change in the reaction pattern from non-reactive to reactive evaporation of the clusters $[Mg,nH_2O]^+$, $n_2\approx 17$, has been highly speculative. Sanekata et al.[10] proposed a Rydberg like ion pair state as the origin of the second product switching and even (hypothetical) proton-transfer was invoked.[70-71] The calculations presented in this work verify most stables structures with a coexistence of the dication Mg^{2+} and a solvated electron, however, without the assumption of any Rydberg state like characteristic. The computed changes in energy ΔH_{vap} and ΔH_{react} as a function of the cluster size n offer first conclusive information about the origin of the second product switching. Both quantities ΔH_{vap} and ΔH_{react} reveal a minimum around n=12. Subsequently ΔH_{vap} and

ΔH_{react} increase again.

As this increase is much steeper for ΔH_{react} it finally becomes larger than ΔH_{vap} (second product switching). The steeper increase of ΔE_{Heact} has to originate from a decrease of the hydration enthalpy of $MgOH^+$ within the hydrated magnesium hydroxide clusters (cf. Fig. 3.10). In $[MgOH,nH_2O]^+$, $n \leq 5$, only first shell hydration is present. Therein OH^- of $MgOH^+$ represents a strongly bound anionic ligand attached to Mg^{2+}. With growing population of the second hydration shell in case of $[MgOH,nH_2O]^+$, $n \geq 12$, at some point the molecular ion $MgOH^+$ as a whole is to be hydrated. In this case hydration requires interaction of OH^- with H_2O molecules located in the second hydration shell. Because of its negative charge OH^- shields the H_2O dipoles from the magnesium cation. This evokes weaker attractive interactions between the magnesium cation and the H_2O dipoles, which are aligned with the O-atom pointing inward. In addition OH^- is limited in its H-bonding abilities within the H-bonding framework of the cluster (cf. Fig. 3.9), as it can only establish a single acceptor H-bond ($^-OH \cdots OH_2$). The calculated $H \cdots O$ distances, e.g. 2.19 Å in $[MgOH,nH_2O]^+$, n=18, indicate that this interaction is weaker than typical water-water hydrogen bonds (≈1.80 Å).

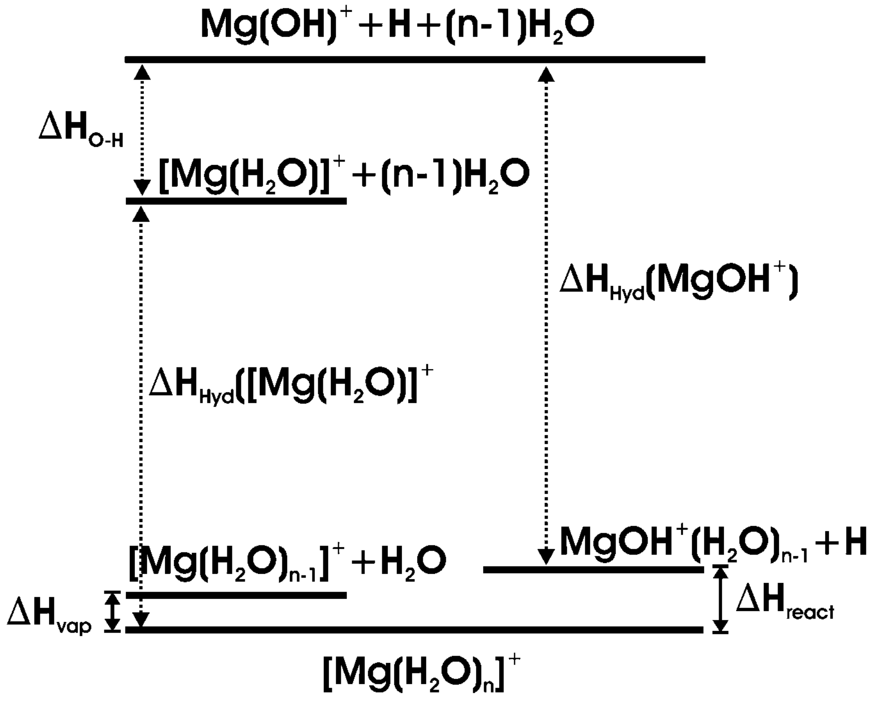

Fig. 3.11 Energy scheme for nonreactive versus reactive decomposition in $[Mg,nH_2O]^+$

This study has shown that in larger $[Mg,nH_2O]^+$ clusters the magnesium is oxidized from Mg^+ to Mg^{2+}, which coexists with a hydrated electron in the cluster. Therefore formation of $MgOH^+$ does not result in a gain in hydration enthalpy in larger cluster sizes which already contain the Mg^{2+} dication with its large hydration enthalpy due to its high positive charge density. In contrast to the hydrated electron which is distributed over a larger volume (cf. calculated SEMs in section C) the OH^- anion is located in the first solvation shell bound to the Mg^{2+} dication. Therefore formation of $MgOH^+$ becomes energetically disfavored as soon as the second hydration shell has reached a critical population, due to the charge screening effect of the OH^- anion. Altogether the experimentally observed second product switching can be rationalized in terms of the coexistence of Mg^{2+} and hydrated electron leading to a higher hydration enthalpy than the $MgOH^+$ molecular core ion.

Processes (eq. 3.1) and (eq. 3.2) are endothermic for all cluster sizes. At finite temperature they may occur nevertheless. Arrhenius kinetics allow for a rough estimate of anticipated time scales. At cluster temperatures of 100-200 K fragmentations rates within the one per second range[75] may arise through processes that are endothermic by 60-80 kJ mol^{-1}.[72] E.g. Rodriguez-Cruz et al.[73] observed the slow blackbody infrared radiative dissociation (BIRD) of $[Ni,7H_2O]^{2+}$ and $[Ni,8H_2O]^{2+}$ at room temperature and determined the threshold dissociation energy of these processes to be 73.7 kJ mol^{-1} and 71.6 kJ mol^{-1}, respectively. Therefore - at least in case of the ICR experiments - the observation of a decay of the clusters is no indication for spontaneous processes. Our calculations indicate that even for large clusters the decay does not become spontaneous but is activated (slowly) through uptake of 300 K black body radiation. In this respect the presented calculations clearly deviate from previous theoretical predictions[9,11].

According to the calculated thermochemistry the decay propensities are expected to switch around $[Mg,nH_2O]^+$, n_1=6-7 and $n_2 \approx 17$. This is in excellent agreement with previous experimental findings[9-10,14]. While Berg et al. were first to observe evaporation reactions in $[Mg,nH_2O]^+$, $n \geq 6$, mass spectra of clusters generated from hydration of magnesium were recorded before[10]. Our ab initio study reveals that from a limiting cluster size n_2 on the hydration energy of the product clusters $[MgOH,(n-1)H_2O]^+$ does not compensate the energy necessary for the breaking of an O-H bond in the H-elimination reaction (eq. 3.1) and the coexistence of Mg^{2+} and hydrated electron becomes favored instead. Hence for the reactant cluster $[Mg,nH_2O]^+$ the evaporation process (eq. 3.2) drops in energy below the H-elimination reaction, accounting for the second product switching at $n_2 \approx 17$.

3.4 Conclusions

The electronic structure of hydrated magnesium monocations $[Mg,nH_2O]^+$, $1 \leq n \leq 19$, exhibits a strong cluster size dependency. With increasing number of H_2O ligands the SOMO evolves from a quasi-valence state (n=3-5), in which the SOMO is not yet detached from the metal atom and has distinct sp hybrid character, to a contact ion pair state. For larger clusters (n=17,19) these ion pair states are best described as solvent separated ion pair states, which are formed by a hydrated dication and a hydrated electron. In $[Mg,nH_2O]^+$, $n \geq 6$, the probability density of the odd electron at the magnesium cation is negligible. For $n \geq 9$ the odd electron is, to an increasing degree, localized within the hydration sphere and its probability density is highest between H-atoms of adjacent H_2O molecules which are located at the cluster surface. This localization of the odd electron results from attractive interactions between the odd electron and dangling H-atoms of H_2O ligands forming "molecular tweezers" $HO\text{-}H \cdots e^- \cdots H\text{-}OH$.

The BLYP calculated energetics of the two competing decay processes, reactive H-elimination (eq. 3.1) and non-reactive H_2O evaporation (eq. 3.2), predict switches of the decay propensities at $n_1=6\text{-}7$ and at $n_2 \approx 17$. This is in excellent agreement with the findings of previous experimental studies[9-10,14] on the collisionless decay of $[Mg,nH_2O]^+$. According to the performed calculations the coexistence of Mg^{2+} and a hydrated electron becomes energetically favored to the formation of $MgOH^+$ in large $[Mg,nH_2O]^+$ clusters due to the charge screening effect of the OH^- ion clusters with a densely populated second solvation shell. With the coexistence of hydrated electron and Mg^{2+} dication becoming favored, the decay propensities of $[Mg,nH_2O]^+$ clusters switch again, which gives rise to the second product switching at $n_2 \approx 17$.

Vertical and adiabatic ionization energies and SOMO volumes (SOMO extent measures SEMs) of $[Mg,nH_2O]^+$ clusters $n \leq 19$ were evaluated at different levels of theory. The SEMs exhibit a pronounced maximum in $[Mg,nH_2O]^+$, n=6-8, with a 6-fold coordinated magnesium cation. In all other investigated clusters the SEMs are significantly smaller. The SEMs serve as benchmark for the diffuseness of the SOMO. The performed calculations reveal that in n=6-8 the SOMOs are substantially more diffuse than in any other $[Mg,nH_2O]^+$ clusters. The contribution of electron correlation and of orbital relaxation to the vertical ionization energy correlate well with the calculated SOMO volumes. In clusters with very diffuse SOMOs (n=6-8) the effect of correlation on the VIEs is at maximum, while orbital relaxation is minimal. Koopmans’ theorem neglects both electron correlation and orbital relaxation. So it provides only a crude approximation to the VIE in n=6-8. For all other investigated clusters Koopmans' theorem is much more appropriate due to error cancellation.

Overall the ionization energies decrease with cluster size n in $[Mg,nH_2O]^+$. However, the decrease is not continous. The steep increase of SOMO volume at n=6 is correlated with the transformation of the SOMO from a sp-hybrid-like orbital in n≤5 to a diffuse SOMO spread over the cluster surface in n=6-8. This coincides with a most prominent drop in ionization energy. In clusters n≥9, in which the odd electron is located within the hydration shell by molecular tweezers $HO\text{-}H\cdots e^{-}\cdots H\text{-}OH$, the vertical ionization energies converge to approximately 5.1 eV (VIE_{MP2}), whereas the adiabatic ionization energies converge to approximately 4.2 eV (AIE_{MP2}). These calculated ionization energies, when compared to VIE and AIE values of e_{aq}^{-}, indicate a partial screening of the odd electron from the magnesium dication. Coulomb attraction between hydrated electron and magnesium dication prevails even in the largest $[Mg,nH_2O]^+$ clusters which form solvent separated ion pairs $Mg^{2+}(H_2O)_ne^{-}$.

The reorganization energies obtained through comparison of AIEs and VIEs of $[Mg,nH_2O]^+$, n≤19, reveal substantial geometry changes upon ionization in n≤5 and n≥9. The structures of these clusters are influenced by localized SOMOs which have either distinct sp-hybrid-like character, as in n≤5, or which are localized within the hydration shell by molecular tweezers, as in n≥9. For n=6-8 the reorganization energies are close to zero.

Theoretical investigations of ionization energies and SOMO volumes in $[Mg,nH_2O]^+$ clusters reveal that interim cluster sizes n=6-8 differ substantially from all other cluster sizes. Only clusters of the kind $[Mg(H_2O)_6,(n-6)H_2O]^+$, n=6-8, with a 6-fold coordinated magnesium cation have diffuse electronic surface states. In all other clusters the SOMO is localized either at the magnesium cation or within the hydration shell.

3.5 References

1 P. Kebarle, *Annu. Rev. Phys. Chem*. 1977, **28**, 445.

2 B. R. Rowe, D. W. Fahey, E. E. Ferguson, F.C. Fehsenfeld, *J. Chem. Phys.* 1981, 753325.

3 R. G. Keesee, A. W. Castleman Jr, *J. Phys. Chem. Ref. Data* 1986, **15**, 1011.

4 P.B. Armentrout, *Annu. Phys. Chem.* 1990, **41**, 313.

5 K. F. Willey, C. S. Yeh, D. L. Robbins, J. S. Pilgrim, M. A. Duncan, *J. Chem. Phys.*, 1992, **97**, 8886.

6 M. Sodupe, C. W. Bauschlicher Jr, *Chem. Phys. Lett.* 1992, **195**, 494.

7 F. Misaizu, M. Sanekata, K. Tsukamoto, K. Fuke, S. Iwata, *J. Phys. Chem.* 1992, **96**, 8259.

8 F. Misaizu, M. Sanekata, K. Fuke, S. Iwata, *J. Chem. Phys.* 1994, **100**, 1161.

9 A. C. Harms, S. N. Khanna, B. Chen, A. W. Castleman Jr, *J. Chem. Phys*. 1994, **100**, 3540.

10 M. Sanekata, F. Misaizu, K. Fuke, S. Iwata, K. Hashimoto, *J. Am. Chem. Soc.* 1995, **117**, 747.

11 H. Watanabe, S. Iwata, K. Hashimoto, F. Misaizu, K. Fuke, *J. Am. Chem. Soc*. 1995, **117**, 755.

12 T. Asada, S. Iwata, *Chem. Phys. Lett.* 1996, **260**, 1.

13 C. Berg, U. Achatz, M. Beyer, S. Joos, G. Albert, T. Schindler, G. Niedner-Schatteburg, V. E. Bondybey, *Int. J. Mass Spectrom. Ion Process* 1997, **167/168**, 723.

14 C. Berg, M. Beyer, U. Achatz, S. Joos, G. Niedner-Schatteburg, V. E. Bondybey, *Chemical Physics* 1998, **239**, 379.

15 C. W. Bauschlicher, Jr., M. Sodupe, H. Partridge, *J. Chem. Phys.* 1992, **96**, 4453.

16 S. E. Rodriguez-Cruz, E. R. Williams, *J. Am. Soc. Mass. Spectrom.* 2001, **12**, 250.

17 A. Amity, F. Muntean, D. Walter, C. Rue, P. B. Armentrout, *J. Phys. Chem. A* 2000, **104**, 692.

18 C.-K. Siu and Z.-F. Liu, *Chem. Eur. J.* 2002, **8**, 3177.

19 R. Ahlrichs, M. Bär, M. Häser, H. Horn, C. Kölmel, *Chem. Phys. Lett.* 1989, **162**,165.

20 M. V. Arnim, R. Ahlrichs, *J. Comput. Chem.* 1998, **19**, 1746.

21 W. Koch, M.C. Holthausen, *A Chemist's Guide to Density Funtional Theory*, Wiley

VCH, Weinheim, 2000, pp. 226-228.

22 A. Köhn, F. Weigend, R. Ahlrichs, *Phys. Chem. Chem. Phys.* 2000, **3**, 711.

23 A. D. Becke, *Phys. Rev. A* 1988, **38**, 3098.

24 C. Lee, W. Yang, R. G. Parr, *Phys. Rev. B* 1988, **37**, 785.

25 K. S. Kim, S. Lee, J. Kim, J. Y. Lee, *J. Am. Chem. Soc.* 1997, **119**, 9329.

26 S. Lee, J. Kim, S. J. Lee, K.S. Kim, *Phys. Rev. Lett.* 1997, **79**, 2038.

27 F. Weigend, R. Ahlrichs, *Phys. Chem. Chem. Phys.* 1999, **1**, 4537.

28 D. M. A. Smith, J. Smets, Y. Elkadi, C. Adamowicz, *J. Chem. Phys.* 1997, **107**, 5788.

29 J. V. Coe, G. H. Lee, J. G. Eaton, S. T. Arnold, H. W. Sarkas, K. H. Bowen, C. Ludewigt, H. Haberland, D. R. Worsnop, *J. Chem. Phys.* 1990, 92, 3980.

30 K. Eichkorn, O. Treutler, H Öhm, M. Häser and R. Ahlrichs, *Chem. Phys. Lett.* 1995, **240**, 283.

31 F.Weigend, M. Häser, H. Patzelt, R. Ahlrichs, *Chem. Phys. Lett.* 1998, **294**, 143.

32 F. Weigend, M. Häser, *Theor Chem Acc* 1997, **97**, 331.

33 O. Chistiansen, H. Koch, P. Jørgensen, *Chem. Phys. Lett.* 1995, **243**, 409.

34 C. Hättig and F. Weigend, J. Chem. Phys. 2000, **113**, 5154.

35 T. Koopmans, *Physica* 1933, **1**, 104.

36 K. S. Kim, I. Park, S. Lee, K. Cho, J. Y. Lee, K. Kim, J. D. Joannopoulos, *Phys. Rev. Lett.*, 1996 **76**, 956.

37 J. Kim, J. Y. Lee, K. S. Oh, J. M. Park, S. Lee, K. S. Kim, *Phys. Rev. A* 1999, **59**, R930.

38 J. Kim, S. B. Suh, K. S. Kim, *J. Chem. Phys.* 1999, **111**, 10077.

39 S. B. Suh, H. M. Lee J. Kim, J. Y. Lee, K. S. Kim, *J. Chem. Phys.* 2000, **113**, 5273.

40 C. G. Bailey, J. Kim, M. A. Johnson, *J. Chem. Phys.* 1996, **100**, 16782.

41 T. Tsurusawa, S. Iwata, *J. Phys. Chem.* 1999, **103**, 6134.

42 T. Tsurusawa, S. Iwata, *J. Chem. Phys.* 2000, **112**, 5705.

43 S. Iwata. T. Tsurusawa *in Advances in Metal And Semiconductor Clusters Volume 5*, ed. M. A. Duncan, Elsevier, Amsterdam, 2001, pp.39-75.

44 M. H. Shen, J. M. Farrar, *J. Phys. Chem.* 1989, **93**, 4386.

45 G. J. Martyna, M. L. Klein, *J. Phys. Chem.* 1991, **95**, 515.

46 J. M. Farrar in *Cluster Ions*, ed. C. Y. Ng, T. Baer, I. Powis, John Wiley and Sons, Chichester, 1993, pp. 266-285.

47 S. G. Donelly, J. M. Farrar, *J. Chem. Phys.* 1993, **98**, 5450.

48 D. W. Smith, O. W. Day, *J. Chem. Phys.* 1975, **62**, 113.

49 O. W. Day, D. W. Smith, C. Garrod, *Int. J. Quantum Chem. Symp.* 1974, **8**, 501.

50 M. M. Morrell, R. G. Parr, and M. Levy, *J. Chem. Phys.* 1975, **62**, 549.

51 R. Ahlrichs, *J. Chem. Phys.* 1976, **64**, 2706.

52 J. Katriel and E. R. Davidson, *Proc. Natl. Acad. Sci U.S.A.* 1980, **77**, 4403.

53 B. T. Pickup and J. G. Snijder, *Chem. Phys. Lett.* 1988, **153**, 69.

54 V. H. Smith and Y. Öhrn, *Queen's Papers in Pure and Applied Mathematics* 1974, **40**, 193.

55 R. C. Morrison, Z. Zhou, and R. G. Parr, *Theor. Chim. Acta* 1992, **86**, 3.

56 J. Olsen and D. Sundholm, *Chem. Phys. Lett.* 1998, **288**, 282.

57 K. Pernal and J. Cioslowski, *J. Chem. Phys.* 2001, **114**, 4359.

58 S. Iwata, T. Tsurusawa, in Advances in Metal And Semiconductor Clusters Volume 5, ed. M. A. Duncan, Elsevier, Amsterdam, 2001, pp. 39-75.

59 T. Tsurusawa, S. Iwata, *J. Chem. Phys.* 2000, **112**, 5705.

60 T. Tsurusawa, S. Iwata, *J. Phys. Chem.* 1999, **103**, 6134.

61 R. Takasu, F. Misaizu, K. Hashimoto, K. Fuke, *J. Phys. Chem. A* 1997, **101**, 3078.

62 I. V. Hertel, C. Hüglin, C. Nitsch, C. P. Schulz, *Phys. Rev. Lett.* 1991, **67**, 1767.

63 F. Misaizu, K. Tsukamoto, M. Sanekata, K. Fuke, *Chem. Phys. Lett.* 1992, **188**, 241.

64 R. N. Barnett and U. Landman, *Phys. Rev. Lett.* 1993, **70**, 1775.

65 K. Hashimoto, S. He, K. Morokumo, *Chem. Phys. Lett.* 1993, **206**, 297.

66 K. Hashimoto, K. Morokuma, *Chem. Phys. Lett.* 1994, **223**, 423.

67 K. Hashimoto, K. Morokuma, *J. Am. Chem. Soc.* 1994, **116**, 11436.

68 W. C. Martin, R. Zalubas, *J. Phys. Chem. Ref. Data* 1980, **9**, 1.

69 J. V. Coe, A. D. Earhart, M. D. Cohen, G. J. Hoffman, H. W. Sarkas, K. H. Bowen, *J. Chem. Phys.* 1997, **107**, 6023.

70 M. Beyer, C. Berg, H. W. Görlitzer, T. Schindler, U. Achatz, G. Albert, G. Niedner-Schatteburg, V. E. Bondybey, *J. Am. Chem. Soc.* 1996, **118**, 7386.

71 V. E. Bondybey, M. Beyer, U. Achatz, S. Joos, G. Niedner-Schatteburg, *Isr. J. Chem.* 1999, **39**, 213.

72 G. Niedner-Schatteburg, V. E. Bondybey, *Chem. Rev.* 2000, **100**, 4059.

73 S. E. Rodriguez-Cruz, R. A. Jockbusch, E. R. Williams, *J. Am. Chem. Soc.* 1998, **120**, 5842.

74 B. M. Reinhard, G. Niedner-Schatteburg, *Phys. Chem. Chem. Phys.* 2002, **4**, 1471.

75 Whereas the time scale in time-of-flight mass spectrometer (TOF-MS) is typically in the range of a few μs, the ICR time scale ranges up to seconds or minutes. Therefore problems connected with a limited time frame of the experiment are generally missing in decay studies with the ICR-MS method. The resulting data are free form any kinetic shift.

4. H_2 Elimination from Hydrated Aluminium Clusters:
Acid - Base Reaction Mediated by Intracluster Proton Transfer

The reactivity of different $[Al,nH_2O]^+$*, n=20, clusters using gradient corrected DFT was investigated. In clusters with the stoichiometry* $[HAl^{III}(OH),19H_2O]^+$ *which contain a 4 fold coordinated, O-H inserted* Al^{III} H_2 *formation was found to occur according to the following mechanism: First a proton is released within the cluster by hydrolysis of a first shell* H_2O*. By successive proton transfer reactions in the hydrogen bonded network of the cluster the proton migrates to the hydridic H at the* Al^{III} *cation. Finally hydride ion and proton recombine to* H_2 *in an acid - base reaction. The activation barrier for this process was determined to be 45 kJ* mol^{-1}*. No* H_2 *formation was found in hydrated* Al^I *clusters* $[Al^I,20H_2O]^+$*.*

4.1 Introduction

Al^{III} hydrates in bulk phase through hexacoordination and yields the aqua ion $[Al^{III}(H_2O)_6]^{3+}$. This ion is acidic ($pK_a = 4.56$):

$$[Al^{III}(H_2O)_6]^{3+} \rightleftharpoons [Al^{III}(OH)(H_2O)_5]^{2+} + H^+_{aq} \qquad (4.1)$$

and the dication has been detected in dilute solution.[1] Over a wide pH range and in "physiological" chloride solutions the monomeric Al^{III} species seem to be $[Al(OH)]^{2+}$, $Al(OH)_3$, and most evidently $[Al(OH)_4]^-$.[2] In particular no indication of coordination with more than four hydroxide ligands was found. Similarly the aluminium hydride anion $[AlH_4]^-$ shows tetrahedral coordination with an average Al-H distance of 1.55 Å in the crystalline $LiAlH_4$ solid. It explosively hydrolizes by water. Ionic water clusters are expected to resemble closely the solvation of ions in aqueous bulk phase solution and act as model systems for solvation processes. They offer an approach to ionic species which are not stable in the bulk phase where they only exist as reactive intermediates for a very limited period of time.

In case of hydrated magnesium cations chapter 3 revealed that the oxidation state of the hydrated magnesium ion gradually increases as a function of cluster size n, finally leading to the coexistence of metal dication Mg^{II} and a hydrated electron within larger clusters. Our findings about water clusters doped with the open shell Mg^I cation (electronic configuration: $[Ne]3s^1$) lead to the question if the solvation of closed shell Al^I (configuration: $[Ne]3s^2$) in water clusters of finite size might lead to a similar oxidation process. This association emanates from black body radiation induced decay studies (BIRD) of hydrated aluminium $[Al,nH_2O]^+$ clusters stored in a FT-ICR mass spectrometer. Bondybey and coworkers observed a reactive decay by elimination of H_2 molecules as well as decay solely by evaporation of H_2O.[6-7] The reactive decay pathway is confined to a size region of n=11-24 and exhibits a pronounced maximum around n=20. This is very similar to the reactivity of $[Mg,nH_2O]^+$ clusters, which exhibit reactive H atom elimination for cluster sizes n= 7-17 and non-reactive decay by evaporation of a H_2O monomer for all other cluster sizes.[4-5]

Due to distinct analogies in the decay behavior of hydrated aluminum cluster cations $[Al,nH_2O]^+$ with that of $[Mg,nH_2O]^+$, hydrated aluminium monocations were discussed as Al^I species: $[Al^I(H_2O)_n]^+$. It was postulated that the observed intracluster H_2 formation is associated with a 2 e^- oxidation of Al^I to Al^{III}.[6-7] H_2 elimination was ascribed to the reaction $[Al^I(H_2O)_{20}]^+ \rightarrow [Al^{III}(OH)_2(H_2O)_n]^+ + H_2$. However, Watanabe and Iwata[8] and Niedner-Schatteburg[9] independently found through ab initio studies of $[Al(H_2O)_{n=1-5}]^+$ that for $n \geq 2$ $[HAl^{III}(OH)(H_2O)_{n-1}]^+$ isomers are significantly more stabilized than those of $[Al^I(H_2O)_n]$. One would expect the energetically favored isomers to prevail. This seriously questions the prior hypothesis that decay of isolated clusters through H_2 elimination is confined to the "high energy isomer" $[Al^I(H_2O)_n]^+$. Finally it should be noted in passing that the H_2 elimination from $[Al,nH_2O]^+$, n=11-24, was experimentally found to involve concomitant evaporation of 2-3 H_2O molecules at a time.[7]

The aim of this study was to find conclusive information whether H_2 elimination from $[Al,20H_2O]^+$ requires oxidation of Al^I or whether it starts from Al^{III}. Therefore ab initio studies of the H_2 formation were performed in hydrated Al^{III} and Al^I clusters. The reaction was found to proceed exclusively through hydrated Al^{III} clusters. According to the performed calculations H_2 is formed in a multi-step intracluster acid base reaction: $[HAl^{III}(OH)(H_2O)_n]^+ \rightarrow ... \rightarrow [Al^{III}(OH)_2(H_2O)_{n-2}]^+ + H_2$. No evidence was found that the H_2 formation is associated with an oxidation of Al^I to Al^{III} within the cluster.

4.2 Computational Details

All calculations were performed in the electronic ground state with density functional theory (DFT). DFT is applicable to fairly large systems which are out of reach for post-Hartree-Fock based ab initio approaches. In DFT ionic hydrogen bonded clusters are generally well treated since electrostatic interactions clearly dominate over dispersion forces. The Becke88 exchange functional[10] with the Lee, Yang and Parr gradient corrected correlation functional[11] (BLYP), which is known to be an efficient density functional with good overall performance, was used throughout. In ab initio molecular dynamics simulation of liquid water BLYP also proved to yield better agreement with experiment than other gradient corrected density functionals.[12] For O and H we employed triple zeta valence type plus polarization (TZVP) basis sets. For Al polarization functions of type 2d1f were added (TZVPP). All calculations were performed using the TURBOMOLE[13-14] quantum chemistry programme package. The RI "resolution of identity" approximation was applied throughout. The then required auxiliar basis sets were chosen as implemented in TURBOMOLE according to the applied basis sets for O, H and Al. Full geometry optimization of various cluster isomers with the stoichiometry $[Al,20H_2O]^+$ were performed, yielding three basic cluster geometries. Each of this geometries contains a pair of adjacent H atoms with potentially attractive interactions. This H···H distance (labelled r_{HH} throughout the rest of this manuscript) was parametrically varied. To overcome possible basis set limitations in these H···H interaction, the above described basis sets have been augmented by a floating point (bond function) with a diffuse (3s2p) basis set as developed by Weigend et al.[15].

4.3 Results and Discussion

For clusters with the stoichiometry $[Al,20H_2O]^+$ we found 3 basic cluster structures (cf. Fig. 4.1): **I** $[Al^I(H_2O)_{20}]^+$ (3 fold coordinated Al^I), **II** $[HAl(OH)(H_2O)_{19}]^+$ (4 fold coordinated Al^{III}), **III** $[HAl(OH)(H_2O)_{19}]^+$ (5 fold coordinated Al^{III}). Clusters of this size have complex energy hypersurfaces with numerous local minima. Although it is unknown whether any of the determined local minima is a global minimum, it is certain that the calculated energies for **I** - **III** are characteristic of the respective structure type. The total energy differs only by a few kJ mol^{-1} as long as the total coordination number and the coordinating ligands (H, OH, H_2O) at the aluminium cation were held constant. The composition of the first solvation shell, hereafter labelled as "ionic core", however, has a significant effect on the total energy (cf. Table 4.1). In **I** only 3 H_2O molecules are attached to the aluminium cation in the first solvation shell; the cluster has an $[Al^I(H_2O)_3]^+$ core. The formal oxidation state of the aluminium cation is +1, a lone electron pair remains located at the aluminium mono-cation (cf. Fig. 4.1, HOMO in **I**). In contrast to the co-existence of metal di-cation and a single hydrated electron as found in large $[Mg(H_2O)_n]^+$ clusters, in case of Al_{aq}^+-isomer **I** a pair of lone electrons remains located at the aluminium cation even in large clusters.

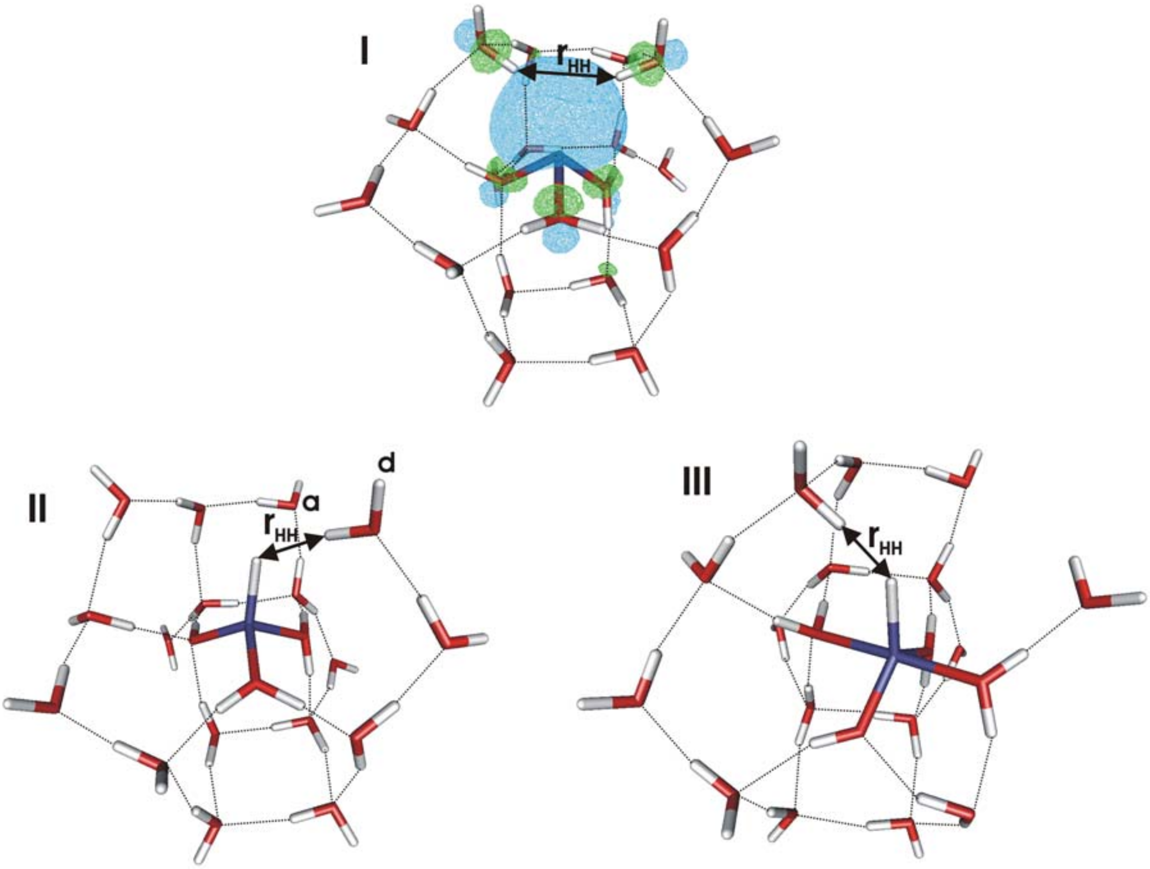

Fig. 4.1 Optimized cluster structures **I - III** with stoichiometry $[Al,20H_2O]^+$. In case of **I** an isosurface plot of the HOMO is included. Whereas I contains a Al^I cation with a formal oxidation state +1 in **II** and **III** its oxidation state is +3. All clusters contain a H···H motive marked with a double headed arrow. In **I** two dangling H atoms of adjacent second shell H_2O form a tweezer like structure embracing the HOMO. In structure **II** and **III** the H···H interaction is between a hydridic H at the Al^{III} cation and a second shell H_2O molecule.The coordination number of the Al^I cation in **I** is 3 with the HOMO occupying an otherwise "vacant" fourth coordination position. In **II** the coordination number of the Al^{III} cation is 4 in **III** it is 5.

Table 4.1 Relative enthalpies (T=0K) of the structures **I-III**

structure	*core*	*ΔH, kJ/mol*
I	$[Al^I(H_2O)_3]^+$	194
II	$[HAl^{III}(OH)(H_2O)_2]^+$	6
III	$[HAl(OH)(H_2O)_3]^+$	0

The coordination number of the aluminium cation does not exceed 3. This holds true for any cluster isomer of type **I** and for all cluster sizes as large as investigated (25 water molecules). The coordination geometry of the aluminium cation is pyramidal and the fourth coordination position is occupied by the highest occupied molecular orbital (HOMO), which reveals decent sp hybrid character.

In case of isomer **II** the coordination number of the aluminium cation is 4. The coordination geometry is still pyramidal, but one of the H_2O ligands is replaced by OH and the fourth position is occupied by H. Both OH and H carry significant effective negative charges, so that they are referred to as hydroxide OH^- and hydride H^-. Altogether isomer **II** has a $[HAl^{III}(OH)(H_2O)_2]^+$ core.

In isomer **III** the aluminium cation is coordinated through 3 H_2O molecules, 1 hydride H^- and 1 hydroxide OH^-, the total coodination number is 5. In this case a $[HAl^{III}(OH)(H_2O)_3]^+$ core is found. Whereas isomers **II** and **III** are similar in total energy **I** is less stable by a large amount (cf. Fig. 4.2). In **I** the formal oxidation state of the aluminium is +1 whereas it is +3 in **II** and **III**. Mulliken population analyses - albeit largely approximate - confirm the differences in the oxidation states.[§] The obvious lack of energetic stability of isomer **I** makes it very doubtful whether it exists on the time scale of the previously performed experiments (tenth of milliseconds to several seconds within an ion trap).

All cluster structures **I - III** contain a structural H···H motive (marked with a two headed arrow in Fig. 4.1): In **II** and **III** a second hydration shell located H_2O molecule is pointing with one H atom towards the hydride ion bound to the aluminium cation. In the tweezer structure of **I** the dangling H atoms of two adjacent H_2O point towards the HOMO located at the aluminium cation. Apparently there is some attractive interaction between the electrophilic dangling H atoms and the lone electron pair at the Al^I cation. At this point we like to emphasize the similarities of this structural motive with the HO-H···e^-···H-OH tweezer structure as found in $[Mg,nH_2O]^+$.[3] H_2 formation within the studied clusters requires the approach of any two H atoms and the question arises which two H atoms react to yield H_2. As the singular H···H contacts (marked by the double headed arrow in Fig. 4.1) are signs of attractive interactions, it is fair to assume that H_2 formation - if at all - occurs along the respective H···H coordinate r_{HH}.

[§] The effective charges (in Coulomb) for Al in the respective structures are the following: **I** (-0.0245), **II** (0.3573), **III** (0.4762).

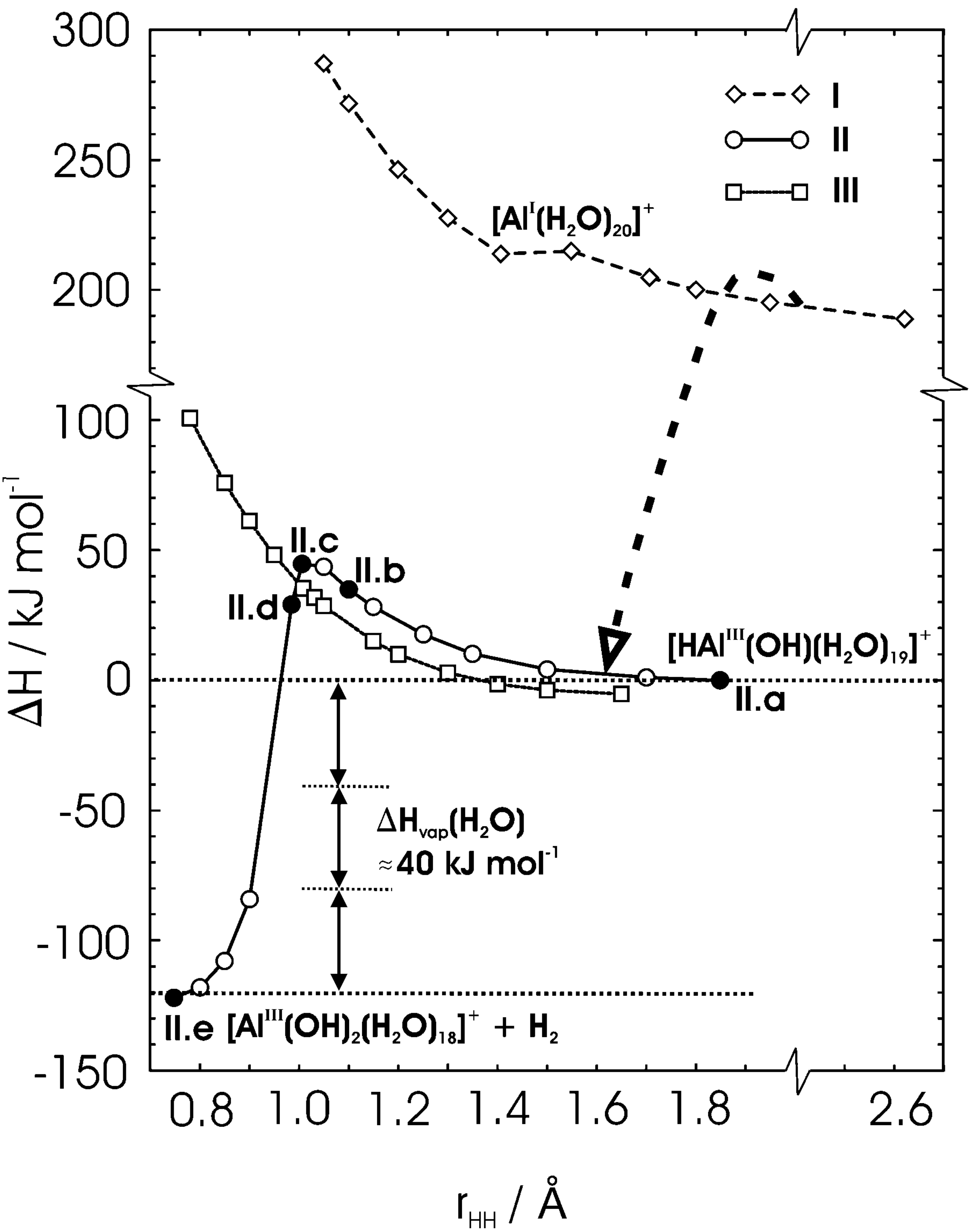

Fig. 4.2 Computed ΔH (T = 0 K) for structures **I** - **III** as a function of the H···H coordinate r_{HH}. In **I** and **III** shortening of r_{HH} is non-reactive and the H···H interaction becomes repulsive. Only in case of **II** H_2 formation is encountered. The activation barrier is 45 kJ mol^{-1} (reaction intermediates II.a - II.c marked as black circles are shown in Fig. 4.3). The reaction enthalpy Δ_rH for the elimination of H_2 for **II** is -122 kJ mol^{-1}. This suffices for evaporation of up to 3 H_2O molecules as observed experimentally.[7] The dashed arrow is meant to indicate that **I** isomerizes into **II** even at large r_{HH}. The activation barrier for this isomerization was calculated to be about 14 kJ mol^{-1} (see text).

Geometry optimizations were performed at fixed H···H distances r_{HH} for isomers **I** - **III**. Starting with the relaxed structure we systematically decreased the H···H distance up to a rise in energy of at most 100 kJ mol^{-1} with respect to the relaxed structure. In Fig. 4.2 the total energies for **I** - **III** are plotted as a function of r_{HH}. In case of **I** and **III** there is no indication of any attractive H···H interaction: The computed energies rise steadily. According to these calculations it is unlikely that **I** or **III** are possible structures of $[Al,20H_2O]^+$ to start the experimentally observed dehydrogenation reaction. As indicated by the arrow in Fig. 4.2 **I** isomerizes into **II** even at large r_{HH}. If instead of r_{HH} the distance d between the aluminium cation and any of the two H atoms of the marked tweezer structure in Fig. 4.1 was held constant at $d \leq 1.850$ Å geometry optimizations let structure **I** isomerize into structure **II**. By variation of d the activation barrier for this transformation was calculated to be about 14 kJ mol^{-1}. At this point it seems as if structure **I** would be a shallow well in a broad rim that decays on either side into **II**.

In isomer **II** the forced shortening of r_{HH} induces concomitant structural changes that finally lead to H_2 elimination. The structural changes along the r_{HH} coordinate lead to a minimum energy path as illustrated in Fig. 4.3: Consecutive proton transfers (II.b - II.d) eventually result in the hydride - oxonium ion adduct II.d $[(H_2O)(HO)_2Al\text{-}H\cdots H_3O]^+$ at $r_{HH} = 0.985$ Å. If r_{HH} is shortened further, H_2 is formed. At $r_{HH} = 0.900$ Å H_3O^+ and H^- have recombined to H_2 and H_2O (II.e). The hydrogen molecule is eliminated and a H_2O molecule has taken the vacant coordination position at the aluminium cation. The activation barrier for this reaction is - by inspection of Fig. 4.2 - about 45 kJ mol^{-1}.

The proton transfer at $r_{HH} = 1.100$ Å, in which a proton moves into the second solvation shell, creates a first shell OH^- and a second shell H_3O^+ ion. According to our calculations this is only the very first step in a series of proton transfers which ultimately result in the formation of H_2. A decrease of r_{HH} below 1.100 Å induces further proton movement through a chain of water molecules to a position adjacent to the nucleophilic hydride ion at the aluminium cation (II.d). It is well known that a proton has a very high "pseudo" mobility through hydrogen bonded chains of water molecules. This migration is outermost effective through the mere rearrangement of bonds (Grothus mechanism). It is this high mobility of the proton which enables the observed reaction: By the deprotonation of the $[HAl^{III}(OH)(H_2O)_2]^+$

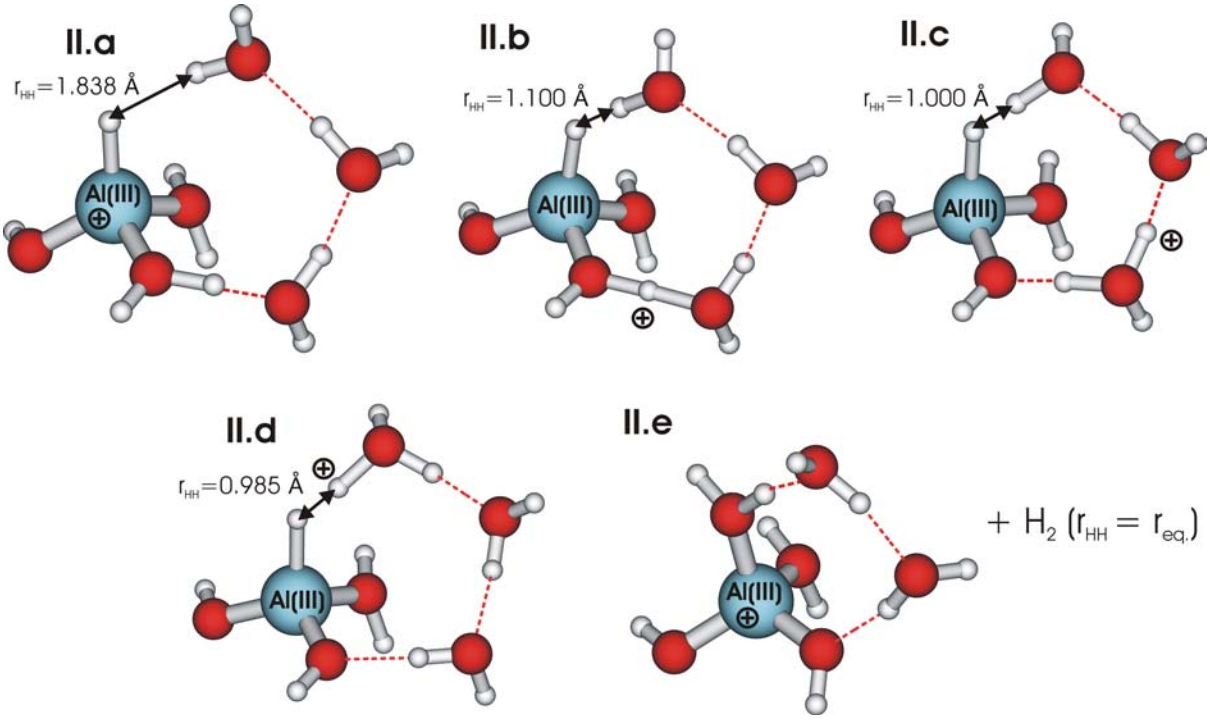

Fig. 4.3 Stucture of the "ionic core" in **II** along the H···H coordinate r_{HH} (marked by the double headed arrow). 15 more "spectator" water molecules are omitted in this figure but included into all calculations. In the relaxed structure II.a the H···H distance is r_{HH} = 1.838 Å. If r_{HH} is shortened to 1.100 Å a proton is released and a second Al^{III}-OH bond is created in a hydrolysis reaction of a first shell H_2O molecule: $H_2O \rightarrow OH^- + H^+$ (II.b - II.c). The proton forms an oxonium ion H_3O^+ within the second solvation shell (II.c). If r_{HH} is shortened further a proton transfer takes place resulting in the hydride - oxonium ion adduct $[(H_2O)(HO)_2Al\text{-}H\cdots H_3O]^+$ (II.d). Effective proton migration is enabled by the mere rearrangement of hydrogen bonds between adjacent H_2O molecules. The net charge migration is also indicated qualitatively. As soon as r_{HH} is shortened below 0.985 Å the proton and the hydride ion in $Al^{III}-H^-$ recombine to H_2 which switches with an adjacent H_2O and escapes (II.e).

core (which yields the neutral $[HAl^{III}(OH)_2(H_2O)]$ core) a proton is released to the second hydration shell (II.c). Net charge migration towards the hydridic H in the then neutral aluminium complex $[HAl^{III}(OH)_2(H_2O)]$ is feasible. This yields an oxonium ion H_3O^+ adjacent to the hydride ion at the aluminium cation forming the hydride - oxonium ion adduct $[(H_2O)(HO)_2Al\text{-}H\cdots H_3O]^+$ (II.d). Finally proton H^+ and hydride ion H^- recombine to form H_2. Thereby the strong nucleophilic hydride ion is converted into a hydrogen molecule, which is a considerably weaker nucleophile. Subsequently H_2 is substituted by a second shell H_2O molecule (II.e). The overall reaction II.a → II.e comprises an acid (H^+) - base (H^-) reaction. The formal oxidation state of the aluminium cation remains unchanged throughout this reaction. It is +3 both in product and educt clusters. In the bulk phase the hydrated Al^{III} ion forms the cation-acid $[Al(H_2O)_6]^{3+}$ (pK_a=4.76). In the very first step of the studied cluster reaction a polarized Al^{III}-OH_2 bond is transformed into a Al^{III}-OH bond and the released

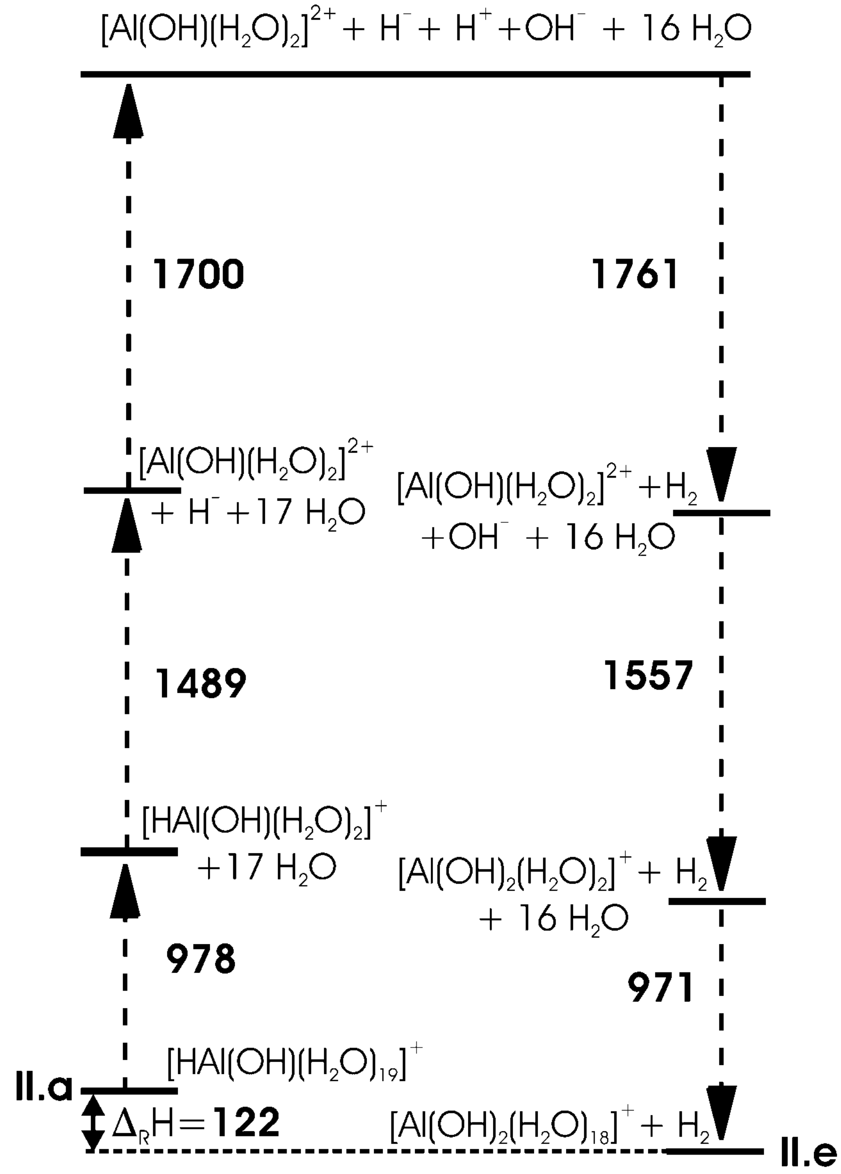

Fig. 4.4 Thermochemical cycle of the H_2 elimination in **II**, ΔH (T = 0 K) values in kJ mol^{-1}. The formation of a second Al^{III}-OH bond and the H_2 formation compensate the energy required for the breakage of a Al^{III}-OH_2 bond and for the hydrolysis of a first shell H_2O molecule.

proton forms an oxonium ion within the second solvation shell. This is true analogue to a classical hydrolysis reaction $H_2O \rightarrow OH^- + H^+$ as it can be observed e.g. for the cation-acid $[Al(H_2O)_6]^{3+}$ in the bulk phase.[16] In this respect the $[HAl^{III}(OH)(H_2O)_2]^+$ core also seems to be amphoteric.

In the course of the H_2-elimination reaction the Al^{III}-H bond is replaced by a Al^{III}-OH bond. The computed energetics for this process are provided in Fig. 4.4. The formation of a second Al^{III}-OH bond (1557 kJ mol^{-1}) and the H_2 formation (1761 kJ mol^{-1}) compensate the energies which are required for the breakage of a Al^{III}-H$^-$ bond (1489 kJ mol^{-1}) and for the hydrolysis of a H_2O molecule (1700 kJ mol^{-1}). De- and re-hydration enthalpies are comparable, 978 and 971 kJ mol^{-1} respectively. The reaction enthalpy (at T=0 K) is computed to be $\Delta_rH = -122$ kJ mol^{-1} . Note, that the thermochemical cycle balances exactly. In this process the swift elimination of the H_2 molecule out of the cluster is a cluster size specific feature. Because of additional caging effects one can expect the hydrogen elimination to be sterically somewhat more demanding in larger clusters. This might lead to an explanation why for even larger cluster sizes (n>24) no decay through H_2 elimination was observed experimentally.

The obtained reaction enthalpy $\Delta_rH = -122$ kJ mol^{-1} is in excellent agreement with the experimental observation[7] that H_2 elimination is typically associated with the evaporation of 2-3 H_2O molecules. When H_2 is formed within the cluster Δ_rH is set free. A minor part is released through the kinetic energy of the eliminated H_2. All of the rest leads to vibrational excitation of the cluster. Relaxation of this "heat" is then achieved by evaporative cooling. The evaporation of a single water monomer consumes the negative of the binding energy of a H_2O molecule to the ionic water cluster of that size ($\Delta H_{vap} \approx 40$ kJ mol^{-1})[17] which is almost identical to the heat of sublimation from bulk ice. If **I** were the reactive cluster species and H_2 would form according to $[Al^{I}(H_2O)_{20}]^+ \rightarrow [Al^{III}(OH)_2(H_2O)_{18}]^+ + H_2$ the reaction enthalpy would be $\Delta_rH = 311$ kJ mol^{-1}. In this case Δ_rH would suffice for the evaporation of about 7 H_2O molecules which is neither observed experimentally nor did we find any evidence of H_2 formation from structure **I** through our calculations. In **II** a proton transfer mechanism leads to the hydride - oxonium ion adduct II.d $[(H_2O)(HO)_2Al\text{-}H\cdots H_3O]^+$ which decays by formation of H_2. A prerequisite for proton migration in chains of water molecules is the possibility of breaking and forming of hydrogen bonds. This prerequisite is fulfilled for **II**. For example the formation of the hydride - oxonium ion adduct $[(H_2O)(HO)_2Al\text{-}H\cdots H_3O]^+$ through proton transfer (II.a - II.d) is associated with the hydrogen atom marked as "d" (cf. Fig. 4.1) slowly aligning with the acceptor molecule "a". Thereby a new hydrogen bond is established. This may be necessary to stabilize the oxonium ion (cf. Fig. 4.3 structure II.d) by providing a complete first solvation shell. The coordination number of the aluminium cation both in product and educt cluster is 4, the coordination geometry is tetraedic.

Why is there no evidence of H_2 formation in structure **III** with a 5 fold coordinated Al^{III} cation? The hydride ion - although one of the most basic elemental ions - has a comparatively large ion radius (~2 Å) and is highly polarizable.[16] In H_2 eliminated $[Al^{III}(OH)_2(H_2O)_{18}]^+$ clusters in which H^- is replaced by a much less polarizable OH^- ion the

Al^{III} cation favors 4 fold coordination. Lower coordination numbers are generally favored for sterical reasons especially when electrostatic repulsion between charged ligands prevails. Isomers with a $[Al^{III}(OH)_2(H_2O)_2]^+$ core are significantly lower in energy (max. 46 kJ mol^{-1}) than those with the $[Al^{III}(OH)_2(H_2O)_3]^+$ core with a 5 fold coordinated Al^{III} cation. Assuming a similar reaction mechanism for the H_2 elimination from **III** as from **II**, we would have to postulate intermediates with a $[HAl^{III}(OH)_2(H_2O)_2]$ core (in analogy to II.c in Fig. 4.3). Three of the ligands (the hydridic H and the hydroxyl ions) carry negative partial charges which leads to enhanced Coulomb repulsion. For simple geometric reasons the Coulomb repulsion in $[HAl^{III}(OH)_2(H_2O)_2]$ would be higher than in tetraedic intermediates of **II**. Therefore it is concluded that the non-reactivity of **III** is largely due to a significantly higher Coulomb repulsion in 5 fold coordinated intermediates.

In previous ICR decay experiments the cluster with the stoichiometry $[Al,20H_2O]^+$ was most efficient in H_2 formation. Nevertheless, decay by fragmentation was also observed. As one quintessence of our calculations we find that in $[Al,20H_2O]^+$ energetically similar isomers (e.g. **II** and **III**) may indeed decay through different pathways. The activation barrier of about 45 kJ mol^{-1} for H_2 elimination in case of **II** can be thermally activated and this process is expected to take place on a sub-second time scale. According to our findings isomer **III**, however, decays solely by fragmentation. The observed branching ratio for a cluster $[Al,nH_2O]^+$ does not only depend on the decay propensities of single isomers but depends on the isomeric composition of the cluster sample under investigation. Unfortunately the ICR technique does not offer more direct structural information. Collection of further structural information, e.g. through appropriate IR spectroscopic experiments in combination with future theoretical studies would help to elucidate further why H_2 elimination from $[Al,nH_2O]^+$ clusters is restricted to the size range $n \approx 11 - 24$.

4.4 Conclusions

H_2 elimination from different isomers of the stoichiometry $[Al,20H_2O]^+$ was investigated by using gradient corrected DFT (BLYP). Three different basic structures for $[Al,20H_2O]^+$ were located: **I** $[Al^I(H_2O)_{20}]^+$ with a 3 fold coordinated Al^I; **II** $[HAl^{III}(OH)(H_2O)_{19}]^+$ with a 4 fold coordinated Al^{III}; **III** $[HAl^{III}(OH)(H_2O)_{19}]^+$ with a 5 fold coordinated Al^{III}. Only in case of **II** H_2 elimination took place. The reaction was found to be mediated by a multi-step intracluster proton transfer mechanism. In a first step H^+ is formed via hydrolysis of a first shell H_2O molecule. In successive reorganization of the hydrogen bonding network this proton is transferred to the hydridic H atom bound to the Al^{III} cation. In an acid - base reaction H_2 is formed by recombination of proton and hydride ion and $[Al^{III}(OH)_2(H_2O)_{18}]^+$ results. The activation barrier was calculated to be 45 kJ mol^{-1}. The performed calculations question preceding speculations in which H_2 formation was postulated to be due to an oxidation of the aluminium cation. We found a conclusive mechanism for the formation of H_2 in hydrated Al^{III} clusters but no indication for a reaction in hydrated Al^{I} clusters.

4.5 References

1 J. W. Akitt and J. M. Elders, J. Chem.Soc. Faraday Trans. 1985, **1**, 1923.

2 M. Venturini and G. Berthou, J. Chem. Soc. Dalton Trans 1987, 1145.

3 B. M. Reinhard, G. Niedner-Schatteburg, Phys. Chem. Chem. Phys. 2002, **4**, 1471.

4 M. Sanekata, F. Misaizu, K. Fuke, S. Iwata, K. Hashimoto, J. Am. Chem. Soc. 1995, **117**, 747.

5 C. Berg, M. Beyer, U. Achatz, S. Joos, G. Niedner-Schatteburg, V. Bondybey, Chemical Physics 1998, **239**, 379.

6 M. Beyer, C. Berg, H. W. Görlitzer, T. Schindler, U. Achatz, G. Albert, G. Niedner-Schatteburg, V. E. Bondybey, J. Am. Chem. Soc. 1996, **118**, 7386.

7 M. Beyer, U. Achatz, C. Berg, S. Joos, G. Niedner-Schatteburg, V. E. Bondybey, J. Phys. Chem. A 1999, **103**, 671.

8 H. Watanabe, S. Iwata, J. Phys. Chem. 1996, **100**, 3377.

9 Gereon Niedner-Schatteburg, habilitation thesis, Technische Universität München, 1996.

10 A. D. Becke, Phys. Rev. A 1988, **38**, 3098.

11 C. Lee, W. Yang, R. G. Parr, Phys. Rev. B 1988, **37**, 785.

12 M. Sprik, J. Hutter, M. Parinello, J. Chem. Phys. 1996, **105**, 1142.

13 R. Ahlrichs, M. Bär, M. Häser, H. Horn, C. Kölmel, Chem. Phys. Lett. 1989, **162**, 165.

14 M. V. Arnim, R. Ahlrichs, J. Comput. Chem. 1998, **19**, 1746.

15 F. Weigend, R. Ahlrichs, Phys. Chem. Chem. Phys. 1999, **1**, 4537.

16 Holleman-Wiberg, Lehrbuch der Anorganischen Chemie, Walter de Gruyter, Berlin 1995.

17 Z. Shi, J. V. Ford, S. Wei, A. W. Castleman, Jr, J. Chem. Phys. 1993, **99**, 8009.

5. Ab Initio Treatment of Magnesium Water Cluster Anions $[Mg,nH_2O]^-$

Geometrical as well as electronic structures of magnesium water cluster anions with the formal stoichiometry $[Mg,nH_2O]^-$, $n \leq 11$, *are investigated through application of various correlated ab initio methods. Different structural archetypes emerge and the excess electron localization mode within them are elucidated. Their stability against electron detachment are predicted through calculation of vertical and adiabatic detachment energies of the most stable cluster geometries. Minimum cluster sizes of vertically and adiabatically stable* $[Mg,nH_2O]^-$ *clusters are discussed. The impact of the excess electron on cluster structures is explored and the extent of the cluster structure reorganization upon electron detachment in* $[Mg,nH_2O]^-$ *is quantified. The aim of this study is to provide predictive guidelines for future experiments.*

5.1 Introduction

Through an enhanced understanding on the molecular level of the physicochemical properties of ions and electrons in bulk liquids and finite cluster systems we anticipate to improve our knowledge of the process of solvation. Stability, structure, and reactivity of hydrated ions as well as the dynamics of the hydration process itself are therefore active areas of research.

Molecular solvation of stable, closed shell cations and anions of atoms and molecules has been subject of research ever since and was reviewed accordingly.[1-5] Reactivity and complexation of open shell, radical cations as originating e.g. from electron impact or photoionization is also extensively studied.[6] Quite in contrast intermolecular electron delocalization was not on the agenda for a long time.[&] By now there are also numerous experimental[11-23] and theoretical[24-44] studies on the hydration of an extra lone electron yielding $(H_2O)_n^-$, also termed hydrated electron. Only very recently Sobolewski and Domcke performed ground breaking studies on the coexistence of a hydrated electron in the vicinity of a hydrated hydronium. They conclude that the microsolvation of a H_3O radical results in the formation of a hydronium cation and a localized electron cloud, both connected by a water

---

[&] Here we emphasize studies with particular insight on the processes at a molecular level. For bulk phase studies on photoelectron hydration see Laubereau and coworkers.[7-10]

network with very strong hydrogen bonds.[41-43] Quite in contrast, our knowledge of energetics, structures and motives of electron localization in anionic hydrated metal-atom clusters is sparse. The work performed so far concentrates mainly on the solvation of closed shell alkali metal anions M^-, M=Li, Na. All findings indicate that in these species the excess electron remains located at the M^- anion in the investigated size regime $M^-(H_2O)_n$, n≈1-12.[45-48]

The electronic structure of $[Mg,nH_2O]^-$ clusters is unknown. A priori there are three different electronic cluster structures conceivable: The excess charge may locate at the metal which would yield an open shell Mg^- [Ne]$3s^2 3p^1$ configuration. The Mg^- anion is to be hydrated in $Mg^-(H_2O)_n$. Alternatively, coexistence of a neutral Mg atom and of the net extra charge separated from each other but within the same cluster is conceivable. The electronic structure would best be described as $Mg(H_2O)_n^-$. One more alternative to consider – in principle – is that of an Mg^{q+} cation plus q+1 electrons all of which are to cosolvate within the same cluster, formally $Mg^{q+}(H_2O)_n^{(q+1)-}$.

From photodetachment studies of hydrated electron clusters it is well known that the electron binding energies of $(H_2O)_n^-$, n≥2, strongly increase with cluster size n.[11-12] Although the Mg atom with its [Ne]$3s^2$ configuration has a negative electron affinity (EA) in its ^1S ground state, it can be speculated that larger $Mg(H_2O)_n^-$ or $Mg^{q+}(H_2O)_n^{(q+1)-}$ clusters might be stable nevertheless. This makes up the key issue of this study: How many H_2O molecules are needed to support a stable bound excess electron in $[Mg,nH_2O]^-$ and what does the electronic structure eventually look like ?

In the preceding chapters 3 – 4 the hydration process and the cluster size dependent evolution of the electronic structures of Mg_{aq}^+ [49-50] and Al_{aq}^+ [51] monocations were analyzed in some detail. In $[Mg,nH_2O]^+$, n≥6, strong evidence was found for the singly occupied molecular orbital (SOMO) to gradually shift away from the Mg^+ monocation into the hydration shell as cluster size n grows. Thus, the Mg^+ monocation is gradually oxidized. Eventually a hydrated Mg^{2+} dication and a hydrated electron coexist within $[Mg,nH_2O]^+$, n≥17. In these clusters the SOMO, which accomodates the odd electron, is found to localize within the hydration shell through stabilization by polar dangling O-H bonds of adjacent H_2O molecules. These $HO\text{-}H\cdots e^-\cdots H\text{-}OH$ structures are referred to as molecular tweezers. This localization mode of the odd electron is reminiscent of the structural motives in anionic water clusters first predicted by K. S. Kim et al.[27-33] and later verified spectroscopically by Johnson and coworkers[13]. The electronic structures of $Mg(H_2O)_n^-$ and $Mg^{q+}(H_2O)_n^{(q+1)-}$ introduced above are expected to share distinct features with the electronic structure of the hydrated magnesium monocations $[Mg,nH_2O]^+$.

In the following the first quantum chemical calculations of $[Mg,nH_2O]^-$, $n \leq 11$ are presented. Relative stabilities of different cluster structures as well as vertical detachment energies (VDEs) are provided. Adiabatic EAs were also determined but the negative of these EAs, which will be denominated as adiabatic detachment energies (ADEs), will be used instead. This facilitates a more convenient comparison to the VDEs. The performed ab initio studies elucidate the electronic structure of $[Mg,nH_2O]^-$ clusters and enable the first prediction of the minimum number of H_2O molecules that are needed to stabilize an excess electron within a water cluster that is doped with a Mg atom.

5.2 Computational Details

Gradient corrected density functional theory (DFT) is applied, using the Becke88 exchange functional[52] together with the Lee, Yang, and Parr corrected correlation functional[53] (BLYP) in order to optimize geometries of $[Mg,nH_2O]^-$, $n \leq 11$. In this very first ab initio study on the $[Mg,nH_2O]^-$ species we restricted our attention to isomers that are made up of nondissociated H_2O molecules. A detailed study of the O-H insertion by Mg in $[Mg,nH_2O]^-$ is in preparation. For cluster sizes $n \leq 6$ we performed extensive geometry optimization through consideration of first and optionally of second shell hydration. For cluster sizes $n \geq 7$ several isomers, as derived from the structural archetypes of smaller clusters, were geometry optimized. In all BLYP calculations triple-ζ valence type plus polarization (TZVP) basis sets were employed for O (11s6p1d)/[5s3p1d] and H (5s1p)/[3s1p]. For Mg (14s8p1d)/[5s4p1d] polarization functions of type 2p1d (TZVPP) were added. Unless otherwise stated the basis sets were used as developed by Ahlrichs and coworkers[54]. In all DFT calculations Coulomb interactions were treated by means of an auxiliary basis set representation of the electron density. The TURBOMOLE[55-56] implementation of the RIDFT[57-58] method (RI=resolution of identity) was used and the required auxiliary basis sets were chosen as implemented. The required grids for the numerical integration of exchange and correlation contributions were chosen second but finest (m4)[56].

Further single point calculations at the second order Møller Plesset pertubation (MP2) level of theory were performed at the BLYP optimized cluster structures. For these calculations the TZVP and TZVPP basis sets of H and O atoms were augmented by diffuse s and p functions on O (orbital exponents: 0.06 each)[34] and a diffuse s function on H (orbital exponent: 0.035)[34]. We refer to these basis sets as TZVPa (O: (12s7p1d)/[6s4p1d], H: (6s1p)/[4s1p]) and TZVPPa (O: (12s7p2d1f)/[6s4p2d1f], H: (6s2p1d)/[4s2p1d]). For Mg the TZVPP basis set was used throughout. All MP2 calculations in this work were performed with the TURBOMOLE implementation of the RI-MP2[59] method and within the standard frozen core approximation. The RI-MP2 algorithm is based on an approximate representation of products of molecular orbitals as a linear combination of atom centered auxiliary basis functions. The required auxiliar basis sets[60] were chosen as implemented in TURBOMOLE, in case of the augmented TZVPPa and TZVPa basis sets we used the auxiliar basis sets for TZVPP and TZVP.

Application of RI-MP2 methods lead to a significant reduction of the computational cost at the expense of insignificant loss in accuracy with regard to straight MP2 methods.[60] RI-MP2 and straight MP2 test calculations on $[Mg,H_2O]^-$ revealed detachment energies that deviate by 0.3% at most. Neutral clusters were described by restricted wavefunctions and anionic clusters were described by unrestricted wavefunctions (RHF and UHF approximation, respectively). The most stable isomers of each cluster size $n \leq 11$ and various selected isomers were further reoptimized at the MP2 level using as large basis sets for O and H as technically possible for us: aug-cc-pVTZ[61] (n=1-3), TZVPPa (n=1-7) and TZVPa ($n \geq 6$). The RI approximation allows for such optimizations of $[Mg,nH_2O]^-$ cluster structures at the MP2 level of theory and with extended basis sets as is necessary for the proper description of the diffuse electronic structures. When indicated zero point energy (ZPE) corrections for MP2 optimized $[Mg,nH_2O]^-$ cluster structures were obtained through vibrational analyses using numeric second derivatives of the energy as implemented within the TURBOMOLE code.

VDEs were calculated as the energy difference of the neutral and the anionic clusters at the geometry of the anions and at various levels of theory. In order to evaluate ADEs, we also optimized the geometries of neutral cluster $[Mg,nH_2O]$, $n \leq 11$, starting from the minimum $[Mg,nH_2O]^-$ cluster structures. To obtain ADEs at the MP2 level of theory for cluster sizes $n \geq 4$ neutral clusters were first BLYP optimized and then MP2 reoptimized.

On top of all of the above complete active space self consistent field (CASSCF)[62-63] single point calculations were performed at the BLYP and MP2 optimized geometries using the ab initio programme package MOLPRO[64]. The active space in these calculation was spanned by the Mg $3s^2$ valence electrons and the excess electron distributed over four orbitals. Moreover, VDEs and ADEs of some BLYP and MP2 optimized $[Mg,nH_2O]^-$ were evaluated at the cluster geometries at the coupled cluster with single and double excitation (CCSD) and non-iterative triples (CCSD(T)) level of theory.[65] Open shell spin unrestricted coupled cluster calculations were performed using the RHF-CCSD[66-67], respectively the RHF-UCCSD(T)[68] method as implemented in the programme package MOLPRO.

5.3 Results and Discussion

A. DFT Calculations

The application of DFT to small molecular systems with net negative charge is potentially problematic. Incomplete cancellation of the self interaction in the approximate exchange-correlation functionals in use today gives rise to a self-repulsion error.[69] However, the more the spurious self-repulsion distributes over larger orbital volume the less significant it becomes.[70] With respect to the performed calculations it is concluded that gradient corrected DFT provides reasonable starting geometries for subsequent application of higher level ab initio methods and useful estimates of the relative stabilities of different $[Mg,nH_2O]^-$ isomers of a given cluster size n. Similarly, the application of BLYP to the study of anionic water clusters $(H_2O)_n^-$ was justified before.[28,32]

B. Cluster Structures and Relative Stabilities

By means of full geometry optimization of $[Mg,nH_2O]^-$ at the BLYP level a general survey of the relative stabilities of typical cluster isomers was obtained. Fig. 5.1 presents typical BLYP optimized cluster structures for $[Mg,nH_2O]^-$, n=1-11. The evaluation of their ground state energies at different levels of theory yields relative stabilities ΔE. Table 5.1 summarizes these values for all investigated cluster sizes n. CASSCF/TZVPa // BLYP calculations were performed in order to check for the applicability of the other single determinant based ab initio methods. However, with the present limited choice of active space the CASSCF calculations do not account for all of the correlation in $[Mg,nH_2O]^-$ to its full extent. The more satisfying it is that for $n \geq 4$ we find a qualitative correspondence of ΔE values from BLYP, MP2/TZVPa // BLYP, MP2/TZVPPa // BLYP and CASSCF/TZVPa // BLYP calculations. For these cluster sizes the same energetic order of the investigated isomers is obtained - regardless of the method.

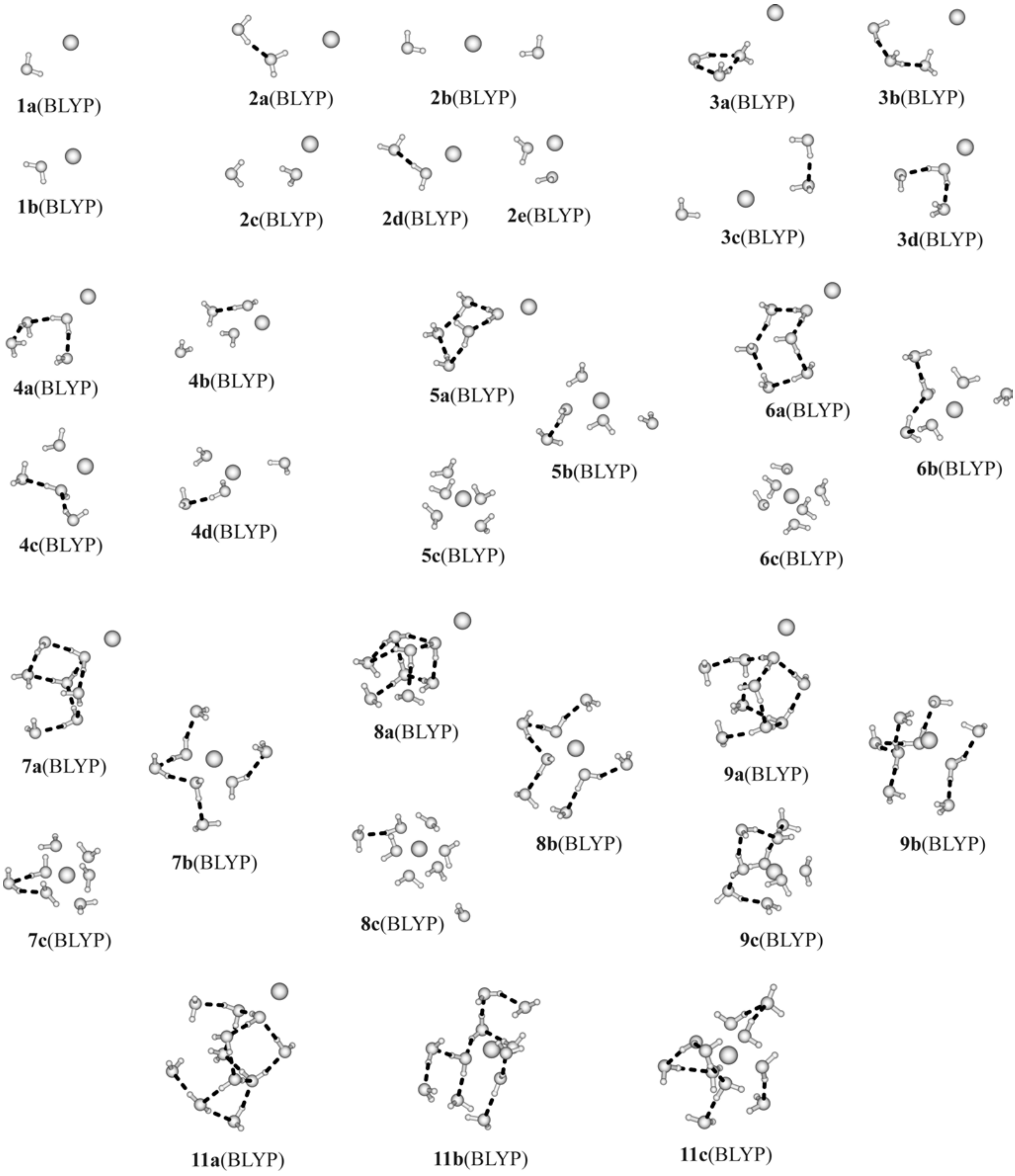

1a(BLYP) **2a**(BLYP) **2b**(BLYP) **3a**(BLYP) **3b**(BLYP)

1b(BLYP) **2c**(BLYP) **2d**(BLYP) **2e**(BLYP) **3c**(BLYP) **3d**(BLYP)

4a(BLYP) **4b**(BLYP) **5a**(BLYP) **6a**(BLYP) **5b**(BLYP) **6b**(BLYP)

4c(BLYP) **4d**(BLYP) **5c**(BLYP) **6c**(BLYP)

7a(BLYP) **8a**(BLYP) **9a**(BLYP) **7b**(BLYP) **8b**(BLYP) **9b**(BLYP)

7c(BLYP) **8c**(BLYP) **9c**(BLYP)

11a(BLYP) **11b**(BLYP) **11c**(BLYP)

Fig. 5.1 Overview of possible $[Mg,nH_2O]^-$, n=1-11, cluster structures, optimized at the BLYP level of theory with TZVP basis sets for O, H and TZVPP for Mg.

Table 5.1 Relative energies ΔE in kJ mol^{-1} and classification (see text) of BLYP optimized $[Mg,nH_2O]^-$ cluster structures.

cluster size n	*structure*	*classification*	*ΔE (BLYP)*	*ΔE (MP2/TZVPa // BLYP)*	*ΔE (MP2/TZVPPa // BLYP)*	*ΔE (CASSCF/TZVPa // BLYP)*
1	**1a**(BLYP)	-	0	0	0	0
	1b(BLYP)	-	27.45	22.68	26.23	30.98
2	**2a**(BLYP)	-	0	0	0	2.44
	2b(BLYP)	-	4.31	4.23	1.06	6.93
	2c(BLYP)	-	24.55	5.34	2.67	12.87
	2d(BLYP)	-	47.69	3.13	5.02	0
	2e(BLYP)	-	62.66	32.03	29.43	48.18
3	**3a**(BLYP)	-	0	11.11	13.80	15.12
	3b(BLYP)	-	1.91	15.66	16.43	16.39
	3c(BLYP)	-	8.46	20.98	20.21	21.13
	3d(BLYP)	-	25.12	0	0	0
4	**4a**(BLYP)	*E*	0	0	0	0
	4b(BLYP)	*SI*	18.33	37.83	40.50	44.58
	4c(BLYP)	*SI*	40.40	44.79	46.98	53.79
	4d(BLYP)	*SI*	45.13	49.81	48.07	64.82
5	**5a**(BLYP)	*E*	0	0	0	0
	5b(BLYP)	*SI*	85.42	84.43	80.09	112.36
	5c(BLYP)	*I*	110.95	150.86	140.31	178.30
6	**6a**(BLYP)	*E*	0	0	0	0
	6b(BLYP)	*SI*	69.46	83.38	69.22	116.20
	6c(BLYP)	*I*	107.82	75.38	71.70	151.13
7	**7a**(BLYP)	*E*	0	0	0	0
	7b(BLYP)	*SI*	76.92	84.03	75.40	75.47
	7c(BLYP)	*I*	117.71	80.47	77.63	116.35
8	**8a**(BLYP)	*E*	0	0	0	0
	8b(BLYP)	*SI*	74.33	64.30	56.21	95.59
	8c(BLYP)	*I*	115.37	78.51	79.85	130.58
9	**9a**(BLYP)	*E*	0	0	0	0
	9b(BLYP)	*SI*	68.14	63.64	55.44	62.97
	9c(BLYP)	*I*	153.76	89.96	99.59	111.00
11	**11a**(BLYP)	*E*	0	0	0	0
	11b(BLYP)	*SI*	51.35	59.10	46.51	56.40
	11c(BLYP)	*I*	97.37	57.76	62.61	98.55

For cluster sizes $n \leq 3$ this is not the case, the energetic order depends on the ab initio component applied. More reliable predictions of the relative stabilities of different isomers of $[Mg,nH_2O]^-$, n=1-3 require geometry optimization at higher levels of theory, which will be discussed later in this manuscript. It is interesting to note, that the variation of energies when evaluated from MP2/TZVPa // BLYP and MP2/TZVPPa // BLYP calculations is modest in general. This indicates that already the TZVPa basis has much of the flexibility required for a proper description of the electronic structure in $[Mg,nH_2O]^-$.

The structures of $[Mg,nH_2O]^-$ clusters with n≤3 are difficult to categorize other than by their electronic structure (cf. section C). Quite in contrast the classification of structures for n≥4 is rationalized in terms of three structural archetypes (labels *E*, *SI* and *I*). In structures of type *E* ("*E*xternal") Mg attaches to a water cluster via a single Mg···OH$_2$ bond. This leads to a so called external solvation of Mg at the water cluster. These clusters, which consist of H_2O molecules arranged in rings or cages, exhibit a striking structural feature: Some adjacent dangling H atoms, that are not involved in O···H hydrogen bonds but belong to different H_2O molecules, almost point onto each other. This is a structural motive as recovered before in H_2O clusters that solvate an excess electron.[27-33] Clustered dangling H atoms (dangling O-H bonds) have been shown before to serve as electrophilic binding sites e.g. for hydrated electrons in $(H_2O)_n^-$,[13,27-33] $[Na,nH_2O]$,[71-73] and $[Mg,nH_2O]^+$ [49-50] clusters. Two or more O-H bonds of adjacent H_2O molecules act as molecular tweezers HO-H···e$^-$···H-OH that localize the electron.

The the latter will be confirmed for $[Mg,nH_2O]^-$ clusters by a detailed analysis of the SOMOs (cf. section C). Nevertheless, it can be resumed at this point that the structural properties of cluster type *E* indicate strong similarities to the postulated $Mg(H_2O)_n^-$ structure.

In clusters of type *SI* ("*Semi-Internal*") the average Mg···O distance between Mg and first shell H_2O molecules is significantly increased (e.g 2.7 Å in case of isomer **7b**(BLYP) vs. 2.2 Å in **7a**(BLYP)). This is due to the fact that the H_2O molecules are not exclusively bound with the O to Mg but some first shell H_2O molecules are orientied with the H atoms pointing to Mg instead.

The Mg···H-OH interactions reveal considerable electron density at Mg, indicative of a low Mg oxidation state. In clusters of type *SI* Mg is located in a cavity built by surrounding H_2O molecules. The H_2O network also contains some O-H oscillators of adjacent H_2O molecules directed at each other that form tweezer structures. Overall clusters of type *SI* exhibit structural features that indicate a Mg atom inside the cluster and the excess electron to be located in the hydration shell by molecular tweezers. The coordination number of Mg is higher than in structures of type *E*. Nevertheless the average Mg···O distance is too large to classify the Mg solvation mode as internal. Instead the situation in these clusters is denoted as semi-internal Mg hydration (*SI*).

In some of the cluster structures with n≥5 "*I*nternal" solvation (*I*) is found, cf. Table 5.1. The Mg is surrounded by up to six first shell H_2O molecules, which are oriented with the O towards the Mg atom. In cluster sizes n≥7, six H_2O molecules remain in the first hydration shell, and n-6 H_2O molecules are located within the second solvation shell. The average Mg···O distance (e.g 2.2 Å in case of isomer **7c**(BLYP)) is significantly shorter than that of structures of type *SI*. Clusters assigned to structure type *I* also contain some dangling H atoms directed at each other. We resume that all investigated cluster types *E, SI* and *I* contain some structural indication of the location of the excess electron within the hydration shell by molecular tweezers. However, the external Mg solvation is energetically clearly favored against semi-internal or internal solvation. The relative stabilities of the investigated isomers reveal the following energetical order of the different structure types: *E* < *SI* < *I*. The CASSCF calculations, as performed on all minimum structures, prove that for isomers assigned to type *E* and *SI*, as well as generally for all $[Mg,nH_2O]^-$ isomers with n≤3, a single electronic reference determinant makes up for more than 92% (generally ≈96%) of the CASSCF wave function. Any other (excited) state contributes by 4% at most. It is only for some cluster structures of type *I* that the ground state contribution drops below 80%. Therefore ab initio methods based on a single determinant are expected to provide reliable energetics for isomers assigned to structure type *E* and *SI* and for all investigated isomers with n≤3. Single determinant based ab initio methods are not suitable, however, to provide a quantitative description of the electronic structure and energetics of clusters with an internally solvated Mg (structure type *I*). Nevertheless, the CASSCF calculations lead to the same energetic order *E* < *SI* < *I* as the qualitative BLYP and MP2 data (cf. Table 5.1). Regardless of the method the isomers assigned to structure type *I* are energetically clearly disvafored with regard to structures of type *E* or *SI*.

Based on the preliminary inquiries up to here, it is concluded that the evaluation of the relative stabilities, especially of cluster sizes n≤3, requires a more detailed investigation at higher levels of theory. For cluster sizes n>3 the discussion will be focussed on minimum structures of type *E*, as structure types *SI* and *I* have proven to be high energy isomers. Hence for $[Mg,nH_2O]^-$, n≥4, only minimum isomers of structure type *E* were MP2 reoptimized in geometry, whereas for n≤3 all cluster structures (**1a**(BLYP)-**3d**(BLYP)) were reoptimized at the MP2 level. The basis set superposition error (BSSE) was computed for all MP2/TZVPPa optimized cluster structures $[Mg,nH_2O]^-$, n≤3, through the full counterpoise method.[74]

This yields similar values for all isomers of same size n. BSSE corrected energy differences between individual isomers are summarized in Table 5.2 (denoted ΔE(BSSE)).

Table 5.2 Relative energies (ΔE) and BSSE corrected ΔE values of MP2 optimized $[Mg,nH_2O]^-$ isomers, n≤3. All units are kJ mol^{-1}.

n	*structure*	*ΔE*	*ΔE (BSSE)*
		(MP2/TZVPPa)	*(MP2/TZVPPa)*
1	**1a**(MP2)	0	0
	1b(MP2)	23.30	26.66
2	**2a**(MP2)	21.73	16.36
	2b(MP2)	23.08	16.07
	2c(MP2)	10.47	6.19
	2d(MP2)	0	0
	2e(MP2)	35.72	36.18
3	**3a**(MP2)	22.75	18.44
	3b(MP2)	23.90	19.57
	3c(MP2)	29.81	22.80
	3d(MP2)	0	0

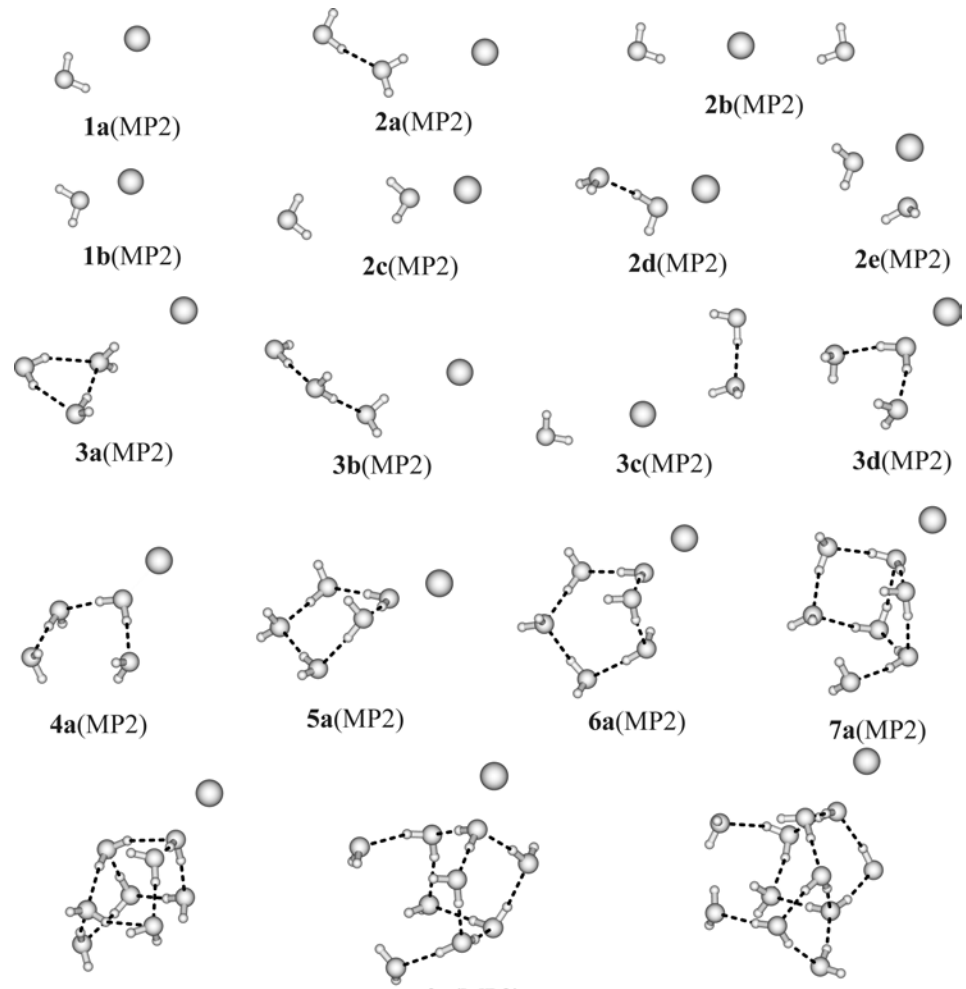

Fig. 5.2 MP2 optimized cluster structures $[Mg,nH_2O]^-$, n=1-11. For the structures on display calculations were performed with the TZVPPa basis for cluster sizes n=1-7 and the TZVPa basis for n=8-11.

The BSSE correction proves to show no significant effect on relative energies and is omitted for larger cluster sizes. The MP2/TZVPPa (n=1-7) and MP2/TZVPa (n=8,9,11) optimized cluster structures are on display in Fig. 5.2. For cluster sizes n≥3 the BLYP generated frameworks of hydrogen bonded rings and cages prove to be surprisingly stable under MP2 reoptimization.

The mutual connectivity endures in all cases but isomer **8a**(BLYP) -> **8a**(MP2), where some hydrogen bonds seem to loosen significantly. In principle the structures for cluster sizes n≤3 seem largely unaffected by MP2 reoptimization as well, however, differences become more apparent if relative stabilities are also considered.

For n=1 and n=3 the relative energetic order of the investigated isomers persists, and the absolute ΔE(MP2/TZVPPa) values differ from ΔE(MP2/TZVPPa // BLYP) values systematically by 2.9–9.6 kJ mol^{-1} (cf. Table 5.2). In case of n=2, however, the relative stability of isomers – as indicated by ΔE – changes upon MP2 reoptimization. In structure **2d**(MP2) the second shell H_2O molecule is rotated such that it is aligned perpendicular to the first shell H_2O molecule, whereas in **2d**(BLYP) both H_2O molecules are in plane. This reorientation of the second shell H_2O molecule leads to a distinct decrease in total energy of **2d**(MP2). However if BSSE and ZPE corrections are included, **2c** is still slightly favored by –0.52 kJ mol^{-1}. This changes when the larger aug-cc-pVTZ basis set is used, geometry optimization at the MP2/aug-cc-pVTZ level of theory yields **2d** to be favored by ΔE(MP2/aug-cc-pVTZ)= −17.30 kJ mol^{-1}, respectively –9.30 kJ mol^{-1} after ZPE correction. The larger basis proves that **2d** is the energetically lowest isomer of all investigated cluster structures with n=2.

A vital point for the following discussion is that the structural motive of clustered dangling H atoms (tweezer structures) as encountered in some BLYP optimized cluster structures remains a characteristic feature of these particular cluster geometries even after MP2 reoptimization.

C. Electronic Structures

This work does not raise the claim to provide a complete analysis of the electronic structure and related properties of all possible isomers within the range of cluster sizes studied. In this very first step of a systematic analysis of the $[Mg,nH_2O]^-$ species, we instead focus on most stable cluster geometries as found empirically. This approach allows for the prediction of cluster size dependent key properties in the size range n=1-11. The hydrogen bonded networks of $[\mathrm{Mg},n\mathrm{H_2O}]^-$ clusters as presented in Fig. 5.2 share some motives with that of anionic water clusters $(\mathrm{H_2O})_n^-$. In all minimum isomers n≥3 as well as for structures **2c**(MP2) and **2e**(MP2) some $^{\delta-}$O-H$^{\delta+}$ bonds of adjacent H_2O molecules point towards each other. Apparently there is some kind of attractive interaction prevailing between these dangling H atoms. This finding is indicative of high electron density to locate between the partially positive charged H$^{\delta+}$ atoms. Such an electron localization mode was first shown to occur in $(\mathrm{H_2O})_n^-$ by K. S. Kim et al.[27-33]. More definite answers on the excess electron localization motive in $[\mathrm{Mg},n\mathrm{H_2O}]^-$ arise from a spatial analysis of the SOMO. We have generated isosurface plots of the SOMOs and of the energetically second highest molecular orbitals (SOMO-1) for the most stable cluster isomers **1a**(MP2), **2d**(MP2), **3d**(MP2), **6a**(MP2), **9a**(MP2) and **11a**(MP2) in Fig. 5.3.

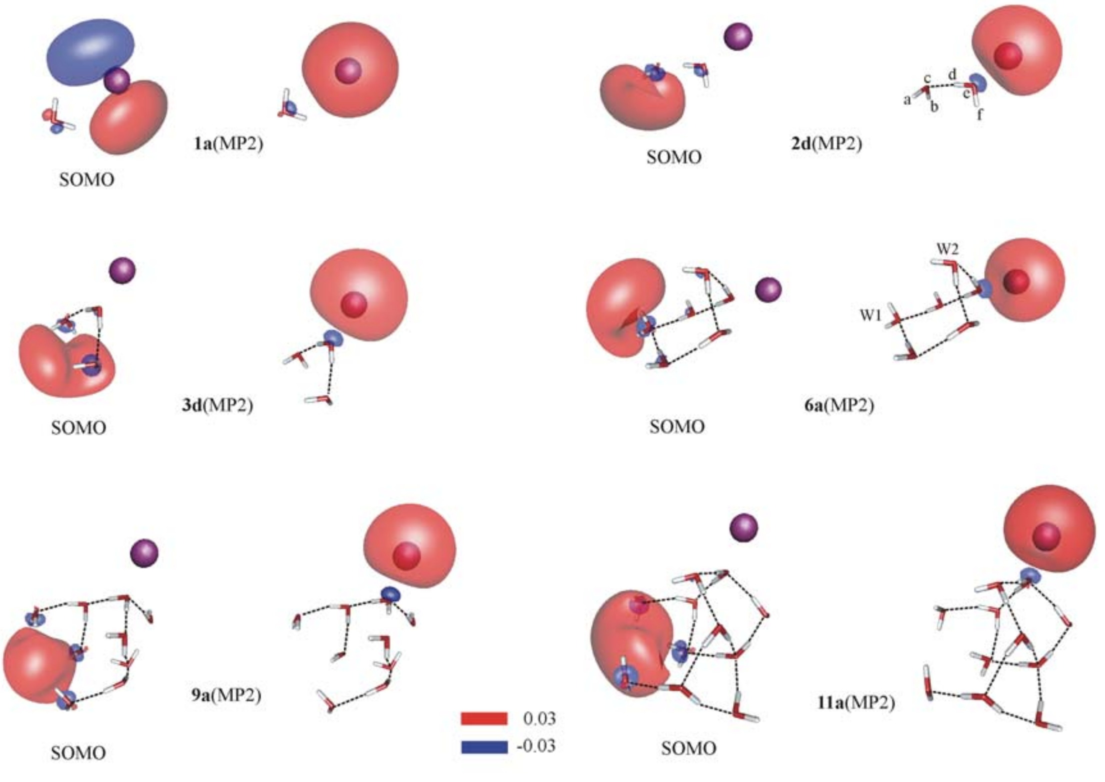

Fig. 5.3 Isosurface plots of the SOMO (left) and the energetically second highest molecular orbital (right) in the most stable of the investigated $[\mathrm{Mg},n\mathrm{H_2O}]^-$ isomers for n=1,2,3,6,9 and 11. For n=1 the shape of the SOMO (two lobes of opposite sign separated by a nodal plane) indicates large contributions from the 3p orbital of the Mg^- anion. For all cluster sizes n≥2 the SOMO has detached from the prior Mg^- anion and is transferred to the water cluster.

As is visible from Fig. 5.3 in **1a**(MP2) the SOMO stems by in large from the 3p orbital of the Mg^- anion (configuration: $[Ne]3s^23p^1$). The electronic structure in **1a**(MP2) is best described by $Mg^-(H_2O)$. The net negative charge density at the Mg^- makes the H_2O ligand coordinate with the H atoms towards Mg^-. Within the SOMO the two lobes of the prior Mg^- 3p orbital polarize as to stretch out towards the electrophilic binding sites of the $H^{\delta+}$ atoms in H_2O. The net negative charge density at the Mg^- makes the H_2O ligand to coordinate with the H atoms towards Mg^-. In structure **2d**(MP2) the SOMO has detached from the Mg center. It has shifted into the second hydration shell where it concentrates at and around two H atoms of the second shell H_2O molecule. The dangling H atom of the first shell H_2O molecule points towards this SOMO. At this point we emphasize that it takes only n=2 in $[Mg,nH_2O]^-$ to clearly separate the excess electron from the Mg atom. In Fig. 5.3 the atoms of structure **2d**(MP2) are labelled in order to facilitate the comparison of the alignments of the H_2O molecules in **2d**(MP2) and the water dimer anion $(H_2O)_2^-$ whose potential hypersurface has only a single minimum. The MP2/aug-cc-pVTZ optimized cluster geometry **2d**(MP2) is compared with the $(H_2O)_2^-$ geometry obtained by Weigend and Ahlrichs[34] by MP2 optimization using aug-cc-pVTZ basis sets augmented with one floating point. In the following we compare our structural data on $[Mg,nH_2O]^-$, n=2, with their data on $(H_2O)_2^-$ (given in parentheses). Both structures have a very small O(c)O(e)H(d) valence angle of 3.4° (1.2°). The distance between the two oxygen atoms O(c),O(e) is shorter in **2d**(MP2) with 266.9 pm (289.1 pm) and the H(a)O(c)H(b)O(e) dihedral angle is also somewhat smaller with 116.0° (145.8°). Although not identical, the alignment of the H_2O molecules is nevertheless similar and it is concluded, that **2d**(MP2) is essentially a $(H_2O)_2^-$ cluster with a Mg atom attached to it: $Mg(H_2O)_2^-$. The stability of **2d**(MP2) versus electron detachment will be addressed later. Here we already mention that $(H_2O)_n^-$, n= 2, is the smallest cluster size with VDE > 0. The water dimer is the smallest water cluster with a stable dipole bound state of the excess electron.

Spatial analyses of the SOMOs in all other most stable $[Mg,nH_2O]^-$ isomers with $2 \leq n \leq 11$ ere also performed. It turns out that these clusters all consist of a Mg atom attached to a $(H_2O)_n^-$ sub-cluster. We therefore refer to them as $Mg(H_2O)_n^-$ in all of the following. Some less stable isomers of larger clusters $n \geq 2$ also contain a Mg^- anion with a SOMO that is, by in large, essentially a Mg 3p orbital like in **1a**(MP2) and **1b**(MP2) (e.g. **2a**(MP2), **2b**(MP2),

3a(MP2) and **3b**(MP2)). However, for n≥2 $Mg^{-}(H_2O)_n$ isomers that have their SOMO detached from the prior Mg^{-} anion are more stable throughout.

In **3d**(MP2) the SOMO is located between two second shell H_2O molecules, each pointing with both O-H bonds to the SOMO. Some clusters with only two H_2O molecules (e.g. **2c**(MP2) and **2e**(MP2)) also contain the SOMO located in tweezer structures. These are less stable than **2d**(MP2), however. $Mg(H_2O)_n^{-}$, n=3, is the smallest cluster with a tweezer structure in the most stable isomer **3d**(MP2) and the SOMO is located between four O-H bonds of two H_2O molecules facing each other. The geometry of the H_2O hexamer in **6a**(MP2) is reminiscent of the "boat" conformation of cyclohexane. This structure facilitates the formation of six hydrogen bonds within the H_2O hexamer and is further stabilized by attractive interactions between the SOMO localized around the O-H bonds of the H_2O molecule labelled as W1 (cf. Fig. 5.3) and one O-H bond of the H_2O labelled as W2. Both the structures of the H_2O network and the positions of the SOMOs in Fig. 5.3 reveal that the excess electron remains at the surface of the $(H_2O)_n^{-}$ sub-clusters in $Mg(H_2O)_n^{-}$, n≥2, where it interacts with polar O-H binding sites of nearby H_2O molecules.

In $Mg(H_2O)_n^{-}$, n=2-11, the SOMO is located in that hemissphere of the $(H_2O)_n^{-}$ sub-cluster which is void of the Mg atom. In principle, either or even both of the Mg $3s^2$ valence electrons may also shift into the water cluster. However, they remain within polarized 3s orbitals at Mg for all cluster sizes n≤11 (cf. Fig. 5.3). The long bond between the Mg atom and the $(H_2O)_n^{-}$ sub-cluster, that it is attached to, seems to arise mainly from induction. Repulsive interactions between the excess electron and the Mg $3s^2$ valence electrons in $Mg(H_2O)_n^{-}$, n≥2, are minimized by the localization of the SOMO in that part of the $(H_2O)_n^{-}$ sub-cluster that opposes the Mg atom.

The electronic structures of the minimum iomers as summarized in Fig. 5.3 could be assigned to two of the three postulated electronic structure types for $[Mg,nH_2O]^{-}$, namely $Mg^{-}(H_2O)_n$ for n=1 and $Mg(H_2O)_n^{-}$ for n≥2. For the sake of completeness it is annotated that in some high energy cluster isomers (type *I*, cf. Table 5.1) the molecular orbital accomodating the two Mg $3s^2$ valence electrons is displaced by first shell H_2O molecules and transferred into the hydration shell. These clusters exhibit the electronic structure $Mg^{2+}(H_2O)_n^{3-}$. Their large ΔE values (cf. Table 5.1) makes them unlikely to exist as stable and observable species within the investigated cluster size regime n≤11, however.

D. Vertical and Adiabatic Detachment Energies (VDEs and ADEs)

Any experimental interrogation of the stability of the clusters takes place on a timescale that is determined by the experimental set up and by the experimental method in use. Time of flight mass spectrometric (TOF-MS) detection methods take place on the μs timescale. It conceivably combines with photodetachment experiments that probe the vertical detachment energy of the clusters. Ion trap mass spectrometric methods facilitate decay studies on much longer timescales which are suited to probe adiabatic stabilities, e.g. only recently the black body infrared radiation induced decay (BIRD) of anionic water clusters was studied in a Fourier Transform Ion Cyclotron Mass Spectrometer (FT-ICR-MS).[23]

Both VDEs and ADEs were determined for the energetically lowest isomers of cluster sizes $n \leq 11$ by multiple correlated ab initio methods. The computed data for the VDEs and ADEs are summarized in Tables 5.3 and 5.4. The close correspondence between detachment energies from MP2 and those from higher correlated ab initio methods (CCSD, CCSD(T)) must be emphasized. Obviously the MP2 method takes into account the bulk part of electron correlation in $Mg(H_2O)_n^-$. This makes MP2 the method of choice for geometry optimization of $Mg(H_2O)_n^-$. It seems to offer an acceptable tradeoff between computational cost and accuracy – the more when the RI approximation is applied. VDEs computed for BLYP optimized cluster structures are included in Table 5.3 for the sake of completeness. Although general trends are reproduced, the detachment energies differ noticeably from those of the MP2 optimized cluster structures except for 1a. For cluster sizes $n>2$ VDEs of BLYP optimized cluster structures are systematically higher than VDEs evaluated at MP2 optimized cluster structures.

The computed VDE data will be analyted in more detail in the following. In case of structure **1a** the VDEs are all negative, irrespective of the applied ab initio method. This makes the cluster – best characterized as $Mg^-(H_2O)$ – instable with respect to electron detachment. The computed VDEs for **1b** were also negative without exception. A single H_2O molecule does not suffice to stabilize the Mg^- anion. **2d**(MP2) exhibits the electronic structure $Mg(H_2O)_n^-$, the SOMO has detached from the prior Mg^- anion and is solvated by the water cluster.

$Mg(H_2O)_2^-$ is the smallest $[Mg,nH_2O]^-$ cluster with such a structure: A neutral Mg atom attaches to a negatively charged hydrogen bonded water sub-cluster $(H_2O)_2^-$. In case of **2d** MP2/aug-cc-pVTZ calculations as well as single point calculations with higher correlated ab initio methods (CCSD,CCSD(T)) with the large aug-cc-pVTZ basis sets for O and H atoms performed at the MP2/TZVPPa optimized geometry (cf. Table 5.3) yield positive values. This makes **2d** stable against photodetachment – at least on short timescales.

Table 5.3 Vertical detachment energies (VDEs) in kJ mol^{-1} of the most stable isomers, n≤11, at various levels of theory.

cluster	*MP2/ TZVPa // BLYP*	*MP2/ TZVPPa // BLYP*	*CCSD/ TZVPPa // BLYP*	*MP2/ TZVPa*	*MP2/ TZVPPa*	*MP2/aug-cc-pVTZ*	*CCSD/ TZVPa // MP2/TZVPPa*	*CCSD/ TZVPPa // MP2/TZVPPa*	*CCSD(T)/ TZVPPa // MP2/TZVPPa*
1a	−72.25	−73.47	−70.79	...	−74.28	−56.25	−70.77	−71.63	−69.93
2d	−22.69	−23.24	−21.13	...	−5.69	5.58	1.97	2.47	5.34
3d	50.63	47.78	56.17	...	32.70	40.56	42.7	41.42	...
4a	73.76	69.69	...	...	49.17	...	59.19	...	...
5a	92.67	88.55	...	...	53.19	...	63.92	...	...
6a	102.13	97.74	...	59.44	60.79	...	70.64	...	...
7a	125.04	120.35	...	86.79	90.98	...	...	...	...
8a	149.50	144.46	...	108.02	...	...	...	...	...
9a	154.89	150.86	...	109.49	...	...	...	...	...
11a	164.72	162.43	...	128.50	...	...	...	...	...

Table 5.4 Adiabatic detachment energies (ADEs) of the most stable $[Mg,nH_2O]^-$ isomers, n≤11, at various levels of theory and with zero point energy corrections (ZPE) when indicated. All units are kJ mol^{-1}.

cluster	*MP2/ TZVPa // BLYP*	*MP2/ TZVPPa // BLYP*	*CCSD/ TZVPPa // BLYP*	*MP2/ TZVPa*	*MP2/TZVPa + ZPE*	*MP2/TZVPPa*	*MP2/TZVPPa + ZPE*
1a	−80.29	−80.20	−80.05	...	...	−79.87	−76.60
2d	−31.50	−32.19	−31.38	...	...	−18.34	−16.26
3d	−15.11	−8.06	−9.54	...	...	3.32	4.44
4a	−14.82	−8.38	...	...	...	4.19	8.48
5a	−10.65	−6.67	...	...	...	2.80	9.51
6a	−17.50	−10.17	...	−1.75	4.64	−0.29	...
7a	−16.00	−5.87	...	−4.94	2.45	−0.96	...
8a	4.34	14.51	...	18.85	25.14	...	...
9a	1.57	9.47	...	9.60	15.47	...	...
11a	19.27	26.68	...	12.23	19.98	...	...

cluster	*MP2/aug-cc-pVTZ*	*CCSD/TZVPa // MP2/TZVPPa*	*CCSD/TZVPPa // MP2/TZVPPa*	*CCSD(T)/TZVPPa // MP2/TZVPPa*
1a	−61.08	−80.15	−79.84	−76.67
2d	−5.23	−12.53	−11.70	−7.31
3d	11.90	7.97	10.67	...
4a	...	14.57	...	...
5a	...	14.82	...	...
6a	...	7.27	...	...
7a	...	...	...	...
8a	...	...	...	...
9a	...	...	...	...
11a	...	...	...	...

This finding is to compare to the “pure” $(H_2O)_2^-$ cluster. Its VDE at the MP2 level of theory with aug-cc-pVTZ basis sets for O and H (augmented with one floating center) of 1.25 kJ mol^{-1} (0.013 eV)[34] agrees well with the experimental findings[11]. The VDE of $Mg(H_2O)_2^-$ (**2d**) at the MP2/aug-cc-pVTZ level of theory increases to 5.58 kJ mol^{-1}, which is a modest but significant effect.

For all $Mg(H_2O)_n^-$ clusters n>2 the VDEs are positive, and they gradually increase with n. For n=11 the VDE equals to 128.50 kJ mol^{-1} (MP2/TZVPa). In case of the $(H_2O)_{11}^-$ species the computed VDEs are in reasonable correspondence with the experimentally determined VDE of ≈70 kJ mol^{-1} (0.72 eV)[11]. Very recently Sobolewski and Domcke[43] computed the vertical binding energies of different $(H_2O)_{11}^-$ isomers to be of the order of 40 – 60 kJ mol^{-1} (0.4 – 0.6 eV). Among the considered $(H_2O)_{11}^-$ isomers in these calculations were both clusters containing a H_3O^+-OH^- ion pair as well as clusters made up of undissociated water molecules. The now calculated VDE of $Mg(H_2O)_{11}^-$ (11a) exceeds the experimentally predicted VDE of the “pure” water anion $(H_2O)_{11}^-$ significantly. The same holds true for smaller $Mg(H_2O)_n^-$ clusters. It is hard to conceive that all of this difference shall attribute to uncertainties and systematic differences between calculations and experiment. Instead we conclude that addition of Mg to $(H_2O)_n^-$ helps to polarize and reorganize $(H_2O)_n$ such that e^- stabilization is significantly enhanced.

The computed ADEs for the most stable investigated $Mg(H_2O)_n^-$ isomers n≤11 are listed in Table 5.4. For $Mg(H_2O)_n^-$ n=3 is the smallest cluster size with positive ADEs. However, the ADEs are positive only for MP2 optimized minimum isomers. In case of BLYP optimized geometries the computed ADEs remain negative. Although BLYP yields geometries that are seemingly close to those from MP2 calculations we find significant differences in the ADEs. Due to the intrinsic problems of density functional theory with diffuse anionic electronic states, geometry optimization at the MP2 level of theory (or equivalent) is mandatory in order to allow for an accurate determination of ADEs.

With increasing cluster size the computed ADEs – other than the VDEs – increase marginally. For n=6 and n=7 we find negative ADEs (at MP2/TZVPPa and MP2/TZVPa level). However, for all clusters with n≥3 the ADEs remain positive after ZPE correction. Higher correlated ab initio methods (CCSD) and the use of larger basis sets (aug-cc-pVTZ) increase the computed ADEs further. This indicates that **3d** and all other $Mg(H_2O)_n^-$ clusters with n>3 are adiabatically stable against spontaneous photodetachment. While **2d** is the smallest cluster with a $Mg(H_2O)_n^-$ structure, **3d** is the smallest cluster that locates the SOMO between O-H bonds of adjacent H_2O molecules. We have described this structural motive as tweezer structures HO-H···e⁻···H-OH before.[49-50] Changes in the localization mode of the excess electron at n=2 and n=3 are nicely correlated with the VDEs becoming positive for **2d** and ADEs becoming positive for **3d**.

The computed ADEs, n≥3, indicate weak bonding of the excess electron in $Mg(H_2O)_n^-$. Although the clusters are adiabatically stable the binding energy just amounts to a few kJ mol^{-1}. In previous black body induced decay studies of mass selected anionic water clusters $(H_2O)_n^-$, it was shown that these clusters may well decay by electron detachment within seconds.[23]

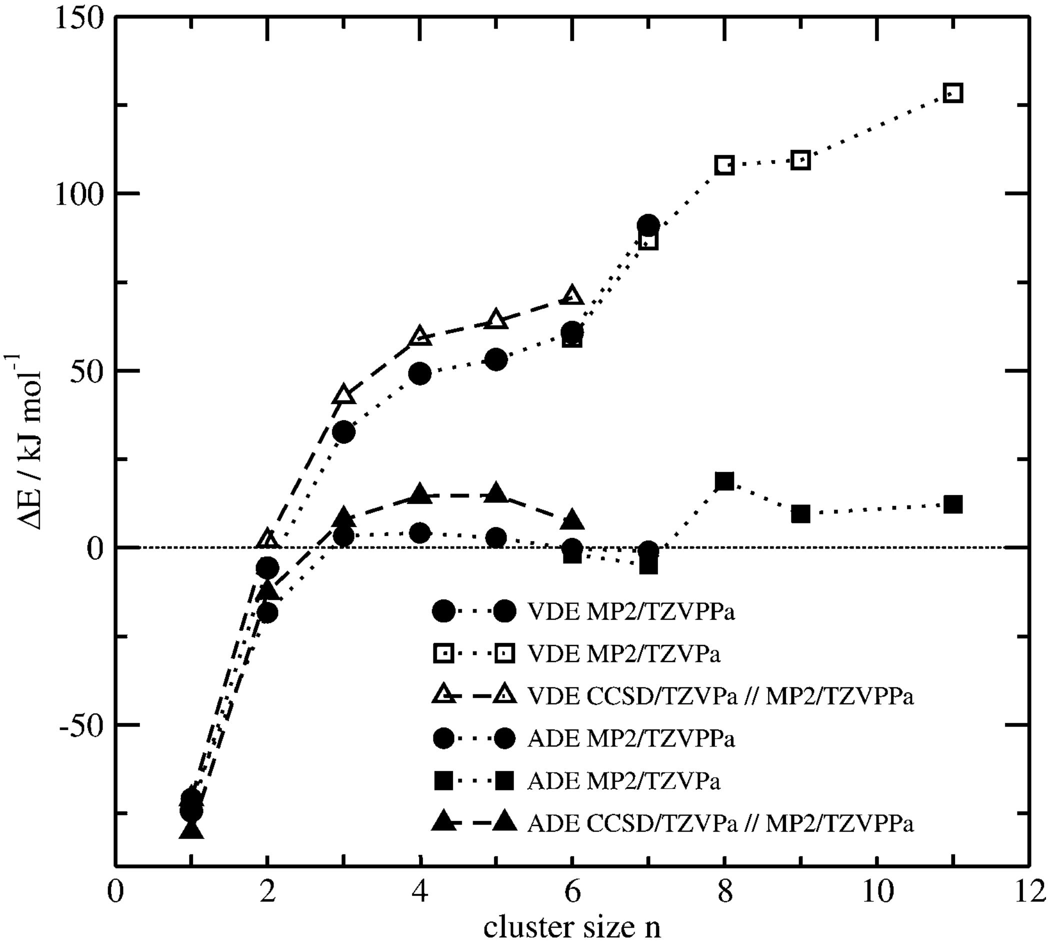

Fig. 5.4 VDEs and ADEs of $[Mg,nH_2O]^-$, n=1-11 at different levels of theory. The performed calculations predict the VDEs to become positive at n=2 and the ADEs to become positive at n=3. For cluster sizes n>2 the increase of the ADEs is less pronounced than for the VDEs. If zero point energy (ZPE) corrections are included the ADE remain positive for all investigated cluster sizes n≥3 (see text).

This shows that the excess electron couples to the intracluster vibrational modes. If the internal energy of the cluster, e.g. after vibrational excitation of the cluster by absorbtion of infrared photons from the thermal background radiation, suffices to overcome the binding energy of the excess electron (≈-ADE), it is eventually detached. In this respect $Mg(H_2O)_n^-$ clusters with their now computed ADEs can serve as an interesting and very sensitive "thermometer" in future experiments. Fig. 5.4 contains selected data of VDEs and ADEs from Tables 5.3 and 5.4 (MP2/TZVPPa ($n \leq 7$), MP2/TZVPa ($n \geq 6$) and CCSD/TZVPa // MP2/TZVPPa ($n \leq 6$)). This emphasizes that the computed VDEs and ADEs diverge with growing cluster size. By definition ADEs consider cluster reorganization upon electron detachment while VDEs do not. Large differences between VDEs and ADEs indicate significant structural changes upon electron detachment.

E. Cluster Reorganization upon Electron Detachment

In Fig. 5.5 we present neutral $[Mg,nH_2O]$ cluster structures **N1a**(MP2) – **N11a**(MP2) as obtained from full geometry optimizations that started from the "most stable" $[Mg,nH_2O]^-$ isomers (cf. Fig. 5.2). By comparison of the structures in both figures it becomes apparent that the neutral clusters do not contain any O-H bonds of adjacent H_2O molecules that point at each other. This trivial change is due to the absence of the prior excess electron. It has, however, strong implications on the structure of the $[Mg,nH_2O]$ species. Detachment eventually leads to a significant reorientation of the cluster structure.

The reorganization energy E_{reorg} is the energy that is released when a cluster adjusts to its new charge state during the detachment process. By convention, E_{reorg} is typically assigned a positive value and is thus calculated as:

$$E_{reorg} = \mathrm{VDE} - \mathrm{ADE} \qquad (5.1)$$

In Fig. 5.6 we show our computed E_{reorg} data (MP2/TZVPPa ($n \leq 7$) and MP2/TZVPa ($n \geq 8$)). Overall we find a linear increase according to:

$$E_{reorg} = 10.6\ n \qquad (5.2)$$

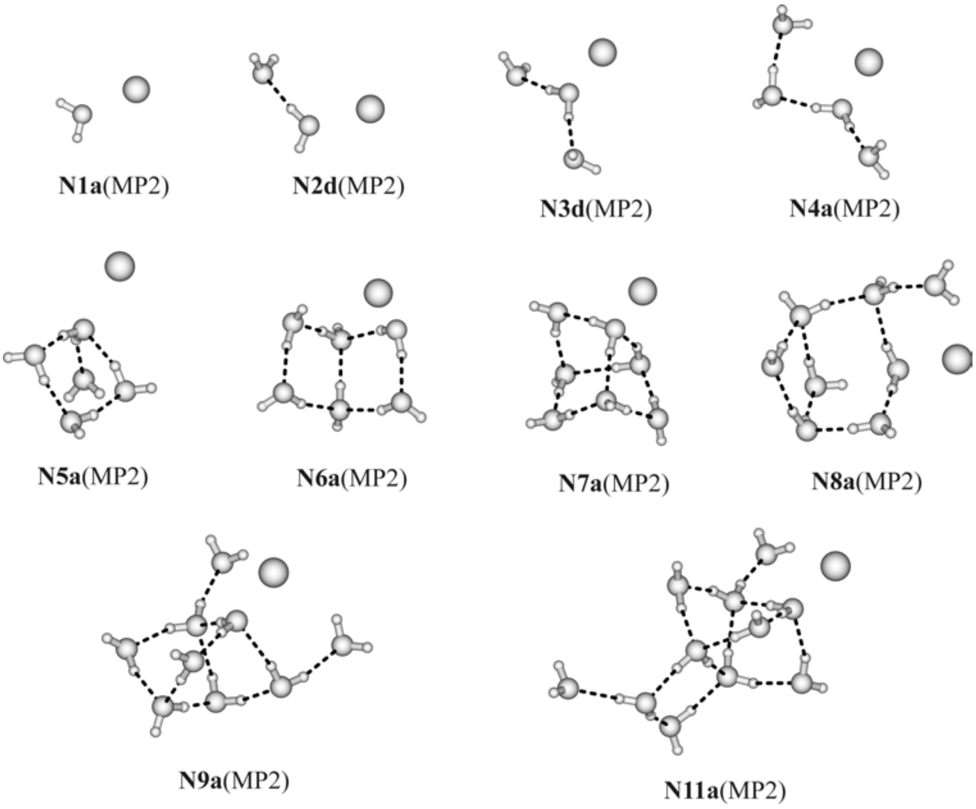

N1a(MP2) **N2d**(MP2) **N3d**(MP2) **N4a**(MP2)

N5a(MP2) **N6a**(MP2) **N7a**(MP2) **N8a**(MP2)

N9a(MP2) **N11a**(MP2)

Fig. 5.5 MP2 optimized neutral [Mg,nH_2O], n=1-11, cluster structures.

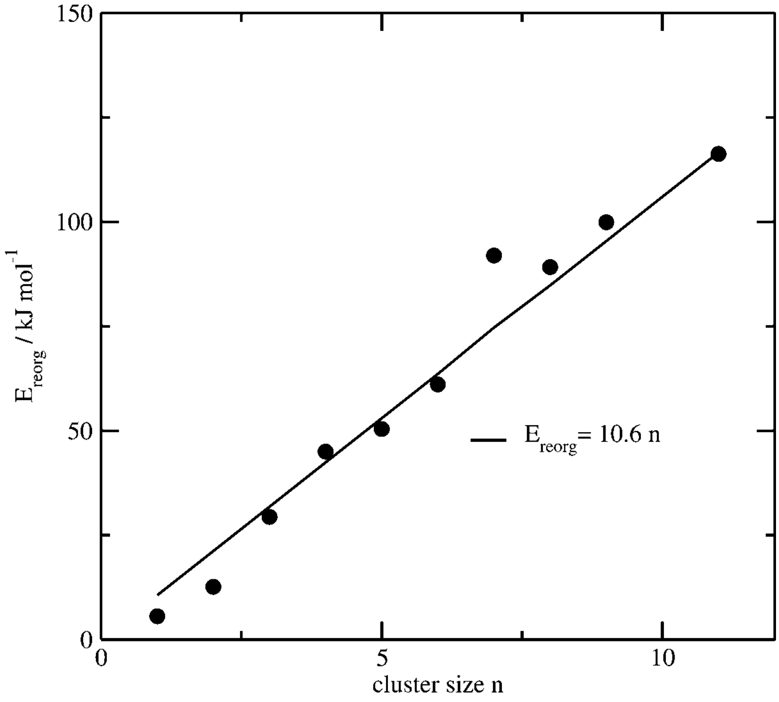

Fig. 5.6 Reorganization energies E_{reorg} as function of cluster size n.

E_{reorg} remains significantly below 20 kJ mol^{-1} at n=1 and n=2. Anionic and neutral cluster geometries of **1a**(MP2) and **N1a**(MP2) as well as of **2d**(MP2) and **N2d**(MP2) are very similar. At n=3 this changes. 3d is the smallest $Mg(H_2O)_n^-$ cluster with a tweezer structure. Upon electron detachment the two H_2O molecules involved start to repell each other. This makes the O···O···O angle enlarge from 83.3° in **3d**(MP2) to 119.7° in **N3d**(MP2). Accordingly, E_{reorg} goes up to about 30 kJ mol^{-1}.

The [Mg,nH_2O] clusters are most appropriately described as neutral $(H_2O)_n$ clusters that have a Mg atom attached to its surface: $Mg(H_2O)_n$. The bond between $(H_2O)_n$ and Mg arises mainly from electrostatic induction between polar H_2O and polarizable Mg. Moreover some optimized neutral cluster structures contain HO-H···Mg contacts (cf. Fig. 5.5). These are due to attractive interactions between the Mg 3s^2 valence electrons and the partially positive charged $H^{\delta+}$ atoms of H_2O molecules at favorable location. The total number of donor-acceptor (HO-H···OH_2) hydrogen bonds is larger in the neutral $(H_2O)_n$ sub-cluster within $Mg(H_2O)_n$ than in the anionic $(H_2O)_n^-$ sub-cluster within $Mg(H_2O)_n^-$. The negative cluster structures are distorted by the excess electron. The high E_{reorg} energies of larger $Mg(H_2O)_n^-$ clusters are mainly due to the formation of new donor-acceptor hydrogen bonds in $Mg(H_2O)_n$. O-H bonds that were involved in the localization of the excess electron in $Mg(H_2O)_n^-$ become dangling in $Mg(H_2O)_n$ ready to involve in hydrogen bonding. With growing cluster size the H_2O networks in $Mg(H_2O)_n^-$ clusters become more floppy and the number of H_2O molecules involved in the electron localization increases. Consequently the reorganization energy upon electron detachment E_{reorg} increases. For n=11 E_{reorg} has increased as high as 116 kJ mol^{-1}.

F. Possible Decay Pathways of [Mg,nH_2O]$^-$

For all cluster sizes n≥2 hydrated magnesium cluster anions consist of a hydrated electron sub-cluster $(H_2O)_n^-$ and a magnesium atom attached to it. The stability of the hydrated electron $(H_2O)_n^-$ was subject of a recent BIRD study.[23] Thermal detachment of the electron was observed to compete with fragmentation for cluster sizes $(H_2O)_n^-$, n<27. This proved that the hydrated electron couples to the vibrational modes of the water cluster. The VDE of $(H_2O)_n^-$, n=27, is 134 kJ mol^{-1}.[11] This value is very similar to the predicted VDE of $Mg(H_2O)_n^-$, n=11, (cf. Fig. 5.4). The computed ADE of $Mg(H_2O)_n^-$, n=11, is of the order of 20 kJ mol^{-1} and can surely be activated by absorption of infrared photons of the thermal background radiation. Therefore it is most probable that hydrated magnesium water cluster anions $Mg(H_2O)_n^-$, n≤11, will not only decay by fragmentation but also by thermal electron detachment, as observed for "pure" $(H_2O)_n^-$ clusters when radiated at 300 K.

In addition it cannot be excluded that reactive decay pathways compete with nonreactive decay pathways (fragmentation, electron autodetachment) in $Mg(H_2O)_n^-$. Reactive decay was observed before for the cationic species $[Mg,nH_2O]^+$ and $[Al,nH_2O]^+$. A priori the following three reactive decay pathways **dp1** – **dp3** are conceivable for gas-phase $[Mg,nH_2O]^-$ cluster anions:

dp1: $[Mg,nH_2O]^- \rightarrow [MgO,(n\text{-}1)H_2O]^- + H_2$

dp2: $[Mg,nH_2O]^- \rightarrow [HMg(OH),(n\text{-}1)H_2O]^-$

dp3: $[Mg,nH_2O]^- \rightarrow [Mg(OH)_2,(n\text{-}2)H_2O]^- + H_2$

All of them involve insertion of Mg into at least one O-H bond of the surrounding water ligands. In the following geometry optimized $Mg(H_2O)_n^-$ cluster structures were chosen as starting "educt" clusters. Energies and electronic structures of the different isomers of the potential product clusters of reaction **dp1** – **dp3** $[MgO,(n\text{-}1)(H_2O)]^-$, $[HMg(OH),(n\text{-}1)(H_2O)]^-$ and $[Mg(OH)_2,(n\text{-}2)(H_2O)]^-$ were investigated by ab initio calculations at the MP2/TZVPPa level of theory for cluster sizes n≤6 and MP2/TZVPa for cluster sizes n>6. In case of **dp1** we could locate minima corresponding to stable product cluster geometries $[MgO,(n\text{-}1)H_2O]^-$ only for cluster sizes n≤2. Larger cluster sizes were found to transform into the dihydroxide $[Mg(OH)_2,(n\text{-}2)H_2O]^-$ in the course of the optimization process. Geometric structures and SOMO shapes of the optimized $[MgO,(n\text{-}1)H_2O]^-$ clusters are shown in Fig. 5.7. For all investigated cluster sizes the SOMO is localized in a 3p orbital of the O ligand. The computed energetics (evaluated at 0 K), which refer to the energetically lowest $[Mg,nH_2O]^-$ isomer of each n, are also included in Fig. 5.7.

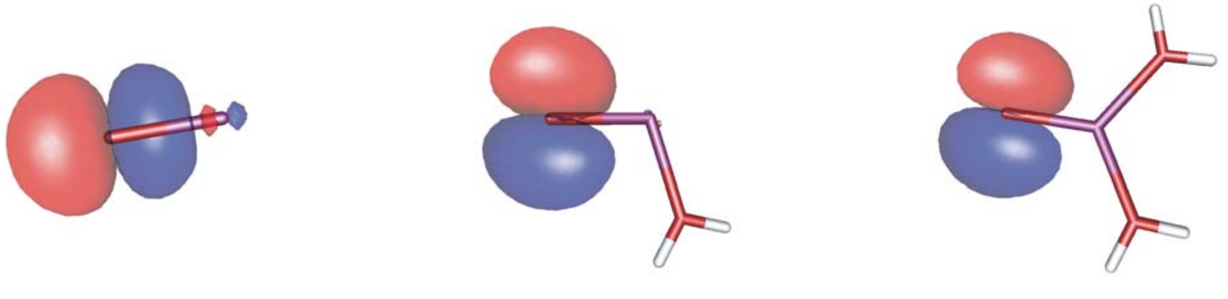

ΔH=+168.23 kJ mol^{-1} ΔH=+245.70 kJ mol^{-1} ΔH=+277.75 kJ mol^{-1}

Fig. 5.7 Structures and isosurface plots of the SOMO in $[MgO(H_2O)_{n-1}]^-$, n=1-3. The computed reaction enthalpies ΔH (0 K) for reaction **dp1** reveal that this process is strongly endothermic.

The computed energetics reveal that the **dp1** reaction is strongly endothermic and will therefore not be a potential decay channel for $Mg(H_2O)_n^-$. In order to evaluate the possibility of a spontaneous decay according to the reaction denominated as **dp2**, structures and energies of $[HMg(OH),(n-1)H_2O]^-$ clusters up to cluster size n=11 were investigated. An overview of all investigated cluster structures is presented in Fig. 5.8.

All of the optimized cluster structures in Fig. 5.8 contain a single H atom in close contact to the magnesium. For a reliable prediction of the most probable decay product of hydrated magnesium water cluster anions the binding energies of the Mg-H bond in $[HMg(OH),(n-1)H_2O]^-$ is highly relevant to evaluate whether O-H insertion according to **dp2** also leads to H elimination. Therefore Mg-H binding energies were calculated for selected cluster isomers. $[Mg(OH),(n-1)H_2O]^-$ start geometries for these calculations (level of theory: MP2/TZVPPa) were generated from $[HMg(OH),(n-1)H_2O]^-$ minimum cluster structures by removal of the H atom. In $[HMg(OH),(n-1)H_2O]^-$ isomers **dp2_2a**, respectively **dp2_2b** the H atom is bound to magnesium by ΔE=-126.67 kJ mol^{-1} respectively ΔE=-129.09 kJ mol^{-1}. According to our calculations the H eliminated species $[Mg(OH),1H_2O]^-$ has only a single minimum on the potential hypersuface (cf. **dp2** in Fig. 5.9). The strong attractive interaction between H and Mg persists in larger $[HMg(OH),(n-1)H_2O]^-$ clusters and for **dp2_6d** the computed Mg-H binding energy has increased to ΔE=-221.15 kJ mol^{-1}. Due to the strong Mg-H binding energies the H atom is expexted to remain bound to the Mg in the course of pathway **dp2** for all cluster sizes n.

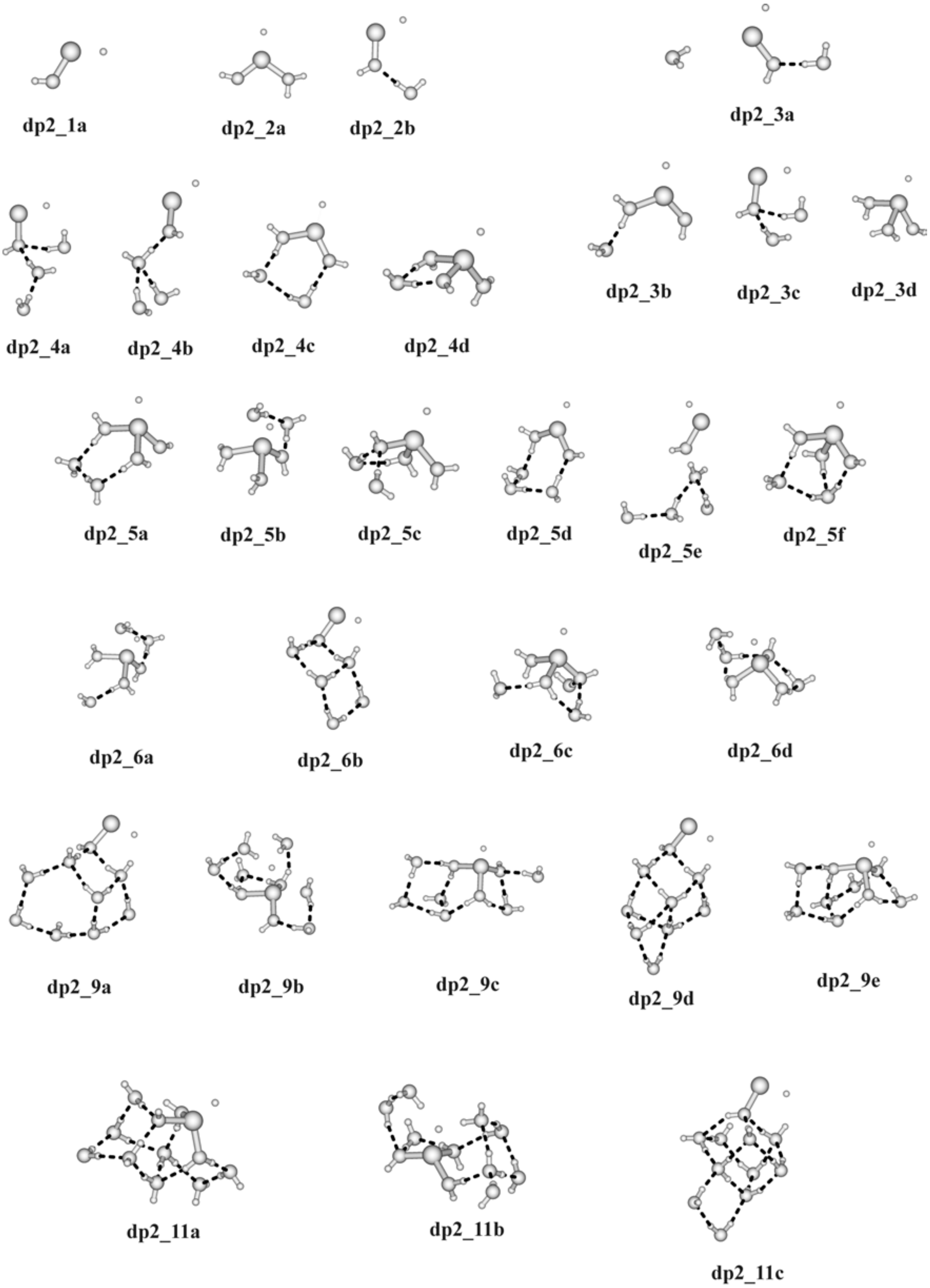

dp2_1a dp2_2a dp2_2b dp2_3a

dp2_4a dp2_4b dp2_4c dp2_4d dp2_3b dp2_3c dp2_3d

dp2_5a dp2_5b dp2_5c dp2_5d dp2_5e dp2_5f

dp2_6a dp2_6b dp2_6c dp2_6d

dp2_9a dp2_9b dp2_9c dp2_9d dp2_9e

dp2_11a dp2_11b dp2_11c

Fig. 5.8 MP2 optimized cluster structures $[HMg(OH),(n\text{-}1)H_2O]^-$, $n \leq 11$. For the structures on display calculations were performed with the TZVPPa basis for cluster sizes $n \leq 6$ and the TZVPa basis for $n > 6$.

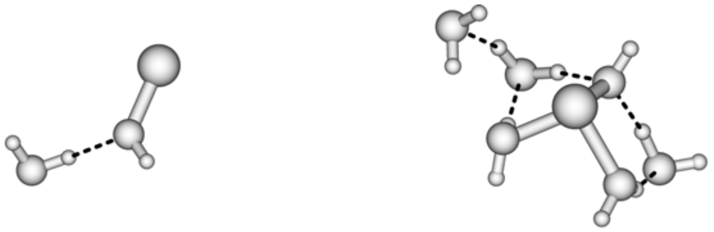

dp2_2
(reoptimized after H removal)

dp2_6d
(reoptimized after H removal)

Fig. 5.9 MP2/TZVPPa optimized **dp2_2** and **dp2_6d** cluster structures after removal of the H atom bound to Mg.

Table 5.5 Relative Energies ΔE between different isomers of $[HMg(OH),(n-1)H_2O)]^-$ product clusters for decay pathway **dp2** and vertical and adiabatic detachment energies (VDE resp. ADE) of selected clusters. All units are kJ mol^{-1}.

cluster size n	*structure*	*Mg coord. number*	*ΔE*	*VDE*	*ADE*
1	**dp2_1a**	2	0	+52.83	-11.37
2	**dp2_2a**	3	+0.58	+11.21	-23.55
	dp2_2b	2	0	+105.02	-22.97
3	**dp2_3a**	2	+49.00	+71.17	-3.43
	dp2_3b	3	+29.54	+30.37	-51.06
	dp2_3c	2	+18.34	+150.91	-39.81
	dp2_3d	4	0	+20.37	-16.28
4	**dp2_4a**	2	+42.90	+172.62	-58.55
	dp2_4b	2	+56.47	+157.78	+38.83
	dp2_4c	3	+46.19	+36.88	-40.20
	dp2_4d	4	0	+24.22	-15.65
5	**dp2_5a**	4	+23.37	+47.09	-38.30
	dp2_5b	4	+18.53	+38.64	-34.12
	dp2_5c	4	+9.72	+47.28	-34.24
	dp2_5d	3	+51.27	+13.51	-25.38
	dp2_5e	2	+72.42	+172.63	-89.88
	dp2_5f	4	0	+45.02	-29.62
6	**dp2_6a**	4	+12.39	+54.75	-27.71
	dp2_6b	2	+40.24	+225.09	+78.67
	dp2_6c	4	+0.88	+37.15	-21.65
	dp2_6d	4	0	+19.28	-19.68
9	**dp2_9a**	2	+83.22	---	---
	dp2_9b	4	+16.93	---	---
	dp2_9c	4	+20.64	+99.53	-3.51
	dp2_9d	2	+64.51	+266.50	-63.84
	dp2_9e	4	0	+50.28	-13.26
11	**dp2_11a**	4	0	+61.78	+9.74
	dp2_11b	4	+42.97	+73.27	-15.89
	dp2_11c	2	+62.95	+250.22	-112.44

In this respect O-H insertion in $[Mg,nH_2O]^-$ differs from what has been found for cationic $[Mg,nH_2O]^+$ clusters, in which formation of MgOH led to the loss of a H atom from the cluster. In the following we will focus on $[HMg(OH),(n-1)H_2O]^-$ as decay product of **dp2**. For cluster size n=2 twofold and threefold coordinated species are close in total energy, but the computed relative energies of the investigated cluster structures indicate that an overall fourfold coordination is energetically clearly favored in $[HMg(OH),(n-1)H_2O]^-$ for cluster sizes $n\geq3$ (cf. Table 5.5). The preferred coordination geometry is tetrahedral for $n\geq3$.

The coordination geometry of Mg has important impact on the computed electron binding energies. The VDEs of $[HMg(OH),(n-1)H_2O]^-$ clusters in Table 5.5 reveal significantly higher electron binding energies in clusters with a twofold coordinated Mg. The SOMOs of different clusters with two, three- and fourfold coordination of the Mg are on display in Fig. 5.10. While in **dp2_1a** and all other cluster structures with a twofold coordinated Mg, the SOMO is spatially confined to the Mg and H atom, in clusters with Mg coordination numbers larger than two, the SOMO has detached from the Mg into the hydration shell, where it resides at or between dangling O-H oscillators of surrounding water molecules. In $[HMg(OH),(n-1)H_2O]^-$, n=1, the SOMO is attached to a single H_2O molecule, whereas in clusters with n>2 the dangling O-H oscillators of adjacent water molecules form molecular tweezers and serve as electrophilic binding sites of the electron within the clusters (cf. structures **dp2_4c**, **dp2_4d**, **dp2_6d** in Fig. 5.10). The different SOMO shapes of twofold and higher coordinated Mg species together with their computed electron binding energies imply a covalent bound state of the excess electron in the twofold coordinated species and a diffuse bound state in the clusters with coordination numbers larger than two. Mulliken population analyses confirm different oxidation states of twofold and higher coordinated Mg. In Fig. 5.10 the Mulliken charges for **dp2_2a** (twofold coordinated Mg) and **dp2_2b** (threefold coordinated) Mg are contained. They show that in **dp2_2a** the excess charge is mainly located at the H atoms of the H_2O monomer attached to the Mg and its Mulliken charge indicates an oxidation state > +1. In contrast in **dp2_2_b** the Mulliken charge at the Mg is +0.28, revealing an almost neutral Mg atom. Only for some high energy isomers with twofold coordinated Mg like **dp2_4b** and **dp2_6b** positive ADEs were obtained. The ADEs of all $[HMgOH,(n-1)H_2O]^-$ minimum isomers are negative, which indicates that the $[HMgOH,(n-1)H_2O]^-$ clusters are instable against spontaneous thermal electron detachment.

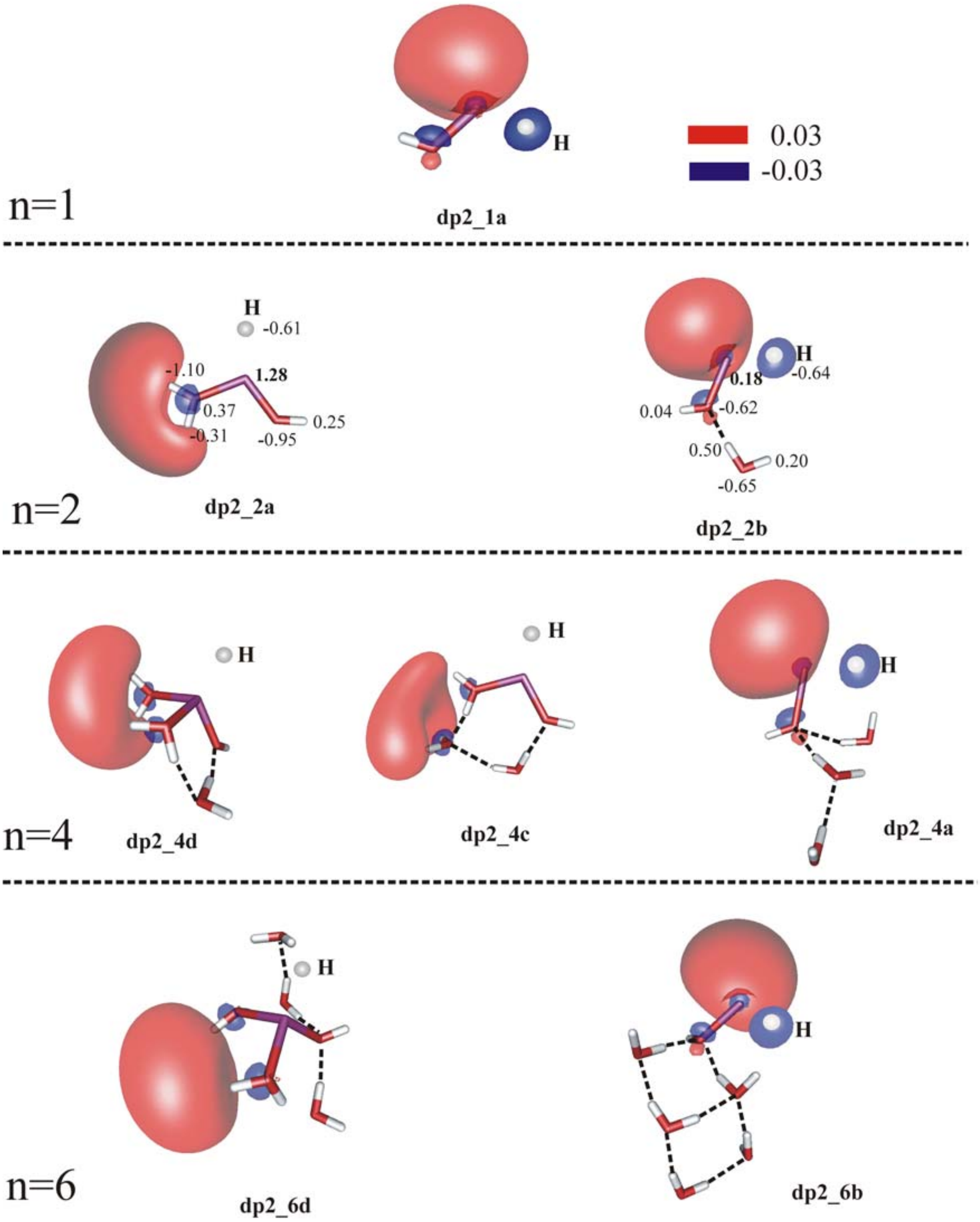

Fig. 5.10 Isosurface plots of the SOMOs of different $[HMg(OH),(n\text{-}1)H_2O]^-$ clusters. The SOMO shapes indicate a covalent bound excess electron for clusters with a coordination number of two and a diffuse bound excess electron for cluster exhibiting coordination numbers of three and four at the magnesium. Mulliken charges (in atomic units) included in structures **dp2_2a** and **dp2_2b** confirm mutual dependence of oxidation states and coordination geometry of Mg.

The product clusters of the remaining possible reactive decay pathway **dp3** are on display in Fig. 5.11. Relative energies of the computed clusters together with coordination number of the central Mg atom as well as VDEs and ADEs of these clusters are listed in Table 5.6.

H_2 is initially formed within the cluster after dual O-H insertion by Mg and was included in preliminary calculations. However, the H_2 molecule is only weakly bound to the Mg atom. For instance in case of cluster **dp3_3a** the Mg-H_2 binding energy was calculated to be -7.72 kJ mol^{-1} (level of theory: MP2/TZVPPa) and it is most probable that the H_2 will be evaporated in the course of the decay process. Hence the data in Table 5.6 and structures in Fig. 5.11 refer to reoptimized cluster geometries with the H_2 molecule assumed at infinite distance.

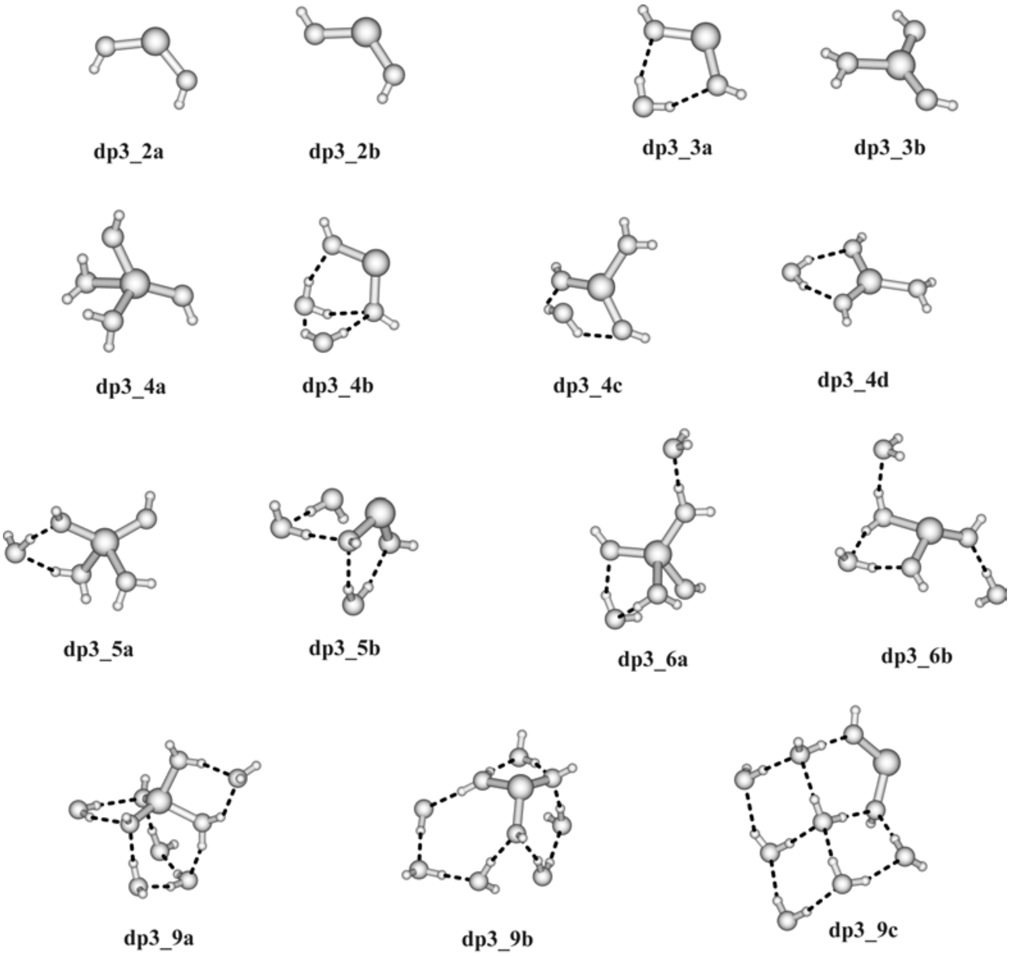
dp3_2a dp3_2b dp3_3a dp3_3b

dp3_4a dp3_4b dp3_4c dp3_4d

dp3_5a dp3_5b dp3_6a dp3_6b

dp3_9a dp3_9b dp3_9c

Fig. 5.11 MP2 optimized cluster structures $[Mg(OH)_2,(n-2)H_2O]^-$, n≤11. For the structures on display calculations were performed with the TZVPPa basis for cluster sizes n≤6 and the TZVPa basis for n>6.

Table 5.6 Relative energies ΔE between different isomers of $[Mg(OH)_2,(n\text{-}2)H_2O]^-$ product clusters for decay pathway **dp3** and vertical and adiabatic detachment energies (VDE resp. ADE) of selected clusters. All units are kJ mol^{-1}.

cluster size n	*structure*	*Mg coord. number*	*ΔE*	*VDE*	*ADE*
2	**dp3_2a**	2	0	+89.78	+16.53
	dp3_2b	2	+4.73	+97.40	+11.71
3	**dp3_3a**	2	0	+142.60	+81.87
	dp3_3b	3	+12.81	+27.68	-9.53
4	**dp3_4a**	4	0	+31.72	-9.95
	dp3_4b	2	+0.89	+183.81	-13.98
	dp3_4c	3	+5.39	+29.50	-24.34
	dp3_4d	3	+11.49	+24.22	-15.65
5	**dp3_5a**	4	0	+17.64	-25.75
	dp3_5b	3	+2.60	+131.99	-30.27
6	**dp3_6a**	4	0	+39.90	-45.52
	dp3_6b	3	+14.54	+68.06	-23.50
9	**dp3_9a**	4	0	+70.34	-9.94
	dp3_9b	3	+17.25	+125.17	-41.14
	dp3_9c	2	+56.14	+278.15	-16.39

The computed VDEs of the investigated $[Mg(OH)_2,(n\text{-}2)H_2O]^-$ show some correlation with the coordination number of the central Mg atom as observed before for $[HMg(OH),(n\text{-}1)H_2O]^-$: Clusters with lower Mg coordination numbers have significantly higher VDEs. The SOMO shapes and the calculated large vertical electron binding energies indicate a valence bound state in all clusters with a twofold coordinated Mg like in **dp3_2a**, **dp3_2b**, **dp3_3a**, **dp3_4b**, and **dp3_9c**. In contrast in $[Mg(OH)_2(H_2O)_{n-2}]^-$ clusters with a threefold coordinated Mg both valence bound states (**dp3_5b**, **dp3_6b**, and **dp3_9b**) and diffuse hydrated electrons (**dp3_3b**, **dp3_4c**, and **dp3_4d**) can be found. The first shell H_2O and OH ligands of **dp3_3b**, **dp3_4c**, and **dp3_4d** lie in plane with the Mg atom. The appearance of the hydrated electron in $[Mg(OH)_2,(n\text{-}2)H_2O]^-$ clusters with a threefold coordinated Mg is limited to those structures which contain all three ligands and the Mg atom in a single plane. In cluster structures with Mg coordination number larger than three the excess electron was exclusively found within the hydration shell. The existence of different electronic states in the investigated clusters is confirmed by the charge distributions within the clusters. As illustrated by the Mulliken charges enclosed for **dp3_3a** and **dp3_3b** in Fig. 5.12 the computed charge distribution implies an oxidation state < +1 for the twofold coordinated Mg opposed to an oxidation state > +1 for the threefold coordinated Mg. In the latter the SOMO has detached from the Mg and resides in the hydration shell.

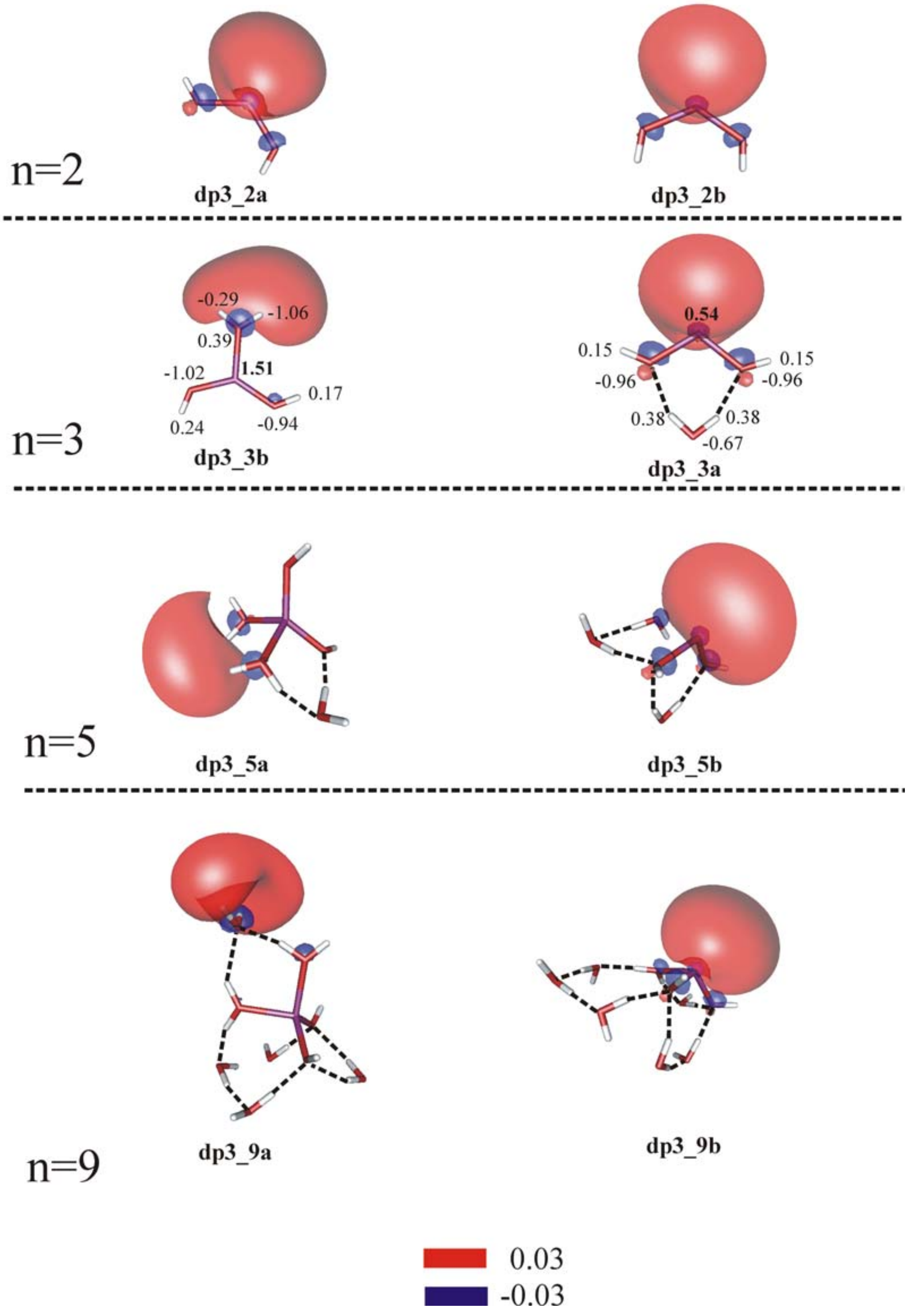

Fig. 5.12 Isosurface plots of the SOMOs of different $[Mg(OH)_2,(n\text{-}2)H_2O]^-$ clusters. The SOMO is located at Mg in clusters with a coordination number of two at the Mg and a diffuse bound excess electron for cluster exhibiting coordination numbers of three and four at Mg. Once more Mulliken charges (in atomic units) for **dp3_3a** and **dp3_3b** confirm the mutual relation of oxidation state and coordination geometry.

For cluster sizes n=2 and n=3 those cluster structures which contain the SOMO located at the Mg are energetically favored. These are the only $[Mg(OH)_2(H_2O)_{n-2}]^-$ clusters, for which the computed ADEs are positive. With growing cluster size structures with a fourfold coordinated Mg containing a weakly bound diffuse hydrated electron become energetically favored.

The geometric and electronic structures of possible products of a reactive decay of $[Mg,nH_2O]^-$ clusters have been presented. In case of **dp1** the reactive decay pathway was determined to be strongly endothermic. The energetics of **dp2** and **dp3**, however, are still an open issue. In the following we refer to the total energy of the lowest $[Mg,nH_2O]^-$ isomer as reference energy for one cluster size n.

The computed reaction enthalpies $\Delta_R H^{0K}$ for **dp2** and **dp3** (Fig. 5.13) range from -125 kJ mol^{-1} for $[HMg(OH),H_2O]^{-1}$ to -300 kJ mol^{-1} for $[Mg(OH)_2,7H_2O]^{-1}$. As $\Delta_R H^{0K}$ of **dp2** and **dp3** become more negative with cluster size the O-H insertion reaction become more and more exothermic. However, there is a spike in $\Delta_R H^{0K}$ (**dp2**) at n=2. This significant increase of $\Delta_R H^{0K}$ (**dp2**) between n=1,2 is correlated with a change of the electronic structure in $[Mg,nH_2O]^-$. While for n=1 the electronic structure was found to be $Mg^-(H_2O)$, in n=2 the electron has detached from Mg and is located within the water cluster: $Mg(H_2O)_2^-$. Due to an increase of electron binding energy, which is connected with the transfer from the excess electron from Mg to the water sub-cluster $(H_2O)_2$, the O-H insertion becomes less exothermic for $Mg(H_2O)_2^-$. For all investigated cluster sizes the $\Delta_R H^{0K}$ values for reaction channel **dp3** are significantly more negative than for **dp2**. The difference in $\Delta_R H^{0K}$ between **dp2** and **dp3** overall increases with cluster size n. For instance the difference $\Delta_R H^{0K}$ (**dp2**) – $\Delta_R H^{0K}$ (**dp3**) is 23.33 kJ mol^{-1} for n=2 but it increases to 77.99 kJ mol^{-1} for n=9. The reaction enthalpies $\Delta_R H^{0K}$ (0 K) for decay pathways **dp2** and **dp3** are <<0, which indicates strongly exothermic reactions. The activation energy for process **dp2** was determined for the formation of H-Mg-OH in $Mg(H_2O)_2^-$ by calculating the total energy along the reaction coordinate. The O-H distance was parametrically variied while all other coordinates were freely optimized. The activation barrier for Mg insertion into the O-H bond was found to be approximately 93 kJ mol^{-1} in $Mg(H_2O)_2^-$ (cf. Fig. 5.14).

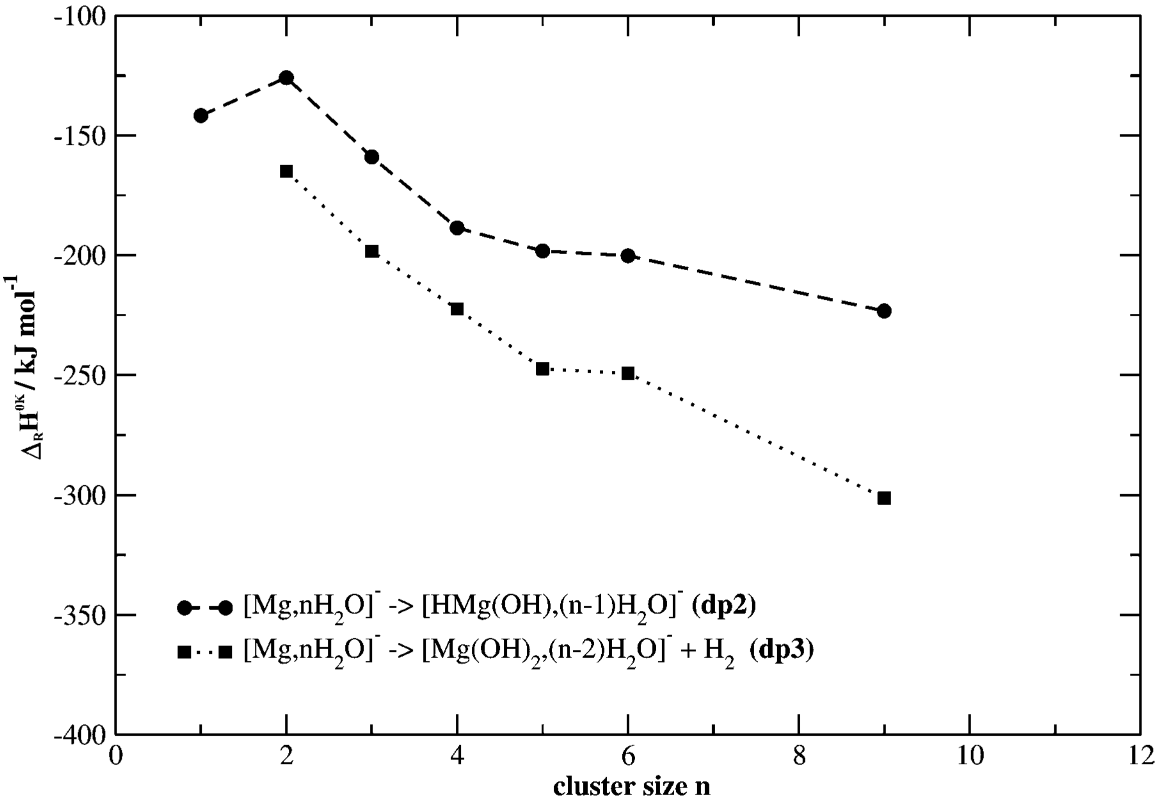

Fig. 5.13 Reaction Enthalpies (0 K) $\Delta_R H^{0K}$ for the reactive decay pathways **dp2** and **dp3**.

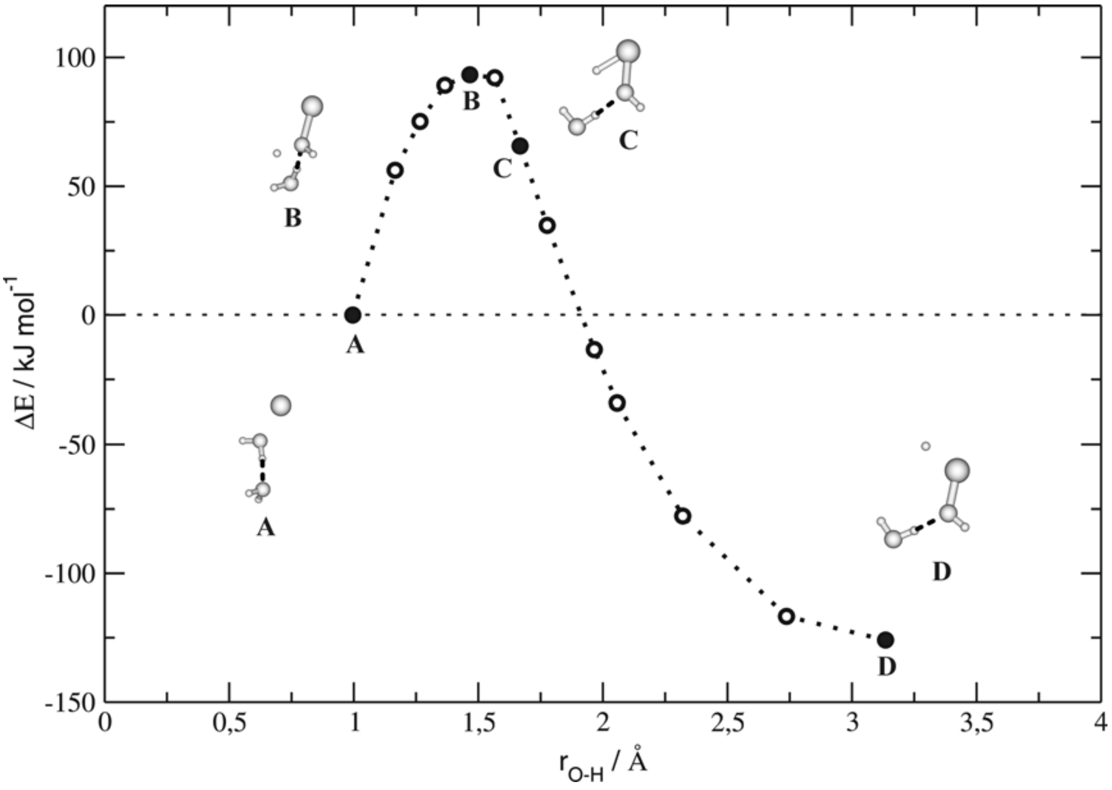

Fig. 5.14 Energy along the reaction coordinate for the insertion of Mg into OH in $Mg(H_2O)_2^-$

This barrier is expected to decrease with growing cluster size due to solvation effects and the reactive decay channel will be accessible by thermal activation (absorbtion from blackbody background radiation) in larger clusters. The activation barrier for **dp3** is estimated to be appproximately twice the barrier of **dp2**, due to the fact that two O-H bonds have to be broken. Assuming simple Arrhenius kinetics **dp3** is therefore not expected to compete with **dp2**. The main reactive decay pathway of $[Mg,nH_2O]^-$ clusters in prospective future experiments is predicted to be single O-H insertion by Mg.

For all $[Mg(OH)_2,(n-2)H_2O]^-$ clusters with n>4 as well for the energetically lowest isomers of $[HMg(OH),(n-1)H_2O]^-$, n=1-10, the computed ADEs are negative. Only for $[HMg(OH),(n-1)H_2O]^-$, n=11, the energetically lowest isomer has a slightly positive ADE of +9.74 kJ mol^{-1}. Hence potential products of the decay reactions **dp2** and **dp3** are expected to be instable against spontaneous thermal electron detachment just like $[Mg,nH_2O]^-$. Spontaneous thermal electron detachment is predicted to occur in educt and product clusters $[Mg,nH_2O]^-$, $[HMgOH,(n-1)H_2O]^-$ (and $[Mg(OH)_2,(n-2)H_2O]^-$). With growing cluster size thermal electron detachment will lose importance as possible decay channel due to the increasing electron affinity of the water sub-cluster. This was observed before for $(H_2O)_n^-$ clusters, where electron detachment was only verified for cluster sizes n≤27. This has important implications for any experimental investigation of anionic water clusters doped with a magnesium atom, as only large clusters with 20 or more water molecules may form. In preliminary experiments Bowen and coworkers produced complex anionic magnesium hydroxide and oxide species (Mg_2OH^-; $Mg_2O(H_2O)n$, n>2; $MgOH(H_2O)^-$) by laser vaporizations, but they could not detect $[Mg,nH_2O]^-$ or products of a reactive decay according to **dp2** or **dp3** in clusters with up to ten water molecules. However, according to our calculations $[Mg,nH_2O]^-$ clusters are stable only for significantly larger cluster sizes.

5.4 Conclusions

Structures and stabilities of hydrated magnesium water cluster anions with the formal stoichiometry $[Mg,nH_2O]^-$, n=1-11, were investigated by application of various correlated ab initio methods (MP2, CCSD, CCSD(T)). While $[Mg,nH_2O]^-$, n=1, exhibits an electronic structure that is best described as $Mg^-(H_2O)$, the “most stable” isomers of n≥2 have the excess electron detached from the Mg^- anion. These clusters contain a Mg atom that is attached to a anionic water sub-cluster $(H_2O)_n^-$, and they are characterized as $Mg(H_2O)_n^-$. The computed vertical detachment energies VDEs become positive for $Mg(H_2O)_n^-$, n≥2, and increase gradually with cluster size. The computed ADEs, which are the negatives of adiabatic electron affinities, become positive through the formation of molecular tweezer structures HO-H···e^-···H-OH in $Mg(H_2O)_n^-$ at n=3. We found strong evidence that ADEs remain positive at all $Mg(H_2O)_n^-$ cluster sizes with n≥3, but the increase with cluster size n is much less pronounced than for the VDEs. This indicates strong structural changes upon electron detachment. The extent of cluster reorganization was quantified by calculating reorganization energies E_{reorg}, which were found to increase linearly with cluster size.

Possible reactive decay pathways of $[Mg,nH_2O]^-$ were investigated and it was found that O-H insertion yielding $[HMgOH,(n-1)H_2O]^-$ respectively $[Mg(OH)_2,(n-2)H_2O]^-$ (dual O-H insertion) is highly exothermic. Due to a lower activation barrier the decay process involving a single O-H insertion is proposed as most probable reactive decay pathway of $[Mg,nH_2O]^-$. SOMOs and electron binding energies imply the excess electron to be covalently bound in small product clusters, like for instance in $[HMgOH,(n-1)H_2O]^-$ (n=1-2) and $[Mg(OH)_2,(n-2)H_2O]^-$ (n=2-3). Larger clusters contain the excess electron solvated by surrounding water molecules located in the hydration sphere like observed for $[Mg,nH_2O]^-$ clusters with n>1.

5.5 References

1 P. Kebarle, *J. Mass Spectrom.* 1997, **32**, 922.

2 A. W. Castleman, *Advances in Gas Phase Ion Chemistry* 1998, **3**, 185.

3 G. Niedner-Schatteburg and V. E. Bondybey, *Chem. Rev.* 2000, **100**, 4059.

4 A. J. Stace, *Phys. Chem. Chem. Phys.* 2001, **3**, 1935.

5 V. E. Bondybey and M. K. Beyer, *International Reviews in Physical Chemistry* 2002, **21**, 277.

6 Most research on this field has been performed by high pressure mass spectrometry (HPMS), see e.g. T. B. McMahon, *Nato Science Series, Series C: Mathematical and Physical Sciences* (1999), 535 (Energetics of Stable Molecules and Reactive Intermediates), pp. 259-280.

7 R. Laenen, T. Roth and A. Laubereau, *Phy. Rev. Lett.* 2000, **85**, 50.

8 M. Assel, R. Laenen and A. Laubereau, *Chem. Phys. Lett.* 2000, **317**, 13.

9 R. Laenen, M. Assel and A. Laubereau, *Bulletin of the Polish Academy of Sciences, Chemistry* 1999, **47**, 283.

10 M. Assel, R. Laenen and A. Laubereau, *J. Phys. Chem. A* 1998, **102**, 2256.

11 J. V. Coe, G. H. Lee, J. G. Eaton, S. T. Arnold, H. W. Sarkas, K. H. Bowen, C. Ludewigt, H. Haberland and D. R. Worsnop, *J. Chem. Phys.* 1990, **92**, 3980.

12 H. Haberland and K. H. Bowen in *Clusters of Atoms and Molecules*, edited by H. Haberland, Springer-Verlag, Berlin, 1994.

13 C. G. Bailey, J. Kim, and M. A. Johnson*, J. Phys. Chem.* 1996, **100**, 16782.

14 P. Ayotte and M. A. Johnson, *J. Chem. Phys.* 1997, **106**, 811.

15 C. G. Bailey and M. A. Johnson, *Chem. Phys. Lett.* 1997, **265**, 185.

16 J. V. Coe, A. D. Earhart, M. D. Cohen, G. J. Hoffman, H. W. Sarkas and K. H. Bowen, *J. Chem. Phys.* 1997, **107**, 6023.

17 P. Ayotte, C. G. Bailey, J. Kim and M. A. Johnson, *J. Chem. Phys.* 1998, **108**, 444.

18 J. Kim, I. Becker, O. Chesnovsky and M. A. Johnson, *Chem. Phys. Lett.* 1998, **297**, 90.

19 P. Ayotte, G. H. Weddle, C. G. Bailey, M. A. Johnson, F. Vila and K. D. Jordan, *J. Chem. Phys.* 1999, **110**, 6268.

20 C. E. H. Dessent, M. A. Johnson, I. Becker and O. Chesnovsky, *Adv. Chem. Phys.* 1999, **106**, 265.

21 S. T. Arnold, R. A. Morris and A. A. Viggiano, *J. Chem. Phys.* 1995, **103**, 9242.

22 S. T. Arnold, R. A. Morris, A. A. Viggiano and M. A. Johnson, *J. Phys. Chem.* 1996, **100**, 2900.

23 M. K. Beyer, B. S. Fox, B. M. Reinhard and V. E. Bondybey, *J. Chem. Phys.* 2001, **115**, 9288.

24 U. Landman, R. Barnett, C. L. Cleveland, D. Scharf and J. Jortner, *J. Phys. Chem.* 1987, **91**, 4890.

25 R. N. Barnett, U. Landman, C. L. Cleveland and J. Jortner, *J. Chem. Phys.* 1988, **88**, 4429.

26 R. N. Barnett, U. Landmann, G. Makov and A. Nitzan, *J. Chem. Phys*. 1990, **93**, 6226.

27 K. S. Kim, I. Park, S. Lee, K. Cho, J. Y. Lee, K. Kim and J. D. Joannopoulos, *Phys. Rev. Lett.* 1996, **76**, 956.

28 J. Kim, J. Y. Lee, K. S. Oh, J. M. Park, S. Lee and K. S. Kim, *Phys. Rev. A* 1999, **59**, R930.

29 J. Kim, S. B. Suh and K. S. Kim, *J. Chem. Phys.* 1999, **111**, 10077.

30 S. Lee, J. Kim, S. J. Lee and K. S. Kim, *Phys. Rev. Lett.* 1997, **79**, 2038.

31 S. B. Suh, H. M. Lee J. Kim, J. Y. Lee and K. S. Kim, *J. Chem. Phys.* 2000, **113**, 5273.

32 J. Kim, J. M. Park, K. S. Oh, J. Y. Lee, S. Lee and K. S. Kim, *J. Chem. Phys.* 1997, **106**, 10207.

33 H. M. Lee, K. S. Kim, *J. Chem. Phys.* 2002, **117**, 706.

34 F. Weigend and R. Ahlrichs, *Phys. Chem. Chem. Phys.* 1999, **1**, 4537.

35 D. M. A. Smith, J. Smets, and L. Adamowicz, *J. Chem. Phys.* 1999, **110**, 3804.

36 Y. V. Novaskovskaya and N. F. Stepanov, *J. Phys. Chem. A* 1999, **103**, 10975.

37 H.-Y. Chen and W.-S. Sheu, *J. Chem. Phys.* 1999, **110**, 9032.

38 D. C. Clary and D. M. Benoit, *J. Chem. Phys.* 1999, **111**, 10559.

39 S. A. Kulkarni, L. J. Bartolotti and R. K. Pathak *J. Chem. Phys*. **2000**, **113**, 2697.

40 Y. V. Novaskovskaya and N. F. Stepanov, *Chem. Phys. Lett.* 2001, **314**, 619.

41 A. L. Sobolewski and W. Domcke, *Phys. Chem. Chem. Phys.* 2002, **4**, 4.

42 A. L. Sobolewski and W. Domcke, *J. Phys. Chem. A* 2002, **106**, 4158.

43 A. L. Sobolewski and W. Domcke, *Phys. Chem. Chem. Phys.* 2003, **5**, 1130.

44 A. Khan, *J. Chem. Phys.* 2003, **118**, 1684.

45 F. Misaizu, K. Tsukamoto, M. Sanekata and K. Fuke, *Surface Review and Letters* 1996, **3**, 405.

46 R. Takasu, F. Misaizu, K. Hashimoto and K. Fuke, *J. Phys. Chem. A* 1997, **101**, 3078.

47 K. Hashimoto, T. Kamimoto and K. Fuke, *Chem. Phys. Lett*. 1997, **266**, 7.

48 K. Hashimoto, T. Kamimoto and K. Daigoku, *J. Phys. Chem A* 2000, **104**, 3299.

49 B. M. Reinhard and G. Niedner-Schatteburg, *Phys. Chem. Chem. Phys*. 2002, **4**, 1471.

50 B. M. Reinhard and G. Niedner-Schatteburg, *J. Chem. Phys*. 2003, **118**, 3571.

51 B. M. Reinhard and G. Niedner-Schatteburg, *J. Phys. Chem. A* 2002, **106**, 7988.

52 A. D. Becke, *Phys. Rev. A* 1988, **38**, 3098.

53 C. Lee, W. Yang and R. G. Parr, *Phys. Rev. B* 1988, **37**, 785.

54 A. Schäfer, C. Huber and R. Ahlrichs, *J. Chem. Phys.* 1994, **100**, 5829.

55 R. Ahlrichs, M. Bär, M. Häser, H. Horn and C. Kölmel, *Chem. Phys. Letters* 1989, **162**, 165.

56 O. Treutler and R. Ahlrichs, *J. Chem. Phys.* 1995, **102**, 346.

57 K. Eichkorn, O. Treutler, H. Ohm, M. Häser and R. Ahlrichs, *Chem. Phys. Lett.* 1995, **242**, 652.

58 K. Eichkorn, F. Weigend, O. Treutler and R. Ahlrichs, *Theor. Chem. Acc.* 1997, **97**, 119.

59 F. Weigend and M. Häser, *Theor. Chem. Acc.* 1997, **97**, 331.

60 F. Weigend, M. Häser, H. Patzelt and R. Ahlrichs, *Chem. Phys. Lett.* 1998, **294**, 143.

61 T. H. Dunning, *J. Chem. Phys.* 1989, **90**, 1007.

62 H.-J. Werner and P. J. Knowles, *J. Chem. Phys.* 1985, **82**, 5053.

63 P. J. Knowles and H.-J. Werner, *Chem. Phys. Lett.* 1985, **115**, 259.

64 Molpro, a package of ab initio programs designed by H.-J. Werner and P. J. Knowles, version 2002.1, R. D. Amos, A. Bernhardsson, A. Berning, P. Celani, D. L. Cooper, M. J. O. Deegan, A. J. Dobbyn, F. Eckert, C. Hampel, G. Hetzer, P. J. Knowles, T. Korona, R. Lindh, A. W. Lloyd, S. J. McNicholas, F. R. Mamby, W. Meyer, M. E. Mura, A. Nicklass, P. Palmieri, R. Pitzer, G. Rauhut, M. Schütz, U. Schumann, H. Stoll, A. J. Stone, R. Tarroni, T. Thorsteinsson and H.-J. Werner.

65 C. Hampel, K. Peterson, and H.-J. Werner, *Chem. Phys. Lett.* 1992, **190**, 1.

66 P. J. Knowles, C. Hampel and H.-J. Werner, *J. Chem. Phys.* 1993, **99**, 5219.

67 P. J. Knowles, C. Hampel and H.-J. Werner, *J. Chem. Phys.* 2000, **112**, 3106.

68 J. D. Watts, J. Gauss, and R. J. Bartlett, *J. Chem. Phys.* 1993, **98**, 8718.

69 W. Koch and M. C. Holthausen, *A Chemist's guide to Density Functional Theory* (Wiley-VCH, Weinheim, 2000), pp. 85-87.

70 N. Rösch and S. B. Trickey, *J. Chem. Phys.* 1997, **106**, 8940.

71 T. Tsurusawa and S. Iwata, *J. Phys. Chem. A* 1999, **103**, 6134.

72 T. Tsurusawa and S. Iwata, *J. Chem. Phys.* 2000, **112**, 5705.

73 S. Iwata and T. Tsurusawa, in *Advances in Metal and Semiconductor Clusters Volume* 5, ed. M.A. Duncan (Elsevier, Amsterdam, 2001), pp. 39-75.

74 S. F. Boys and F. Bernardi, *Mol. Phys.* 1970, **19**, 553.

75 C. Berg, U. Achatz, M. Beyer, S. Joos, G. Albert, T. Schindler, G. Niedner-Schatteburg and V. E. Bondybey, *Int. J. Mass Spectrom. Ion Processes* 1997, **167/168**, 723.

76 C. Berg, M. Beyer, U. Achatz, S. Joos, G. Niedner-Schatteburg and V. E. Bondybey, *Chem. Phys.* 1998, **239**, 379.

77 M. Beyer, C. Berg, H. W. Görlitzer, T. Schindler, U. Achatz, G. Albert, G. Niedner-Schatteburg and V. E. Bondybey, *J. Am. Chem. Soc.* 1996, **118**, 7386.

78 Kit H. Bowen, Johns Hopkins Univerity USA, Personal Communication, 2003.

6. Complexation of Metal Ions by Oligopeptides in the Presence of Water: Structure and Stability of Hydrated Zn^{II}/Carnosine Complexes

6.1 Introduction

L-Carnosine (β-alanyl-L-histidine) is a naturally occuring dipeptide discovered by Gulewitsch and Amiradzibi[1] at the beginning of the 20th century. The compound is present in the muscle and brain tissues of humans and other vertebrates in high concentrations,[2,3] and it is the major β-alanine source in the human body.[4] Although its physiological role is not yet fully established, carnosine and related dipeptides have been considered to have numerous biological roles as including pH buffering, regulation of enzyme activity, and inibition of oxidative reactions. Among antioxidant mechanisms reported for carnosine are its ability to inactivate reactive oxygen species, scavange free radicals and chelate prooxidative metal ions.[3,5-8] It was also postulated that carnosine interacts with aldehyde lipid oxidation products through Schiff base or Michael addition-type reactions.[3,9-10] This could help to protect biological tissues from oxidation as aldehydes are known to form adducts with DNA, proteins, enzymes, and lipoproteins resulting in changes of their biological activity. Although recent research indicates that the ability of carnosine to form adducts with aldehydic lipid oxidation products is lower than e.g. for glutathione, the higher concentrations of carnosine especially in skeletal muscle are likely to make it the most important molecule that forms aldehyde adducts.[11] Altogether, carnosine is a highly multifunctional antioxidant species, that not only inactivates free radicals but also chelates prooxidative metal ions and conjugates with toxic aldhehydic lipid oxidation products.

Zn^{II} ions are also known to possess some antioxidant effect. They decrease the susceptibility of specific sulfhydryl groups to oxidation and they compete with prooxidant metal ions, like Fe^{II} and Cu^{I}, for binding sites. Because both Zn^{II} and carnosine possess antioxidant properties, it could be expected that some synergy would arise from zinc-carnosine chelate compounds. In fact synergic interaction of carnosine and Zn^{II} ions have been reported for the treatment of human gastric ulcers.[12,13] A Zn^{II}/carnosine complex (polyprezin, Z-103) was shown to exert an antioxidant property in a tube experiment, to protect gastric mucosa from experimental ulceration in vivo, and to accelerate the healing of gastric ulcers in humans. In addition β-Alanyl-L-histidinato zinc (AHZ), in which the Zn^{II} ion is chelated to carnosine has proven high potential as pharmacological tool in osteoporosis.[14]

The zinc ions in AHZ may accumulate in bone cells because the metal ion binds to the hydroxyapatite of the bone tissue. However, the mechanism of the zinc uptake in the bones and the role of the reversibly bound chelate ligand carnosine is still unknown.

Given all the potential medical applications of carnosine based compounds, the nature of the molecular interactions of carnosine with metal ions, especially Zn^{II}, is significant. Thorough knowledge of the coordination mode of a simple histidine containing dipeptide like carnosine may moreover be expanded to the coordination abilities of peptide linkages in general and the specific role of N_π and N_τ donor atoms in the binding.

The conformation of carnosine in aqueous solution at pH=7 has been investigated by ^1H- and ^{13}C-NMR experiments. A "most probable" molecular conformation was reported in which the β-alanyl is folded towards the imidazole ring. The structure of solid carnosine is known from x-ray structure analysis.[15] The imidazole moiety exists in the N^3-H tautomeric form, whereas in most of its complexes the N^1-H tautomer is present.[4]

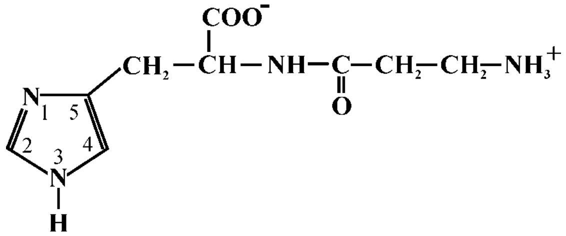

Fig. 6.1 Structural formular of the N^3-H tautomeric form of zwitterionic carnosine

For the Zn^{II}/carnosine complex the crystal structure has not been reported so far. Analyses of the solid by IR and NMR techniques suggest a polymeric structure.[16,17] Previous studies on Cu^{II}/carnosine species formed in aqueous solution obtained by UV-visible spectroscopy, potentiometry, ESR, NMR, visible and ultraviolett-circular dichroism agree in determining the dimeric complex $[(Carn\text{-}2H),Cu]_2$ as the most relevant specied formed in the case of copper.[4] In a recent ES-TOF-MS study it was found that in case of Zn^{II}/carnosine the monomer $[(Carn\text{-}H),Zn^{II}]^+$ complex is most abundant in solution.[18]

The intrinsic stability of biomolecules with charged functionalities is determined by the gas-phase acidities and basicities of these groups. Ionic species are further stabilized either by counterions that provide favorable electrostatic interactions or by solvation by polar species, especially water. The dipeptide carnosine has three groups that can undergo acid-basid reactions in a pH range from 1-10: the carboxylic acid group, an ammonium group and the protonated N^3 imidazole group. When deprotonated all of these groups act as binding sites for metal ions, hence carnosine is a polydentate ligand and different Zn^{II}/carnosine complex structures are feasible.

In this manuscript the structure and stability of carnosine, hydrogen-bonded carnosine oligomers and metal(II)/carnosine complexes will be investigated by using ES-ICR-MS, gas-phase H/D exchange techniques and ab initio calculations. The structural changes of carnosine upon Zn^{II} ion complexation and the effect of hydration on the Zn^{II}/carnosine complex structure are of special interest.

6.2 Experimental Details

Experiments were performed using a Bruker Daltonics ApexIII, actively shielded 7 T FT-ICR mass spectrometer, equipped with an external Apollo ES-API ion source. Carnosine samples were prepared by diluting 20 µl 0.04 M carnosine stock solution with 980 µL of a $CH_3OH/H_2O/CH_3COOH$ (49.5:49.5:1) respectively a $CH_3OH/D_2O/CHCOOH$ (49.5:49.5:1) mixture in case of liquid phase H/D exchange experiments. Zn^{II}/carnosine samples were obtained by diluting 100 µL of an equimolar ($7x10^{-4}$ M) $ZnCl_2$/carnosine stock solution with 900 µL of an CH_3OH/H_2O (3:6) mixture. Samples were introduced into the source at a flow rate of 2µL/min. The ionspray voltage was fixed at 4.4 kV and the orifice potential (declustering potential) was varied from 50-270 V. The electrosprayed ions were accumulated in a hexapole ion trap for 0.3-0.5 s. By applying a repulsive voltage the ions were subsequently expelled into an ion transfer system of static ion lenses which guided the ions into the ICR “infinity cell” located within the high-field region of the superconducting magnet. The background pressure within the trap was approximately $4x10^{-10}$ mbar. To study H/D exchange reactions in the gas-phase, deuterating gases were introduced into the ICR cell using a Balzer leak valve. The static gas pressures during exchange reactions was kept constant at $7.5x10^{-8}$ mbar. Exchange kinetics of mass selected carnosine complex ions were recorded after ejection of all unwanted higher and lower mass ions. To account for a possible off resoncance excitation of the ions of interest experiments were performed both with and without ejecting the ^{13}C isotopomeres by rf excitation. Mass spectra were recorded and processed with the Xmass software from Bruker Daltonics.

6.3 Computational Details

If not otherwise stated, all calculations were performed in the electronic ground state with density functional theory (DFT). We chose the Becke88 exchange functional[19] with the Lee, Yang and Parr gradient corrected correlation functional[20] (BLYP), because it has proven to provide accurate structures and energetics both for ionized water clusters[21,22] and small dipeptides[23]. BLYP is applicable even to large systems as it scales with $\leq N^3$ (N = number of basis functions) when charge fitting is used. Ahlrichs' triple-ζ valence type plus polarization (TZVP) basis sets were applied on all atoms.[24] All calculations were performed using the DFT implementation of the TURBOMOLE[25-26] quantum chemistry programme package. The "resolution of identity" (RI) approximation (charge fitting approach) was applied throughout. In this approach the Coulomb J contribution to the two electron interelectronic repulsion is approximated by expanding the molecular electron densities in atom centered auxiliary basis sets. The standard auxiliar J basis sets implemented in TURBOMOLE were used.[27] Due to the lack of dispersion the applicability of DFT to hydrogen bonded systems is potentially problematic. To assure that BLYP/TZVP is capable to treat even delicate hydrogen bonded systems correctly, test calculations on the neutral water dimer were performed which yielded a binding energy of 23.77 kJ mol^{-1}. This is in good agreement with the MP2 basis set limit of 20.67 kJ mol^{-1}.[28] Vibrational analysis was performed using the numeric second derivatives of the energy, as implemented within the TURBOMOLE code.

6.4 Results and Discussion

A. High Resolution Mass Spectrometry of Aqueous Solutions of Carnosine

The positive mode ES-FT-ICR mass spectrum of an aqueous solutions of carnosine is shown in Fig. 6.2. It reveals three progressions of protonated carnosine multimeres in charge states q= +1, +2 and – for the first time – in +3. The peaks belonging to the three different progressions of $[n\times\mathrm{Carn}+\mathrm{H}]^{+}$, $[m\times\mathrm{Carn}+2\times\mathrm{H}]^{2+}$, and $[l\times\mathrm{Carn}+3\times\mathrm{H}]^{3+}$ superimpose for $m/z > 700$. Here we use the notation $[k\times\mathrm{Carn}+q\times\mathrm{H}]^{q+}$ to denote van der Waals complexes of k Carnosine monomers in charge state q+. The resolution of the spectra in this work (≅ 1ppm over the whole mass range) is significantly higher than in previous ES-MS studies of carnosine. The isotopic fine structure of the recorded peaks is readily resolved and allows an unambigious assignment to the different protonated carnosine multimers.

Even in case of a superposition of several multimeres of different charge states, the isotopic pattern of the recorded peaks facilitates the identification of the superlying species (cf. Fig. 6.2). Multimeres of the following stoichiometry were verified in the spectra: $[n\times\text{Carn}+\text{H}]^{+}$ with n=1-7, $[m\times\text{Carn}+2\text{H}]^{2+}$, with m=7-15, and $[l\times\text{Carn}+3\text{H}]^{3+}$ with l=16-17. Next to the progression of the different carnosine multimers the spectra also contain peaks of a variety of decomposition products of carnosine and its multimeres. The orifice voltage of the ES source was varied from 50 to 220 V. Various fragments of carnosine and its multimeres were recorded for all skimmer voltages. The intensity of the NH_3 eliminated carnosine at m/z=210.0876 was observed to decline with decreasing orifice voltage. At 50 V it was no longer detectable. In contrast carnosine and its multimeres $[n\times\text{Carn}+\text{H}]^{+}$, $[m\times\text{Carn}+2\text{H}]^{2+}$, and $[l\times\text{Carn}+3\text{H}]^{3+}$ were detected at all orifice voltages. The overall best signal/noise ratio was obtained with an orifice voltage of approximately 120 V.

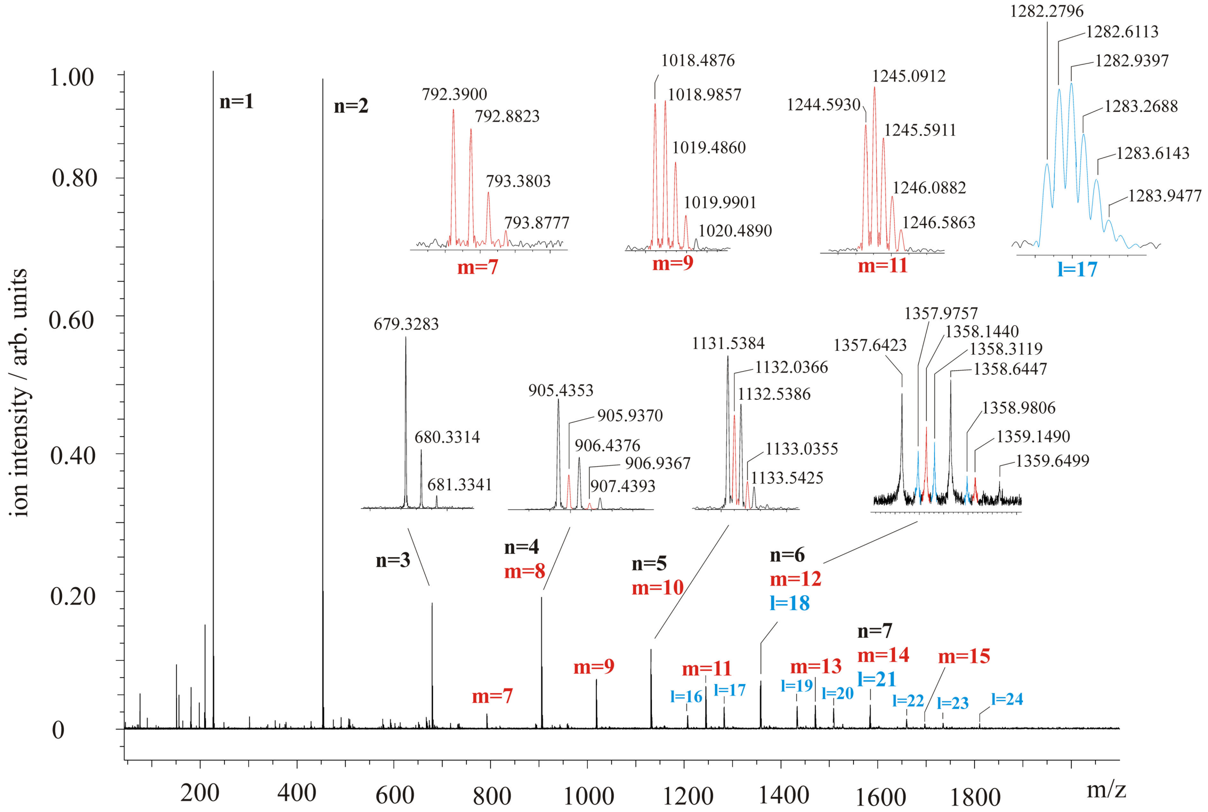

Fig. 6.2 Positive mode ES-FT-ICR mass spectrum of an aqueous solution of carnosine at pH=3.2. Progressions of three different protonated carnosine multimers: $[n\times\text{Carn}+\text{H}]^{+}$, n=1-7, $[m\times\text{Carn}+2\text{H}]^{2+}$, m=7-15 (red), and $[l\times\text{Carn}+3\text{H}]^{3+}$, l=16-24 (blue), are detected. The inlets show that even for superimposing peaks the isotopic fine structure are resolved.

B. Liquid-Phase H/D Exchange of Carnosine

Hydrogen atoms at sites like amines, carboxylic acids, alcohols and amide groups are often referred to as labile hydrogen atoms in peptides and proteins as they exchange against deuterium when the molecule is exposed to a deuterating solvent. The rates of exchange differ substantially between different sites of a peptide and are strongly pH dependent. The exchange kinetics give some insight into the liquid phase conformation of the peptide as protons attached to heteroatoms experience slower exchange when they are involved in H-bonded structures like for e.g. α-helices and β-sheets or when they are sterically inaccessible to the solvent. Condensed phase H/D exchange combined with ES mass spectroscopy has proven to be a powerful tool for protein conformational studies, as the mass spectra obtained from proteins in folded and unfolded states usually exhibit differences in molecular masses and charge distributions.[29-31]

In the first step of a systematic analysis of carnosine and its complexes carnosine was exposed to D_2O in solution to reveal the liquid phase H/D exchange behavior of carnosine and of oligomers of hydrogen bonded carnosine monomers. The number of exchanged hydrogens in protonated carnosine $[\mathrm{Carn+H}]^+$ and its "clusters" - like e.g. the protonoated carnosine dimer $[2\times\mathrm{Carn+H}]^+$ – might reveal some insight into the structure of these species. Two different kinds of liquid phase H/D exchange experiments were performed:

(a) 20 µL carnosine stock solution was mixed with 980 µL $D_2O/CH_3OH/CH_3OOH$ (49.5/49.5/1) and the mixture was subsequently sprayed and continously analyzed by ES-FT-ICR mass spectroscopy.

(b) 50 µL carnosine stock solution was mixed with 500 µL D_2O and incubated at room temperature. After different times Δt 100 µL of this mixture was diluted with 900 µL $H_2O/CH_3OH/CH_3OOH$ (49.5/49.5/1) and analyzed by ES-FT-ICR mass spectroscopy.

Spectra from both approaches (a) and (b) are on display in Fig. 6.3 respectively Fig. 6.4. Compared to spectra obtained without D_2O (cf. Fig. 6.2) the spectra are far more complex and do not contain protonated carnosine multimers $[k\times\mathrm{Carn}+q\times\mathrm{H}]^{q+}$ larger than the protonated dimer $[2\times\mathrm{Carn+H}]^+$. Instead various (deuterated) carnosine and carnosine multimer decomposition products are detected, some of which are shown and assigned in the insets to Fig. 6.4. The kinetics of the liquid phase H/D exchange in case of carnosine is too fast to be determined with ES-ICR mass spectroscopy, which allows mass analysis of the

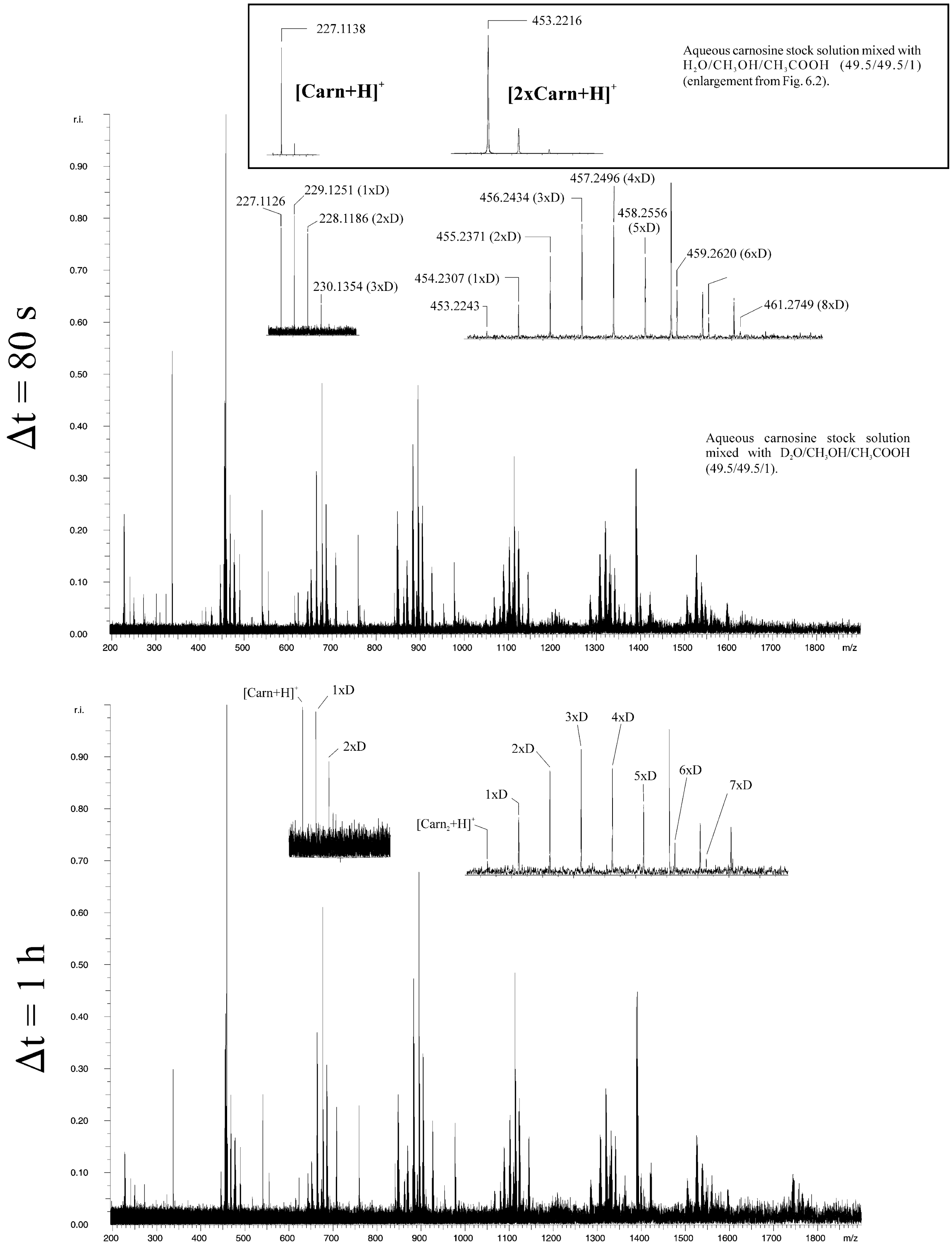

Fig. 6.3 Approach (a): ES mas spectra of 20µL Carnosine stock solution in 980 µL $D_2O/CH_3OH/CH_3COOH$ (49.5/49.5/1) 80s and 1h after mixture. Besides from protonated carnosine $[Carn+H]^+$ and protonated carnosine dimer $[2\times Carn+H]^+$ no further carnosine multimeres were identified in the spectra, which contain series of fragmentation products instead. The peaks assigned to $[Carn+H]^+$ and $[2\times Carn+H]^+$ are magnified in the insets. Up to three resp. eight hydrogens are exchanged after 80s. The number of exchanged hydrogens does not increase with time, but spectra taken at longer Δt differ in relative abundances (and signal/noise ratio).

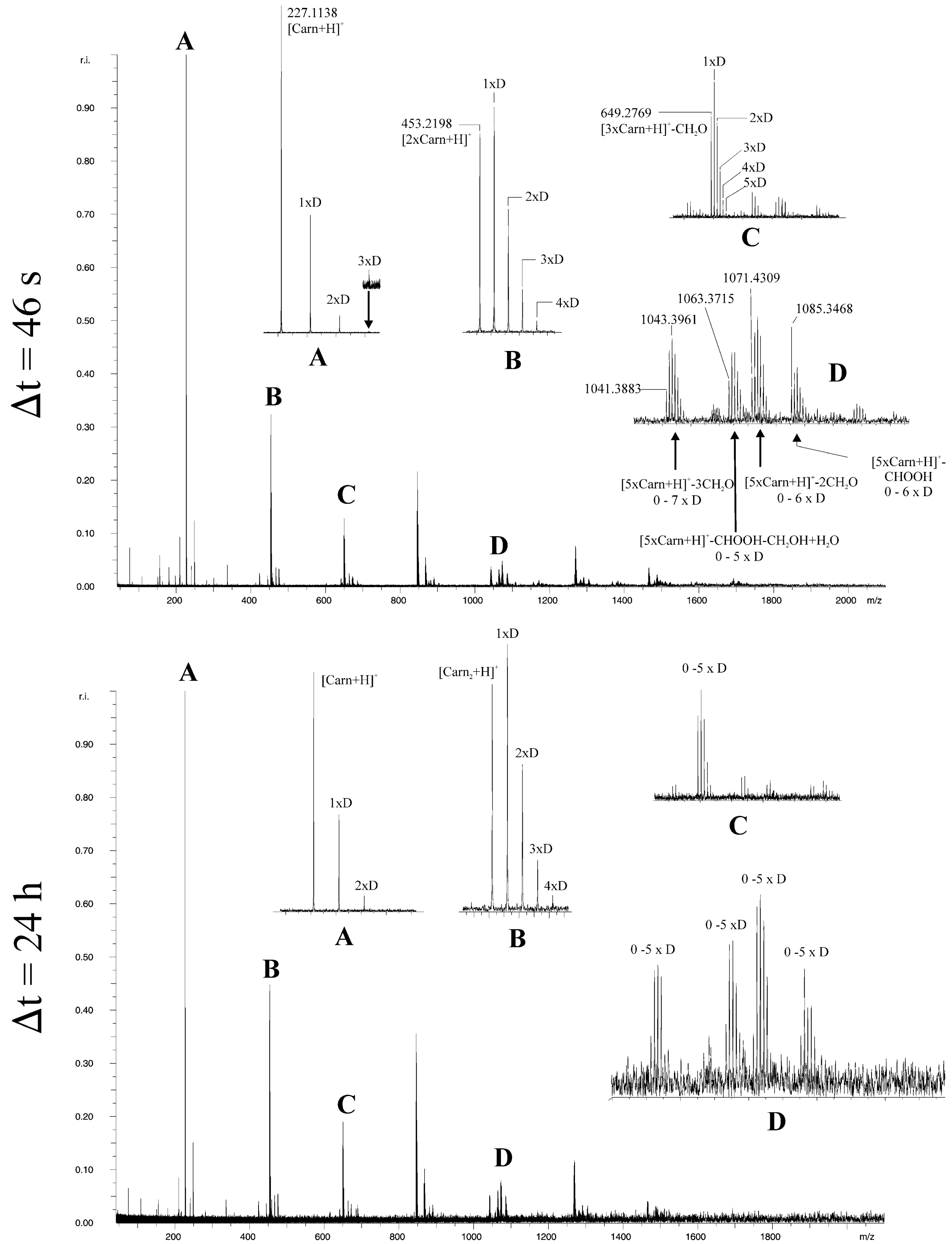

Fig. 6.4 Approach (b): 50 µL carnosine stock solution were mixed with 500 µL D_2O and incubated at room temperature for Δt. Subsequently 100 µL of this mixture was diluted with 900 µL $H_2O/CH_3OH/CH_3COOH$ (49.5/49.5/1) and analyzed by ES-FT-ICR mass spectroscopy. Besides of various carnosine and carnosine multimere decomposition products (see for example insets **C** and **D**) the spectra contain $[Carn+H]^+$ and $[2\times Carn+H]^+$. $[Carn+H]^+$ contains two exchanged hydrogens, and $[2\times Carn+H]^+$ four (see text for details). Spectra taken at different exposure times Δt exhibit only minor changes in relative abundances. The total number of exchanged hydrogens remains unaffected.

reaction solution only several seconds after the start of the exchange. As can be seen from Figures 6.3 and 6.4 after this period of time all exchangeable hydrogens are already exchanged.

The maximum number of exchanged hydrogens is three in case of the protonated carnosine $[Carn+H]^+$ and eight in case of the protonated dimer $[Carn_2+H]^+$. Approach (a) yields higher numbers of exchanged hydrogens than approach (b). In Fig. 6.4 the peak corresponding to protonated carnosine with three hydrogens exchanged against deuterium is low in intensity after $\Delta t=46s$ and below noise level after $\Delta t=24h$. The recorded peak intensity is low enough to be ascribed exclusively to ^{13}C isotopomeres of protonated carnosine monomers $[Carn+H]^+$ with one or two exchanged hydrogens, marked as 1×D and 2×D in Fig. 6.4. In contrast, in Fig 6.3 the significantly higher peak intensity at m/z=230.1354 clearly identifies triple H/D exchange. For the protonated dimer, approach (a) shows eight exchanged protons but approach (b) only four. As the spraying solution in case of approach (b) largely consists of water, some deuterium atoms can quickly back-change with hydrogens of the surrounding solvent.

Thus, approaches (a) and (b) allow for a qualitative evaluation of the exchange rates of labile hydrogens. The difference in total numbers of detected H/D exchanges between approach (a) and (b) indicate that in protonated carnosine $[Carn+H]^+$ one of the three exchanged hydrogens exchanges much faster than the other two. Similarly in the protonated dimer four of the total of eight labile, exchangeable hydrogens are found to back-change on a much shorter time scale.

The surprising finding concerning the liquid phase H/D exchange of dissolved carnosine is that the protonated monomer exchanges only a total of three hydrogen atoms against deuterium, while under the same conditions in the protonated dimer up to eight hydrogens are exchanged. This means an average of four exchanged hydrogens per monomer ! This finding suggests liquid phase H/D exchange is promoted upon dimer formation.

C. High Resolution Mass Spectrometry of Zn^{II}/Carnosine Complexes.

The formation of possible Zn^{II}/carnosine complexes is limited by solubility restrictions. The extent of complex formation is appreciable only around pH=6, for pH>7.5 precipitation occurs even in the presence of excess ligands.[4] The ES-ICR mass spectrum of an aqeous solution of an equimolar carnosine:$ZnCl_2$ solution at pH=6.8 is presented in Fig. 6.5. Besides protonated carnosine $[Carn+H]^+$ and decomposition producs of carnosine like e.g. protonated

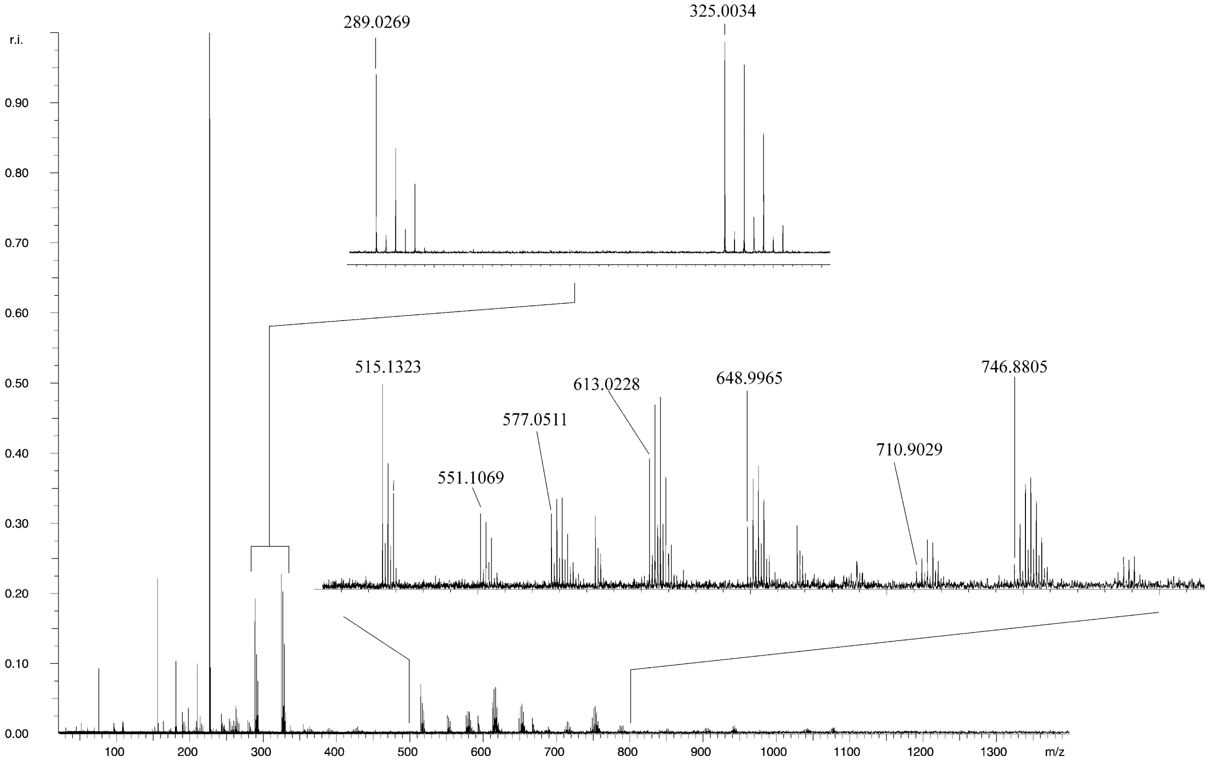

Fig. 6.5 ES-FT-ICR mass spectrum of an aqeuous solution of $ZnCl_2$ and carnosine at pH=6.8.

Table 6.1 Assignment of cationic Zn^{II}/carnosine complexes detected in the ES mass spectra of an aqueous solution of $ZnCl_2$ and carnosine at pH=6.8.

m/z	*Assignment*
289.0269	$[\text{Carn-H,Zn}^{\text{II}}]^+$
325.0034	$[\text{Carn-H,Zn}^{\text{II}},2\times H_2O]^+$
515.1323	$[2\times\text{Carn-H,Zn}^{\text{II}}]^+$
551.1069	$[2\times\text{Carn-H,Zn}^{\text{II,}},2\times H_2O]^+$
577.0511	$[2\times\text{Carn-3H},2\times\text{Zn}^{\text{II}}]^+$
613.0228	$[2\times\text{Carn-3H},2\times\text{Zn}^{\text{II}},2\times H_2O]^+$
648.9965	$[2\times\text{Carn-3H},2\times\text{Zn}^{\text{II}},2\times H_2O]^+$
710.9029	$[2\times\text{Carn-5H},3\times\text{Zn}^{\text{II}},2\times H_2O]^+$
746.8805	$[2\times\text{Carn-5H},3\times\text{Zn}^{\text{II}},2\times H_2O]^+$
784.8720	$[2\times\text{Carn-5H},3\times\text{Zn}^{\text{II}}+4\times H_2O]^+$

histidine at m/z=156.0765, the spectrum presented in Fig. 6.5 shows several peaks ascribed to the Zn^{II}/carnosine complexes, reported in Table 6.1. Complexes containing up to 3 zinc atoms and two carnosine molecules are identified by mass and isotopic fine structure. The spectrum even contains larger Zn^{II}/carnosine complexes at m/z > 750 a.u. but these cannot be definitively identified by their isotopic fine structure due to an insufficient signal/noise ratio.

It is interesting to note that next to Zn^{II}/carnosine complexes, various $Zn^{II}(OH_2)_2$/carnosine complexes were also detected. Complexes containing a single H_2O molecule or more than two H_2O molecules per Zn^{II} dication do not occur up to clusters with m/z≈800 a.u. In clusters with m/z<800 a.u., water is exclusively contained in pairs of two. This is indicative of the existence of pairs of hydrophilic binding sites within Zn^{II}/carnosine complexes. The spectrum shown in Fig. 6.5 was taken with an orifice voltage (declustering voltage) of 120 V, but orifice voltages of up to 270 V were applied and Zn^{II}/carnosine complexes containing pairs of water molecules were observed throughout. The observation that H_2O ligands remain with the Zn^{II}/carnosine complex under spraying conditions that are found to be strongly desolvating otherwise demands strong binding energies of the attached water molecules that can only arise from charge dipole interactions between the Zn^{II} dication and H_2O molecules bound directly to it. It can be excluded that hydrogen bonded water molecules remain with the complex to declustering voltages up to 270 V. In blackbody radiation induced decay experiments (BIRD) of mass selected $[\text{Carn-H},Zn^{II},2\times H_2O]^+$ complexes at room temperature loss of H_2O did not occur. It required additional excitation in sustained off resonance irradiation and collision induced dissociation (SORI-CID) experiments to achieve fragmentation of mass selected $[\text{Carn-H},Zn^{II},2H_2O]^+$ complexes. As shown in Fig. 6.6, SORI-CID leads to the simultaneous loss of two H_2O molecules from $[\text{Carn-H},Zn^{II},2xH_2O]^+$.

ES is considered as a gentle “ionization” technique that allows the generation of intact noncovalent complexes in the gas-phase.[32-34] ES-MS has been succesfully applied to the investigation of metal-protein interactions in solution and was used to detect the stoichiometry of metal-ion binding to peptides/proteins with clear determination of stoichiometry before.[35] The detection of both Zn^{II}/carnosine and $Zn^{II}(OH_2)_2$/carnosine complexes trough ES-MS is indicative of the coexistence of two types of Zn^{II} carnosine complexes in the liquid phase, which differ significantly in the binding energies of attached H_2O ligands. Potential structures and relative energetics of these two entities, as indicated by ES-MS, have been investigated by ab initio calculations.

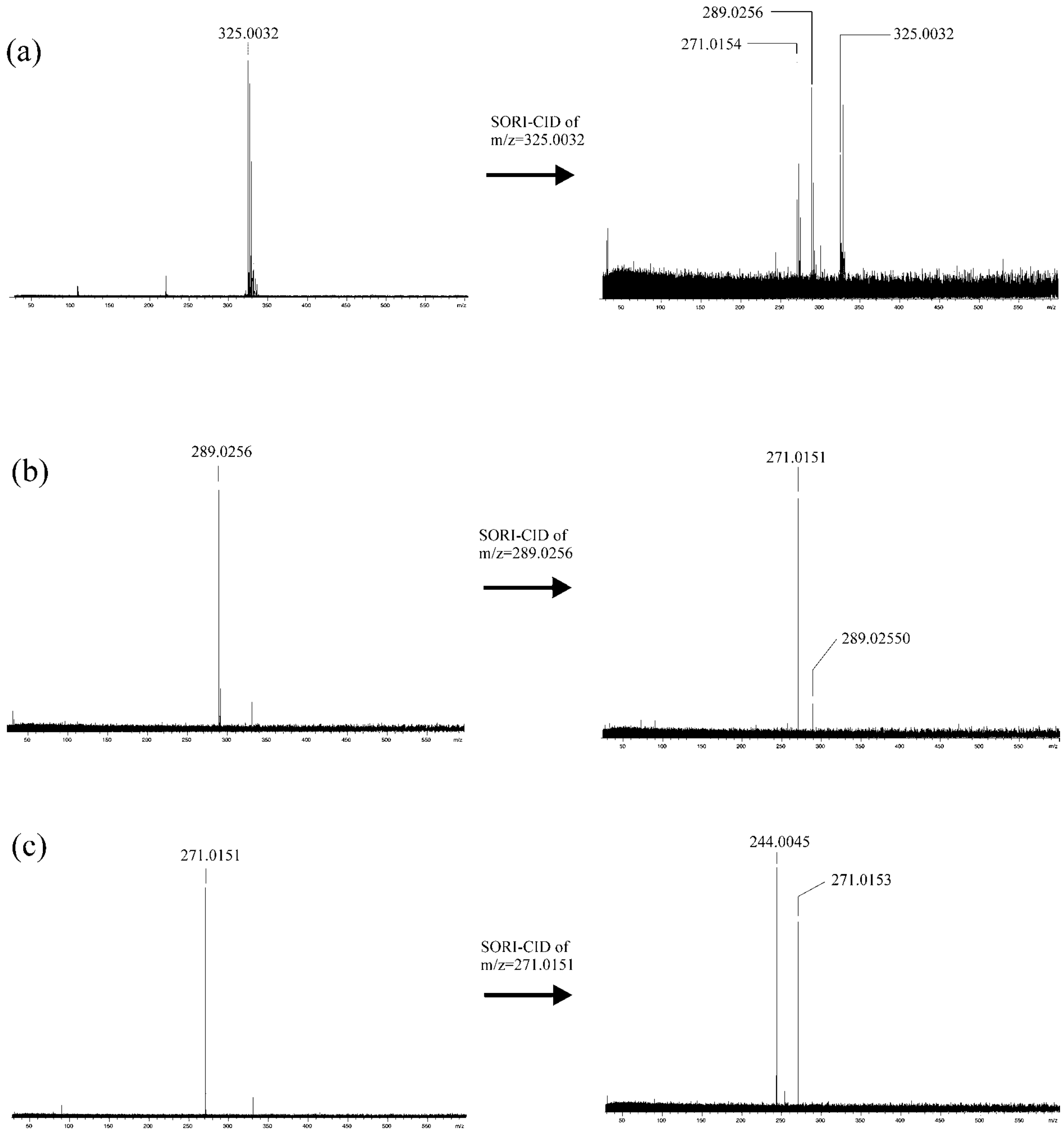

Fig. 6.6 SORI-CID of mass selected Zn^{II}/carnosine complexes $[Carn\text{-}H+Zn(OH_2)_2]^+$ (m/z=325.0032) leads to the formation of the H_2O eliminated species $[Carn\text{-}H,Zn^{II}]^+$ (m/z=289.0256) and $[Carn\text{-}H_3O,Zn^{II}]^+$ (m/z=271.0151). The latter results from H_2O elimination of vibrationally excited $[Carn\text{-}H+Zn]^+$ (m/z=289.0256) as revealed through SORI-CID of mass selected $[Carn\text{-}H+Zn]^+$. The release of H_2O from $[Carn\text{-}H+Zn]^+$ is indicative of the formation of an intramolecular peptide bond between the free amino terminus and the carboxylic acid residue of histidine. Excited $[Carn\text{-}H_3O+Zn]^+$ decays via release of HCN into $[Carn\text{-}H_3O\text{-}HCN+Zn]^+$ at m/z=244.0045. In contrast to (a) in (b) (c) only the peak with the lowest mass of each of the Zn^{II}/carnosine complexes was used in the SORI-CID experiments, which led to an increase the signal to noise ratio.

D. Structure and Stability of Protonated Carnosine and Zn^{II}/Carnosine complexes

Carnosine is considered as an effective biological pH buffer and serves as proton buffer for those tissues which have a preferentially glycolytic type of energy supply.[36] It has three groups that can undergo acid-base reactions: the carboxylic acid (pK=2.594), the ammonium group (pK=6.774) and the protonated N^3 (cf. Fig. 6.1) imidazole group (pK=9.372).[4] The structure of carnosine in aqeous solution has been studied by NMR leading to some structural proposition for the zwitterion. The structure of the gas-phase protonated carnosine [Carn+H]$^+$ relevant to our mass spectrometric studies has not been investigated before.

In Fig. 6.7 different BLYP/TZVP optimized [Carn+H]$^+$ structures are presented. N^3-H tautomers are found to be energetically clearly favored to N^1-H tautomers. As might have been perceived by the corresponding pK values, structure (d) in which the imidazole ring is protonated instead of the N-terminus of carnosine, is higher in energy than the minimum structures of both N^3-H and N^1-H isomers by 33.30 resp. 15.13 kJ mol^{-1}. Therefore it is expected that in gas-phase [Carn+H]$^+$ the proton resides at the ammonium group.

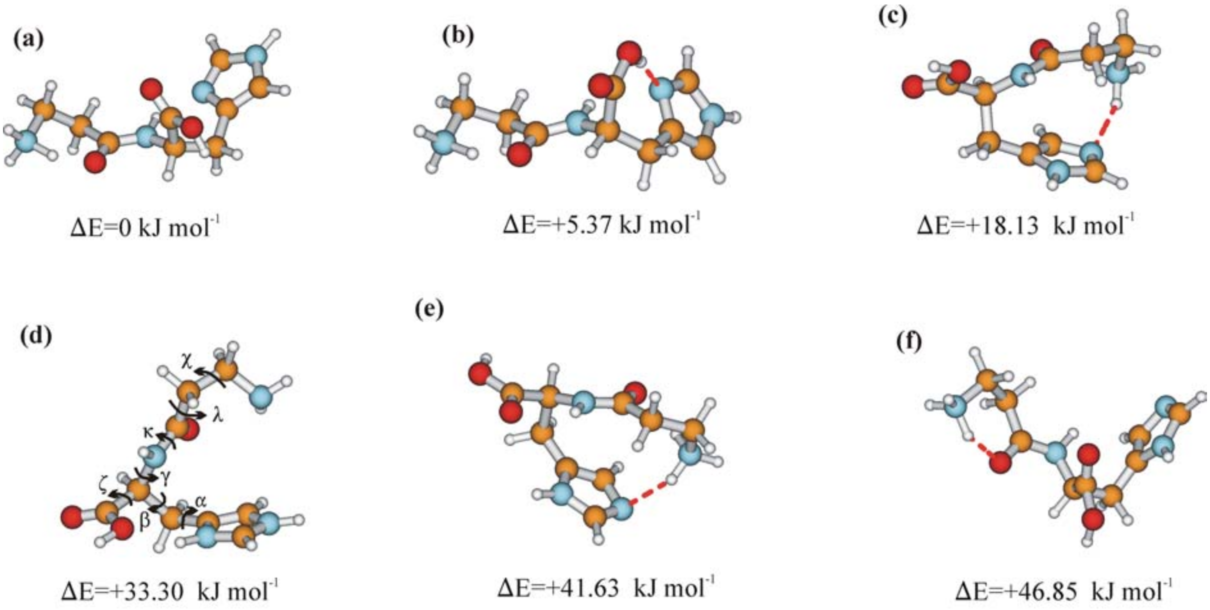

ΔE=0 kJ mol^{-1}

ΔE=+5.37 kJ mol^{-1}

ΔE=+18.13 kJ mol^{-1}

ΔE=+33.30 kJ mol^{-1}

ΔE=+41.63 kJ mol^{-1}

ΔE=+46.85 kJ mol^{-1}

Fig. 6.7 Different protonated carnosine [Carn+H]$^+$ structures. Structures (a) and (b) are N^3-H tautomers, (c),(e) and (f) are N^1-H tautomers whereas in (d) both imidazole nitrogens are protonated.

The N^3-H tautomer (a) that has a conformation that allows for a close contact between the ammonium group and the carbonyl group of the peptide bond as well as between the N^1 of the imidazole ring and NH of the peptide bond are found to be energetically slightly favored to (b) where the acttractive interaction between NH and N^1 of (a) is replaced through a hydrogen bond between the carboxyclic acid group -COOH and N^1.

The conformations of the different isomers of gas-phase protonated carnosine in Fig. 6.7 are described by the angles of rotations $\alpha,\beta,\gamma,\kappa,\lambda,\chi,\zeta$ that are defined in structure (d) of Fig.6.7 and listed for all $[\mathrm{Carn+H}]^+$ structures in Table 6.2. The large range of possible angle of rotations reveals a high order of conformational flexibility of carnosine. While different conformers differ significantly in $\alpha,\beta,\gamma,\lambda,\zeta$ the degree of freedom of κ and χ is limited. The values for κ, which denotes the angle of torsion around the peptide bond –N(H)-CO-, are close to 180° except for (c) with –159.57° (≈200.43°). This deviation from the expected 180° for a plane peptide bond indicates a significant deformation of the rigid peptide bond in case of (c). Nevertheless (c) is found to be the favored N^1-H tautomer of carnosine, which is due to intramolecular stabilization by attractive interactions between N^3 of the imidazole and the ammonium group and between the carboxylic acid residue -COOH and NH of the peptide bond. Apparently in (c) these interactions are more effective than in any other N^1-H tautomer.

Table 6.2 Angles of rotation $\alpha,\beta,\gamma,\kappa,\lambda,\chi,\zeta$ of $[\mathrm{Carn+H}]^+$ structures (a)-(f) from Fig.6.7

	α	β	γ	ζ	κ	λ	χ
(a)	-53.32	57.22	164.39	171.16	171.76	-140.24	-53.59
(b)	18.13	-77.78	131.99	-62.02	175.42	-141.96	-53.15
(c)	107.90	-37.69	84.04	-23.19	-159.57	165.47	-42.74
(d)	57.85	32.51	67.36	-59.74	174.00	156.56	-56.82
(e)	77.81	46.41	172.75	162.33	171.57	-139.06	-54.70
(f)	77.99	45.12	173.21	161.03	172.08	-139.98	-54.61

In our calculations of the isolated, gas-phase protonated carnosine $[\mathrm{Carn+H}]^+$ the N^3-H tautomers are energetically favored to N^1-H tautomers. From ^{15}N NMR experiments the fraction p of the N^1-H tautomer of carnosine in aqueous solutions was estimated to be approx. 68%. This indicates that in solution, where the most probable carnosine form is that of a zwitterion, the N^1-H tautomers are somewhat lower in energy. To consider solvation effects upon $[\mathrm{Carn+H}]^+$ structures (a) and (c) from Fig.6.7 were reoptimized applying the Conductor-like Screening Model (COSMO), which is a continuum solvation model where the solute molecule forms a cavity within the dielectric continuum permittivity ε. An electrostatically ideal solvent with $\varepsilon=\infty$ was assumed. In these calculations the enegetic preference of the N^3-H tautomer reduces to only 3 kJ mol^{-1}. Hence we conclude that for protonated carnosine in acidic aqueous solution the fraction of both tautomers should be close to 0.5.

While the precipitate from Zn^{II}/carnosine solutions has been identified to possess a polymeric structure and different structural propositions have been presented, the structure of solvated Zn^{II}/carnosine complexes is still unknown. In Fig. 6.8 four [Carn-H,Zn]$^+$ structures out of a total of fifteen BLYP/TZVP optimized [Carn-H,Zn]$^+$ complexes are presented. Liquid phase NMR studies indicated the preponderance of the N^3-H carnosine tautomer in theses complexes. The computed differences in total energy between different [Carn-H,Zn]$^+$ complexes affirm a strong energetic preference of complexes containing the N^3-H tautomer. According to our BLYP calculations, complexes containing the two tautomers differ in energy by at least 85 kJ mol^{-1}. Carnosine is a polydentate ligand which is expected to have six potential metal coordinating sites: the nitrogen atoms N^1 and N^3 of the imidazole ring, one carboxylate group –COO$^-$, one amino group, and the nitrogen atom of the peptide bond.

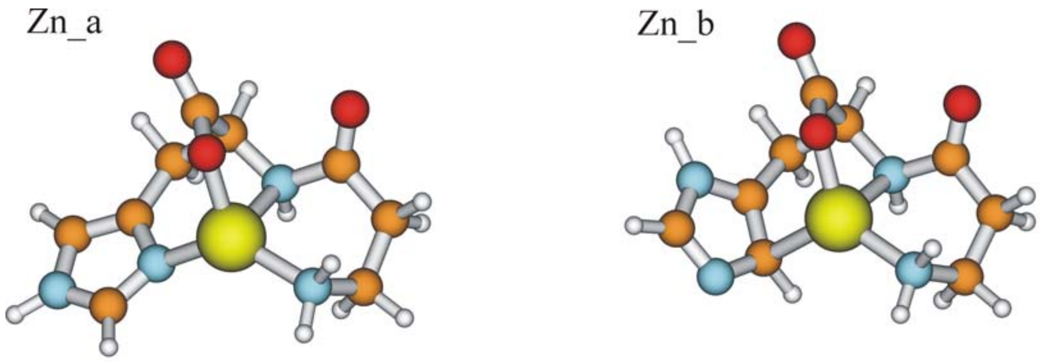

N^3-H, ΔE= 0 kJ mol^{-1} N^1-H, ΔE= +85.61 kJ mol^{-1}

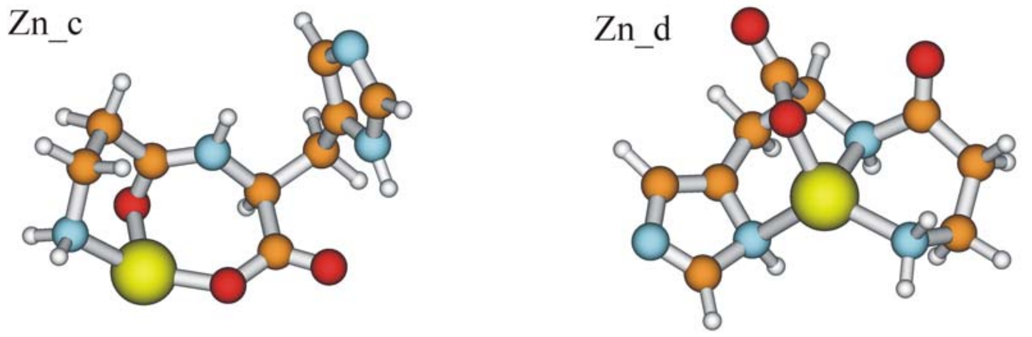

N^1-H, ΔE= +97.10 kJ mol^{-1} N^1-H, ΔE= +146.64 kJ mol^{-1}

Fig.6.8 BLYP optimized [Carn-H,Zn^{II}]$^+$ complex structures and relative energies.

Only in $[\text{Carn-H,Zn}^{II}]^+$ complexes containing the N^3-H tautomer of carnosine fourfold coordination to Zn^{II} through the – on account of their negative charge or basicity – preferential binding sites is possible (cf. Zn_a in Fig.6.8). These binding sites are the non-protonated nitrogen atom N^1 of the imidazole group, the carboxylate group, the amino group and the nitrogen atom of the peptide bond. According to our calculations for complexes containing the N^1-H tautomer of carnosine complexation of Zn^{II} through the non-protonated nitrogen atom of the imidazole group N^3 is not possible due to steric reasons. The imidazole group coordinates with the protonated N^1 or C^4 (cf. structures Zn_b and Zn_d in Fig.6.8) to Zn^{II} instead. The resulting complex structures are energetically clearly disfavored with regard to complex Zn_a. Complex Zn_c with only threefold coordination of Zn^{II} through the carboxylate group, the amino group and the carbonyl of the peptide bond is close in energy to Zn_b (fourfold Zn^{II} coordination involving C^4) and even favored to Zn_d (fourfold coordination involving N^1) by -49.54 kJ mol^{-1}.

Table 6.3 Angles of rotation $\alpha,\beta,\gamma,\kappa,\lambda,\chi,\zeta$ of $[\text{Carn-H,Zn}^{II}]^+$ complexes Zn_a – Zn_d from Fig.6.8

	α	β	γ	ζ	κ	λ	χ
Zn_a	-27.35	66.51	168.76	-23.52	175.71	-32.22	-48.74
Zn_b	98.07	68.77	176.09	-28.20	176.18	-33.27	-49.18
Zn_c	81.33	52.43	151.10	45.03	168.55	-93.33	-46.35
Zn_d	-63.12	72.37	173.02	-28.78	176.32	-30.41	-50.50

As perceived from the angles of rotation (listed in Table 6.3) the conformations of carnosine ligands in Zn_a and Zn_d are very similar, except for a difference in α by approx. 36°. This twist of the imidazole ring of the N^1-H tautomer in Zn_d is necessary to facilitate a direct contact between N^1 and Zn^{II} in Zn_d. For smaller angles attractive interactions between N^1 and Zn^{II} are inhibited by the hydrogen atom bound to N^1, located in line between the metal ion and N^I. Although the conformations of the N^1-H and N^3-H tautomers of carnosine in Zn_a and Zn_d are very similar, they differ in total energy by 146.64 kJ mol^{-1}. In case of protonated carnosine $[\text{Carn+H}]^+$ the N^3-H tautomer was found to be favored to the N^1-H tautomer by 18.71 kJ mol^{-1}. The much larger difference between Zn_a and Zn_d mainly arises from the weaker $N^I(H)$-Zn^{II} bond in Zn_d compared to the undisturbed N^I-Zn^{II} bond in Zn_a. The carnosine ligand in Zn_b also has a conformation close to that of carnosine in Zn_a, except for the alignment of the imidazole ring, as is distinct from the α values. The difference in total energy of 85.61 kJ mol^{-1} between Zn_a and Zn_b is again due to the bond energy of the N^I-Zn^{II} bond in Zn_a being larger than that of the $C^4(H)$-Zn^{II} bond in Zn_b. In case of Zn_c similar arguments do not apply, as the carnosine conformation differs significantly from that in the complexes.

It is interesting to note that in the minimum structures of $[\text{Carn+H}]^+$ and $[\text{Carn-H,Zn}^{\text{II}}]^+$, the conformations of carnosine as given by the angles of rotation for (a) in Table 6.2 and Zn_a in Table 6.3 are similar, except for some deviations in α, ζ, and λ. These angles are immediately involved in the coordination of the Zn^{II} dication as they determine the orientiation of the imidazole ring including the N^1 and N^3 nitrogen atoms (α), the carboxylate group (ζ) and the amino group of the alanyl (λ).

The ES mass spectrometric studies have yielded some indications of the existence of two different Zn^{II}/carnosine species which differ in the relative H_2O binding energies of the first two H_2O molecules attached to the complex. In one case all of the water molecules are stripped from the complex during the declustering stage following the actual ES process leading to $[\text{Carn-H,Zn}^{\text{II}}]^+$. In the other case the complex exhibits higher binding energies for

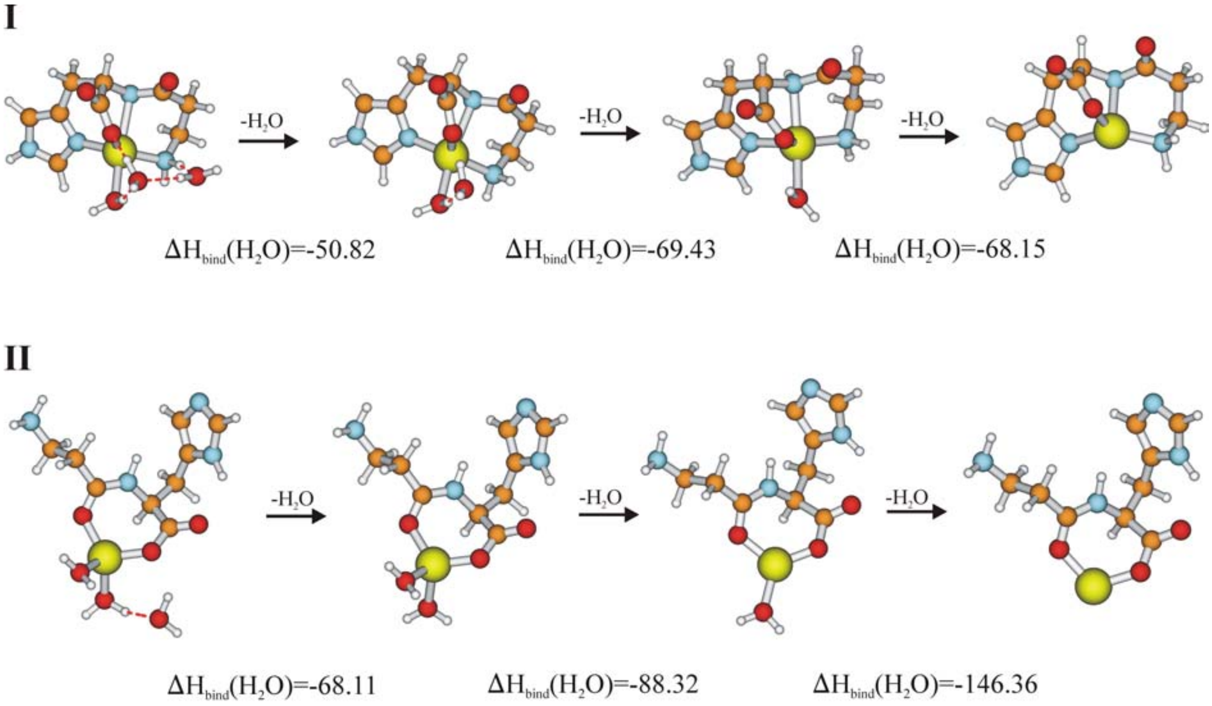

Fig. 6.9 Stepwise dehydration of hydrated Zn^{II}/carnosine complexes, ZPE corrected binding enthalpies ΔH_{bind} (0K) are given in kJ mol^{-1}. In complex type I Zn^{II} is complexed internally within a "binding pocket" formed by carnosine. In complexes of type II the metal dication is not enclosed by carnosine but remains at the surface of the complex ligand. The stepwise H_2O binding enthalpies are significantly higher for complexes of type II. In contrast to complexes of type II, for which the stepwise binding enthalpies increase with decreasing cluster size in type I complexes the stepwise binding enthalpies for $[\text{Carn-H,Zn}^{\text{II}}(\text{OH}_2)_2]^+$ and $[\text{Carn-H,Zn}^{\text{II}}(\text{OH}_2)]^+$ are almost equal. The calculated ΔH_{bind} even indicate a slightly stronger $\text{Zn}^{\text{II}}\text{-OH}_2$ bond in $[\text{Carn-H,Zn}^{\text{II}}(\text{OH}_2)_2]^+$ than in $[\text{Carn-H,Zn}^{\text{II}}(\text{OH}_2)]^+$.

two H_2O ligands, which prevents the H_2O to be removed from the complex, giving rise to the observed $[\text{Carn-H},\text{Zn}^{II},2\times H_2O]^+$ species. The number of possible isomers for hydrated Zn^{II}/carnosine complexes is abundant. In this study more than 30 different Zn^{II}/carnosine complexes were investigated with up to three water molecules attached. As might have been expected, the binding energies of H_2O ligands attached to Zn^{II} are significantly higher than those of H_2O molecules which are hydrogen bonded to the carnosine ligand. Therefore in complexes with the formal stoichiometry $[\text{Carn-H},\text{Zn}^{II},p\times H_2O]^+$ the H_2O ligands will be located at Zn^{II} and the complexes will be denominated as $[\text{Carn-H},\text{Zn}^{II}(OH_2)_p]^+$ in the following.

Distinct structural features allow for abstraction of these structures into two main structural archetypes (I, II). In complexes of type I the carnosine ligand encloses the Zn^{II} in some kind of binding pocket in which the maximum coordination number of the Zn^{II} dication is five. Four coordination sites are occupied by different carnosine binding sites and one is occupied by H_2O. The second H_2O ligand is located in the second hydration shell and is hydrogen bonded to the first shell H_2O ligand and the carboxylate. Additional water molecules are hydrogen bonded to polar N-H or O-H bonds of carnosine or available water molecules, respectively.

In Zn^{II}/carnosine species of type II, the Zn^{II} dication is attached to the “surface” of carnosine rather than enclosed by it. The maximum coordination number of Zn^{II} is four, up to two coordination sites are occupied by H_2O ligands. The remaining two sites are occupied by the carbonyl of the peptide bond and the carboxylate group. The third and any further water molecules are hydrogen bonded to H_2O ligands bound directly to the Zn^{II} dication. Structures and stepwise hydration energies of different complexes of type I and II are given in Fig.6.9.

It is important to note that the H_2O ligand binding energies are significantly lower for complexes with a fivefold coordinated Zn^{II} (type I) than for complexes with a fourfold coordinated Zn^{II} (type II). The now calculated binding energies of H_2O to complex types I and II offer a possible explanation for the experimental observation that a certain fraction of Zn^{II}/carnosine complexes contain H_2O molecules always in pairs of two. Complexes of type II contain two strongly bound H_2O ligands (ΔH_{bind}=-88.32 resp. –146.36 kJ mol^{-1}). The third is bound by –68.11 kJ mol^{-1}, which is of the same magnitude as for the first two H_2O monomers bound to complexes of type I. In case the declustering stage of the used ES source cleaves only H_2O ligands bound by less than approximately 80 kJ mol^{-1}, [Carn-H,Zn^{II}(OH_2)$_2$]$^+$ and [Carn-H,Zn^{II}]$^+$ will be the dehydration products from complexes of type I and II coexistent in the liquid phase.

The Zn^{II}/carnosine complexes have been observed to form adducts in liquid solution. The stoichiometries of these adducts as listed in Table 6.1 suggest chain-structures like [(H_2O)$_2$Zn^{II}-(Carn-2H)-Zn^{II}-(Carn-H)]$^+$ at m/z=613.0228, [(H_2O)$_2$Zn^{II}-(Carn-2H)-Zn^{II}(OH_2)$_2$-(Carn-H)]$^+$ at m/z 648.9965, and [(H_2O)$_2$Zn^{II}-(Carn-2H)-Zn^{II}-(Carn-3H)- Zn^{II}(OH_2)$_2$]$^+$ at m/z 710.9029 etc.. It is obvious that complexes of type II can easily concanate with each other, as the carnosine chelate ligands in these complexes have free binding sites with which they can coordinate to Zn^{II} dications of other type II complexes. In contrast in complexes of type I the Zn^{II} is contained within the "binding pocket" formed by the carnosine which shields the metal ion from other potential ligands. In addition all of the potential metal coordination sites of the deprotonated carnosine chelate ligand in type I complexes are attached to the bound Zn^{II} dication. Hence concanation to another Zn^{II} is hindered for these complexes. For steric reasons complexes of type I are less suitable to assemble multimers than complexes of type II. It must be noted that complexes of type I are energetically clearly favored to complexes of type II. However, formation of multimers might lead to a decrease in total energy and whether the experimentally recorded [Carn-H,Zn^{II}(OH_2)$_2$]$^+$ complexes are fragments of these multimers or exist with them in equilibrium (in solution) cannot be excluded.

E. Proton Affinities of Carnosine and Zn^{II}/Carnosine Complexes

There are only few experiments that provide information of the gas-phase structures of peptides or proteins.[37-38] Mass spectroscopic techniques like collision induced dissociation (CID) have been successfully applied to identify amino acid compositions and sequences of proteins and peptides. However, these method are not suitable to reveal the secondary structure of a peptide.[39-43] Traditional (IR) absorption spectroscopy is not applicable in the gas-phase due to low concentrations and IR multiphoton absorption induced fragmentation is for large biomolecules in many respects complementary to CID. Therefore probing the chemical reactivity is still by far the most prominent experimental method to reveal properties and structures of complex molecules in the gas-phase. In a number of experimental studies H/D exchange has been used to examine proteins in the gas-phase.[44-51] In addition gas-phase H/D exchange of small molecules was used to distinguish between isomeric species and to deduce reaction mechanisms.[52-56]

For protonated glycine oligomers Gly_nH^+ it was observed that n=2 exchanges all labile hydrogens with D_2O while n=1 and n>3 do not exhibit facile exchange.[37] However, when ND_3 was used as deuterating agent all labile hydrogens were observed to exchange for n=1-5. This intriguing finding was ascribed to substantial differences between the gas-phase proton affinities (resp. the gas-phase basicities) of larger Gly_n peptides. The gas-phase proton affinity PA (resp. gas-phase basicity GB) is defined as $-\Delta H$ (resp. $-\Delta G$) for the reaction $[M+H]^+ \rightleftharpoons MH^+$. In case of Gly_nH^+ the size dependent reactivity with D_2O was attributed to substantial differences between the PAs of Gly_n and D_2O for n>3. As the PA of ND_3 (≈854 kJ mol^{-1})[57] is larger than that of D_2O (691 kJ mol^{-1})[57], Gly_nH^+ ,n=1-5, were observed to exchange with ND_3 due to a smaller differences in PAs. Correlation between the extent of H/D exchange for a molecule and the absolute difference in PAs between the molecule and the exchange reagent was found before in several studies. Some groups report that H/D exchange cannot occur between species which differ by more than ≈80 kJ mol^{-1}, while other have observed exchange between species which differ by more than ≈200 kJ mol^{-1} in their PAs.

Both the PA of carnosine and the effect of aggregation or ion complexation on the PA of carnosine are unknown. Knowledge of relative PAs of carnosine, carnosine multimers, and Zn^{II}/carnosine complexes would reveal important details of a fundamental property of this important biomolecule as the gas-phase acidities/basicities of the reactive groups determine the reactivity in the liquid phase. In addition potential differences in the PAs might reveal the effect of multimer formation and ion complexation on intrinsic molecular properties of the monomer. The insight into the process of complexation and oligomerization gained with carnosine may even be generalized to some extent to larger peptides and enzymes for which metal complexation is often a prerequisite for biological activity. Hence the PAs of carnosine, the carnosine dimer and different (hydrated) Zn^{II}/carnosine complexes were determined from ab initio calculations. A possible correlation between calculated PAs and H/D exchange was investigated by exposing mass selected $[n\times Carn+H]^+$ and Zn^{II}/carnosine species, stored in a FT-ICR ion trap, to deuterating reagents. The excess of H/D exchange was monitored as function of time.

To determine the absolute PAs of the carnosine species of interest from ab initio calculations it had to be verified first that a method is chosen that is applicable to large systems like the investigated (hydrated) Zn^{II}/carnosine complexes and still yields accurate values. High level ab initio MO theory[57] and density functional theory[58] have been proven to yield PAs within <10 kJ mol^{-1} of the experimental value – provided that the basis set is appropriate. In their benchmark calculations Peterson et al. predicted the gas-phase PA (T=298 K) of H_2O at the CCSD(T) level of theory using correlation-consistent basis sets up to quintuple-ξ (aug-cc-p5TZ), and find PA=690.78 kJ mol^{-1}. Post-Hartree-Fock based ab initio methods have a disadvantageous scaling with the number of basis functions. For large systems like those of interest in this work, especially when large basis sets are required, density functional theory is much more efficient due to its more favorable scaling with size. Therefore we restricted ourselves to DFT in the following calculations, unless otherwise stated. To validate whether BLYP/TZVP yield reasonable estimates of gas-phase PAs, H_2O was chosen as testcase. The PA of H_2O at T=298 K, is obtained from the zero point energy corrected (ZPE) energy differences ΔE_{ZPE} of the reaction $H_2O + H^+ \rightleftharpoons [H_3O]^+$ as obtained through BLYP/TZVP. Conversion of ΔE_{ZPE} to an enthalpy at 298 K requires the addition of a $p\Delta V$ (-RT) term as well as additional translational and rotational temperature dependent energy terms, which were assumed to have their classical values. A potential temperature dependence of the vibrations was ignored and the PA was obtained by adding 5/2 RT to the negative of the computed ΔE_{ZPE}. According to this scheme a PA of 688.08 kJ mol^{-1} is obtained for H_2O at T=298 K. This is very close to the value predicted by Peterson et al. (ΔPA=2.70 KJ mol^{-1}) and confirms that TZVP/BLYP yields good estimates of gas-phase PAs. It will be applied to calculate the PAs of carnosine and carnosine complexes in the following.

In order to determine gas-phase PAs of carnosine, geometry optimization of the neutral molecule structures were performed using the optimized structures of the energetically lowest N^1-H and N^3-H tautomers denominated (a) and (c) in Fig. 6.7 as start geometries (after removal of one proton). The location of the preferred deprotonation site was determined by comparison of the computed deprotonation energies of all possible sites. The energetically lowest located minima of neutral N^3-H and N^1-H tautomers are shown in Fig. 6.10. According to the performed BLYP/TZVP calculations the PAs at 298 K of the N^3-H and N^1-H tautomers of neutral carnosine are approximately 974.8 kJ mol^{-1} and 968.9 kJ mol^{-1}, respectively. The PAs of neutral Zn^{II}/carnosine complexes [Carn-2H,Zn^{II}] and [Carn-2H,Zn,2×H_2O] (type I and II), which contain the doubly deprotonated carnosine ligand $(Carn\text{-}2H)^{2-}$, were also calculated.

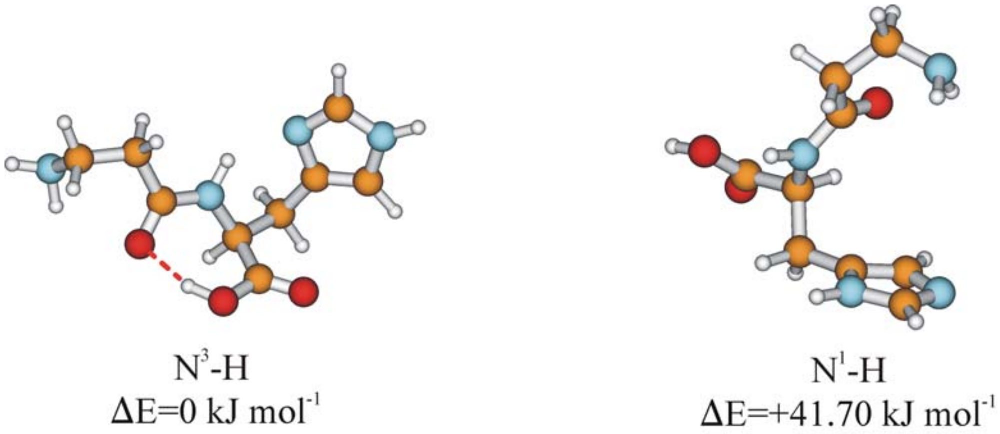

Fig. 6.10 BLYP/TZVP optimized minimum structures of N^3-H and N^1-H tautomers of neutral carnosine.

In analogy to the procedure performed for protonated carnosine, energetically preferred [Carn-H,Zn^{II}]$^+$ and [Carn-H,Zn^{II}(OH$_2$)$_2$]$^+$ complex structures were chosen as start geometries for geometry optimizations of the neutral complexes after removal of a single proton. As the [Carn-H,Zn^{II}]$^+$ and [Carn-H,Zn^{II}(OH$_2$)$_2$]$^+$ complexes contain different "labile", i.e. exchangeable hydrogen atoms, we generated different starting geometries by removing all hydrogen atoms – but only one at a time - from [Carn-H,Zn^{II}]$^+$ and [Carn-H,Zn^{II}(OH$_2$)$_2$]$^+$ complexes. The resulting energetically lowest BLYP/TZVP optimized structures of neutral [Carn-2H,Zn] and [(Carn-H,Zn(OH$_2$)$_2$)-H] (type I and II) complex structures are shown in Fig. 6.11.

While for [Carn-2H,Zn^{II}] structures containing the carboxylic acid residue and the peptide bond deprotonated are energetically lowest, in [Carn-2H,Zn^{II}(OH$_2$)$_2$] complexes of type I and II complexes resulting from hydrolysis of a first shell H$_2$O ligand leading to a strong Zn^{II}-OH bond are favored to structures with a deprotonated peptide bond by approximately 13 kJ mol^{-1} in case of the [(Carn-H,Zn^{II}(OH$_2$)$_2$)-H] complex of type I. In [(Carn-H,Zn(OH$_2$)$_2$)-H] complexes of type II which do not contain the N of the peptide bond bound to the Zn^{II} dication, the complex containing an OH$^-$ ligand attached to the Zn^{II} dication is lower in energy by approximately 123 kJ mol^{-1} compared to those species with a deprotonated peptide bond.

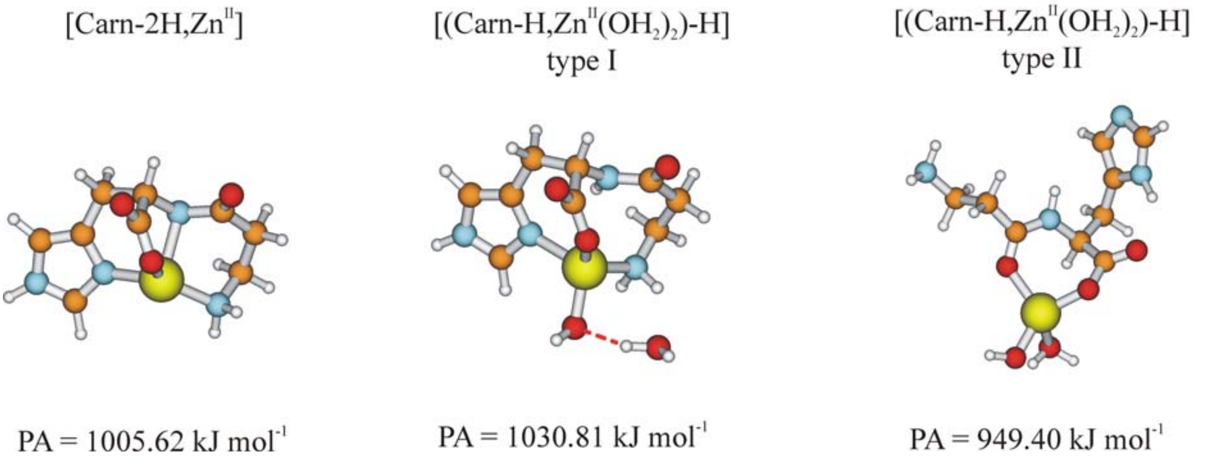

Fig. 6.11 BLYP/TZVP optimized minimum structures and proton affinities at 298 K of [Carn-2H,Zn] and [(Carn-H,Zn(OH$_2$)$_2$)-H] complexes of type I (Zn^{II} ion is enclosed in binding pocket formed by the carnosine ligand) and II (Zn^{II} is attached to the "surface" of the carnosine ligand).

The performed calculations reveal that PAs of Zn^{II}/carnosine complexes [Carn-2H,Zn^{II}] and [(Carn-H,Zn^{II}(OH$_2$)$_2$)-H]$^+$ (type I) are larger with regard to that of carnosine by approximately 30-40 kJ mol^{-1}, respectively 56-62 kJ mol^{-1}, whereas the PA of [(Carn-H,Zn^{II}(OH$_2$)$_2$)-H] complexes of type II is found to be smaller by 20-25 kJ mol^{-1}.

The mass spectra of aqueous solutions of carnosine contain a series of protonated carnosine oligomers with the formal stoichiometry [n×Carn+H]$^+$. To evaluate the effect of oligomerization on the PA, the PA of the dimer [2×Carn] was also computed. Similar to the scheme describe before for protonated carnosine and Zn^{II}/carnosine complexes, in a first step different protonated carnosine dimer structures were geometry optimized to obtain an overview of possible [2×Carn+H]$^+$ structues and energies. In a second step the labile hydrogens of the protonated dimer were removed and the neutral complexes were reoptimized.

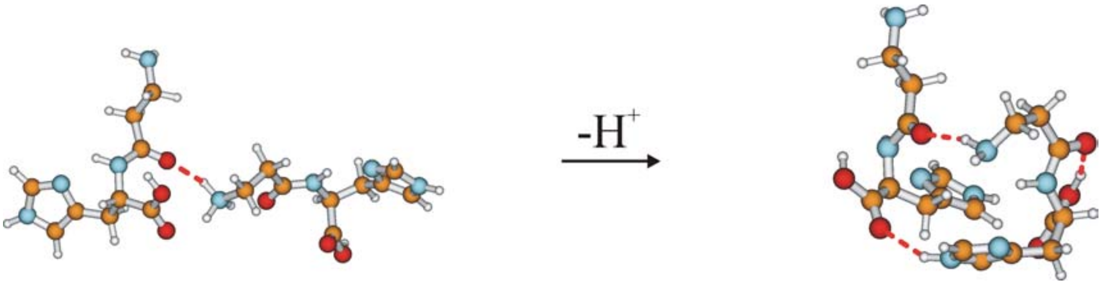

Fig. 6.12 BLYP/TZVP optimized structures of the protonated carnosine dimer [2×Carn+H]$^+$ (left) and the neutral dimer [2×Carn] (right).

The energetically lowest $[2\times Carn+H]^+$ and $[2\times Carn]$ complexes obtained according to this scheme are shown in Fig. 6.12. The PA of the depicted neutral dimer was computed to be 1047 kJ mol^{-1} at T = 298 K. This value is higher than the PAs of carnosine ($\Delta PA \approx +41$ kJ mol^{-1}) and neutral $[Carn-2H,Zn^{II}]$ complexes ($\Delta PA \approx +5$ kJ mol^{-1}) and confirms that protonation of the oligomers leads to a significant increase of intermolecular forces between the carnosine monomers.

F. Gas-Phase H/D Exchange of Protonated Carnosine (Multimers) and Zn^{II}/Carnosine Complexes

In this chapter the technique of gas-phase H/D exchange is utilized to probe fundamental properties of carnosine like e.g. its PA and the effect of oligomerization and metal coordination upon these properties. The mass spectra of aqueous carnosine solutions contain several species identified as protonated oligomers of hydrogen bonded carnosine monomers $[Carn_n+H]^+$. The structure and properties of these interesting species are important as they might serve as model systems for larger peptides. Many (multi) enzyme complexes consist of weakly bonded enzyme “subunits” and the influence of weak interactions between these subunits on the activity of the whole is far from beeing thoroughly understood on a molecular level. As outlined in the introduction structure and properties of Zn^{II}/carnosine complexes are interesting for themselves but they might also serve as model system for larger metalloproteins. Therefore the properties of the observed Zn^{II}/carnosine species were also investigated by gas-phase H/D exchange experiments. To facilitate an unambigous interpretation of the experimental data, these are supplemented by DFT calculations.

Gas-phase H/D exchange of small peptides and related compounds has been subject of intense research before, and all of the studies performed agree that even for a system such small as a dipeptide, the H/D exchange is a very complex process. It was suggested that the mechanism depends on the PAs of the different species by Beauchamp and coworkers[37]. For species whose proton affinities differ by less than ~80 kJ mol^{-1} hydrogen exchange was postulated to occur via formation of a strong hydrogen bonded species.

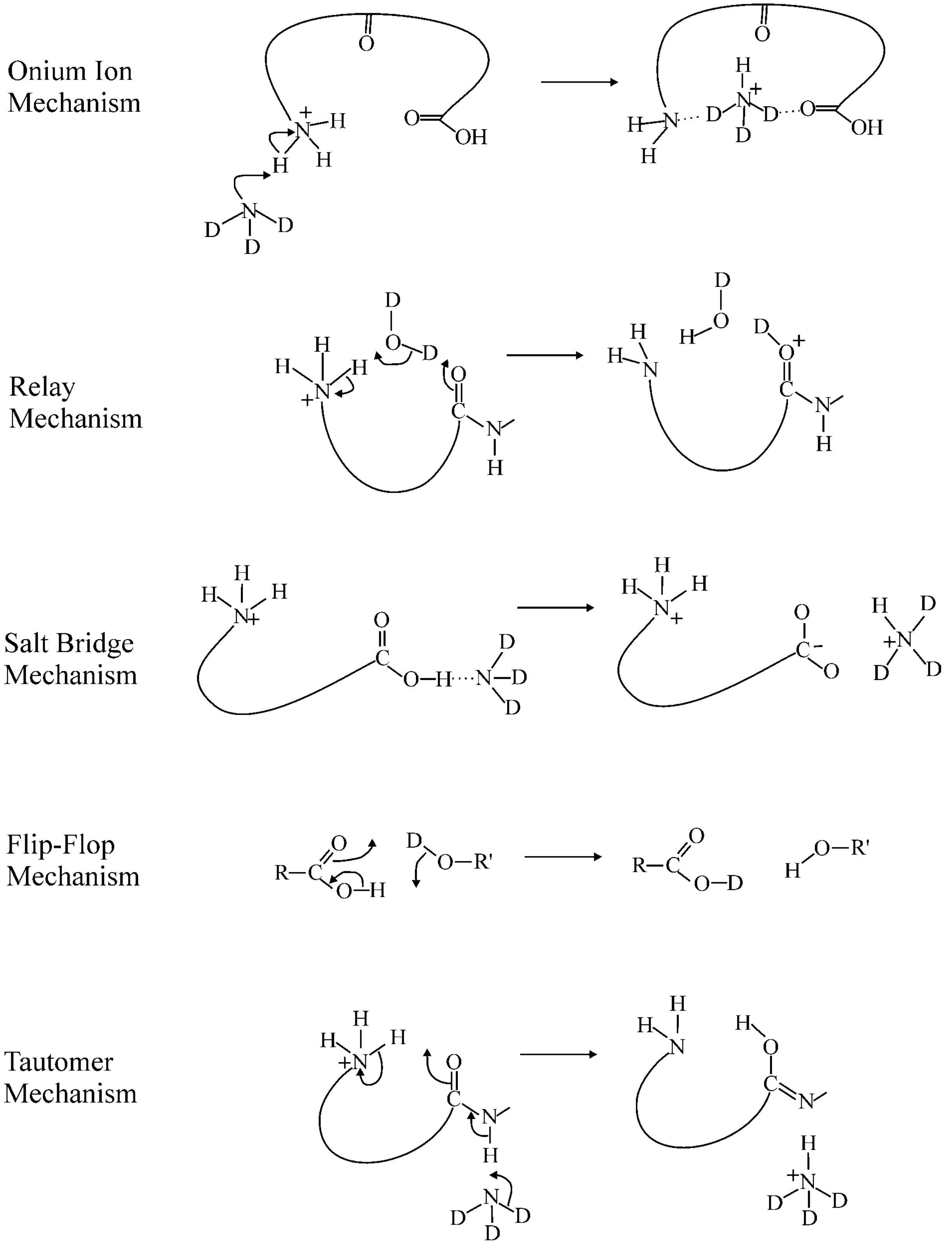

Fig. 6.13 Summary of H/D exchange mechanisms as discussed in Ref. 25.

In contast for cluster species whose PAs differ by more than ~80 kJ mol^{-1} more complex exchange mechanisms were suggested. For example, in case of glycine oligomers (different than for carnosine oligomers the term "oligomers" denominates a macromolecule, in which glycine monomers are covalently linked through peptide bonds) up to five different exchange mechanisms were discussed (cf. Fig. 6.13). An "onium ion mechanism" was proposed for protonated glycine oligomers which exchange with basic reagents such as ND_3. In its course, a nominally endothermic proton transfer from the N-terminus is accompanied by simultaneous solvation of the resultant ammonium ion. For less basic reagents like D_2O, whose PA does not suffice to overcome the endothermicity of proton transfer from the peptide, a relay mechanism in which the deuterating reagent shuttles a proton from the N-terminus to a slightly less basic site (amide oxygen) was proposed. The calculated PAs of carnosine differ from those of D_2O and ND_3 by significantly more than 80 kJ mol^{-1}. The mechanisms of H/D exchange as given in Fig. 6.13 surely apply to $[n\times\text{Carn}+\text{H}]^+$ well. However, it is not a priori clear, whether they also apply to H/D exchange in Zn$^{\text{II}}$/carnosine complexes, in which the carnosine ligand is deprotonated and the positive charge is located at the Zn$^{\text{II}}$ dication.

H/D Exchange with D_2O

D_2O as deuterating gas yielded the exchange of up to three hydrogen atoms in protonated carnosine $[\text{Carn}+\text{H}]^+$, up to four in the protonated carnosine dimer $[2\times\text{Carn}+\text{H}]^+$ but only two in the protonated trimer $[3\text{xCarn}+\text{H}]^+$. Lager complexes $[n\times\text{Carn}+\text{H}]^+$, n>3, were not observed to exchange hydrogen against deuterium atoms at all. In case of the Zn$^{\text{II}}$ containing carnosine complexes H/D exchange was exclusively observed in the case of $[\text{Carn-H,Zn}]^+$, for which three hydrogens were found to exchange, as many as in the protonated carnosine monomer $[\text{Carn}+\text{H}]^+$. For $[\text{Carn-H,Zn}^{\text{II}}(\text{OH}_2)_2]^+$ and all other Zn$^{\text{II}}$/carnosine complexes with more than one carnosine chelate ligand no H/D exchange was encountered. Thus the total number of exchanged hydrogens does not increase with growing complex size. This holds true for $[n\times\text{Carn}+\text{H}]^+$ and for Zn$^{\text{II}}$/carnosine complexes. This finding is indicative of a retardation of the exchange process either due to steric hindrances in larger complexes or due to an increase of PA with complex size (≈ number of carnosine monomers).

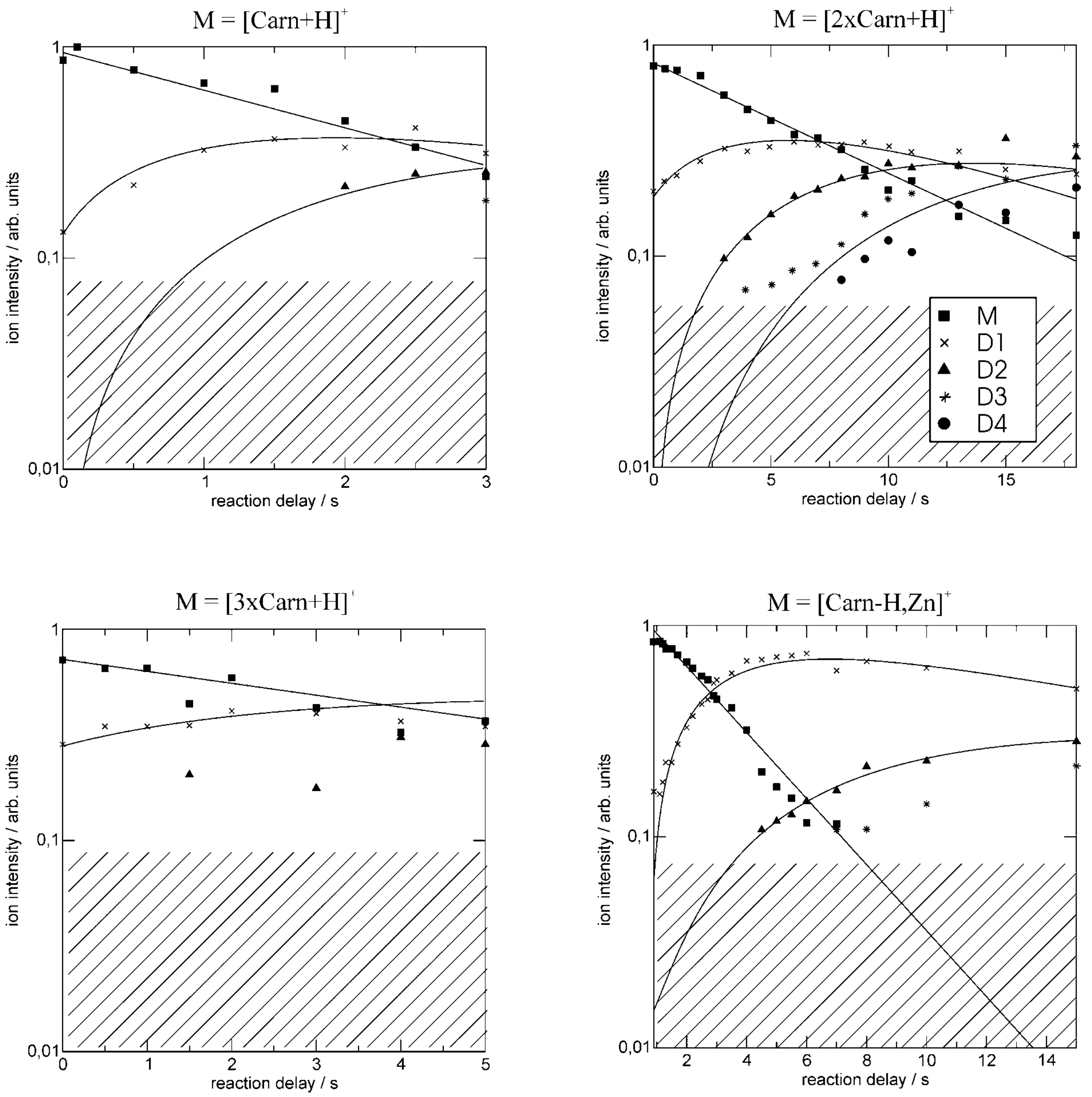

Fig. 6.14 Time plot of the deuterium exchange of different Zn^{II}/carnosine complexes. M denotes the "mother" without deuterium, in D1 one H has been exchanged against D in D2 two and so forth.

Table 6.4 Unimolecular H/D exchange rates for different carnosine complexes assuming sequential exchange

Complex	*D1*	*D2*	*D3*	*D4*
[Carn+H]$^+$	0.41±0.12	0.47±0.15	0.43±0.15	---
[2×Carn+H]$^+$	0.12±0.03	0.14±0.03	0,13±0.04	0.06±0.04
[3×Carn+H]$^+$	0.13±0.10	0.14±0.05	---	---
[Carn-H,Zn]$^+$	0.36±0.08	0.06±0.03	0.09±0.03	---

The time plots of the resulting ion intensities in the course of the H/D exchange reactions of $[n\times Carn+H]^+$, n=1-3, and $[Carn\text{-}H,Zn]^+$ are given in Fig. 6.14. For the following analysis it is important to note that the conception of the first gas-phase H/D exchange event to occur exclusively at the most reactive site is too simple. It is more realistic to assume that different sites of exchangeable hydrogen atoms have different exchange probabilities and that a peptide species nominal with one hydrogen exchanged against deuterium, actually is comprised of a distribution of species labeled with deuterium at different sites.

Due to inter- and (in larger complexes) also intramolecular proton (deuteron) transfers, e.g. between the N-terminus and the carboxylic acid residue, exchanged deuterons can also be distributed over the peptide. For reasons of simplicity we will confine mechanistic reflections to the most reactive species.

In case of the protonated carnosine monomer $[n\times Carn+H]^+$ the H/D exchange mechanism proposed by Beauchamp and coworker (cf. Fig. 6.13) for protonated glycine oligomers applies. When D_2O is used as deuterating reagent a relay mechanism is most probable for protonated carnosine due to the relatively low PA of D_2O (~691 kJ mol^{-1}). If the deuterating agent is more basic, like in case of ND_3 (PA= 854 kJ mol^{-1}), an onium ion mechanism is most probable. These two processes and all of the other mechanisms summarized in Fig. 6.13 assume the N-terminus of the peptide to be protonated, or – like for the flip flop mechanism – to contain an acidic H atom. This requirement is surely met in case of carnosine $[Carn+H]^+$ and the protonated carnosine oligomers $[n\times Carn+H]^+$, n=1-3.

The H/D exchange rates of $[n\times Carn+H]^+$, n=1-3, and $[Carn\text{-}H,Zn^{II}]^+$ are listed in Table 6.4. It is important to note that the data as given in Table 6.4 assume sequential H/D exchange, i.e. only a single hydrogen atom is exchanged against a deuterium during one collision. We also investigated the possibility of two exchanges at a time, but the resulting exchange rates lie within the error margins of the sequential exchange. The exchange rates of $[n\times Carn+H]^+$, n=1-3, exhibit a sharp drop of the exchange rates between the protonated carnosine monomer n=1 and the dimer n=2, whereas the corresponding exchange rates of the dimer n=2 and trimer n=3 are close to each other. For oligomers larger than n=3 no H/D exchange was encountered.

In analogy to the decrease of the total number of exchanged hydrogens with growing complex size, the H/D exchange rate decelerate with growing size in $[n\times Carn+H]^+$. This can be due to (a) steric reasons, the labile hydrogen atoms could become less accessible with growing cluster size, (b) to an increase of the PAs of $[n\times Carn+H]^+$ with growing cluster size n, or to a combination of (a) and (b). Assuming an Arrhenius type of kinetics the exchange of the proton is expected to be the slower the higher the proton binding energy (which correlates with the activation barrier) is. According to the performed ab initio calculations (see section E) the PA of carnosine is indeed increased by aggregation to carnosine oligomers. The positive charge of $[n\times Carn+H]^+$ is stabilized by attractive charge-dipole interactions which increase the monomer binding energies. In $[n\times Carn+H]^+$ ionic hydrogen bonds are formed between the protonated sites (hydrogen donor) and more acidic sites (hydrogen acceptor) like e.g. a free N-terminus of another monomer. These ionic hydrogen bonds are lost upon removal of the proton. The monomer binding energy in the protonated dimer $[2\times Carn+H]^+$ was calculated to be about -73 kJ mol^{-1}, while for the located minimum of the neutral carnosine dimer, the binding energy was determined to be -17 kJ mol^{-1}. The large difference in binding energies of almost 50 kJ mol^{-1} is indicative of a significant increase of the attractive interactions beween the carnosine monomers due to protonation. We note in passing that in the geometry optimizations of the neutral carnosine dimer salt bridge formation through intramolecular acid-base reactions ($Carn\text{-}COOH + Carn\text{-}NH_2 \rightarrow Carn\text{-}COO^- + Carn\text{-}NH_3^+$) was also considered, but charge separation proved not to be stable for the dimer according to the performed DFT calculations.

The observed reactivity of $[n\times Carn+H]^+$ in the H/D exchange reaction is understood assuming the H/D mechanisms proposed by Beauchamp and coworkers. With growing complex size n the steric hindrance and the PA of the species increases, decelerating the H/D exchange, until for $n>3$ (in case of D_2O as deuterating gas) H/D exchange is no longer observable.

According to the performed ab initio calculations the PAs of all investigated Zn^{II}/carnosine complexes differ substantially from that of D_2O. Therefore any potential H/D exchange is expected to proceed via one of the mechanisms introduced in Fig. 6.13. The H/D exchange mechanisms most probable for protonated carnosine and protonated carnosine oligomers – relay mechanism and onium ion mechanism – are not applicable to Zn^{II}/carnosine complexes. In the singly charged metal containing species the carnosine ligand is deptrotonated and exists as $(Carn\text{-}H)^-$. Other mechanisms besides the onium ion and relay mechanism were put forward by Beauchamp and coworkers like the salt bridge mechanisms, the flip flop mechanism, or the tautomer mechanism.

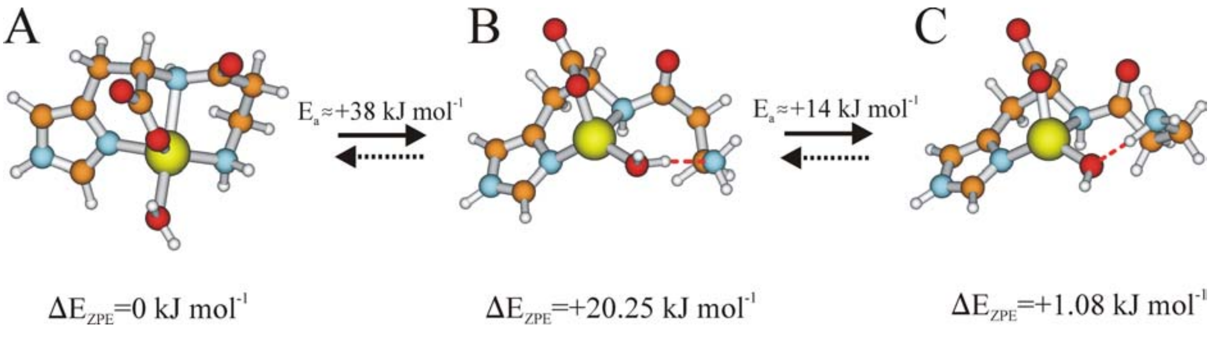

Fig. 6.15 Proposed mechanism of H/D exchange in [Carn-H,Zn^{II}]$^+$. In the first step a D_2O ligand attached to the Zn^{II} dication inserts into the Zn···NH_2- bond. Subsequently the D_2O ligand hydrolyses into a D^+, which is transferred to the N terminus of carnosine, and a OH^-, which remains bound to the Zn^{II} dication.

However, all of these mechanisms share the prerequisite of an ammonium group -NH_3^+, or as in case of the flip-flop mechanism, at least an acidic hydrogen atom like that of an carboxylic acid residue -COOH. The deprotonated carnosine ligand in [Carn-H,Zn]$^+$ has neither an ammonium group –NH_3^+ nor an carboxylic acid residue -COOH. Nevertheless H/D exchange is found to occur in [Carn-H,Zn^{II}]$^+$. One carnosine ligand does not suffice to occupy all coordination sites of the Zn^{II} dication and the Zn^{II} dication in [Carn-H,Zn^{II}]$^+$ is coordinatively unsaturated (cf. Fig. 6.11). As soon as the vacant coordination sites at the Zn^{II} dication are occupied either by H_2O ligands or by a second carnosine ligand the H/D exchange is no longer observed. Hence for Zn^{II}/carnosine complexes H/D exchange is exclusively observed for [Carn-H,Zn]$^+$. Therefore it is postulated that attachment of D_2O ligand to the metal ion is the first fundamental step of the H/D exchange mechanism in [Carn-H,Zn^{II}]$^+$ (cf. A in Fig. 6.15). Due to the high charge density of the Zn^{II} dication the O-D bonds of the D_2O ligands attached to Zn^{II} are strongly polarized. The acidic D atoms interact with the basic sidechains of the carnosine ligand and the $^{\delta-}$O-D$^{\delta+}$ bond is inserted into the Zn-NH_2-Carn bond (cf. B in Fig. 6.15). Subsequently D_2O is hydrolyzed into a hydroxyl (OD^-) anion and a deuteron D^+, which reacts with the N-terminus of carnosine to form an ammonium (R-NDH_2^+) ion (cf. C in Fig. 6.15). Overall the reaction is only slightly endothermic and the activation barriers of approximately 38.2 resp. 13.7 kJ mol^{-1} can be activated on a subsecond timescale. The average internal energy of the ions generated in the ES source is mainly determined by the thermal energy gained in the heated capillary of the ES source (T=418 K), the energy gain in the capillary-skimmer region (potential difference: 50 – 270 V) and the energy gain by collision with the deuterating gas in the ICR cell. It has been shown before that the internal energy of electrosprayed ions is sufficiently high to activate barriers of the order of 40 kJ mol^{-1}.[59-62]

Following the deuteron transfer to the N-terminus of carnosine, the O···D hydrogen bond is replaced by O···H through rotation of the ammonium group around the $^+DH_2N$-Carn bond axis (rotational barrier ≈20 kJ mol^{-1}). In the back-reaction of Fig.6.15 the proton involved in this O···H hydrogen bond is transferred to the OD^- anion resulting in the formation of DHO. The NH of the peptide bond –NHCO– is also attached to the Zn^{II} dication, and the acidic hydrogen atom might be exchanged versus deuterium by a similar mechanism as the one in Fig. 6.15. Therefore it is speculated that the three experimentally observed hydrogen atoms are the two located at the amino terminus of carnosine and the one of the peptide bond.

6.5 Conclusions

The structures and stabilities of protonated carnosine, different protonated carnosine oligomers $(n\times Carn+H)^+$ and of (hydrated) Zn^{II}/carnosine complexes were investigated by high resolution ES-MS and ab initio calculations. The performed mass spectrometric studies indicate two different Zn^{II}/carnosine complex structures which differ significantly in their H_2O binding energies. If present at all, H_2O is always contained in pairs of two. This is attributed to two different Zn^{II} complexation modes in Zn^{II}/carnosine complexes: The Zn^{II} ion is either complexed “internally” within a binding pocket formed by carnosine, so that Zn^{II} is screened from H_2O, or Zn^{II} is complexed “externally” at the surface of the carnosine ligand. DFT calculations reveal that in the open structures the Zn^{II} ion coordinates to only two carnosine atoms. Consequently the solvent has easy access to the unscreened metal ion and two H_2O ligands will occupy vacant coordination sites. This leads to a tetrahedrally coordinated Zn^{II} ion with two strongly bound first shell H_2O ligands in accordance with the experimental observation.

Gas-phase H/D exchange reactions of protonated carnosine oligomers $(n\times Carn+H)^+$, n=1-3, and (hydrated) Zn^{II}/carnosine complexes with D_2O were performed to investigate complex structures and to probe relative proton affinities of the corresponding (deprotonated) neutral structures. Formation of van der Waals complexes $(n\times Carn)^+$, n>1, leads to a significant increase in proton affinity, as attractive interactions between carnosine monomers are enhanced through protonation. H/D exchange is known to proceed efficiently when the difference between the proton affinities of the reagent and deprotonated analyte is small.

However, in case of Zn^{II}/carnosine complexes H/D exchange is exclusively observed for $[Carn\text{-}H,Zn^{II}]^+$, even though the computed proton affinity of the hydrated complex $[(Carn\text{-}2H,Zn^{II}(OH_2)_2)\text{-}H]$ is lower than that of $[Carn\text{-}2H,Zn^{II}]$ and closer to that of D_2O by approximately 56 kJ mol^{-1}. This finding is indicative of a H/D exchange mechanism that is promoted by vacant Zn^{II} coordination sites. Different than for $(n\times Carn+H)^+$ proton transfer mechanisms, which assume a protonated site or at least an acidic group, are not applicable in the case of $[Carn\text{-}H,Zn^{II}(OH_2)_p]^+$, p=0,2. The carboxylic acid group of the ligand is deprotonated and the remaining most acidic group is the –NH– of the peptide bond (which is available both in p=0 and p=2). Instead an alternative H/D exchange mechanism is proposed for $[Carn\text{-}H,Zn^{II}(OH_2)_p]^+$, which involves coordination of D_2O to the Zn^{II} ion and requires free coordination sites at the Zn^{II} dication. This requirement is fulfilled in $[Carn\text{-}H,Zn^{II}]^+$ but not in $[Carn\text{-}H,Zn^{II}(OH_2)_2]^+$.

In the first step of the proposed H/D exchange mechanism a D_2O ligand attaches to the Zn^{II} dication. Subsequently, in a second reaction step, D_2O inserts into the $Zn^{II}\cdots NH_2$- bond between the metal ion and the N-terminus of carnosine. Due to the high charge density of the Zn^{II} metal ion, the O-D bonds are strongly polarized, and D_2O hydrolyzes into D^+, which is transferred to the N-terminus, and OD^-, which remains bound to the Zn^{II} dication (D_2O + H_2N-Carn -> $DO^-\cdots{}^+DH_2N$-Carn). By rotation of the ammonium group around the $^+DH_2N$–Carn bond axis, the $DO^-\cdots{}^+DH_2N$-Carn hydrogen bond is replace by a $DO^-\cdots{}^+HDHN$-Carn hydrogen bond. In the back-reaction the proton involved in this hydrogen bond is transferred to the OD^- and DHO is formed, completing the H/D exchange ($DO^-\cdots{}^+HDHN$-Carn -> DOH + DHN-Carn). The maximum activation barrier along the reaction coordinate of this process has been calculated to be 38 kJ mol^{-1}.

6.6 References

1 W. S. Gulewitsch, S. Amiridzibi, *Ber. Dtsch. Chem. Ges.* 1900, **33**, 1902.

2 K. G. Crush, *Comput. Physiol.*, 1970, **34**, 3.

3 R. Kohen, Y. Yamamoto, K. C. Cundy, B. N. Ames, *Proc. Natl. Acad. Sci. USA*, 1988, **85**, 3175.

4 E. J. Baran, *Biochemistry* 2000, **65**, 928.

5 A. A. Bpldyrev, A. M. Dupin, E. V. Bindel, S. E. Severin, *Comp. Biochem. Physiol.*, 1988, **89B**, 245.

6 E. A. Decker, A. D. Crum, J. T. Calvert, *J. Acric. Food. Chem.*, 1992, **40**, 756.

7 O. I. Arouma, M. J. Laughton, B. Halliwell, *Biochem. J.*, 1989, **264**, 863.

8 C.-L. Hsieh, Y.-C. Ho, H. H. Lai, G. C. Yen, *Journal Of Food and Drug Analysis*, 2002, **10**, 47.

9 G. Kansci, C. Genot, A. Meynier and Gilles Gandemer, *Food Chemistry*, 1997, **60**, 165.

10 C.-L. Hsieh, Y.-C. Ho, H. H. Lai, G. C. Yen, *Journal Of Food and Drug Analysis*, 2002, **10**, 47.

11 E. A. Decker, S. A. Livisay, S. Zhou, *Biochemistry*, 2000, **65**, 901.

12 S. H. Wong, C. H. Cho, X. W. Ogle, *Pharmacology*, 1986, **33**, 94.

13 H. Aiza, T. Yoneta, H. Morita K. Seto, Y. Hori, M. Seki, Y. Ikeda, *Ulcer Res.*, 1993, **20**, 127.

14 M. Yamaguchi, *Current Medicinal Chemistry*, 1995, **1**, 358.

15 H. Itoh, T. Yamane, T. Ashid, M. Kakudo, *Acta Chrytallogr.*, 1977, **B3,** 2959.

16 A. Torreggiani, S. Bonora, G. Fini, *Biopolymers*, 2000, **57**, 352.

17 E. Farkas, I. Sóvágó, A. Gergeley, *J. Chem. Soc. Dalton. Trans.*, 1983, 1545.

18 P. Mineo, D. Vitalini, D. la Mendola, E. Rizzarelli, E. Scamporrino, G. Vecchio, *Rapid Commun. Mass Spetrom.* 2002, **16**, 722.

19 A. D. Becke, *Phys. Rev. A*, 1988, **38**, 3098.

20 C. Lee, W. Yang, R. G. Parr, *Phys. Rev. B* 1988, **37**, 785.

21 A. P. Lyubartsev, K. Laasonen, A. Laaksonen, J. Chem. Phys. 2001, 114, 3120.

22 G. Bruge, M. Bernasconi, M. Parinello, *J. Chem. Phys.* 1999, **110**, 4734.

23 R. Vargas, J. Garzas, B. P. Hay, D. A. Dixon, *J. Phys. Chem. A* 2002, **106**, 3213.

24 A. Schäfer, C. Huber, R.Ahlrichs *J. Chem. Phys.* 1994, **100**, 5829.

25 R. Ahlrichs, M. Bär, M. Häser, H. Horn, C. Kölmel, Chem. Phys. Lett. 1989, **162**, 165.

26 M. V. Arnim, R. Ahlrichs, *J. Comput. Chem.* 1998, **19**, 1746.

27 K. Eichkorn, O. Treutler, H. Öhm, M. Häser, R. Ahlrichs, Chem. Phys. Lett. 1995, **240**, 283.

28 M. Schutz, S. Brdarski, P.-O. Widmark, R. Lindh, G. Karlstrom, *J. Chem. Phys.* 1997, **107**, 4597.

29 V. Katta, B. T. Chait, *J. Am. Chem. Soc.* 1993, **115**, 6317.

30 J. J. Englander, C. Del Mar, W. Li et al., *Proc. Natl. Acad. Sci USA* 2003, **100**, 7057.

31 D. R. Reed, S. R. Kass, *J. Am. Soc. Mass Spectr.* 2001, **12**, 1163.

32 J. A. Loo, Studying non-covalent protein complexes by electrospray ionization mass spectrometry. *Mass Spectrom Rev.* 1977, **16**, 1.

33 R. D. Smith, K. J. Light-Wahl, The observation of non-covalent interactions in solution by electrospray ionization mass spectrometry-promise, pitfalls and prognosis. *Biol. Mass Spectrom.* 1993, **22**, 493.

34 H. J. Cooper, M. A.Case, G. L. McLendon, A. G. Marshall, *J. Am. Chem. Soc.*, 2003, **125**, 5331.

35 C. L. Gatlin, F. Tureček, Electrospray Ionization of Inorganic and Organometallic Complexes in Electrospray Ionization Mass Spectrometry, Fundamentals, Instrumentation and Application, Ed. R. B. Cole, John Wiley & Sons, Inc., New York, 1997.

36 S. E. Severin, Proc. Plen. Sess. VI Int. Congr. Biochem., N. Y., pp. 45-61.

37 S. Campbell, M. T. Rodgers, E. M. Marzluff, J. L. Beauchamp, *J. Am. Chem. Soc.* 1995, **117**, 12840.

38 M. F. Jarrold, *Annu. Rev. Phys. Chem.*, 2000, **51**, 179.

39 K. Biermann, Methods in Enzymology, Ed. J. McCloskey, Academic Press, San Diego, CA, 1990, Vol. 193, p351.

40 R. S. Johnson, S. A. Martin, K. Biemann, Int. *J. Mass Spectrom. Ion Processes*, 1988, **86**, 137.

41 D. F. Hunt, J. R. III. Yates, J. Shabanawitz, S. Winston, C. R. Hauer, *Proc. Natl. Acad. Sci. USA.*, 1986, **83**, 6233.

42 B. L. Schwartz, M. M. Bursey, Biol. Mass Spetrom. 1991, **21**, 92.

43 W. Staudenmann, P. James, Proteome Research: Mass Spectrometry, Ed. P. James, Springer, Berlin, 2001, pp143.

44 C. J. Cassady, S. R. Carr, *J. Mass Spectrom.*, 1996, **31**, 247.

45 B. E. Winger, K. J. Light-Wahl, A. L. Rockwood, R. D. Smith, *J. Am. Chem. Soc.*, 1992, **114**, 5897.

46 D. Suckau, Y. Shi, S. C. Beu, M. W. Senko, J. P. Quinn et al., *Proc. Natl. Acad. Sci. USA*, 1993, **90**, 790.

47 T. D. Wood, R. A. Chorush, F. M. Wampler, D. P. Little, P. B. O' Connor, F. W. McLafferty, *Proc. Natl. Acad. Sci. USA*, 1995, **92**, 2451.

48 S. J. Valentine, D. E. Clemmer, *J. Am. Chem. Soc.*, 1997, **119**, 3558.

49 F. W. McLafferty, Z. Guan, U. Haupts, T. D. Wood, N. L. Kelleher, *J. Am. Chem. Soc.*, 1998, **120**, 4732.

50 M. A. Freitas, C. L. Hendrickson, M. R. Emmet, A. G. Marshall, *Int. J. Mass Spectrom.*, 1999, **187-189**, 565.

51 F. Wang, M. A. Freitas, A. G. Marshall, B. D. Sykes*, Int. J. Mass Spectrom.*, 1999, **192**, 319.

52 B. S. Freiser, R. L. Woodin, J. L. Beauchamp, *J. Am. Chem. Soc.*, 1975, **97**, 6893.

53 A. Ranasinghe, R. G. Cooks, S. K. Sethi, *Org. Mass Spectrom.*, 1992, **27**, 77.

54 R. R. Squires, V. M. Bierbaum, J. J. Grabowski, C. H. DePuy, *J. Am. Chem. Soc.* 1983, **105**, 5185.

55 S. G. Lias, *J. Phys. Chem.*, 1984, **88**, 4401.

56 D. F. Hunt, S. K. Sethi, *J. Am. Chem. Soc.*, 1980, **102**, 6953.

57 K. A. Peterson, S. S. Xantheas, D. A. Dixon, T. H. Dunning, Jr., *J. Phys. Chem. A*, 1998, **102**, 2449.

58 B. S. Jursic, *Theochem* 1999, **487**, 193.

59 D. Laszlo, R.M. A. Heeren, C. Collette, E. De Pauw, K. Vekey, *J. Mass Spectrom.* 1999, **34**, 1373.

60 B. B. Schneider, D. J. Douglas, D. D. Y. Chen, *J. Am. Soc. Mass Spectrom.* 2001, **12**, 772.

61 Z. Takats, L. Drahos, G. Schlosser, K. Vekey, *Anal. Chem.* 2002, **74**, 6427.

62 C. Collette, E. De Pauw, *Rapid Commun. Mass Spectrom.* 1998, **12**, 165.

7. Coordination versus Internal Reaction in Niobium-Acetonitrile Complexes Probed by Infrared Radiation Multiphoton Dissociation Spectroscopy

Experimental IR multiphoton dissociation spectra of metal containing ion-molecule complexes with the formal stoichiometry $[Nb,nCH_3CN]^+$*, n=4-5, are compared to ab initio IR absorption spectra throughout the spectral "fingerprinting" range 780-2500* cm^{-1}*, as provided by the Free Electron Laser at Clio, Orsay, France. The vibrational spectra provide clear evidence for a square planar high spin quintet* $[Nb^I(NCCH_3)_4]^+$ *complex. For n=5 additional vibrational bands between 1300-1600* cm^{-1} *are interpreted in terms of C-C coupling in* $[Nb,5CH_3CN]^+$*. Screening on the basis of ab initio calculations leads to an assignment of the recorded spectrum in terms of a metallacyclic species* $[Nb^{III}(NCCH_3)_3(N{=}C(CH_3)C(CH_3){=}N)]^+$ *with an electronic triplet state. The observed processes upon fourfold and fivefold coordination of* Nb^I *with* CH_3CN *in the gas-phase are complexation only and reductive nitrile coupling respectively. The minimum energy pathways of the reductive nitrile coupling reaction from* $[Nb^I(NCCH_3)_n]^+$*, n=4-5, investigated for singlet, triplet and quintet states (S=0,1,2) by density functional theory, account well for the observed (non-) reactivity. In ground state (triplet, S=1)* $[Nb^I(NCCH_3)_5]^+$*, the reaction is found to be exothermic and the activation barrier amounts to approximately 49 kJ* mol^{-1}*, whereas for ground state quintet (S=2)* $[Nb^I(NCCH_3)_4]^+$ *the reaction is endothermic and requires activation of >>116 kJ* mol^{-1}*. Close but incomplete correspondence of IR-MPD and IR absorption spectra is discussed in terms of the underlying mechanism.*

7.1 Introduction

Reactions that form new C-C bonds are the key steps in the catalytic synthesis of almost any organic compound. E.g. the McMurry C-C coupling of two aldehydes or ketones yields vicinal diols when catalyzed by titanium at low temperatures.[1] Reductive nitrile C-C coupling happens to nitrile complexes or to metal nitriles in the presence of halides.[2] While some reactions of cationic niobium-clusters with acetonitrile have been subject of mass spectrometric studies under single collision conditions,[3-4] the structures of niobium-acetonitrile complexes and clusters are still unknown. Other than in bulk phase solutions the IR spectroscopy of isolated gas-phase complexes is not complicated by ligand solvent interactions. Moreover, ab initio modelling allows for an unambigious interpretation of the gas-phase IR spectra that provides a powerful tool for structure determination. However, IR spectroscopic studies of isolated gas-phase complexes face the inherent problem of low number densities which do not allow application of traditional IR absorption techniques. In this work the vibrational spectra of niobium-acetonitrile complexes are investigated by IR multiphoton dissociation spectroscopy (IR-MPD)[5] instead. After absorption of an IR photon, internal vibrational relaxation (IVR) within the excited complex randomizes the excitation energy out of the excited vibrational mode into the heat bath of all the accessible modes. IR-MPD spectroscopy relies on this ready coupling and that at least a single fragmentation channel of the complex is effectively activated. Although the IR-MPD technique can cope with the inherent problem of the low concentration of ions in the gas phase, this technique suffers from the lack of common high power tunable light sources for the full range of the chemical infrared. The spectral range of e.g. line tunable CO_2 lasers is limited to a spectral range between 930 ~ 1085 cm^{-1} and modern optic parametric oscillators (OPOs) do not cover spectral ranges below ≈2200 cm^{-1}. It was shown before[6-10] that a free electron laser (FEL) is suitable to activate IR-MPD over a wide frequency range yielding data that closely mimic IR absorption spectra.[11-12] The IR-MPD spectra mimics the IR absorptions spectra closely but it does not resemble it perfectly. Problems in the assignments of the recorded IR-MPD spectra may arise from so called “dark absorptions”, which denominate vibrational resonances that do not lead to detectable fragmentation signals, either due to an inefficient multiphoton absorbtion or due to ineffective energy transfer from the excited mode into an accessible fragmentation channel.

7.2 Experimental and Computational Methods

The IR spectra were recorded at the “Centre Laser Infrarouge d’Orsay” (CLIO) FEL facility. CLIO is based on a 10 to 50 MeV electron accelerator and has a very large wavelength range in the infrared from 3 to 75 μm, which is continously tuneable over a wide spectral range ($\Delta\lambda/\lambda \approx 2.5$). The FEL temporal structure is composed of trains of macropulses with a duration of 8 μs at a repetition rate of 25 Hz. Each of these macropulses contains 500 micropulses, which are only a few picoseconds long. The FEL laser light was focussed into the center of a 1.25 Tesla Fourier Transform Ion Cyclotron Resonance (FT-ICR) ion trap by a spherical mirror of 1m focal length (estimated laser spot size ≈ 400 μm).[13] The open design of the ICR cell in use provides good optical access to its center, facilitating spectroscopic investigations of ions stored within it. Atomic Nb^{I} monocations were generated by Nd:YAG laser driven ablation off a niobium target adjacent to the ICR cell. Acetonitrile (MeCN) was admitted into the cell through a pulsed valve at 3.5x10^{-6} mbar for 200 ms. Subsequently Nb^I ions were allowed to form complexes with CH_3CN for 1 s, and those complexes with the formal stoichiometry $[Nb,nCH_3CN]^+$ were mass selected by resonant frequency ejection techniques. Exposure to FEL IR radiation (average power ≈ 280 mW) for 2s led to multiphoton absorption and complex fragmentation when resonant with a fundamental vibration. Fragment ion intensities and parent ion "dips" were recorded as function of the FEL wavelength in order to obtain the experimental IR-MPD spectra.

If not otherwise stated ab initio IR absorption spectra were calculated at the B3LYP level of theory and for singlet, triplet and quintet spin states. This method was chosen as several calibration calculations have proved that this functional yields accurate geometries and vibrational frequencies in transition metal compounds,[14-15] provided that spin orbit coupling is small. In Nb^I spin orbit coupling is of the order of 150 cm^{-1} and can still be ignored. Ahlrichs polarized triple-ζ basis sets were applied for C,N,H.[16] Relativistic effective core potential[17] and Ahlrichs polarized triple-ζ basis set described the Nb (1s-3d) and valence electrons respectively. In order to determine activation barriers for the reductive nitrile coupling reactions we parametrically varied the C-C distance between two adjacent acetonitrile ligands MeCN, while all other coordinates were freely optimized. All calculations were performed with the TURBOMOLE[18] ab initio program.

7.3 Results and Discussion

A. IR-MPD Spectra of Niobium-Acetonitrile Complexes $[Nb,nCH_3CN]^{+}$[#], n=4-5

All of the recorded vibrational bands of complexes with the formal stoichiometry $[Nb,4CH_3CN]^+$ (Figure 1) are close to the vibrations of the free CH_3CN molecule[19] except for the $\delta^{rock}(CH_3)$ mode at 1090 cm^{-1}, which is significantly blue shifted. The ν(CN) band is

---

[#] The notation $[Nb,nCH_3CN]^+$ refers exclusively to the formal stoichiometry of a cluster and does not contain any structural information.

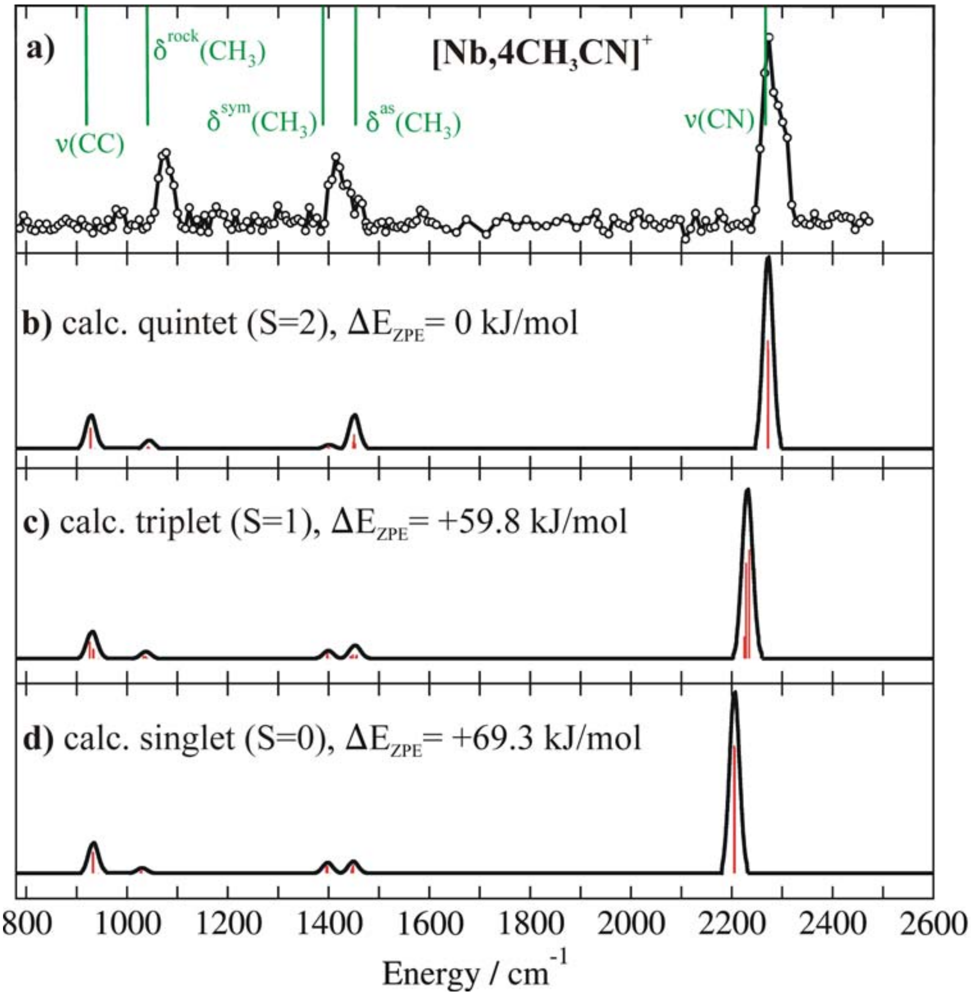

Figure 1. Experimental IR-MPD spectrum (a) of the $[Nb,4CH_3CN]^+$ complex and calculated spectra (b-c) (red lines: calculated vibrations) of $[Nb^I(NCCH_3)_4]^+$ in various spin states (FWHM of 10 cm^{-1} assumed). Green lines in (a) indicate normal modes of the free CH_3CN molecule.

pertubed due to a Fermi like resonance with the δ(CH_3) + ν(CC) combination band, which is known from free acetonitrile to appear at 2300 cm^{-1}.[20] In the ν(CC) stretch mode region (below 1000 cm^{-1}) the recorded level is down to noise level which is due to a decrease in FEL FEL power at the end of its scan range.

At first glance the experimental spectra do not contain any evident indication of a potential reaction beyond complex formation. To substantiate this assertion, we calculated the IR spectra of several optimized $[Nb,4CH_3CN]^+$ complex structures of assumed spin states (S=0,1,2). Among the investigated complex structures were structures with non-reactive first and also second shell coordination as well as cluster structures resulting from potential intracluster reactions (refer to supplementary material for all of these IR absorption spectra). The calculated IR absorption spectrum of quintet (S=2) $[Nb^I(NCCH_3)_4]^+$, with four first shell acetonitrile ligands bound directly to the niobium monocation, matches the experimental spectrum best. Nb^I-acetonitrile complexes with three first shell and one second shell acetonitrile ligand as well as singlet $[Nb^I(MeCN)_3(NCCH_3)]^+$, which contains one acetonitrile ligand and one 2,4,6-trimethyltriazine ligand $(MeCN)_3$ bound to Nb^I, also show a basic correspondence to the experimental spectrum in all spin states S=0,1,2 (cf. supplementary material a). However, as these complexes are energetically clearly disfavored by >100 kJ mol^{-1} with regard to $[Nb^I(NCCH_3)_4]^+$, their existence on the timescale of the performed experiments (several seconds) is extremely improbable.

B3LYP/TZVP calculations of $[Nb^I(NCCH_3)_4]^+$ in the assumed spin states (S=0,1,2) reveal distinct geometries of different relative stabilities. The fourfold coordination of Nb^I is most stable when square planar and high spin quintet (S=2, ΔE_0=0 kJ/mol). It is distorted tetrahedral when triplet (S=1, ΔE_0=+59.8 kJ/mol) and tetrahedral when low spin singlet (S=0, ΔE_0=+65.6 kJ/mol). We further confirmed the preference of the high spin quintet against the triplet and singlet by energy calculations at the MP2/TZVP level of theory. The quintet is found to remain energetically favored to the triplet and singlet by 68.6 kJ mol^{-1} and 54.2 kJ mol^{-1}, respectively. Relative energies and – independently – the predicted redshift of the CN stretch vibration, that anti-correlates with total spin, agree in the assignment of the experimental spectrum to the square planar high spin (S=2) complex $[Nb^I(NCCH_3)_4]^+$.

The IR-MPD spectrum of $[Nb,5CH_3CN]^+$ (Figure 2) is more complex than that of $[Nb^I(NCCH_3)_4]^+$. Additional vibrational bands, shifted away from those of the acetonitrile monomer (cf. green lines), appear between 1300 – 1550 cm^{-1}. They can neither be assigned to shifted $\delta^{sym}(CH_3)$ nor to shifted $\delta^{as}(CH_3)$ deformation vibrations of the gas-phase MeCN. Various reasons are conceivable, in principle, for the new vibrational bands between 1300 – 1550 cm^{-1}. They might arise from second shell CH_3CN molecules in $[Nb,5CH_3CN]^+$, that have bands in the same region as first shell acetonitrile ligands but shifted. Alternatively, the new bands might be indicative of a chemical modification due to an internal reaction.

The IR absorption spectra of various conceivable coordination complexes – including structures with second shell coordination – and of products of potential intracluster reactions were calculated. The IR absorption spectra were computed for the B3LYP/TZVP optimized complex structures in the electronic singlet, triplet and quintet states (for a comprehensive list of IR absorption spectra please refer to supplementary material), respectively.

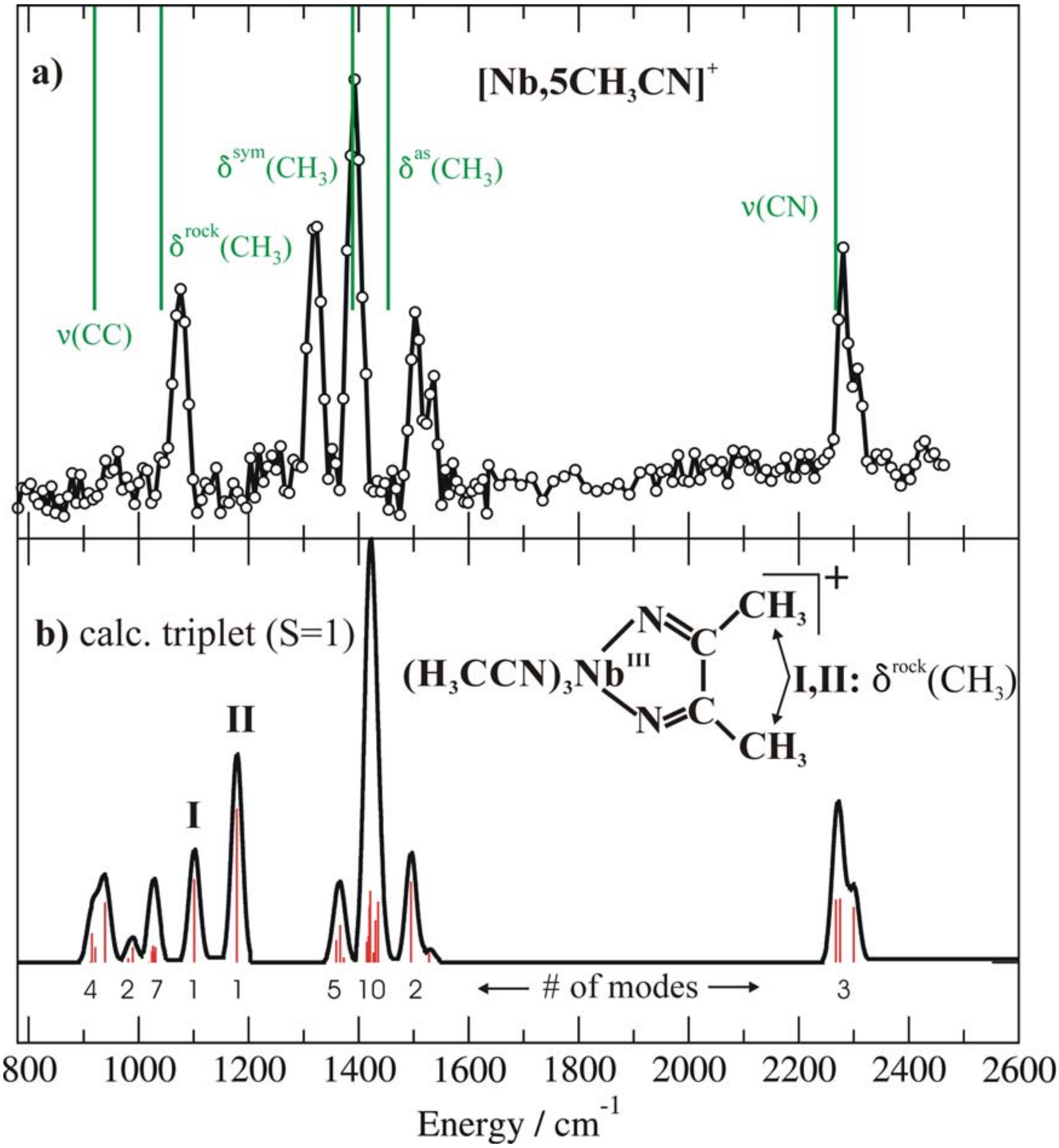

Figure 2. Experimental IR-MPD spectrum (a) of the complex $[Nb,5CH_3CN]^+$ and calculated spectrum (b) of triplet $[Nb^{III}(NCCH_3)_3(N{=}C(CH_3)C(CH_3){=}N)]^+$. Details as in Figure 1. Spectra of other structures and spin states (not shown) deviate strongly from (a).

Any single calculated spectral predictions in terms of conceivable combinations of coordination and spin state fail to resemble all of the recorded band structures. The absorption spectra of coordination complexes with first and second shell acetonitrile ligands resemble closely that of the coordination complexes with only first shell acetonitrile ligands. The spectra of these complexes do not show any vibrational bands apart from those of the free acetonitrile shifted by small margins as observed for $[Nb^I(NCCH_3)_4]^+$ before (cf. Figure 1). Therefore it seems likely that the experimentally observed vibrational bands between

1300 – 1550 cm^{-1} indicate a covalent bond modification within the complex of the formal stoichiometry $[Nb,5CH_3CN]^+$.

Screening on the basis of calculated IR absorption spectra leads to an assignment of the recorded spectrum in terms of a metallacyclic species $[Nb^{III}(NCCH_3)_3(N{=}C(CH_3)C(CH_3){=}N)]^+$ (inset to Figure 2) with a triplet state (S=1). Calculated and experimental spectra agree in position and shape of the ν(CN) mode at 2290 cm^{-1} and – most important – in the structured region between 1300-1550 cm^{-1}. As in the case of n=4 the experimental $\delta^{rock}(CH_3)$ at 1095 cm^{-1} is somewhat blue shifted with regard to the calculated band position, and the predicted ν(CC) is much too weak in IR-MPD. Correspondence between calculated and recorded spectra lends confidence to our assignment – except for those predicted IR bands labelled I and II that seemingly lead only to fragmentation at most up to the recorded noise level. The absence of these bands may arise from a lack of high state density as is necessary to achieve efficient multiphoton dissociation of anharmonic modes.

Bands I and II are the only anticipated bands that arise from a single calculated mode. All other recorded bands originate from 2 to 10 IR active vibrational modes per band. Most noteably the two recorded bands adjacent to the red and blue of those bands missing comprise of seven and five modes, respectively. While single photon absorption into bands I and II surely takes place, any further photon would have to absorb into a red shifted hot band that runs off resonance with respect to the fundamental due to anharmonicity. Thus energy uptake from the FEL radiation becomes inefficient and fragmentation is hampered. Note, that any band comprising of multiple vibrational fundamentals is much less affected by anharmonicity induced walk off (if at all). Low quantum efficiency in the low energy part of the spectrum at less than maximum laser power may have amplified this attenuation. In addition a possible heavy atom effect might hinder the energy flow amongst excited and fragmenting modes and induce some non-ergodic fragmentation pattern.[21-22] The absence of single IR absorption bands has occurred in otherwise well understood FEL-IR-MPD spectra before[9-10] and does not question the conclusive assignment of the recorded spectrum to the novel metallacyclic complex in principle.

B. Coordination versus Reactive Nitrile Coupling in $[Nb,nCH_3CN]^+$, n=4,5

The recorded IR-MPD spectra of $[Nb,nCH_3CN]^+$, n=4,5, yield convincing spectroscopic evidence of an internal reaction in case of n=5 as opposed to non-reactive coordination in case of n=4. By comparison with calculated IR absorption spectra (cf. Figure 2) the IR-MPD spectrum of n=5 was assigned to the metallacyclic species $[Nb^{III}(NCCH_3)_3(N{=}C(CH_3)C(CH_3){=}N)]^+$ in an electronic triplet state (S=1), whereas in case of n=4 the IR-MPD spectrum was assigned to the coordination complex $[Nb^{I}(NCCH_3)_4]^+$ in an electronic quintet state (S=2). Both entities, n=4 and n=5, have assembled stepwise in the gas-phase. Therefore the observed $[Nb^{III}(NCCH_3)_3(N{=}C(CH_3)C(CH_3){=}N)]^+$ species must have formed from $[Nb^{I}(NCCH_3)_5]^+$ according to the redox-reaction (7.1).

$$[Nb^{I}(NCCH_3)_5]^+ \text{ -> } [Nb^{III}(NCCH_3)_3(N{=}C(CH_3)C(CH_3){=}N)]^+ \quad (7.1)$$

In the course of this reaction, two adjacent acetonitrile ligands react with each other and with Nb^{I} to form two covalent Nb-N bonds and one interlinking C-C bond by formation of a 5-ring. While the two CH_3CN ligands are reduced in the course of this reaction, quintet Nb^{I} is oxidized to triplet Nb^{III}.

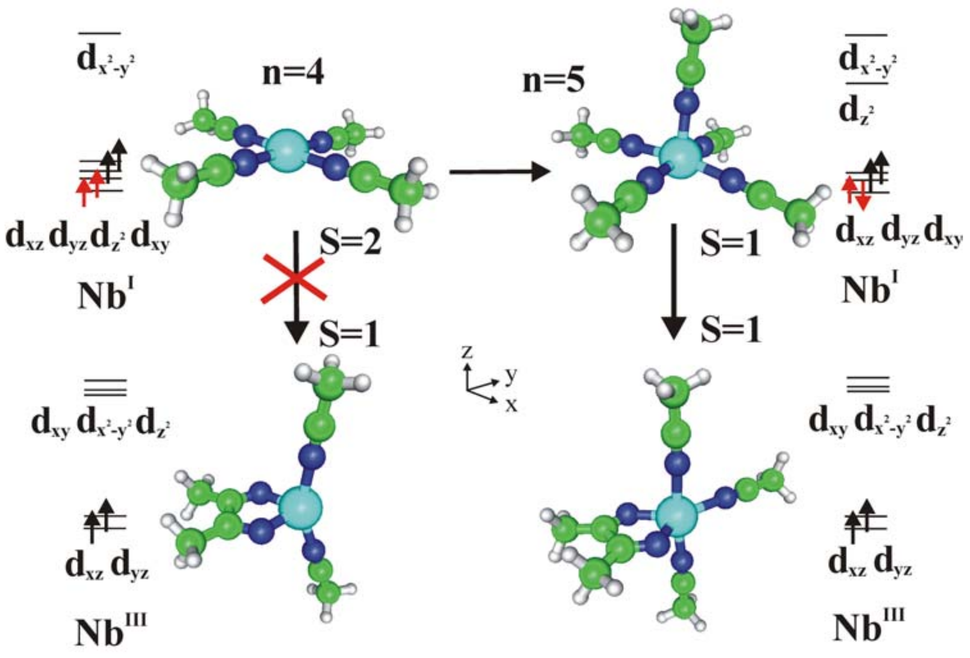

Figure 3. Proposed reaction scheme for $[Nb^{I}(CH_3CN)_n]^+$, n=4-5. For n=4 the square planar high spin complex is stable. Addition of a fifth CH_3CN ligand induces spin change and subsequent C-C coupling (see text).

The experimental observation that reductive nitrile coupling takes place in $[Nb^{I}(NCCH_3)_5]^+$ but not in $[Nb^{I}(NCCH_3)_4]^+$ indicates a strongly size dependent reactivity of niobium-acetonitrile complexes. The findings from the IR-MPD experiments and from the B3LYP/TZVP calculations together allow for the following interpretation of the observed (non-)reactivity in terms of total spin conservation (cf. Figure 3). This makes the planar, high spin complex $[Nb^{I}(NCCH_3)_4]^+$ stable against reductive nitrile coupling (into low spin products). Upon attachment of the fifth acetonitrile ligand, however, the $d(z^2)$ orbital is forced to rise in energy and the triplet state becomes energetically favored in $[Nb^{I}(NCCH_3)_5]^+$. In a subsequent concerted nitrile coupling reaction, triplet $[Nb^{I}(NCCH_3)_5]^+$ reacts under spin conservation to the metallacycle species $[Nb^{III}(NCCH_3)_3(N{=}C(CH_3)C(CH_3){=}N)]^+$.

In $[Nb^{I}(NCCH_3)_4]^+$ formation of triplet $[Nb^{III}(NCCH_3)_2(N{=}C(CH_3)C(CH_3){=}N)]^+$ from quintet $[Nb^{I}(NCCH_3)_4]^+$ involves the change of the total electron spin. Such a change in total electron spin is sometimes referred to as “forbidden”. Actual thermal reactions usually proceed on a single potential energy surface (PES). Nevertheless, chemical reactions can occur on two or more different PES, but this requires a (radiationless) transition from one to another PES in the course of the reaction. These transitions are possible in the vicinity of a crossing of two different PES where spin orbit coupling mediates the transition with a certain probability p. This depiction of a spin change in chemical reactions assumes the transition to proceed between two different diabatic spin states, which is only valid when spin orbit coupling is not strong. This assumption certainly applies to Nb^{I} where spin orbit coupling is of the order of $\approx 150\ cm^{-1}$. If spin orbit coupling is strong the system passes the PES crossing on the lowest adiabatic (mixed spin) surface, and the process does not differ from a spin allowed process anyway. As there is no strict spin conservation in an association reaction (collisions involve additional scattering angular momentum) the necessary spin flips may occur indeed, and the low spin complex forms.

One possible explanation for the observed differences in the reactivity of quintet $[Nb^{I}(NCCH_3)_4]^+$ and triplet $[Nb^{I}(NCCH_3)_5]^+$ is spin conservation due to a low transition probability between different PES in the course of the reductive nitrile coupling reaction. Only for $[Nb^{I}(NCCH_3)_4]^+$ the C-C coupling reaction involves the change of the spin state (cf. Figure 3) from S=2 in $[Nb^{I}(NCCH_3)_4]^+$ to S=1 in $[Nb^{III}(NCCH_3)_2(N{=}C(CH_3)C(CH_3){=}N)]^+$, whereas in case of $[Nb^{I}(NCCH_3)_5]^+$ the spin is conserved in the course of the reaction. However, it has been demonstrated before that in organometallic chemistry gas-phase reactions can involve a change in spin multiplicity.[23,24] Formally spin forbidden reactions have been observed to occur in various transition metal reactions, to name only a few we refer to the recombination reactions of neutral $Cr(CO)_6$ fragments with CO,[25-28] ligand dissociation in $Mn(CO)_x^+$,[29] or the methane to methanol conversion in the MO^+/CH_4 system (M=Co, Ni, Fe). The latter has been investigated in detail both experimentally[30-32] and theoretically[33-38]. Spontaneous spin flips might occur in transition metal complexes, provided that the surfaces of different multiplicity have an opportunity to interact – the completion of this requirement depends on the chemical nature of the metal ion and the ligands, the number of attached ligands, and the coordination geometry. The interactions between different PES can change in niobium-acetnonitrile complexes with growing complex size and are difficult to predict a priori, so that spin conservation alone cannot account for the observed differences in $[Nb^I(NCCH_3)_5]^+$, n=4,5.

As a matter of fact detailed knowledge of the reaction energetics and reaction barriers of the C-C coupling reaction in $[Nb^I(NCCH_3)_n]^+$, n=4-5, as function of the spin state is mandatory in order to elucidate the observed chemical behaviour. We calculated the minimum energy path connecting products and educts of the reductive nitrile coupling reaction as function of the reaction coordinate (C-C distance) and for various spin states (S=0,1,2) in $[Nb^I(NCCH_3)_n]^+$, n=4-5, at the B3LYP level of theory. The obtained reaction coordinates together with selected complex structures are shown in Figure 4. Relative energies ΔE in kJ mol^{-1} are plotted against the carbon-carbon distance $r_{C\text{-}C}$ between two reacting acetonitrile ligands MeCN. In $[Nb^I(NCCH_3)_4]^+$ the ground spin state is the quintet (S=2, structure g), while in $[Nb^I(NCCH_3)_5]^+$ the triplet (S=1, structure *d*) is energetically favored. If it is assumed that in $[Nb^I(NCCH_3)_4]^+$ the system can "hop" from the quintet to the triplet PES in the vicinity of the crossing at $r_{C\text{-}C} \approx 2.3$ Å an activation energy $E_a = 116$ kJ mol^{-1} results for the reductive nitrile coupling reaction in $[Nb^I(NCCH_3)_4]^+$.

However, the geometries of the complexes along the total spin S=2 (quintet) reaction coordinate differ distinctly from those of the S=1 (triplet) and S=0 (singlet) coordinate. This is best exemplified for $[Nb^I(NCCH_3)_4]^+$ geometries near the crossings of the minimum energy paths of the quintet (S=2) with that of the triplet (S=1) and singlet (S=0) b and e, respectively (cf. Figure 4). Structures b (S=0) and e (S=1) each contain two acetonitrile ligands perpendicular to the plane formed by the remaining two acetonitrile ligands, whereas all complexes of the S=2 path are planar.

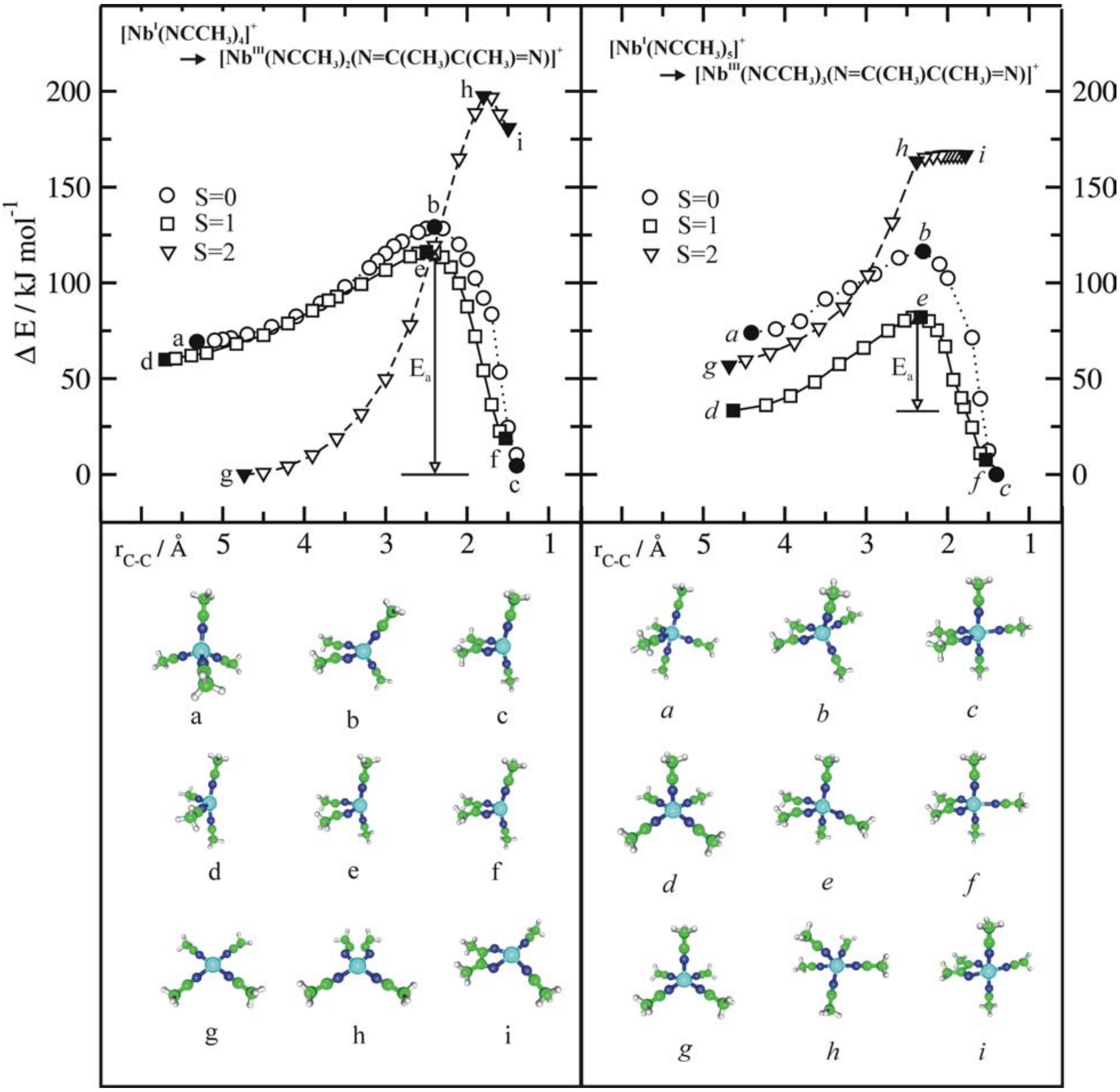

Figure 4. B3LYP reaction coordinates and structures along the $r_{C\text{-}C}$ reaction coordinate for the intramolecular reductive nitrile coupling reaction in $[Nb^I(CH_3CN)_n]^+$, n=4 (left) and n=5 (right), with total spin S=0,1,2.

Due to these significant differences in the geometries of quintet and both singlet and triplet $[Nb^I(NCCH_3)_4]^+$ complexes the (vertical) transition probability from quintet to singlet and triplet states is close to zero. Consequently the reaction coordinate of the quintet is essentially non-reactive due to an activation energy E_a of significantly more than 116 kJ mol^{-1} (estimated).

Even if intersystem crossings were feasible in $[Nb^I(NCCH_3)_4]^+$ and the reaction could proceed from g to c in Figure 4, the reaction would still be endothermic by ΔH_{ZPE} (T=0K) = +13.23 kJ mol^{-1}. In contrast for ground state triplet $[Nb^I(NCCH_3)_5]^+$ the reductive nitrile coupling reaction *d* -> *f* is exothermic by ΔH_{ZPE} (T=0K) = -15.49, or – if spin flops are possible and the reaction can proceed from *d* -> *c* – by ΔH_{ZPE} (T=0K) = -22.72 kJ mol^{-1}.

The computed energetics and activation barriers provide a straightforward explanation of the experimentally encountered reactivity of $[Nb^I(NCCH_3)_4]^+$, n=4,5: While in ground state $[Nb^I(NCCH_3)_5]^+$ the reductive nitrile coupling is exothermic and accessible through an activation barrier of 49 kJ mol^{-1} (which Arrhenius like kinetics overcomes within sub-millisec.)[§], in ground state $[Nb^I(NCCH_3)_4]^+$ the reductive nitrile coupling reaction is endothermic and retarded due to a significantly higher activation barrier ($E_a \approx 116$ kJ mol^{-1}).

7.4 Conclusions

We recorded the FEL-IR-MPD spectra of mass selected cationic niobium acetonitrile complexes with the formal stoichiometry $[Nb,nCH_3CN]^+$, n=4-5, in the spectral range 780 – 2500 cm^{-1}. In case of n=4 the recorded vibrational bands are close to those of the free CH_3CN molecule and the experimental spectra do not contain any evident indication of a potential reaction beyond complex formation. By comparison with B3LYP calculated IR absorption spectra the recorded IR-MPD spectrum is assigned to high spin (quintet, S=2), planar $[Nb^I(NCCH_3)_4]^+$. In contrast in n=5 new vibrational bands shifted away from those of the acetonitrile monomer are observed between 1300 – 1550 cm^{-1}. These bands cannot be assigned to shifted $\delta^{sym}(CH_3)$ or to shifted $\delta^{as}(CH_3)$ deformation vibrations of the gas-phase acetonitrile monomer but are evidence of a chemical modification within $[Nb,nCH_3CN]^+$, n=5, due to an intramolecular reaction. Screening on the basis of B3LYP calculated IR absorption spectra allow for an assignment of the recorded spectra to the metallacyclic species $[Nb^{III}(NCCH_3)_3(N{=}C(CH_3)C(CH_3){=}N)]^+$ (triplet, S=1). This is indicative of spontaneous intramolecular reductive nitrile coupling reaction in $[Nb^I(NCCH_3)_5]^+$. Calculated reaction coordinates explain the experimentally observed differences in reactivity between ground state $[Nb^I(NCCH_3)_4]^+$ and $[Nb^I(NCCH_3)_5]^+$. The reductive nitrile coupling reaction is exothermic and accessible (E_a=49 kJ mol^{-1}) only in $[Nb^I(NCCH_3)_5]^+$ whereas in

---

[§] Preexponential factors A (in $k=Ae^{-Ea/kT}$) for gas-phase first order kinetics P->E are typically of the order of 1×10^{12} s^{-1} - 1×10^{14} s^{-1}.[39] This leads to rate constants k (at 300 K) between 2940 s^{-1}and 29.4×10^4 s^{-1}, corresponding to average life times $\tau=1/k$ of P between τ=0.34 ms and τ=3.4 µs, respectively.

$[Nb^{I}(NCCH_3)_4]^+$ the reaction is found to be endothermic and retarded by significantly higher activation barriers (E_a>>116 kJ mol^{-1}).

7.5 Supporting Information

Supplementary Material (a)

IR absorption spectra (unscaled B3LYP frequencies) and relative energies ΔE_{ZPE} of various $[Nb,4CH_3CN]^+$ complex structures

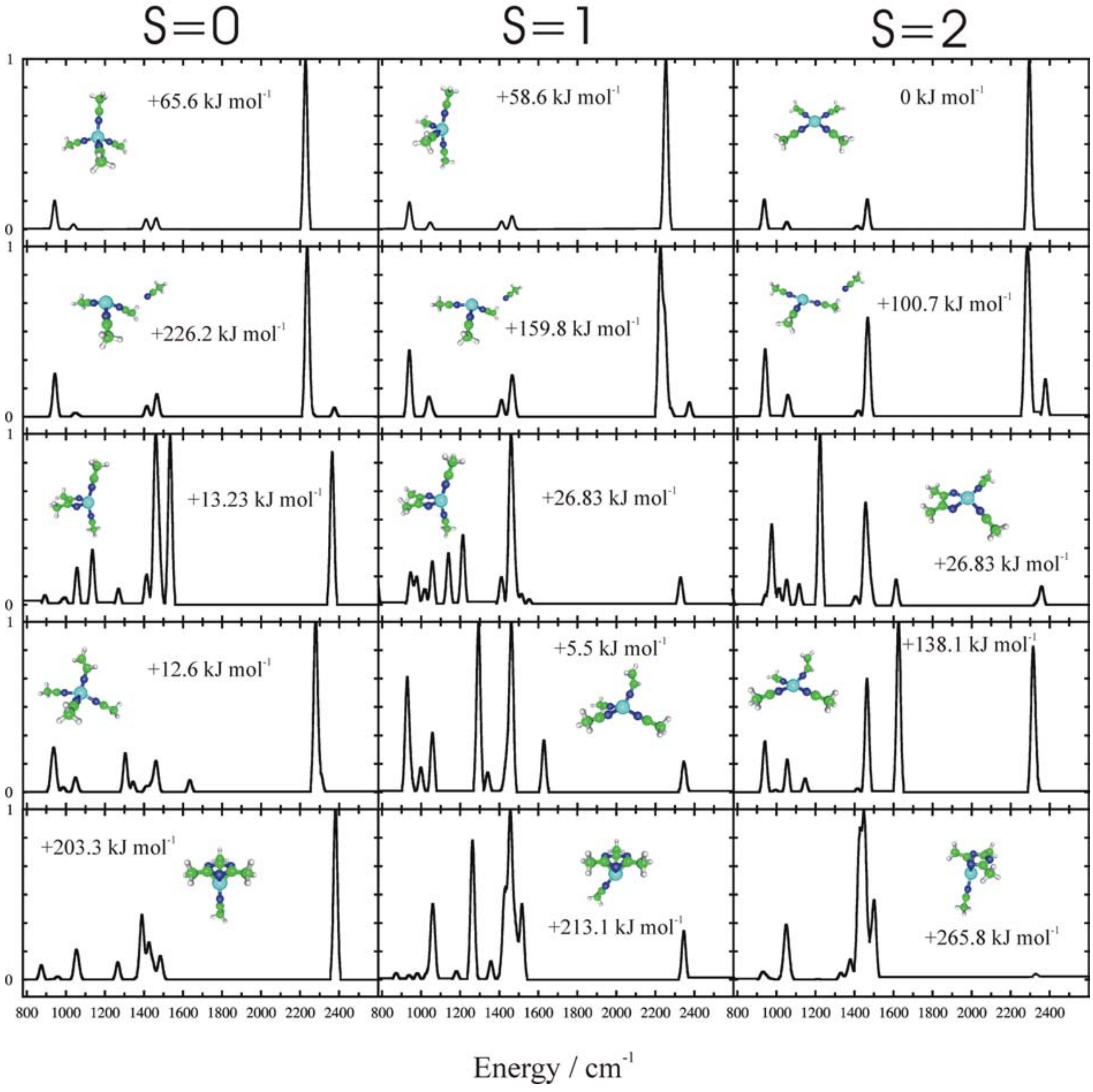

Supplementary Material (b)

IR absorption spectra (unscaled B3LYP frequencies) and relative energies ΔE_{ZPE} of various $[Nb,5CH_3CN]^+$ complex structures

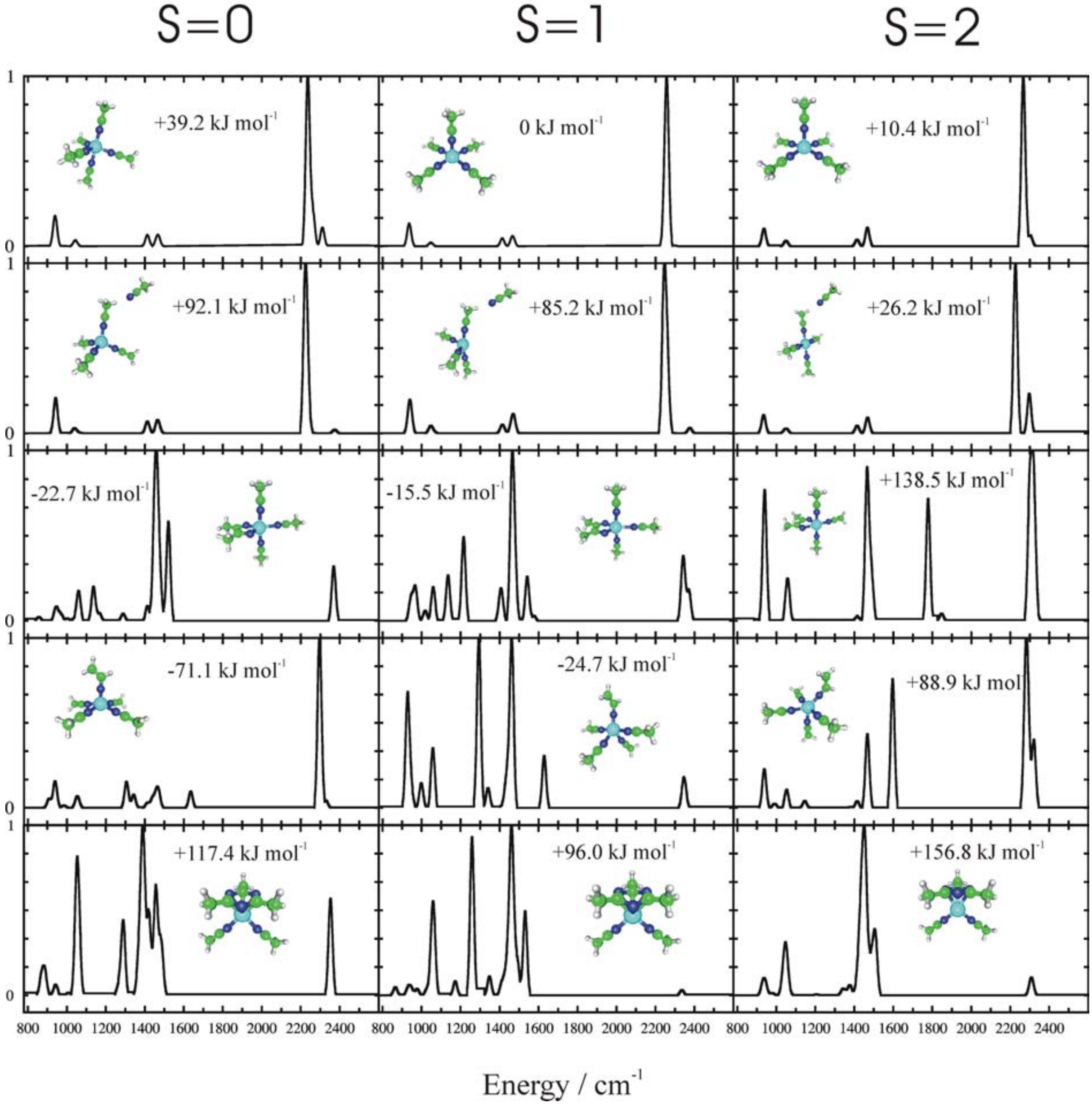

7.6 References

1 Corey, E. J.; Danheiser, R. L.; Chandrasekan, S. *J. Org. Chem.* 1976, **41**, 260.

2 Sattelberger, A. P.; Wilson, Jr., R. B. *J. Am. Chem. Soc.* 1980, **102**, 7111.

3 Finn, P. A.; King, M. S.; Kilty, P. A.; McCarley, R. E. *J. Am. Chem. Soc.* 1975, **97**, 220.

4 Berg, C.; Schindler, T.; Niedner-Schatteburg, G.; Bondybey, V. E. *J. Chem. Phys.* 1995, *102*, 4870.

5 (a) Dunbar, R. C. *Int. J. Mass Spectrom.* 2000, **200**, 571. (b) Duncan, M. A. *Int. J. Mass Spectrom.* 2000, **200**, 545.

6 Oomens, J.; Meijer, G.; von Helden, G. *J. Phys. Chem. A* 2001, **105**, 8302.

7 Oomens, J.; Bakker, J. M.; Sartakov, B. G.; Meijer, G.; von Helden, G. *Chem. Phys. Lett.* 2003, **367**, 576.

8 Lemaire, J.; Boissel, P.; Héninger, G.; Mauclaire, G.; Bellec, G.; Mestdagh, H.; Simon, A.; Le Caër, S.; Ortega, J. M.; Glotin, F.; Maitre, P. *Phys. Rev. Lett.* 2002, **89**, 273002.

9 van Heijnsbergen, D.; von Helden, G.; Meijer, G.; Maitre, P.; Duncan, M. A. *J. Am. Chem. Soc.* 2002, **124**, 1562.

10 Jones, W.; Boissel, P.; Chiavarino, B.; Crestoni, M. E.; Fornarini, S.; Lemaire, J.; Maitre, P. *Angew. Chem. Int. Ed.* 2003, **42**, 2057.

11 Bray, R. G.; Cox, D. M.; Hall, R. B.; Horsley, J. A.; Kaldor, A.; Kramer, G. M.; Levy, M. R.; Priestly, E. *J. Phys. Chem.* 1983, **87**, 429.

12 Crofton, M. W.; Price, J. M.; Lee, Y. T. In *Clusters of Atoms and Molecules II*; Haberland, H., Ed.;Springer-Verlag: Berlin, 1994.

13 Maitre, P.; Le Caër, S.; Simon, A.; Jones, W.; Lemaire, J.; Mestdagh, H.; Héninger, M.; Mauclaire, G.; Boissel, P.; Prazeres, R.; Glotin, F.; Ortega, J. M. *Nucl. Instrum. Methods Phys. Res. Sect. A* 2003, **507,** 541.

14 Sodupe, M.; Branchadell, V.; Rosi, M.; Bauschlicher, C. W., Jr.; *J. Phys. Chem. A* 1997, **101**, 7854.

15 Bauschlicher C. W., Jr.; Ricca, A.; Partridge, H.; Langhoff, S. R. in *Recent Advances in Density Functional Theory*, Ed. D. P. Chong, World Scientific Publishing Co., Singapore 1997, Part II.

16 Schäfer, A.; Huber, C.; Ahlrichs, R. *J. Chem. Phys.* 1994, **100**, 5829.

17 Andrae, D., Haeussermann, M.; Dolg, M.; Stoll, H.; Preuss, H. *Theor. Chim. Acta* 1990, **77**, 123.

18 Treutler, O.; Ahlrichs R. *J. Chem. Phys.* 1995, **102**, 346.

19 Dimitrova, Y. *J. Mol. Struct. (Theochem)* 1995, **343**, 25.

20 Koga, Y.; Kondo, S.; Saeki, S.; Person, W. B. *J. Chem. Phys.* 1984, **88**, 3152.

21 Baer, T.; Hase, W. H. *Unimolecular Reaction Dynamics: Theory and Experiment*; Oxford University Press: New York, 1996, 12.

22 Zhitneva, G. P. *Chem. Phys. Lett.* 1999, **307**, 379.

23 Poli, R.; Harvey, J. N. *Chem. Soc. Rev.* 2003, **32**, 1.

24 Schröder, D.; Shaik, S.; Schwarz, H. *Acc. Chem. Res.* 2000, **33**, 139.

25 Seder, T. A.; Church, S. P.; Ouderkirk, A. J.; Weitz, E. *J. Am. Chem. Soc.* 1985, **107**, 1432.

26 Sedler, T. A.; Church, S. P.; Weitz, E. *J. Am. Chem. Soc.* 1986, **108**, 4721.

27 Fletcher, T. R.; Rosenfeld, R. N. *J. Am. Chem. Soc.* 1986, **108**, 1686.

28 Fletcher, T. R.; Rosenfeld, R. N. *J. Am. Chem. Soc.* 1988, **110**, 2097.

29 Dearden, D. V.; Hayashibara, K.; Beauchamp, J. L., Kirchner, N. J.; van Koppen, P. A. M.; Bowers, M. T. *J. Am. Chem. Soc.* 1989, **111**, 2401.

30 Schröder, D.; Schwarz, H. *Angew. Chem. Int. Ed. Engl.* 1995, **34**, 1973.

31 Clemmer, D. E.; Aristov, N.; Armentrout, P.B. *J. Phys. Chem.* 1993, **97**, 544.

32 Clemmer, D. E.; Chen, Y.-M.; Khen, F. A.; Armentrout, P. B. *J. Phys. Chem.* 1994, **98**, 6522.

33 Shiota, Y.; Yoshizawa, K. *J. Chem. Phys.* 2003, **118**, 5872.

34 Yoshizawa, K.; Shiota, Y.; Yamabe, T. *Chem. Eur. J.* 1997, **3**, 1160.

35 Yoshizawa, K.; Shiota, Y.; Yamabe, T. *J. Am. Chem. Soc.* 1998, **120**, 564.

36 Yoshizawa, K.; Shiota, Y.; Yamabe, T. *Organometallics* 1998, **17**, 2825.

37 Yoshizawa, K.; Shiota, Y.; Kagawa, Y.; Yamabe, T. *J. Phys. Chem A* 2000, **104**, 2552.

38 Shiota, Y.; Yoshizawa, K. *J. Am. Chem. Soc.* 2000, **122**, 12317.

39 Wilkinson, F. *Chemical Kinetics and Reaction Mechanisms*, Van Nostrand Reinhold: Wokingham, 1980, p 124.

8. Summary

Clusters bridge the gap between single atoms or molecules and the condensed phase and it is well known that the properties of clusters strongly depend on their size. The challenge of cluster science is to obtain a deeper understanding of the molecular foundation of the observed cluster specific properties/reactivities and their dependence on size. Hence in this work the reactivity and physico-chemical properties of different microsolvated metal ions have been investigated both by different experimental techniques and complementing quantum chemical calculations. The major results of this work will be summarized briefly in the following.

Hydrated magnesium and aluminum monocations exhibit a peculiar cluster size dependent reactivity: Only for a limited intermediate cluster size regime reactive decay via H and H_2 elimination is observed for $[Mg,nH_2O]^+$ and $[Al,nH_2O]^+$ clusters respectively. Although at first the experimentally observed reactivity indicates analogue redox reactions forming H and H_2 from water clusters doped with open shell Mg^+ (configuration: $[Ne]3s^1$) and closed shell Al^+ ($[Ne]3s^2$), detailed quantum chemical modelling of these reactions in $[Mg,nH_2O]^+$ and $[Al,nH_2O]^+$ clusters indicate fundamental differences.

The electronic structure of hydrated magnesium monocations $[Mg,nH_2O]^+$, $1 \leq n \leq 19$, exhibits a strong cluster size dependency. With increasing number of H_2O ligands the SOMO evolves from a quasi-valence state (n=3-5), in which the singly occupied molecular orbital (SOMO) is not yet detached from the metal atom and has distinct sp-hybrid character, to a contact ion pair state. For larger clusters (n=17,19) these ion pair states are best described as solvent separated ion pair states, which are formed by a hydrated dication and a hydrated electron. With growing cluster size the SOMO moves away from the magnesium ion to the cluster surface, where it is localized through mutual attractive interactions between the electron density and dangling H-atoms of H_2O ligands forming "molecular tweezers" $HO\text{-}H\cdots e^-\cdots H\text{-}OH$. The properties of these complexes were investigated in detail by computing vertical and adiabatic ionization energies, SOMO volumes, and reorganization energies upon removal of the odd electron. In $[Mg,nH_2O]^+$ the calculated properties exhibit distinct changes at n=6-7 that correlate with the change of the electronic cluster structure.

The BLYP calculated energetics of the two experimentally encountered decay processes in $[Mg,nH_2O]^+$, reactive H-elimination and non-reactive H_2O evaporation, predict switches of the decay propensities at $n_1=6\text{-}7$ and at $n_2\approx17$. This is in excellent agreement with the findings of previous experimental studies on the collisionless decay of $[Mg,nH_2O]^+$. According to the performed calculations the coexistence of Mg^{2+} and a hydrated electron becomes energetically favored to the formation of $MgOH^+$ in large $[Mg,nH_2O]^+$ clusters due to the charge screening effect of the OH^- ion clusters with a densely populated second solvation shell. With the coexistence of hydrated electron and Mg^{2+} dication becoming favored, the decay propensities of $[Mg,nH_2O]^+$ clusters switch again, which gives rise to the second product switching at $n_2\approx17$.

In case of the hydrated aluminum monocations $[Al,nH_2O]^+$, cluster size n=20 was chosen for a detailed investigation of the reactive H_2 decay pathway, as H_2 formation was reported to be most efficient for n=20. Different isomers of the formal stoichiometry $[Al,20H_2O]^+$ were investigated by using gradient-corrected DFT (BLYP) and three different basic structures for $[Al,20H_2O]^+$ were identified: (a) $[Al^I(H_2O)_{20}]^+$ with a threefold coordinated Al^I; (b) $[HAl^{III}(OH)(H_2O)_{19}]^+$ with a fourfold coordinated Al^{III}; (c) $[HAl^{III}(OH)(H_2O)_{19}]^+$ with a fivefold coordinated Al^{III}. In ground state $[Al^I(H_2O)_{20}]^+$ (a) which contains aluminum in oxidation state +1 the $3s^2$ valence electrons remain located at the aluminium monocation. Different than for open shell magnesium monocations no electron transfer into the hydration shell is observed for closed shell Al^I. However, clusters of type (a) are high energy isomers ($\Delta E\approx+190$ kJ mol^{-1}) and the activation barrier for reaction into cluster type (b) or (c) is only approximately 14 kJ mol^{-1}.

H_2 elimination was found to be limited to cluster type (b), for which the reaction is mediated by a multistep intracluster proton transfer mechanism. In a first step H^+ is formed via hydrolysis of a first shell H_2O molecule. In a successive reorganization of the hydrogen bonding network this proton is transferred to the hydridic H atom bound to the Al^{III} cation. Finally proton and hydride ion recombine in an acid-base reaction and form H_2. The activation barrier of this process was calculated to be +45 kJ mol^{-1}. The obtained reaction enthalpy $\Delta_rH = -122$ kJ mol^{-1} is in excellent agreement with the experimental observation that H_2 elimination is typically associated with the evaporation of 2-3 H_2O molecules, as the H_2O monomer bindind energies in ionic water clusters with 20 water molecules are of the order of

$\Delta_{vap}H \approx -40$ kJ mol^{-1}. The performed studies reveal a conclusive mechanism for the formation of H_2 in hydrated Al^{III} clusters but no indication of H_2 formation in hydrated Al^{I} clusters.

In hydrated magnesium monocations the magnesium dication was found to coexist with a hydrated electron in larger cluster sizes. This proves that intermolecular electron delocalization – previously almost exclusively studied in "pure" $(H_2O)_n^-$ and $(NH_3)_n^-$ clusters – can also be an important issue for water clusters doped with an open shell metal cation. If a single electron can coexist in a water cluster doped with a magnesium cation, the question of the electronic structure of anionic water clusters doped with a metal atom arises naturally. Structures and stabilities of hydrated magnesium water cluster anions with the formal stoichiometry $[Mg,nH_2O]^-$, n=1-11, were investigated by application of various correlated ab initio methods (MP2, CCSD, CCSD(T)). While for $[Mg,nH_2O]^-$, n=1, an electronic structure was found that is best described as $Mg^-(H_2O)$, the "most stable" isomers of n≥2 have the excess electron detached from the metal anion. These clusters contain a Mg atom that is attached to an anionic water sub-cluster $(H_2O)_n^-$, and they are characterized as $Mg(H_2O)_n^-$. We determined the stability of these complexes against electron detachment by calculating VDEs and ADEs. The VDEs become positive for $Mg(H_2O)_n^-$, n≥2, and increase gradually with cluster size. The computed ADEs, which are the negatives of adiabatic electron affinities, become positive through the formation of molecular tweezer structures HO-H$\cdots e^-\cdots$H-OH in $Mg(H_2O)_n^-$ at n=3. For the cationic metal water clusters insertion of the metal monocation into at least one O-H bound of a solvent H_2O molecule was found to be energetically highly favored. Therefore O-H insertion by Mg was considered in $[Mg,nH_2O]^-$ as well, and indeed O-H insertion – yielding $[HMgOH,(n-1)H_2O]^-$ respectively $[Mg(OH)_2,(n-2)H_2O]^-$ (dual O-H insertion) – is strongly exothermic. Due to a lower activation barrier the decay process involving a single O-H insertion is proposed as most probable reactive decay pathway of $[Mg,nH_2O]^-$. SOMO surfaces and electron binding energies imply the excess electron to be covalently bound in small product clusters, like e.g. in $[HMgOH,(n-1)H_2O]^-$ (n=1-2) and $[Mg(OH)_2,(n-2)H_2O]^-$ (n=2-3). Larger clusters contain the excess electron solvated by surrounding water molecules located in the hydration sphere like observed before for $[Mg,nH_2O]^-$ clusters with n>1. However, the calculated ADEs for $[HMgOH,(n-1)H_2O]^-$ respectively $[Mg(OH)_2,(n-2)H_2O]^-$ indicate that this species might be adiabatically instable for n <11.

Metal cations surely have high relevance in numerous biological processes, and as most biological processes take place in aqueous solution hydrated metal ions will be involved. However, when going from in vitro to in vivo one has to consider that different high affinity chelate ligands prevent high concentrations of free metal ions. In biological systems solvent molecules (i.e. water) compete with different solvated chelate ligands for coordination sites at the metal ion and the solvent and chelate ligands are in mutual interactions with each other and the metal ion. These interactions were investigated for the hydration of Zn^{II}/carnosine complexes. Carnosine is a naturally occurring dipeptide with a high affinity to metal cations like Cu^{II}, Zn^{II}, Mn^{II}, and Ni^{II}. The performed mass spectrometric studies indicate two different Zn^{II}/carnosine complex structures which differ significantly in their H_2O binding energies. If present at all, H_2O is always contained in pairs of two. This is attributed to two different Zn^{II} complexation modes in Zn^{II}/carnosine complexes: The Zn^{II} ion is either complexed "internally" within a binding pocket formed by carnosine, so that Zn^{II} is screened from H_2O, or Zn^{II} is complexed "externally" at the surface of the carnosine ligand. DFT calculations reveal that in the open structures the Zn^{II} ion coordinates to only two carnosine atoms. Consequently the solvent has easy access to the unscreened metal ion and two H_2O ligands can occupy vacant coordination sites leading to a tetrahedrally coordinated Zn^{II} ion with two strongly bound first shell H_2O ligands in accordance with the experimental observation.

Gas-phase H/D exchange reactions of protonated carnosine oligomers $(n\times Carn+H)^+$, n=1-3, and (hydrated) Zn^{II}/carnosine complexes with D_2O were performed to investigate complex structures and to probe relative proton affinities of the corresponding (deprotonated) neutral structures. Formation of van der Waals complexes $(n\times Carn)^+$, n>1, leads to a significant increase in proton affinity, as attractive interactions between carnosine monomers are enhanced through protonation. H/D exchange is known to proceed efficiently when the difference between the proton affinities of the reagent and deprotonated analyte is small. However, in case of Zn^{II}/carnosine complexes H/D exchange is exclusively observed for $[Carn\text{-}H,Zn^{II}]^+$, even though the computed proton affinity of the hydrated complex $[(Carn\text{-}2H,Zn^{II}(OH_2)_2)\text{-}H]$ is lower than that of $[Carn\text{-}2H,Zn^{II}]$ and closer to that of D_2O by approximately 56 kJ mol^{-1}. This finding is indicative of a H/D exchange mechanism that is promoted by vacant Zn^{II} coordination sites. Different than for $(n\times Carn+H)^+$ proton transfer mechanisms, which assume a protonated site or at least an acidic group, are not applicable in the case of $[\mathrm{Carn\text{-}H,Zn^{II}(OH_2)_p}]^+$, p=0,2. The carboxylic acid group of the ligand is deprotonated and the remaining most acidic group is the –NH– of the peptide bond (which is available both in p=0 and p=2). Instead an alternative H/D exchange mechanism is proposed for $[\mathrm{Carn\text{-}H,Zn^{II}(OH_2)_p}]^+$, which involves coordination of D_2O to the Zn^{II} ion and requires free coordination sites at the Zn^{II} dication. This requirement is fulfilled in $[\mathrm{Carn\text{-}H,Zn^{II}}]^+$ but not in $[\mathrm{Carn\text{-}H,Zn^{II}(OH_2)_2}]^+$.

In the first step of the proposed H/D exchange mechanism a D_2O ligand attaches to the Zn^{II} dication. Subsequently, in a second reaction step, D_2O inserts into the $Zn^{II}\cdots NH_2$- bond between the metal ion and the N-terminus of carnosine. Due to the high charge density of the Zn^{II} metal ion, the O-D bonds are strongly polarized, and D_2O hydrolyzes into D^+, which is transferred to the N-terminus, and OD^-, which remains bound to the Zn^{II} dication (D_2O + H_2N-Carn -> $DO^-\cdots{}^+DH_2N$-Carn). By rotation of the ammonium group around the $^+DH_2N$–Carn bond axis, the $DO^-\cdots{}^+DH_2N$-Carn hydrogen bond is replace by a $DO^-\cdots{}^+HDHN$-Carn hydrogen bond. In the back-reaction the proton involved in this hydrogen bond is transferred to the OD^- and DHO is formed, completing the H/D exchange ($DO^-\cdots{}^+HDHN$-Carn -> DOH + DHN-Carn). The maximum activation barrier along the reaction coordinate of this process has been calculated to be 38 kJ mol^{-1}.

Internal reactions within microsolutions can lead to modifications of the chemical structure of the microsolutions that are not traceable with mass spectrometry, simply because the chemical modification does not result in a change of the mass of the gas-phase complex. In this case structural information are mandatory. Experimental information about the structure of gas-phase ion-solvent complexes are provided only by optical spectroscopy, like for example IR spectroscopy. However, gas phase ions are usually produced under isolated conditions so that traditional IR absorption spectroscopy is not applicable due to low number densities. Instead some kind of IR action spectroscopy has to be used. In the last chapter of this work the Free Electron Laser IR Multi Photon Dissocition (FEL-IR-MPD) spectra of mass selected cationic niobium acetonitrile complexes with the formal stoichiometry $[\mathrm{Nb,nCH_3CN}]^+$, n=4-5, in the spectral range 780 – 2500 cm^{-1} are reported. In case of n=4 the recorded vibrational bands are close to those of the free CH_3CN molecule and the experimental spectra do not contain any evident indication of a potential reaction beyond complex formation. By comparison with B3LYP calculated IR absorption spectra the recorded spectra is assigned to high spin (quintet, S=2), planar $[Nb^{I}(NCCH_3)_4]^+$. In contrast in $[Nb,nCH_3CN]^+$, n=5, new vibrational bands shifted away from those of the acetonitrile monomer are observed between 1300 – 1550 cm^{-1}. These bands cannot be assigned to shifted $\delta^{sym}(CH_3)$ or to shifted $\delta^{as}(CH_3)$ deformation vibrations of the gas-phase acetonitrile monomer and are evidence of a chemical modification due to an intramolecular reaction. Screening on the basis of B3LYP calculated IR absorption spectra allow for an assignment of the recorded spectra to the metallacyclic species $[Nb^{III}(NCCH_3)_3(N{=}C(CH_3)C(CH_3){=}N)]^+$ (triplet, S=1). This is indicative of an intramolecular reductive nitrile coupling reaction to have occurred in $[Nb^{I}(NCCH_3)_5]^+$. Calculated reaction coordinates explain the experimentally observed differences in reactivity between ground state $[Nb^{I}(NCCH_3)_4]^+$ and $[Nb^{I}(NCCH_3)_5]^+$. The reductive nitrile coupling reaction is exothermic and accessible (E_a=49 kJ mol^{-1}) only in $[Nb^{I}(NCCH_3)_5]^+$, whereas in $[Nb^{I}(NCCH_3)_4]^+$ the reaction is found to be endothermic and retarded by significantly higher activation barriers (E_a>116 kJ mol^{-1}).

9. Zusammenfassung

Cluster schliessen die Lücke zwischen isolierten Atomen/Molekülen und der kondensierten Phase und ihre Eigenschaften hängen stark von ihrer Grösse ab. Das besondere Interesse bei der Untersuchung von Clustern und ihren Eigenschaften liegt nun darin, ein tiefergehendes Verständnis für die molekularen Grundlagen der beobachteten clusterspezifischen Eigenschaften und ihrer Abhängigkeit von der Grösse zu erhalten. In dieser Arbeit wurden die Reaktivität und die physikochemischen Eigenschaften von verschiedenen solvatisierten Metallionen, sogenannten „Mikrolösungen“ (engl.: microsolutions) sowohl durch Anwendung unterschiedlicher experimenteller Techniken, als auch durch begleitende quantenchemische Rechnungen untersucht. Die wichtigsten Resultate werden im Folgenden kurz zusammengefasst.

Die Reaktivitäten von hydratisierten Magnesium und Aluminium-Monokationen weisen eine deutliche Abhängigkeit von der Clustergrösse auf: In $[Mg,nH_2O]^+$ und $[Al,nH_2O]^+$ Clustern sind die H bzw. H_2 Eliminierungsreaktion auf ein eng umrissenes Grössenintervall beschränkt. Die experimentell beobachteten Zerfallsreaktionen, Eliminierung eines H Atoms aus $[Mg,nH_2O]^+$, bzw Eliminierung eines H_2 Moleküls aus $[Al,nH_2O]^+$, weisen zunächst auf analoge Redoxreaktionen in Wasserclustern mit offenschaligem Mg^+ ($[Ne]3s^1$) oder geschlossenschaligem Al^+ ($[Ne]3s^2$) hin. Die in dieser Arbeit durchgeführten quantenchemischen Rechnungen zeigen jedoch, dass die zugrunde liegenden Reaktionen fundamental unterschiedlich sind.

Die elektronische Struktur von hydratisierten Magnesium-Monokationen $[Mg,nH_2O]^+$, $1 \leq n \leq 19$, ist stark von der Clustergrösse abhängig. Mit zunehmender Zahl von H_2O Liganden, entwickelt sie sich von einem Valenzzustand (n=3-5), bei dem sich das SOMO (engl.: Singly Occupied Molecular Orbital) noch nicht vom Metallatom losgelöst und starken sp-Hybrid Charakter hat, zu einem Kontaktionenpaar aus Mg^{2+} und hydratisiertem Elektron. In grösseren Clustern (n=17,19) werden diese Ionenpaare am genauesten als durch Solvensmoleküle getrennte Ionenpaare beschrieben. Mit zunehmender Clustergrösse entfernt sich das SOMO immer weiter vom Magnesium-Kation und wandert an die Oberfläche des Clusters, wo es durch attraktive Wechselwirkungen zwischen der Elektronendichte und nicht an Wasserstoffbrückenbindungen beteiligten H Atomen von H_2O Liganden lokalisiert wird.

Bildlich gesprochen wird das Elektron durch Pinzetten, die von H-O Oszillatoren gebildet werden (HO-H···e$^-$···H-OH), lokalisiert. Die Eigenschaften dieser Cluster wurden detailliert durch Berechnung der vertikalen und adiabatischen Ionisierungsenergien, der SOMO Volumina und der Reorganisierungsenergien nach Entfernung des ungeraden Elektrons untersucht. Die berechneten Eigenschaften zeigen die auffälligsten Veränderungen bei Clustergrössen n=6-7, was sehr genau mit den Änderungen in der elektronischen Clusterstruktur korreliert.

Die mit Hilfe der BLYP Methode berechneten Energien der für $[Mg,nH_2O]^+$ experimentell beobachteten Zerfallskanäle – reaktive H-Eliminierung und nicht-reaktive H_2O Evaporation – sagen jeweils eine Änderung des vorherrschenden Zerfallskanals bei n_1=6-7 beziehungsweise bei $n_2 \approx 17$ voraus. Dies stimmt sehr gut mit den experimentellen Beobachtungen für den Zerfall von $[Mg,nH_2O]^+$ Clustern unter kollisionsfreien Bedingungen überein. Die durchgeführten Rechnungen zeigen, dass die Koexistenz von Mg^{2+} mit einem hydratisierten Elektron relativ zur Bildung von $MgOH^+$ mit zunehmender Population der 2. Hydratationsschale wieder günstiger wird. Das OH^- Anion schirmt die positive Ladung des Mg^{2+} ab, wodurch die attraktiven Ladungs-Dipol Wechselwirkungen zwischen den H_2O Molekülen in der 2. Hydratationsschale und dem Mg^{2+} geschwächt werden. Sobald mit zunehmender Clustergrösse die Koexistenz von hydratisiertem Elektron und Mg^{2+} Dikation gegenüber der H-Eliminierung – die zur Bildung von $MgOH^+$ führt – bevorzugt ist, ändern sich die Zerfallseigenschaften des $[Mg,nH_2O]^+$ Clusters wieder. Das erklärt den zweiten Wechsel in den Zerfallseigenschaften bei $n_2 \approx 17$.

Im Falle der hydratisierten Aluminium-Monokationen $[Al,nH_2O]^+$, wurde die Clustergrösse n=20 für eine genaue Analyse des reaktiven H_2 Zerfallskanal ausgewählt, da die H_2 Bildung im Falle von n=20 am effizientesten ist. Verschiedene Isomere mit der formalen Stöchiometrie $[Al,20H_2O]^+$ wurden mit Gradienten-korrigierter DFT (BLYP) berechnet und es konnten 3 unterschiedliche Strukturtypen gefunden werden: (a) $[Al^I(H_2O)_{20}]^+$ mit einem dreifach koordinierten Al^I; (b) $[HAl^{III}(OH)(H_2O)_{19}]^+$ mit einem vierfach koordinierten Al^{III}; (c) $[HAl^{III}(OH)(H_2O)_{19}]^+$ mit einem fünffach koordinierten Al^{III}. Im $[Al^I(H_2O)_{20}]^+$ Cluster bleiben die $3s^2$ Valenzelektronen am Aluminium-Monokation. Anders als beim offenschaligen Magnesium-Monokation wird im Falle des geschlossenschaligen Al^I kein Elektronentransfer in die Hydratationssphäre beobachtet. Bei Clustern des Typs (a)

$[Al^{I}(H_2O)_{20}]^+$ handelt es sich aber um ein „Hochenergieisomer“, dessen Energie ungefähr 190 kJ mol^{-1} über denen von (b) und (c) liegt, und die Barriere für die Umwandlung von (a) nach (b) oder (c) beträgt nur ungefähr 14 kJ mol^{-1}.

Die durchgeführten quantenchemischen Rechnungen ergaben, dass H_2 Eliminierung nur für den Clustertyp (b) möglich ist. Dabei wird die H_2 Eliminierung durch einen Protonentransfermechanismus innerhalb des Wasserstoffbrückennetzwerkes des Clusters vermittelt. In einem ersten Schritt wird ein Proton H^+ durch eine Hydrolysereaktion eines direkt an das Al^{III} gebundenen H_2O Moleküls freigesetzt. In einer anschliessenden Restrukturierung des Wasserstoffbrückennetzwerkes wird dieses Proton zum hydridischen Wasserstoffatom am Al^{III} transferiert. Schliesslich rekombinieren das Proton und das Hydridion in einer klassischen Säure-Base Reaktion und bilden H_2. Die Aktivierungsbarriere für diese Reaktion wurde zu +45 kJ mol^{-1} bestimmt. Die berechnete Reaktionsenthalpie Δ_rH=-122 kJ mol^{-1} passt gut zu der experimentellen Beobachtung, dass die H_2 Bildung immer mit der Abdampfung von 2-3 H_2O Molekülen einhergeht (die typische H_2O Monomerbindungsenergie in Wasserclustern dieser Grösse beträgt $\Delta_{vap}H \approx -40$ kJ mol^{-1}). Die durchgeführten Studien liefern einen schlüssigen Mechanismus für die H_2 Bildung in hydratisierten Al^{III} Clustern, sie enthalten aber kein Anzeichen für eine H_2 Eliminierungs-Reaktion in hydratisierten Al^{I} Clustern.

In hydratisierten Magnesium-Monokationen wurden für grosse Clustergrössen eine Koexistenz zwischen hydratisiertem Elektron und Magnesium-Dikation beobachtet. Das zeigt, dass intermolekulare Elektronendelokalisierung, die zuvor fast ausschliesslich an „reinen“ $(H_2O)_n^-$ und $(NH_3)^-$ Clustern untersucht wurde, auch in Wasserclustern mit einem offenschaligen Metallkation Relevanz haben kann. Die Frage nach der Stabilität und der möglichen elektronischen Struktur von anionischen Metallwasserclustern stellt sich dann zwangsläufig. In dieser Arbeit wurden Struktur und Stabilität von hydratisierten Magnesium-Anionen mit der formalen Stöchiometrie $[Mg,nH_2O]^-$, n=1-11, mit verschiedenen korrelierten ab initio Methoden (MP2, CCSD, CCSD(T)) untersucht. Während das Elektron in $[Mg,nH_2O]^-$, n=1, noch am Magnesium lokalisiert ist und die elektronische Struktur am besten als $Mg^-(H_2O)$ beschrieben wird, hat es sich in den energetisch niedrigsten Clusterisomeren mit $n \geq 2$ von dem Metallanion gelöst und ist stattdessen in der Solvathülle gebunden. Diese Cluster bestehen aus einem Magnesiumatom Mg, das an ein hydratisiertes

Elektron $(H_2O)_n^-$ angelagert ist. Die Stabilität dieser Cluster gegen Elektrondetachment wurde durch Berechnung von VDEs and ADEs bestimmt. Die VDEs werden für $Mg(H_2O)_n^-$, $n \geq 2$, positiv und nehmen dann kontinuierlich mit steigender Clustergrösse zu. Die berechneten ADEs, welche gleich der negativen adiabatischen Elektronenaffinität sind, werden positiv für Strukturen mit molekularen Pinzetten $HO\text{-}H \cdots e^- \cdots H\text{-}OH$ in $Mg(H_2O)_n^-$, $n \geq 3$. In Wasserclustern mit einem Metallkation war die Insertion des Metallions in mindestens eine O-H Bindung eines Wasserliganden exotherm. Daher wurde O-H Insertion durch Mg in $[Mg,nH_2O]^-$ untersucht. Tatsächlich ist auch in diesem Falle O-H Insertion, die zu Strukturen wie $[HMgOH,(n-1)H_2O]^-$, beziehungsweise $[Mg(OH)_2,(n-2)H_2O]^-$ (zweifache O-H Insertion) führt, stark exotherm. Aufgrund einer niedrigeren Aktivierungsbarriere ist der Reaktionskanal, der nur eine O-H Insertion erfordert, der Wahrscheinlichere. Struktur und Lage der SOMOs, sowie die berechneten Bindungsenergien des Überschusselektrons deuten darauf hin, dass es in kleinen Clustern wie $[HMgOH,(n-1)H_2O]^-$ (n=1-2) und $[Mg(OH)_2,(n-2)H_2O]^-$ (n=2-3) kovalent gebunden ist. In grösseren Clustern ist es dagegen in der Hydratsphäre lokalisiert, wie zuvor bereits in $[Mg,nH_2O]^-$, $n>1$, beobachtet. Die berechneten ADEs von $[HMgOH,(n-1)H_2O]^-$ beziehungsweise $[Mg(OH)_2,(n-2)H_2O]^-$ deuten darauf hin, dass diese adiabatisch instabil sind für Clustergrössen $n<11$.

Metallkationen haben hohe Relevanz in einer Vielzahl von biologischen bzw. biochemischen Prozessen, und da diese meistens in wässriger Lösung stattfinden, werden hydratisierte Metallionen beteiligt sein. Beim Übergang von in vitro nach in vivo muss man jedoch bedenken, dass unter physiologischen Bedingungen Chelatliganden mit hoher Bindungsaffinität zu bestimmten Metallionen eine hohe Konzentration an freien Metallionen dieser Art verhindern. In biologischen Systemen konkurrieren Solvensmoleküle (also in der Regel Wasser) und verschiedene solvatisierte Chelatliganden um freie Koordinationsstellen am Metallion, so dass Solvensmoleküle, Chelatliganden und Metallionen in wechselseitigen Beziehungen zueinander stehen. Diese Wechselwirkungen wurden für die Hydratisierung des Zn^{II}/Carnosine Komplexes untersucht. Carnosine ist ein natürlich vorkommendes Dipeptid, mit einer hohen Affinität zu Cu^{II}, Zn^{II}, Mn^{II}, und Ni^{II} Ionen. Massenspektrometrische Untersuchungen von Zn^{II}/Carnosine Komplexen (aus wässriger Lösung) deuten auf zwei unterschiedliche Zn^{II}/Carnosine Komplexstrukturen hin, die sich deutlich in ihren H_2O Bindungsenergien unterscheiden. Falls H_2O überhaupt gebunden ist, kommt es immer in

Paaren von zwei vor. Dies wird auf das Vorliegen von zwei unterschiedlichen Zn^{II} Komplexierungsarten zurückgeführt: Das Zn^{II} Ion ist entweder intern, innerhalb einer vom Carnosine gebildeten Bindungstasche komplexiert, so dass das Metallion von Lösungsmittelmolekülen weitgehend abgeschirmt ist oder extern an der Oberfläche des Liganden. In der offenen Struktur können nur zwei Carnosine-Bindungstellen an das Zn^{II} Ion koordinieren, so dass Wassermoleküle freien Zugang zum Zn^{II} Ion haben. Zwei H_2O Solvensmoleküle können freie Koordinationsstellen am Zn^{II} Ion besetzen, was zu einer tetraedrischen Koordinationsgeometrie am Zn^{II} Ion mit zwei stark gebundenen Wasserliganden in der ersten Koordinationssphäre führt.

Die relativen Protonenaffinitäten der (hydratisierten) Zn^{II}/Carnosine Komplexe und verschiedener Carnosine Oligomere $(n\times Carn+H)^+$, n=1-3, wurden sowohl experimentell durch H/D Austauschexperimente mit D_2O als deuterierendem Reagenz, als auch durch ab initio Rechnungen untersucht. Die Bildung von van der Waals Komplexen $(n\times Carn+H)$, n>1, geht einher mit einer deutlichen Steigerung der Protonenaffinität, da die attraktiven Wechselwirkungen zwischen den Carnosine Monomeren durch Protonierung deutlich verstärkt werden. So liegt die Protonenaffinität des Carnosine Dimers um $\Delta PA \approx +41$ kJ mol^{-1} höher als die des Monomers.

H/D Austauschreaktionen sind immer dann effizient, wenn die Protonenaffinitäten des deuterierenden Reagenzes und des deprotonierten Analyten ungefähr gleichgross sind. In Zn^{II}/Carnosine Komplexen wird H/D Austausch jedoch nur für $[Carn\text{-}H,Zn^{II}]^+$ beobachtet, obwohl die berechnete Protonenaffinität des deprotonierten (hydratisierten) Komplexes $[(Carn\text{-}H,Zn^{II}(OH_2)_2)\text{-}H]$ circa 56 kJ mol^{-1} näher an der von D_2O liegt, als die für $[Carn\text{-}2H,Zn^{II}]$ berechnete Protonenaffinität. Dies impliziert, dass im Falle der H/D Austauschreaktion zwischen D_2O und Zn^{II}/Carnosine Komplexen freie Koordinationsstellen am Zn^{II} eine Voraussetzung für die Reaktivität sind. Anders als im Falle der protonierten Carnosine Oligomere $(n\times Carn+H)^+$ sind Protonentransfermechanismen, die eine protonierte funktionelle Gruppe oder zumindestens eine azide Gruppe voraussetzen, nicht auf den H/D Austausch im Falle von $[Carn\text{-}H,Zn^{II}(OH_2)_p]^+$, p=0,2, anwendbar. Der Histidin-Carbonsäurerest in $[Carn\text{-}H,Zn^{II}(OH_2)_p]^+$ ist deprotoniert und die verbleibende azideste Stelle ist die –NH– Gruppe der Amidbindung, die sowohl in $[Carn\text{-}H,Zn^{II}(OH_2)_2]^+$ als auch in $[Carn\text{-}H,Zn^{II}]^+$ vorliegt. Stattdessen wurde ein alternativer H/D Austauschmechanismus in $[Carn\text{-}H,Zn^{II}(OH_2)_p]^+$ vorgeschlagen, der die Koordination des D_2O an das Zn^{II} Ion voraussetzt. Diese Voraussetzung ist in $[\text{Carn-H,Zn}^{\text{II}}]^+$ erfüllt aber – aufgrund mangelnder freier Koordinationsstellen am Zn^{II} – nicht in $[\text{Carn-H,Zn}^{\text{II}}(\text{OH}_2)_2]^+$.

Im ersten Schritt des H/D Austausches in $[\text{Carn-H,Zn}^{\text{II}}]^+$ bindet ein D_2O Molekül an das Zn^{II} Ion und wird anschliessend, in einem zweiten Schritt, in die $\text{Zn}^{\text{II}}\cdots\text{NH}_2$- Bindung zwischen dem Metallion und dem N-Terminus des Carnosine insertiert. Aufgrund der hohen Ladungsdichte am Zn^{II} sind die O-D Bindungen stark polarisiert, und D_2O hydrolysiert bereitwillig in D^+, welches auf den N-Terminus des Carnosine übertragen wird, und ein OD^-, das am Zn^{II} gebunden bleibt (D_2O + H_2N-Carn -> $DO^-\cdots{}^+DH_2N$-Carn). Durch Rotation der Ammonium-Gruppe um die ${}^+DH_2N$–Carn Bindungsachse wird die $DO^-\cdots{}^+DH_2N$-Carn Wasserstoffbrückenbindung durch eine $DO^-\cdots{}^+HDHN$-Carn Wasserstoffbrückenbindung ersetzt. In der Rückreaktion wird das Proton, das an dieser Wasserstoffbrückenbindung beteiligt ist, auf das Hydroxidanion übertragen und DHO gebildet ($DO^-\cdots{}^+HDHN$-Carn -> DOH + DHN-Carn). Damit ist der H/D Austausch komplett. Die maximale Aktivierungsenergie entlang der Reaktionskoordinate dieses Prozesses beträgt 38 kJ mol^{-1}.

Intramolekulare Reaktionen innerhalb gasförmiger Metallion-Solvent Clustern, sogenannten Mikrolösungen, können zu einer Modifikation der chemischen Struktur des Clusters führen, die nicht mit Massenspektometrie nachweisbar ist. Dies ist nur dann der Fall, wenn die Reaktion mit einer Massenänderung einhergeht. In diesem Fall sind Informationen über die Struktur des Clusters notwendig, um Aussagen über die Art der chemischen Reaktion geben zu können. Experimentell können Strukturinformationen von gasförmigen Metallion-Lösungsmittel Komplexen u.a. mit Hilfe von spektroskopischen Methoden, wie z.B. der IR-Spektroskopie gewonnen werden. Da aber gasförmige Ionen im allgemeinen unter isolierten Bedingungen in der Gasphase erzeugt werden, ist die IR-Absorptionsspektroskopie nur bedingt einsetzbar, aufgrund geringer Ionenkonzentrationen. Alternativ muss man eine Art „IR-Action“ Spektroskopie verwenden, bei der eine durch die IR-Strahlung hervorgerufene Wirkung (action) detektiert wird. Durch Verwendung der Freien Elektronen Laser IR Multiphotonen Dissoziationsspektroskopie (FEL-IR-MPD) konnten die IR Spektren von massenselektierten Niob-Acetonitril Komplexen mit der formalen Stöchiometrie $[\text{Nb,nCH}_3\text{CN}]^+$, n=4,5 im spektralen Bereich 780 cm^{-1} – 2500 cm^{-1} aufgenommen werden. Für n=4 sind die erhaltenen Vibrationsbanden nahe an denen des freien, gasförmigen Acetonitril. Die aufgenommenen Spektren liefern keinen Hinweis auf irgendeine Reaktion, die über die Komplexierung des Niob-Monokations hinausgeht. Durch Vergleich mit B3LYP berechneten IR Absorptionsspektren konnten die aufgenommenen Spektren dem planaren, high-spin $[Nb^I(NCCH_3)_4]$ Komplex im Quintett (S=2) Zustand zugeordnet werden.

Für $[Nb,nCH_3CN]^+$, n=5, wurden neue Vibrationsbanden zwischen 1300 – 1500 cm^{-1} detektiert, deren Lage sich deutlich von denen des freien Acetonitrils unterscheiden. Diese Banden können nicht verschobenen $\delta^{sym}(CH_3)$ oder $\delta^{as}(CH_3)$ Banden des gasförmigen Acetonitril zugeordnet werden und deuten eindeutig auf chemische Modifikationen aufgrund intramolekularer Reaktionen hin. Der Vergleich des IR-MPD Spektrums von n=5 mit berechneten IR Absorptionsspektren einer Vielzahl möglicher Isomere mit der Stöchiometrie $[Nb,nCH_3CN]^+$, n=5, und verschiedenen Spinmultiziplitäten, erlaubt eine bestmögliche Zuordnung des aufgenommenen Spektrum zu der metallacyclischen Species $[Nb^{III}(NCCH_3)_3(N{=}C(CH_3)C(CH_3){=}N)]^+$ in einem elektronischen Triplett Zustand (S=1). Dies deutet darauf hin, dass in einer intramolekularen reduktiven Nitrilkopplungsreaktion zwei Acetonitril Liganden miteinander gekoppelt werden. Die berechneten Reaktionskoordinaten für die potentielle Nitrilkopplungsreaktion in $[Nb^I(NCCH_3)_n]$, n=4,5, erklären den deutlichen Unterschied in der Reaktivität. Die reduktive Nitrilkopplung ist nur für $[Nb^I(NCCH_3)_n]$, n=5, exotherm und über eine Aktivierungsbarriere von 49 kJ mol^{-1} erreichbar, wohingegen sie für $[Nb^I(NCCH_3)_n]$, n=4, endotherm ist und mit einer deutlich höheren Aktivierungsbarriere (E_a>116 kJ mol^{-1}) verbunden ist.

10. Acknowledgement

This work has benefited from intense interaction with fellow researchers in various places. I want to thank all those who contributed to this work:

- It has been a great pleasure and experience to do research with Prof. Dr. Gereon Niedner-Schatteburg. His ideas, knowledge, and advise are the fundament of this work.
- Dipl. Chem. Anita Lagutschenkov has contributed significantly to all chapters of this work by reading the script carefully and giving helpful advise. Special thanks for the reaction coordinates in chapter 7 !
- Thanks to Philippe Maitre, Joel Lemaire, Pierre Boissel, and Michel Ortega for introducing me to the Free Electron Laser Spectroscopy.
- The computing projects in this thesis would not have been possible without the help of the IT-Service Team Elmar Gerwalin and Thomas Weber.
- Dipl. Ing. Stefan Joos for valuable support not only in the lab.
- Collaboration with the "next generation" Britta Pfeffer, Steffi Wies, Alex Uhl, Thorsten Daubenfeld was delighting.
- The intense discussion with Prof. Dr. Kit H. Bowen during my stay at the Johns Hopkins University is an invaluable experience, and some of the ideas presented in chapter 5 origin in discussions at Johns Hopkins.
- Dr. Sotiris S. Xantheas for stimulating discussions about the quantum chemical description of solvation processes.
- Inge Krull for help in getting me started in Kaiserslautern.
- I have had the pleasure to learn physical chemistry from great teachers, I am especially indebted to Prof. Dr. Vladimir E. Bondybey, Prof. Dr. H. J. Neusser, Dr. Martin Beyer, and Prof. Dr. Notker Rösch.

I am very happy to acknowledge a scholarship from the Otto Wipprecht foundation, which will support my stay at the Biophysical Sciences Division of the Lawrence Berkeley National Laboratory (LBNL), Berkeley, California in 2005.

Dr. Bjoern Markus Reinhard

born 08/26/1974 in Essen, Germany

Present Address: Department of Chemistry
Technical University Kaiserslautern
Erwin-Schrödinger-Str. 52
67653 Kaiserslautern, Germany
E-mail: bmr@chemie.uni-kl.de

Education

Doctorate	Technical University Kaiserslautern		2003
Diploma	Technical University Munich	Chemistry (Major: Methods of Spectroscopy and Quantum Chemistry)	2000
Intermed. Diploma	University of Bielefeld	Chemistry	1997
Civil Service			1995
Abitur (General Qualification for University Entrance)	Heinrich-Heine-Gymnasium Bottrop		1994

additional courses/schools:

Minerva Summer School "Computational Quantum Chemistry" organized jointly by Lise-Meitner-Minerva Center for Computational Quantum Chemistry (Hebrew University and the Technion, Israel) and the Technical University Berlin (10/2002).

GDCh (German Society of Chemistry) course "High Resolution Biopolymer Mass Spectrometry" at the University of Konstanz, Germany (organizer: Prof. Dr. M. Przybylski) (11/2002).

Professional Experience

Research

2001-2003 Doctoral Research
Advisor: Prof. Dr. Gereon Niedner-Schatteburg
Department of Chemistry, Technical University Kaiserslautern, Germany

Thesis: *Chemistry of Microsolvated Metal Ions*

applied techniques: FT-ICR-MS, ab initio calculations, and infrared multiphoton fragmentation spectroscopy (in cooperation with laboratoire chimie physique, equipe IPG, Université de Paris Sud, Orsay, France)

2000 Diploma
Advisor: Prof. Dr. Vladimir E. Bondybey, PhD
Department of Chemistry, Technical University Munich, Germany

Thesis: *Blackbody Radiation Induced Decay of Hydrated Electrons in a Fourier-Transform-Ion-Cyclotron Mass Spectrometer (FT-ICR-MS)*

1997-2000 Advanced Study Period
Advisor: Dr. Wolfgang Scherer
Department of Chemistry, Technical University Munich, Germany

Interpretation of Experimental and Theoretical Charge Density of Tetrasulfur Tetranitride with the Atoms in Molecules Theory

Teaching

(a) Exercise Course in "Composition of Matter, an Introduction to Basic Concepts of Physical Chemistry" Summer Semester 2001
(b) Exercise Course in "Chemical Kinetics" Winter Semester 2001/2002
(c) Exercise Course in "Chemical Thermodynamics" Summer Semester 2002
(d) Supervision of Practical Courses in Physical Chemistry 2001 - 2003

Awards

1994	Book Award of the Fonds of the German Chemical Industry for best Abitur in Chemistry
2004	Otto Wipprecht Fellowship
2004	Scholarship for the 51. Annual Western Spectroscopy Association Conference

Publications in Peer Reviewed Journals

1. “Molecular recognition in the solid state: topology of experimental and theoretical charge densities for tetrasulfur tetranitride” W. Scherer, M. Spiegler, B. Pedersen, M. Tafipolsky, W. Hieringer, B. Reinhard, A. Down, G. S. McGrady, *Chem. Commun.* **7**, 635 (2000).
2. “Wet electrons and how to dry them“ M. K. Beyer, B. S. Fox, B. M. Reinhard, and V. E. Bondybey, *J. Chem. Phys*. **115**, 9288 (2001).
3. “Co-existence of hydrated electron and metal di-cation in $[Mg,nH_2O]^+$ ” B. M. Reinhard and G. Niedner-Schatteburg, *Phys. Chem. Chem. Phys.* **4**, 1471 (2002).
4. “H_2 Elimination from Hydrated Aluminum Clusters: Acid-Base Reactions Mediated by Intracluster Proton Transfer” B. M. Reinhard and G. Niedner-Schatteburg, *J. Phys. Chem. A* **106**, 7988 (2002).
5. “Ionization energies and spatial volumes of the singly occupied molecular orbital in hydrated magnesium clusters $[Mg,nH_2O]^+$ ”, B. M. Reinhard and G. Niedner-Schatteburg, *J. Chem. Phys.* **118**, 3571 (2003).
6. “Ab initio treatment of magnesium water cluster anions $[Mg,nH_2O]^-$, $n \leq 11$” B. M. Reinhard and G. Niedner-Schatteburg, *Phys. Chem. Chem. Phys.* **5**, 1970 (2003).
7. “Coordination versus Internal Reaction in Niobium-Acetonitrile Complexes Probed by Infrared Multiphoton Dissociation Spectroscopy” B. M. Reinhard, A. Lagutschenkov, J. Lemaire, P. Boissel, P. Maitre and G. Niedner-Schatteburg, *J. Phys. Chem. A* in press.

Poster Presentations

“Blackbody Fragmentation of Cationic Ammonia Clusters”
Brigitte Fox, Bjoern M. Reinhard and V. E. Bondybey
(Spring Meeting of the German Physical Society DPG, Berlin, Germany, 04/2000)

“Reactivity and Energetics of Hydrated Cationic Magnesium Clusters”
Bjoern M. Reinhard and G. Niedner-Schatteburg
(Clustersymposium, Herzogenhorn, Germany, 10/2000)

“Coexistence of Hydrated Electron and Magnesium Dication in $[Mg,nH_2O]^+$”
Bjoern M. Reinhard and Gereon Niedner-Schatteburg
(Gordon Research Conference on Molecular and Ionic Clusters, Ventura, USA, 01/2002)

“H_2 Elimination from Hydrated Aluminum Clusters: Acid-Base Reactions Mediated by Intracluster Proton Transfer”
Bjoern M. Reinhard and Gereon Niedner-Schatteburg
(Minerva School “Computational Quantum Chemistry”, Berlin, Germany, 10/2002)

“H_2 Eliminiation from Hydrated Aluminum Clusters $[Al,nH_2O]^+$: Acid-Base Reaction Mediated by intracluster proton transfer”
Bjoern M. Reinhard and Gereon Niedner-Schatteburg
(Gordon Research Conference on Gaseous Ions, Ventura, USA, 03/2003)

"Ionization Energies and Spatial Volumes of the Singly Occupied Molecular Orbital in Hydrated Magnesium Clusters $[Mg,nH_2O]^+$"
Bjoern M. Reinhard and Gereon Niedner-Schatteburg
(Spring Meeting of the German Physical Society DPG, Hannover, Germany, 03/2003)

"Hydrated Group(II) Metal Water Cluster Anions"
Bjoern M. Reinhard and Gereon Niedner-Schatteburg
(Spring Meeting of the German Physical Society DPG, Hannover, Germany, 03/2003)

Invited Talks

"Coexistence of Hydrated Electron and Metal Cation in Water Clusters"
(Conference of the DFG-Forschergruppe *Low-Energy Electron Collisions*, Kaiserslautern, Germany, 04/25/2003.)

"Chemistry of Microscolvated Metal Ions"
(UC Berkeley Special Seminar, Berkeley, USA, 07/10/2003.)

"Spin Selection Rules in Niobium-Acetonitrile Cation Complexes: Coordination vs. Internal Reaction"
(Johns Hopkins University Special Seminar, Baltimore, USA, 07/16/2003).